MAGNETIC FIELDS AND X-RAY EMISSION IN PRE-MAIN SEQUENCE STARS

Colin Philip Johnstone

A Thesis Submitted for the Degree of PhD
at the
University of St Andrews

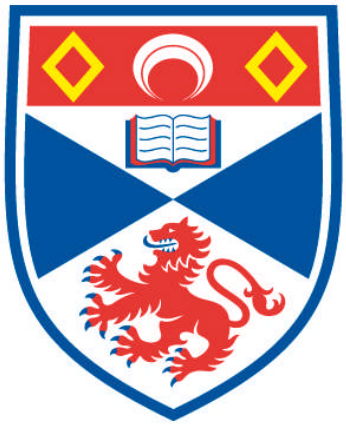

2012

Magnetic Fields and X-ray Emission in Pre-main Sequence stars

by

Colin Philip Johnstone

Submitted for the degree of Doctor of Philosophy in Astrophysics

October 2012

Declaration

I, Colin Johnstone, hereby certify that this thesis, which is approximately 50,000 words in length, has been written by me, that it is the record of work carried out by me and that it has not been submitted in any previous application for a higher degree.

Date Signature of candidate

I was admitted as a research student in September 2008 and as a candidate for the degree of PhD in September 2008; the higher study for which this is a record was carried out in the University of St Andrews between 2008 and 2012.

Date Signature of candidate

I hereby certify that the candidate has fulfilled the conditions of the Resolution and Regulations appropriate for the degree of PhD in the University of St Andrews and that the candidate is qualified to submit this thesis in application for that degree.

Date Signature of supervisor

Copyright Agreement

In submitting this thesis to the University of St Andrews we understand that we are giving permission for it to be made available for use in accordance with the regulations of the University Library for the time being in force, subject to any copyright vested in the work not being affected thereby. We also understand that the title and the abstract will be published, and that a copy of the work may be made and supplied to any bona fide library or research worker, that my thesis will be electronically accessible for personal or research use unless exempt by award of an embargo as requested below, and that the library has the right to migrate my thesis into new electronic forms as required to ensure continued access to the thesis. We have obtained any third-party copyright permissions that may be required in order to allow such access and migration, or have requested the appropriate embargo below.

The following is an agreed request by candidate and supervisor regarding the electronic publication of this thesis:

(i) Access to printed copy and electronic publication of thesis through the University of St Andrews.

Date Signature of candidate

Date Signature of supervisor

Abstract

In this thesis, I use numerical models of stellar coronae to investigate coronal magnetic fields, X-ray emission, and accretion geometries of classical T Tauri stars. This is based on recently published Zeeman-Doppler Imaging (ZDI) magnetograms. I also investigate the effects of time-variable eclipsing of stellar flares on their observed lightcurves.

I investigate how our ability to model stellar magnetic processes is affected by missing magnetic flux in observed ZDI magnetograms and find that the loss of unresolved small-scale field regions has a significant effect on our ability to model magnetically confined X-ray emitting coronae. However, it has little effect on predicted large scale field structures.

I survey the sample of classical T Tauri stars with existing ZDI magnetograms and find that the field complexity is correlated with field strength and stellar rotation rate, such that rapidly rotating stars have weak complex fields, and slowly rotating stars have strong simple fields. It is not clear whether this is a result of the finite resolution of the ZDI technique, magnetic star-disc interactions, or the evolution of pre-main sequence stars. Using observed X-ray emission measures and temperatures for each of these stars, I model the closed X-ray emitting coronae and find that they typically extend several stellar radii from the stellar surface. The coronal extent is primarily determined by the complexity of the magnetic field, with simple fields extending a large distance from the stellar surface, and more complex fields being truncated closer to the stellar surface. Using observed mass accretion rates, I predict circumstellar disc truncation radii for these stars and find that they are typically several stellar radii from the stellar surface, with the locations of accretion footpoints being a strong function of the field strengths and complexities. In several cases, the disc is truncated significantly outside the maximum radius at which the corona can extend. This result is significant as studies into magnetospheric accretion generally assume that the magnetic field has a closed geometry at the inner edge of the disc.

The lightcurve of a typical stellar flare consists of a single impulsive rise phase followed by a slower exponential decay. However, a large number of the observed flares do not possess typical morphologies, and instead show multiple rise phases, or large dips in their lightcurves. Using the largest flares observed by the *Chandra* Orion Ultradeep Project, I show that these

atypical lightcurves could have been caused by the time variable eclipsing of typical flares due to the rotation of the host stars. However, this interpretation is unable to account for the large number of atypical lightcurves in the COUP flare sample, and so other physical mechanisms must be involved. Significantly, I find that most flares that are eclipsed by their host stars still retain typical lightcurves showing no obvious signs of eclipsing.

Acknowledgements

I have been at the University of St Andrews from September 2004 to May 2012 studying physics as an undergraduate and a postgraduate and playing Ultimate Frisbee (until that non-contact sport gave me too many injuries to continue). When I first finished my undergraduate degree in May 2008, I had not applied for any PhD positions. In fact I had already organized to move to California (where I was originally hatched) and teach at the school founded by my grandmother Anne Crowden. By chance, there happened to still be a PhD position open at the time and my Masters project supervisor, Professor Moira Jardine, was able to help me get it. Moira became my supervisor again and is the person most responsible for my being able to finish my PhD and continue as a scientist when I leave St Andrews.

Within a few days of writing this, I will be joining the 'Pathways to Habitability' project at the University of Vienna as a postdoctoral researcher. This would not be possible if it was not for the help of Moira, Duncan Mackay, Hongsheng Zhao, and Scott Gregory who all wrote reference letters for me.

Outside of St Andrews, a lot of people are responsible for my being able to study physics full time. In the last two and a half decades, my family and the society that I live in has given me everything that I need to live healthily and comfortably and I cannot think of anything that I have done to deserve such treatment.

Contents

List of Figures

List of Tables

1 Introduction

1.1 Stellar magnetic fields

Although in situ detections of stellar magnetic fields are not possible, the Zeeman effect on atomic or molecular spectral lines gives a direct method of measuring stellar magnetic fields. Spectral lines are formed by electron transitions between bound energy levels in an atom or molecule[1]. The energy of the emitted/absorbed photon is given by

$$E = |E_f - E_i| \tag{1.1}$$

In an atom (the Zeeman effect in molecular lines is more complicated and not discussed here), in the presence of a magnetic field of strength B, degenerate energy levels with angular momentum quantum number J are split into $2J + 1$ energy levels with the shift in energy of $\mu_0 B g M$, where μ_0 is the Bohr magneton, g is the Landé factor for the energy level, and M

[1]This description of the Zeeman effect is largely based on the description given by Donati & Landstreet (2009).

is the magnetic quantum number with integer values in the range $-J$ to J. The energy of transitions between two shifted energy levels is shifted by an amount

$$\Delta E = \Delta E_f - \Delta E_i = \mu_0 B \left[(g_f - g_i) M_f + (M_f - M_i) g_i \right] \tag{1.2}$$

For dipole transitions, $\Delta M = M_f - M_i$ has possible values of 0, and ± 1. The original spectral line, corresponding to the case where $B = 0$, is therefore split into several lines, each one corresponding to a different value of ΔE. For each of the three values of ΔM, the spectral line is split into several components corresponding to each value of M_i and M_f. For the $\Delta M = 0$ case (i.e. where $M_i = M_f$), these are called the π components and the energy shifts are given by $\mu_0 B M_f (g_f - g_i)$, and since $M_f = -J, -J+1, ..., J-1, J$, the components of the spectral line are shifted symmetrically about the wavelength of the unshifted line. For the $\Delta M = \pm 1$ cases, these are called the σ components and the energy shifts are given by $\mu_0 B[(g_f - g_i)M_f \pm g_i]$ and therefore the components are distributed symmetrically about points shifted to longer and shorter wavelengths than the unshifted line. If $J_i = 0$, $J_f = 0$, or $g_i = g_f$, each of the components of the π component correspond to the same energy transition and therefore have the same wavelength. This is also true for the σ components. Therefore, the original spectral line is only split into three components, collectively called the Zeeman triplet. Magnetic fields can therefore be detected in unpolarized spectral line profiles as a splitting of the spectral lines, or in most cases, as the σ components are shifted by an amount that is smaller than the width of the unperturbed line, as a broadening of spectral lines. The σ components are circularly polarized in opposite directions. The directions of the circular polarization depends on the orientation of the magnetic field with respect to the line-of-sight. Therefore, magnetic fields can also be detected in circularly polarized line profiles. Field strengths derived from unpolarized line profiles have the advantage that they suffer less from the underestimation of field strengths in unresolved regions of the stellar surface, unlike field strengths derived from circular polarization. The polarized line profiles have the advantage that they provide unambiguous detections of magnetic fields, unlike Zeeman broadening in unpolarized line profiles which can often be hard to distinguish from broadening due to other mechanisms. Polarized line profiles also give large amounts of information about the orientation of the magnetic fields.

Magnetic fields on the Sun were first directly detected by Hale (1908a) who found Zeeman

splitting in sunspot spectral lines consistent with $\sim$ 2900 G fields[2]. The existence of a weaker field over the entire solar surface was later proved by Hale (1913) and Hale et al. (1918), although they overestimated its strength by about an order of magnitude. The first detection of a magnetic field on another star was made by Babcock (1947) who estimated polar field strengths of $\sim$ 1500 G for the Ap star 78 Vir. Babcock (1958a) produced the first catalog of magnetic stars, claiming to have detected the Zeeman effect in 89 stars, with another 66 probable detections, most of which are A-type stars. Babcock (1958b) noticed that all of the A-type stars that showed evidence of hosting magnetic fields were chemically peculiar (i.e. Ap) stars. Magnetic fields were later discovered on white dwarfs (Kemp 1970; Angel 1977).

Detecting magnetic fields on late-type stars was not as easy. Babcock (1958a) reported field detections on nine late-type stars, but later studies were unable to confirm any of these detections (Preston 1967). The difficulty may have been due to the fact that the early methods for detecting fields on the Sun and other stars relied on circular polarization. This was necessary since the wavelength shifts of the different components of a spectral line caused by the Zeeman effect is usually smaller than the width of the original spectral line and the various components cannot be resolved. However, if the visible stellar surface contains regions of opposite polarity field, the circular polarisation signatures from these regions will cancel each other out, causing a weakened field to be measured (e.g. Brown & Landstreet 1981). Robinson (1980) developed a technique for measuring field strengths based on unpolarised light in which a fraction of the surface, f, is assumed to be covered in magnetic regions of strength B. Using this technique, Robinson et al. (1980) provided the first reliable detections of magnetic fields on late-type stars. They measured surface averaged field strengths, given by fB, of a few kG on ξ Boo A and 70 Oph A.

Reliable early surface averaged magnetic field measurements on late type stars were collected by Saar (1990), Saar (1996b), and Saar (2001). A recent updated collection is given by Reiners (2012). They showed that late type stars possess a range of surface averaged field strengths, from $\sim$0.1 kG to $\sim$4 kG, and that the strength of a star's magnetic field is clearly related to its mass and rotation rate. Saar (1996b) found a clear relation between rotation rate

[2]Prior to this, Bigelow (1889) suggested that the Sun hosts a large magnetic field based on the shapes of coronal plumes observed during solar eclipses. Other clues to the existence of the solar magnetic field existed, such as the observation by Sabine (1852) that the levels of variations in the Earth's magnetic field correlate well with the number of sunspots on the stellar surface. George Hale's motivation for attempting to observe the Zeeman effect in sunspot spectra came from his incorrect theory that sunspots lie in the centre of vortices, or whirls (Hale 1908b). He speculated that the existence of charged particles in these vortices might produce strong magnetic fields.

and magnetic field strength, which I reproduce in Fig. 1.1, given by $fB \propto P_{rot}^{-1.7}$. The relation between field strength and Rossby number ($Ro = P_{rot}/\tau_c$, where P_{rot} and τ_c are the rotation period and convective turnover timescale respectively) appears to be even better (Saar 2001). These correlations are not unexpected for stars with similar internal structures to the Sun. Most of the magnetic flux seen on the solar surface is thought to originate in the layer between the radiative core and the outer convective envelope called the tachocline where the rotation rate changes rapidly with radius. For more rapidly rotating stars, the shear in the tachocline is stronger, and so it is reasonable to think that this can lead to stronger magnetic fields. The relation between rotation rate and magnetic field strength is not so clear for lower mass fully convective main-sequence stars of spectral type M7 and later (see Fig. 1.2). Only a weak correlation is seen for stars of spectral type M7-M7.5, and a weaker correlation is seen for M8.0 type stars. No clear correlation is seen for M8.5-M9.5 type stars (Reiners & Basri 2010).

The relation between magnetic field strength and rotation rate is consistent with the observed relations between rotation and indirect indicators of magnetic activity, such as X-ray emission and Ca II H+K emission[3]. For instance, Skumanich (1972) famously found that both rotation rate and Ca II H+K emission decay with stellar age and speculated that this is a result of a relation between rotation rate and magnetic activity. As discussed in Section 1.2, more rapidly rotating stars show higher levels of X-ray emission, though this relation does saturate at very high rotation rates. The saturation of X-ray emission is accompanied by the saturation of all other indirect indicators of magnetic activity at Rossby number of $\sim$0.1. Reiners et al. (2009) found clear evidence that this saturation is also accompanied by the saturation of the magnetic field in a sample of M type stars. The saturation of the magnetic field in fast rotators shown in Fig. 1.1 and occurs at values of surface averaged magnetic field strength of $\sim$2-3 kG, with no fields stronger than $\sim$4 kG. It is unclear whether this saturation is present for earlier type stars as Zeeman broadening is hard to detect in rapidly rotating F-K type stars due to strong rotational broadening (rotational broadening is not such a problem in M type stars due mainly to their smaller radii).

[3]The Ca II H+K emission lines at 3968.5Å and 3933.7Å respectively are commonly used indicators of magnetic activity on the Sun and on other stars. Charles Augustus Young noticed that the emission in these lines varied over the solar disc with its highest intensity being at the limb and in regions of sunspots and faculae (Joy & Wilson 1949). Babcock & Babcock (1955) used solar magnetograms, produced using the solar magnetograph invented by Babcock (1953), to find that regions of strong emission in the Ca II H+K lines tend to coincide with regions of strong magnetic fields. Further studies confirmed and quantified this strong correlation (e.g. Schrijver et al. 1989).

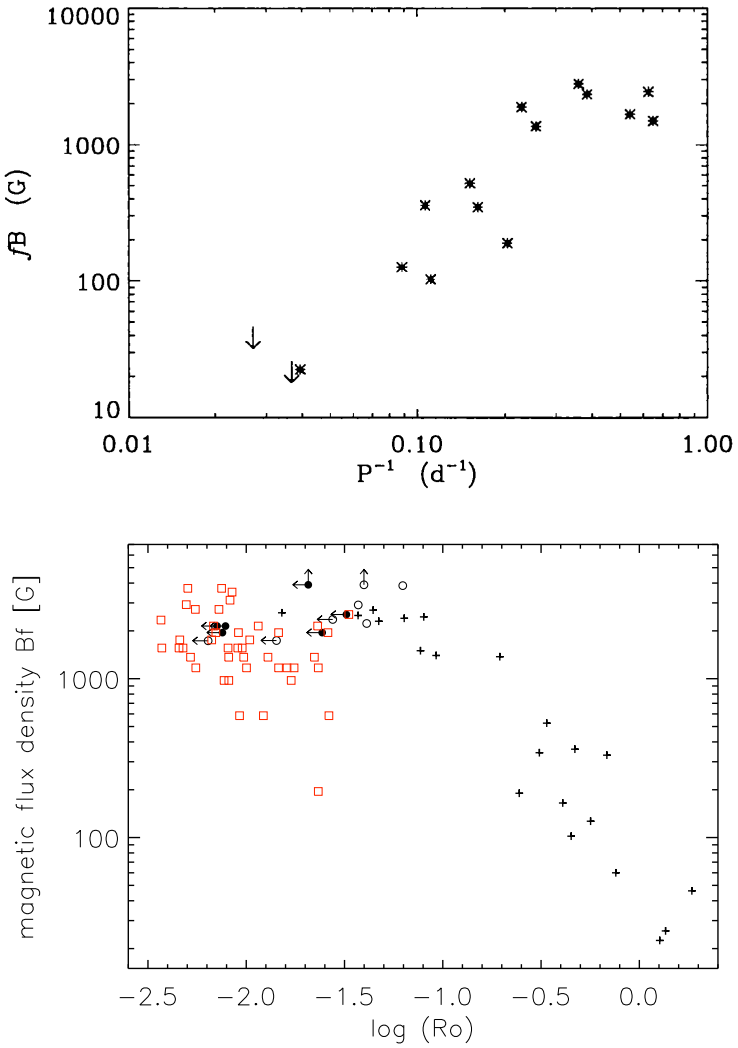

Figure 1.1: *Upper panel*: reproduced from Saar (1996a) showing surface averaged magnetic field strength fB against inverse rotation period for a sample of stars. *Lower panel*: reproduced from Reiners (2012) showing fB against Rossby number for a sample of Sun-like stars (crosses), M0-M6 type stars (circles), and M7-M9 type stars (red squares).

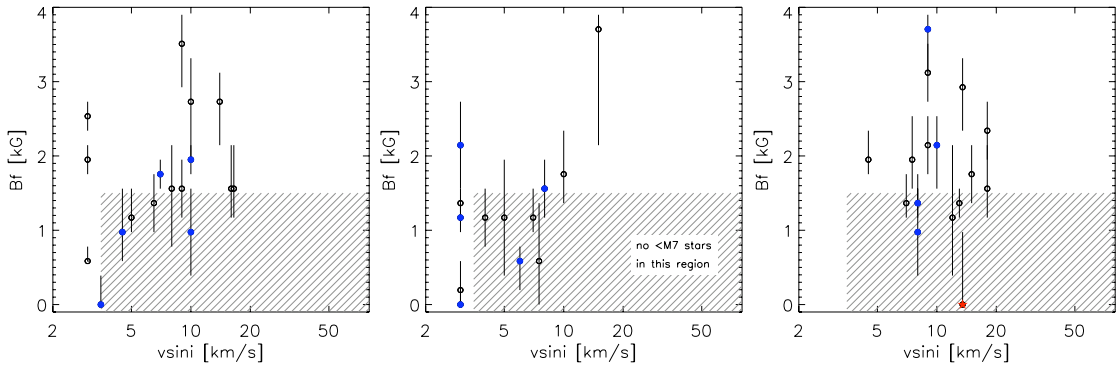

Figure 1.2: Reproduced from Reiners & Basri (2010). Surface averaged magnetic field strength fB for a sample of late M type stars showing a weak correlation between rotation rate and fB for stars of spectral type M7-M7.5 (left panel), a weaker correlation for M8.0 type stars (middle panel), and no clear correlation for M8.5-M9.5 type stars (right panel).

As with the solar magnetic field, stellar magnetic fields have highly complex geometries that diverge significantly from simple dipole configurations. This can be seen in several ways. For instance, methods that use circular polarization signatures to measure field strengths generally underestimate these strengths relative to the measurements given by unpolarized line profiles. This is due to the cancellation of the circular polarization signals from regions on the stellar surface of opposite polarity field. Johns-Krull et al. (1999b) measured a surface averaged field strength of 2.5 kG for the classical T Tauri star BP Tau. Assuming that BP Tau's field is a pure axisymmetric dipole, they predicted that they should measure an average line-of-sight component of the field of $B_z \sim 600$ G (where B_z in this case is not just the magnitude, but also takes into account the direction of the field, such that opposite polarity regions cancel out). However, using high-resolution spectropolarimetry, Johns-Krull et al. (1999a) was unable to detect a net polarization in photospheric absorption lines, putting an upper limit on the average longitudinal field of ± 200 G, indicating that the strongest regions of the star's magnetic fields are held in non-dipolar field structures. Reiners (2012) collected measurements for the surface averaged field strengths derived using polarized and unpolarized line profiles for a sample of main-sequence M dwarfs and found that in general, the values derived from circular polarized light are less than 10% of those derived from unpolarized light. This is shown in Fig. 1.3.

The complex topologies of stellar magnetic fields can also be indirectly inferred from observations of the distributions of starspots. Starspots are the stellar analogue of Sunspots, which coincide spatially with regions of strong magnetic field on the solar surface. It is reasonable to assume that starspot locations trace the locations of strong magnetic fields on stel-

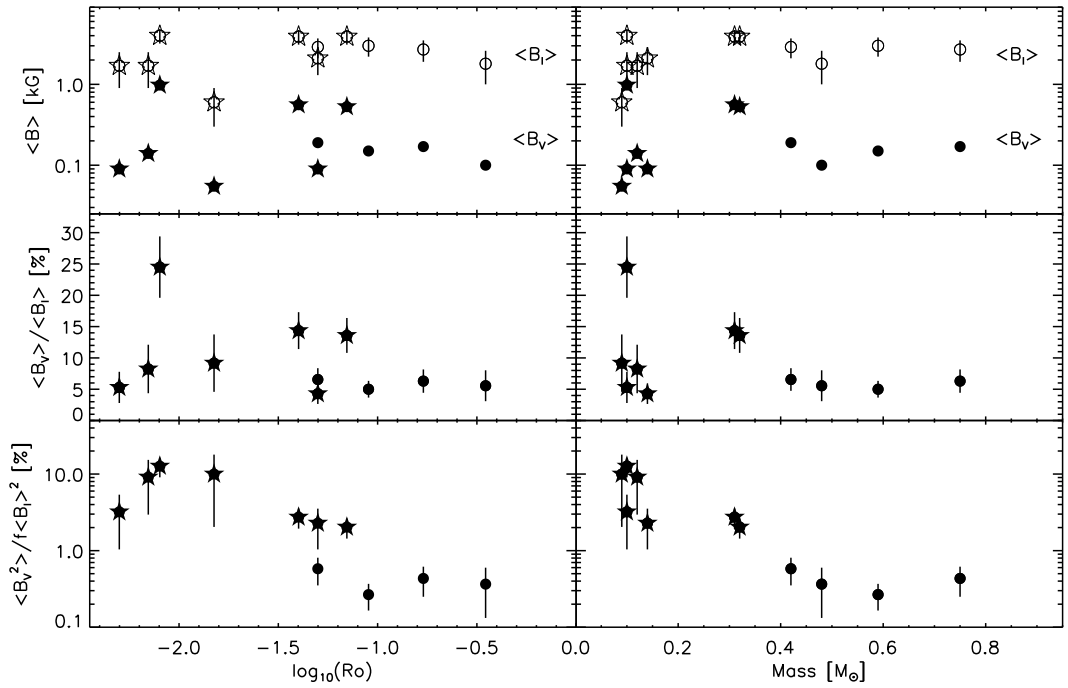

Figure 1.3: Reproduced from Reiners (2012). *Upper panels*: surface averaged field strengths derived using unpolarized light $< B_I >$ (open symbols) and polarized light $< B_V >$ (closed symbols) for a sample of main-sequence M dwarfs. *Middle panels*: the ratio $< B_V > / < B_I >$ for the stars in the sample. *Lower panels*: the ratio of magnetic energies $< B_V^2 > / f < B_I >^2$ for the stars in the sample. Stars show fully convective stars and circles show stars with radiative cores.

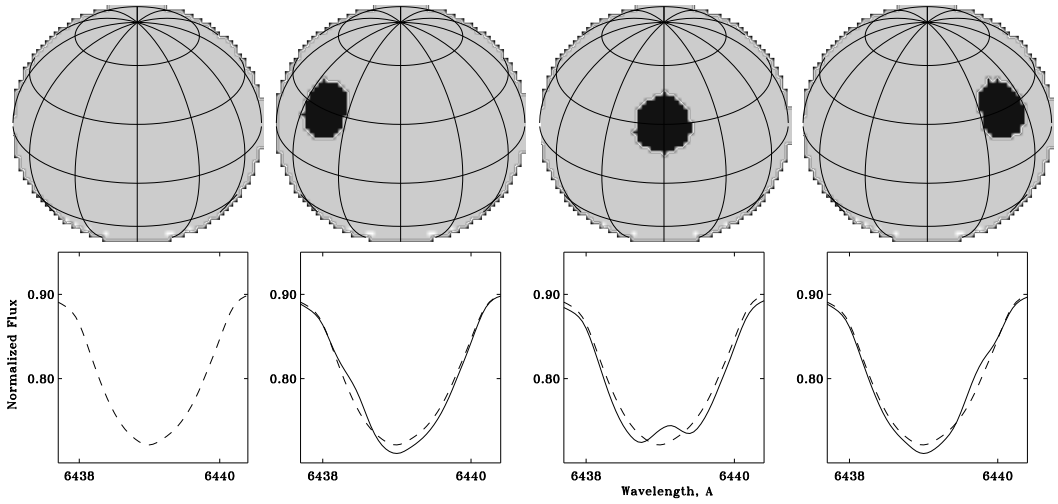

Figure 1.4: Reproduced from Berdyugina (2005). Cartoon showing the effect that a starspot has on a single absorption line as it moves across the stellar disc due to the rotation of the star.

lar surfaces. The locations of starspots can be mapped using the Doppler Imaging technique, originally proposed by Deutsch (1958), which relies on the fact that as stars are rotating, the radial velocity of a point on the stellar surface is a function of the position of that point. The effect that any feature on the stellar surface has on the light that comes from the star will depend upon its location on the surface. Consider a single spectral line that is rotationally broadened. As a feature rotates into view, it will affect the shorter wavelength side of the spectral line only. As the star rotates, the portion of the spectral line that is affected by the feature moves from the shorter wavelength part of the line to the centre of the line, and then to the longer wavelength part. Therefore, information can be gained about the longitudinal position of a feature on the stellar surface. The location in the spectral line that is affected by the feature as it first rotates into view is also a function of the latitude of the feature. A feature near the equator will have a larger velocity than one at a higher latitude because it will be further from the stellar rotation axis. Therefore, information can also be gained about the latitude of the feature. This is shown for a single starspot in Fig. 1.4. Doppler Imaging of several stars, such as the rapid rotators ($P_{rot} \approx 0.5$ days) V374 Peg (Donati et al. 2006a) and AB Dor (Hussain et al. 2007), have shown complex brightness distributions. For an extensive review of starspot observations, see Strassmeier (2009).

An early attempt to extend the Doppler Imaging technique to give information about the distribution of magnetic flux over the stellar surface was the Magnetic Surface Imaging (MSI) technique developed by Saar et al. (1992). MSI attempts to invert the unpolarised line pro-

files of Zeeman sensitive spectral lines to constrain the distribution of field over the surface. However, since unpolarised line profiles yield no information about the orientation of the surface field, the MSI technique requires arbitrary assumptions about the field orientation. Semel (1989) presented the Zeeman-Doppler Imaging (ZDI) technique, which uses circular polarized line profiles. The spectropolarimetric signature (i.e. the circular polarization as a function of wavelength) is sensitive to the orientation of the magnetic field, and therefore, ZDI can yield information about all three components of the magnetic field over the stellar surface. The ZDI technique was first used to detect the magnetic field of an unresolved star by Donati et al. (1989), and to produce the first magnetic maps by Donati et al. (1992). Donati et al. (1997) presented spectropolarimetric detections of magnetic fields on 14 stars. Almost all of them showed complex circularly polarised line profiles, indicating that the fields are non-dipolar, with the stellar surface covered in regions of opposite polarity field. Donati & Collier Cameron (1997) used the ZDI technique to reconstruct the surface magnetic field for the young rapidly rotating star AB Dor. They found that AB Dor hosts a strong magnetic field covering a large fraction of the visible surface in a highly complex configuration (see Fig. 1.5).

Since these initial results, ZDI magnetograms have been published for a large number of main-sequence and pre-main sequence stars. For instance, repeated observations of the young F7-type star τ Bootis have shown reversals in the polarity of the magnetic field at the visible pole (Donati et al. 2008c; Fares et al. 2009). These reversals appear to be periodic with a period of $\sim$2 years, and may be the first direct detection of a magnetic cycle on a star other than the Sun. It is worth noting here that Poppenhaeger et al. (2012) failed to detect an X-ray cycle on τ Bootis.

Donati et al. (2008b), Morin et al. (2008b), and Morin et al. (2010) conducted a survey of a large number of main-sequence M dwarfs and found a clear link between the structures and strengths of these fields and the internal structures of their host stars. Donati et al. (2008b) reconstructed the large scale field topologies of six early M dwarfs, all of which host radiative cores, and found that the fields of the higher-mass stars in their sample were predominantly non-axisymmetric with most of the magnetic energy in the toroidal component of the field and only 18-53% of the magnetic energy in the poloidal component. However, the two lowest mass stars in the sample (OT Ser and CE Boo) possessed fields that are primarily axisymmetric and poloidal, with 67-95% of the magnetic energy in the poloidal component. The surface averaged magnetic fields of these stars were found to vary between 27 G and 172 G, and

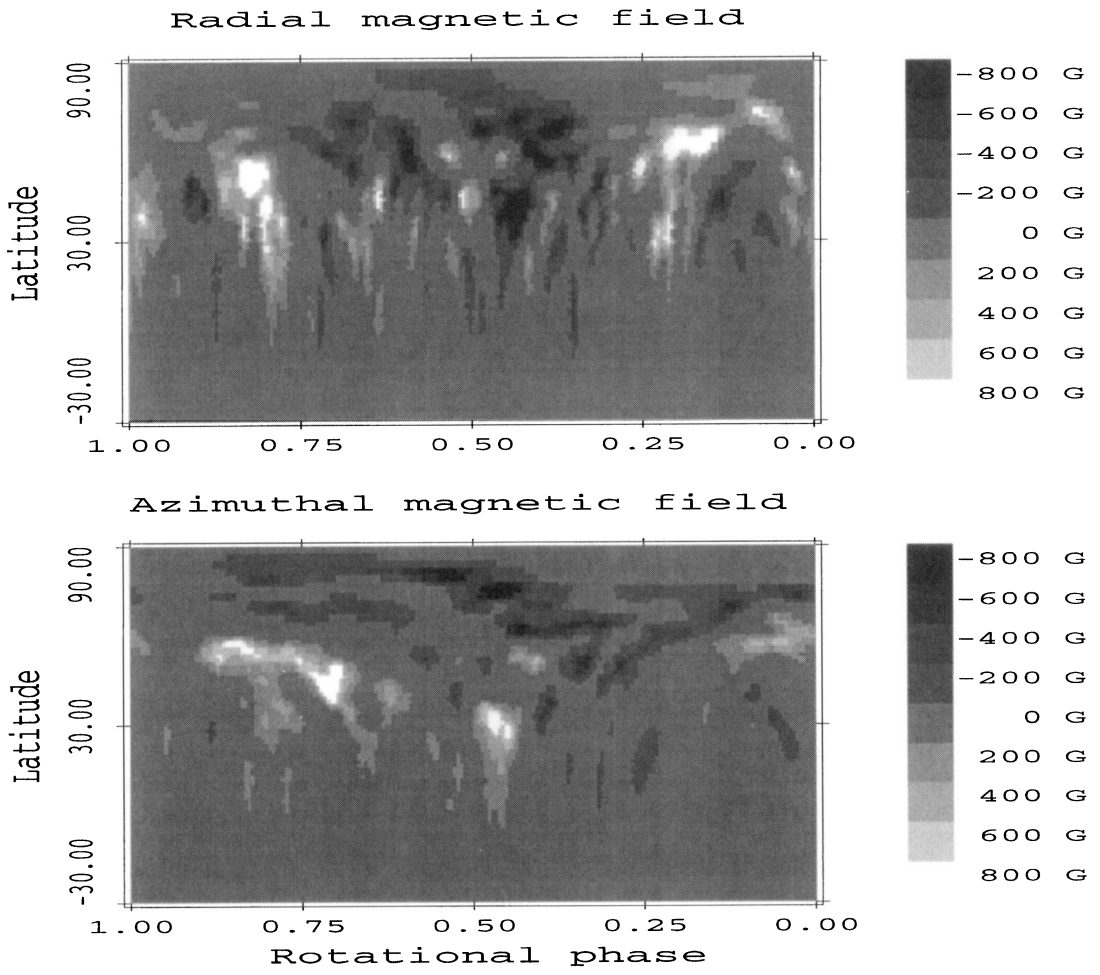

Figure 1.5: Reproduced from Donati & Collier Cameron (1997). Early ZDI reconstruction of the magnetic structure of AB Dor.

were not correlated with stellar mass. They suggested that the difference in the field structure between the higher mass and lower mass stars in the sample is related to the difference in the internal structures of these stars, with the low mass stars having much smaller radiative cores than the high mass stars. Morin et al. (2008b) analysed a sample of five M4-type stars, all of which lie on the fully convective boundary, and found that their large scale fields are primarily axisymmetric and poloidal, with 87-99% of the magnetic energy held in the poloidal component of the field and typical surface averaged field strengths of ~ 0.5 kG. These fields are significantly stronger than those on the sample of early M dwarfs. Morin et al. (2010) reconstructed the large-scale magnetic topologies of six late fully convective M dwarfs and found that the stars in the sample show either strong simple axisymmetric fields, or weak more complex non-axisymmetric fields.

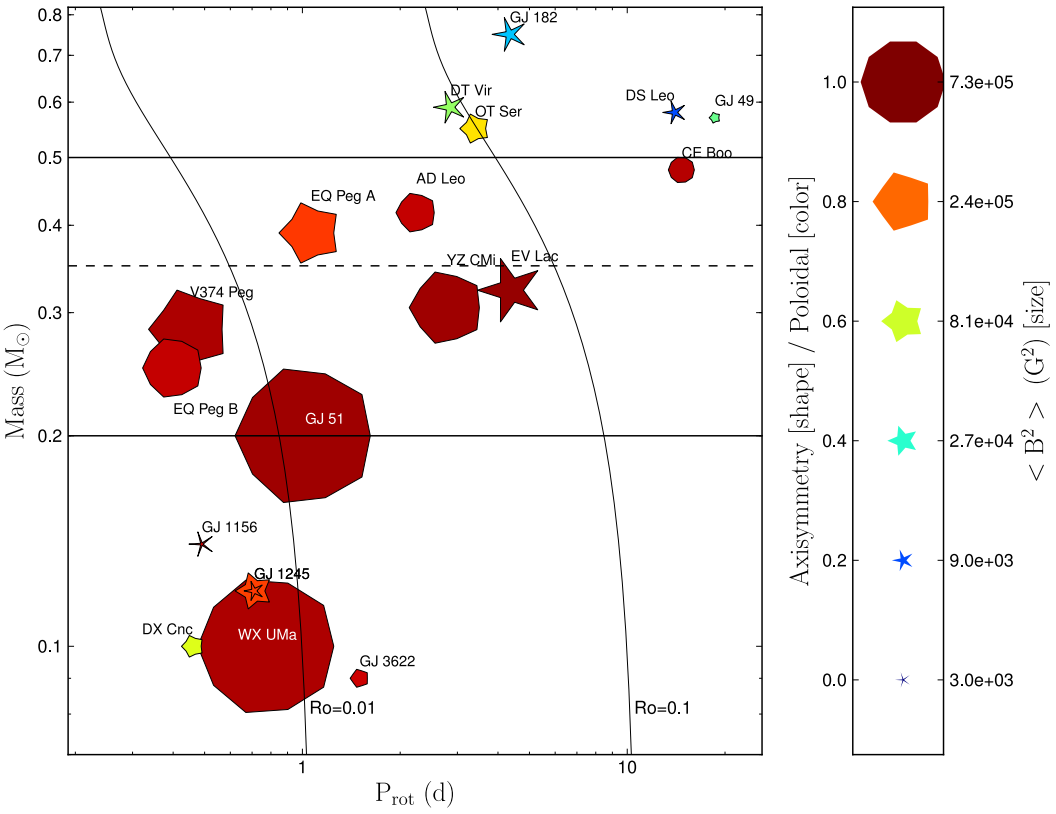

Figure 1.6: Reproduced from Morin et al. (2010). Stellar mass against rotation period for the sample of M dwarfs with published ZDI magnetograms. The size of each point represents the strength of the star's magnetic field and the shape represents the degree of axisymmetry. Decagons represent purely axisymmetric fields, and sharp complex shapes represent more non-axisymmetric fields. The colour represents the fraction of the magnetic energy held within the poloidal component of the field. The dashed horizontal line shows the fully convective limit.

A similar result is seen for the sample of classical T Tauri stars that have been studied using the ZDI technique. In this sample, stars that are not old enough to have developed radiative cores show strong simple fields, similar to fully convective stars in the sample of M dwarfs, and stars that are no longer fully convective have weaker complex fields. The exception for this is the low-mass star V2247 Oph which is unlikely to develop a radiative core, and yet has a highly complex field structure. These results are reviewed in more detail in Section 1.3.2.

1.2 X-ray emission

One of the most important manifestations of stellar magnetic activity is X-ray emission. On the Sun, X-ray emission primarily originates from magnetically confined coronal structures, as shown in Fig. 1.7. X-ray emission from the solar corona was first detected using V-2 rockets by Burnight (1949) and the first direct imaging of the Sun in X-rays was by Blake et al. (1963) who demonstrated that the emission originates from plasma of temperatures $\sim 10^6$ K located above magnetic active regions. Since then, X-ray imaging of the solar corona, primarily from the X-ray telescopes on *Skylab* in the 70s and the *Yohkoh* telescope in he 90s, has shown that the solar X-ray emitting corona is made up of closed magnetic field structures. The link between X-ray emission and closed magnetic loops is further strengthened by the observations of coronal holes, which are regions of open magnetic field that are dark in X-rays due primarily to the low densities of plasma in these regions. As can be seen in Fig. 1.7, the total solar X-ray luminosity closely traces the solar magnetic cycle, with the maximum luminosity at magnetic maximum. Fisher et al. (1998) and Pevtsov et al. (2003) showed that over the solar surface, the photospheric magnetic flux is strongly correlated with the X-ray luminosity of coronal regions. This correlation, shown in Fig. 1.8, is true over the quiet Sun, X-ray bright points, solar active regions, and the entire solar disc.

The first detection of X-ray emission from stars other than the Sun came in the mid-70s. Catura et al. (1975) detected X-ray emission from the binary system Capella and found a luminosity of $\sim 10^{31}$ erg s^{-1} from plasma with a temperature of $\sim 10^{6.9}$ K. This was interpreted as a scaled up version of solar activity (Mewe et al. 1975). A detailed review of the early X-ray observations of stars other than the Sun is given by Güdel (2004). Using the *Einstein* observatory, Vaiana et al. (1981) identified 143 X-ray emitting stars and showed that X-ray emission is ubiquitous among all types of stars. Since then, observations primarily using the *Einstein* observatory, ROSAT, XMM-Newton, and *Chandra* have dramatically improved our understand-

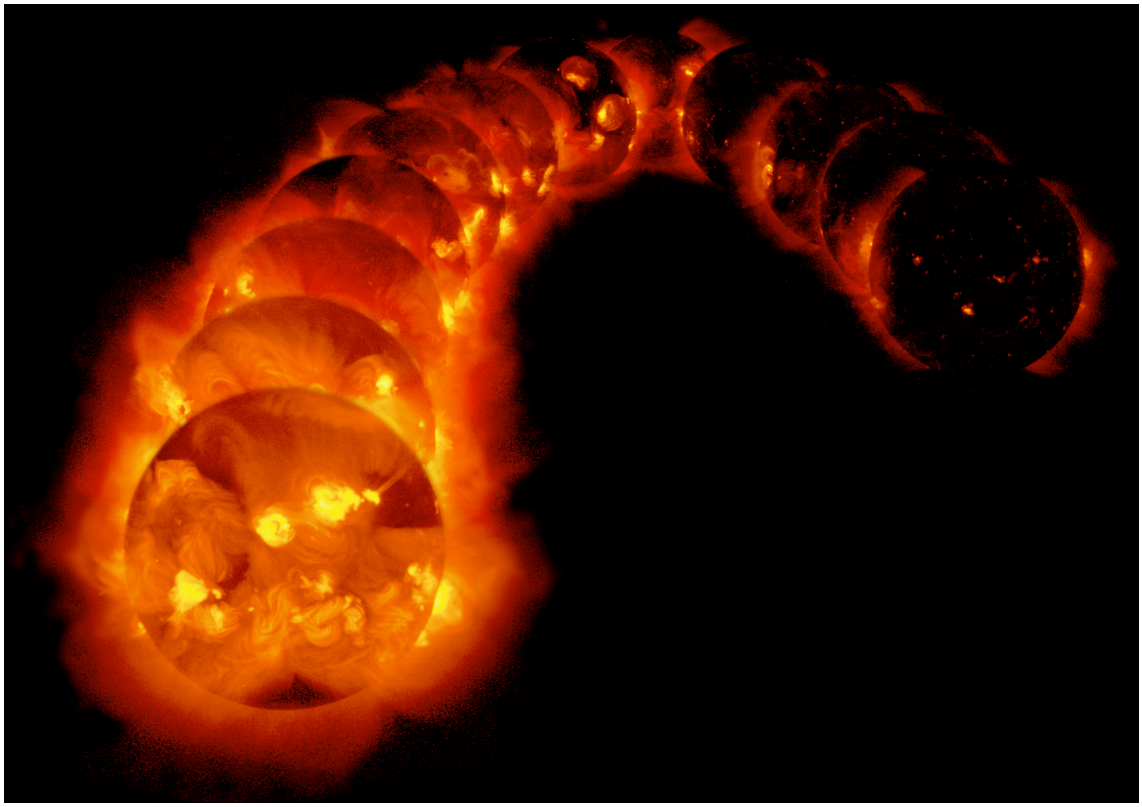

Figure 1.7: The solar X-ray emitting corona over half of a solar cycle from a time of maximum activity in 1991 on the left to a time of minimum activity in 1995 on the right. The solar X-ray image is from the Yohkoh mission of ISAS, Japan. The X-ray telescope was prepared by the Lockheed-Martin Solar and Astrophysics Laboratory, the National Astronomical Observatory of Japan, and the University of Tokyo with the support of NASA and ISAS.

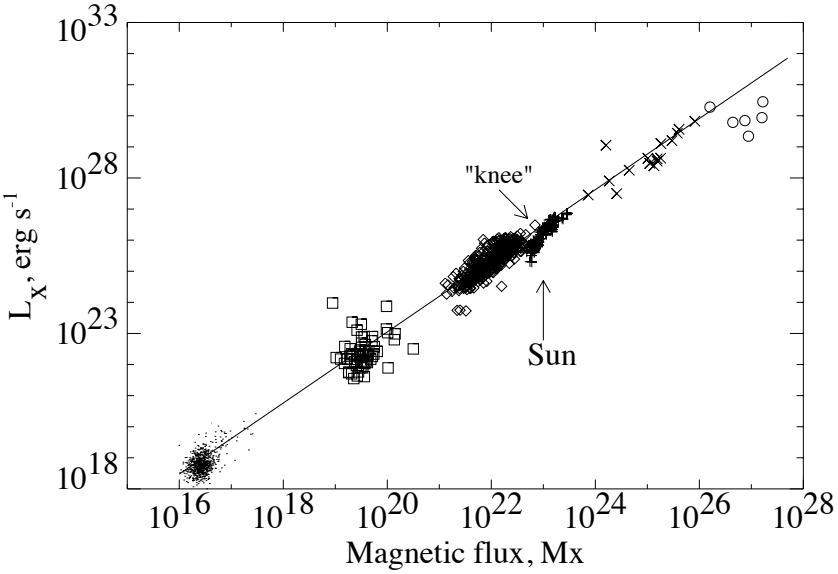

Figure 1.8: Reproduced from Pevtsov et al. (2003). Correlation between X-ray luminosity and magnetic flux for regions of the quiet Sun (dots), solar X-ray bright points (squares), solar active regions (diamonds), the entire solar disc (pluses), G, K, and M dwarfs (crosses), and T Tauri stars (circles).

ing of stellar X-ray emission. Most notably, the ROSAT All-Sky Survey (RASS) detected over 145,000 sources (Voges et al. 1999).

The relation between stellar magnetic activity and X-ray emission seen on the Sun extends very clearly to other stars. This can be seen for the low mass main-sequence stars and T Tauri stars in Fig. 1.8, indicating that stellar X-ray emission primarily originates from similar physical mechanisms, i.e. closed coronal magnetic field structures. One of the interesting results from the large amount of information that we now possess about stellar X-ray emission is the strong correlation between X-ray luminosity and rotation rate. This is expected given the correlation between magnetic flux and rotation rate, discussed in the last section, and the correlation between X-ray emission and magnetic flux. This was identified by Vaiana et al. (1981) who found that some of the young rapid rotators in their sample were also above-average X-ray emitters. Pallavicini et al. (1981) found that for late-type stars, there is a clear correlation between X-ray luminosity and rotational velocity given by $L_x \propto (v \sin i)^{1.9}$. Similar relations were found by Maggio et al. (1987) and Wood et al. (1994). A recent diagram showing this correlation is given by Wright et al. (2011) and reproduced here in Fig. 1.9. One feature of the X-ray activity-rotation relationship that was first noted by Micela et al. (1985) and can clearly be seen in Fig. 1.9 is the saturation of X-ray emission at high rotation rates. This is related to the saturation of magnetic field strengths shown in Fig. 1.1. The critical

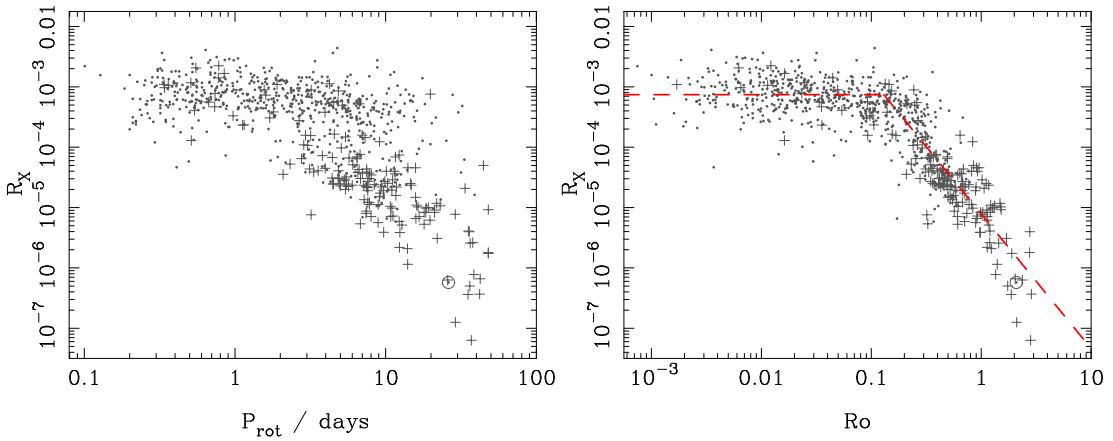

Figure 1.9: Reproduced from Wright et al. (2011). X-ray luminosity as a fraction of bolometric luminosity against rotation period (left) and Rossby number (right).

rotation rate at which X-ray activity saturates is a function of spectral type, with saturation taking place at slower rotation rates for lower mass stars (Pizzolato et al. 2003). Prosser et al. (1996) found that at extremely high rotation rates, X-ray emission actually begins to decrease. This effect is called 'supersaturation'.

Several mechanisms have been proposed for the saturation and supersaturation phenomena. Vilhu (1984) proposed that the saturation of X-ray emission might be a result of the saturation of the dynamo processes responsible for the generation of the magnetic field, such that as the rotation rates of stars increase beyond the saturation point, the amount of magnetic flux produced by the stellar dynamo does not increase. This interpretation is contradicted by O'dell et al. (1995) who showed that surface spot coverage, which they assume traces magnetic activity, does not saturate at the rotation rate that would be expected given the observed X-ray saturation. However, the observed saturation of the surface averaged field strengths for rapidly rotating main-sequence M dwarfs supports this interpretation. Alternatively, Vilhu (1984) proposed that the X-ray emission might be saturated at the point where the stellar surface becomes completely covered in active regions. However, if this was the case, only small amounts of rotational modulation of X-ray emission would be expected from saturated stars, in contradiction to observations (Flaccomio et al. 2005). Jardine & Unruh (1999) proposed that the saturation phenomenon might be caused by centrifugal stripping of coronal plasma. As the stellar rotation rate increases, the corotation radius (i.e. the radius at which an object rotating at Keplerian velocities is corotating with the stellar surface) moves towards the star. If the stellar magnetic field is distorted by centrifugal forces at the corotation radius, faster rotators will have less extended coronae. At low rotation rates, the coronal plasma will

be at relatively low densities. As rotation rate increases, the corotation radius will move towards the star, and thus the coronal extent will decrease. Initially, this decrease in the size of the corona is overcome by a corresponding increase in the plasma density due to centrifugal forces, leading to increased coronal emission. However, at a critical rotation rate, the decrease in the coronal size overcomes the increase in plasma density and the coronal emission initially saturates, and then begins to decrease. This can account for the observed saturation and supersaturation of X-ray emission from rapidly rotating stars.

1.3 Classical T Tauri stars

T Tauri stars (TTSs) are young, low-mass, pre-main sequence stars that are characterised by large irregular variability and the presence of strong chromospheric emission lines. They were first classified by Joy (1945) who estimated that they have spectral types from F5 to G5. Joy (1945) noticed that absorption lines typically seen in stellar spectra are not present in some TTSs and showed that the strengths of emission lines (many of which are present in the solar chromospheric emission spectrum) varied from star to star, and also varied in time for each star.

The spectra of TTSs vary in both the depths of photospheric absorption lines, and the strengths of emission lines. Based on the differences in spectra, TTS are separated into two groups: classical T Tauri stars (CTTSs) and weak-line T Tauri stars (WTTSs; often NTTSs for naked T Tauri stars). Although more sophisticated methods are often used, the most common method for distinguishing between CTTSs and WTTSs is by using the equivalent width (EW) of the Hα emission line: stars with Hα EW greater than 10 Å are classified as CTTSs. The spectra of CTTSs generally show several strong emission lines, such as the Hα and Ca II IRT lines, and shallower absorption features due to the superposition of the normal photospheric spectrum with an extra bluish continuum spectrum: this effect is called 'veiling'. Four examples of TTS spectra are given in Fig. 1.10. The lower spectrum is for the WTTS TAP 57, which shows no clear Hα or Ca II IRT line emission, and several photospheric absorption features. The upper spectrum is for the strongly-accreting CTTS DR Tau, which shows strong Hα and Ca II IRT line emission, but no clear photospheric absorption features. For a review of TTS spectra, see Basri (2007). CTTSs also show excess continuum emission in UV, optical, and IR superimposed on their normal photospheric black-body spectrum. This was found by Mendoza V. (1966) and confirmed by subsequent observations. Fig. 1.11 shows observed and

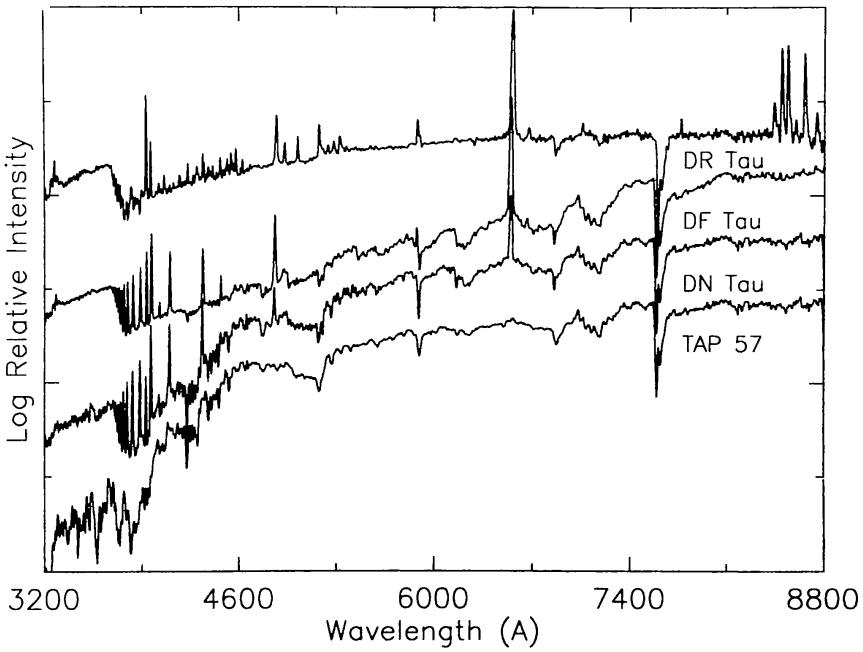

Figure 1.10: Reproduced from Bertout (1989). Optical spectra for four T Tauri stars with different levels of accretion. The lower star is a WTTS and thus has no accretion. The level of accretion increases from TAP 57 to DR Tau, thus causing the increase in veiling of photospheric absorption lines and the strength of the Hα emission line ($\lambda \sim 6500$ Å). The Ca II IRT lines ($\lambda \sim 8500$ Å) are clearly visible in the spectrum of DR Tau.

modelled spectral energy distributions (SED) for the CTTSs AA Tau and BP Tau. The dashed line shows the expected photospheric contribution and the black dots show the observed fluxes. Clearly at several wavelengths, the excess emission dominates over the normal stellar blackbody emission.

The difference between CTTSs and WTTSs originates from the fact that CTTSs are surrounded by circumstellar discs and are actively accreting material from the inner edges of their discs. The IR excesses seen in CTTS SEDs are a result of the absorption and reemission of stellar photons by dust at the inner edges of these discs, and the excess UV continuum and line emission originates from the base of accretion shocks where accreting material, falling at approximately free-fall velocities (typically ∼100-500 km s^{-1}) impacts the stellar chromosphere (Basri & Bertout 1989; Koenigl 1991). Further evidence for this interpretation comes from the strong correlation between IR excess, UV excess, millimeter continuum emission, and Hα emission (Kenyon & Hartmann 1995). WTTSs are generally considered to be in a more advanced stage of their evolution, having lost their circumstellar discs and therefore stopped accreting. This interpretation is supported by the observations of transitional discs that show weak near-IR excess emission while still retaining strong mid-IR excess emission

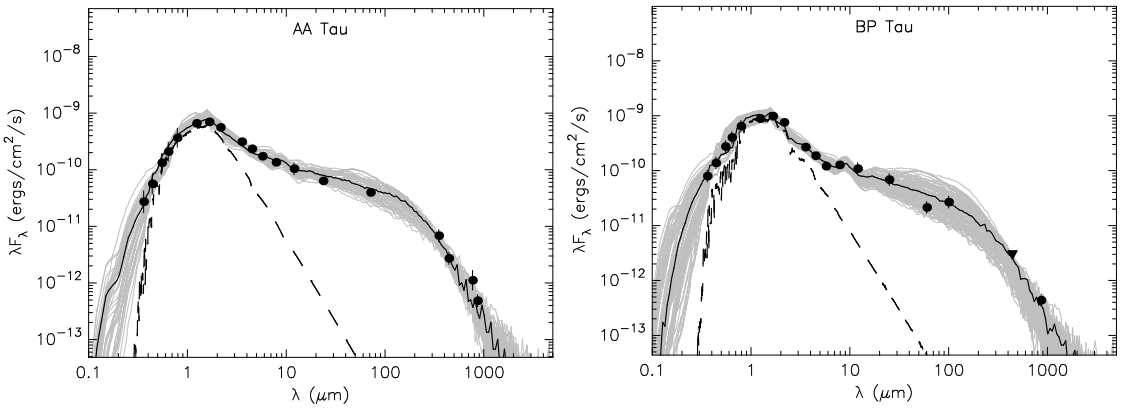

Figure 1.11: Reproduced from Robitaille et al. (2007). Observed (black points) and modelled spectral energy distributions for the CTTSs AA Tau and BP Tau. In each plot, the dashed line shows the contribution from the central star, and the solid black line shows the best fit model assuming excess continuum emission from accretion shocks at UV wavelengths, and a circumstellar disc at IR wavelengths.

(Strom et al. 1989; Najita et al. 2007). The SEDs of these objects imply that their discs have evolved to a state where they are optically thin out to ∼1-20 AU.

1.3.1 Circumstellar discs and accretion

Circumstellar discs are formed as a result of the conservation of angular momentum and the gravitational collapse of molecular clouds. Discs begin to form immediately after the beginning of the collapse and in general last ∼10 Myr. For a recent review of the formation and evolution of protoplanetary discs, see Williams & Cieza (2011). Although there are indirect indicators of the presence of circumstellar discs around CTTSs, such as IR excess emission in SEDs and the eclipsing of the central star by the warped inner disc edge (see the case of AA Tau discussed in Section 4.1.1), direct imaging of circumstellar discs is also possible. This was first carried out by O'dell & Wen (1994) and McCaughrean & O'dell (1996). McCaughrean & O'dell (1996) used the *Hubble Space Telescope* to observe dark silhouettes against the bright background of the Orion Nebula. The discs in their sample extend up to 1000 AU from the central star.

Early disc and accretion models, such as the one presented by Lynden-Bell & Pringle (1974), assumed that discs extend all the way to the stellar surface and accretion occurs onto the star through a boundary layer. Although stars with weak fields may accrete through a boundary layer, CTTSs appear to have magnetic fields that are strong enough to truncate their discs far from their surfaces. Ghosh et al. (1977), Ghosh & Lamb (1979a), and Ghosh & Lamb (1979b) developed a model for accretion onto magnetic neutron stars where cir-

cumstellar disc material is disrupted at the Alfvén surface, which is where the kinetic energy density in the disc is balanced by the magnetic energy density. Outside the Alfvén surface, disc material orbits the central star at Keplerian velocities. Inside of the Alfvén surface, the flow of material is dominated by the magnetic field and is highly sub-Keplerian. Therefore, material accretes onto the central star and is channelled along magnetic field lines. When the material impacts the stellar surface, it causes accretion shocks at high densities ($n_e \sim 10^{12} - 10^{13}$ cm^{-3}) and temperatures of a few MK (typical CTTS coronal temperatures are ~ 10 MK). This model was applied to CTTSs by Camenzind (1990) and Koenigl (1991). Evidence that discs are truncated far from the stellar surface, and not at a boundary layer at the stellar surface, comes from several sources. If material accreted onto the stellar surface through a boundary layer, it would be expected to add significant amounts of angular momentum to the star, which contradicts the fact that CTTSs have relatively slow rotation rates. The shapes of CTTS SEDs are consistent with holes separating the stellar surface from the inner edge of the disc, and inverse P-Cygni profiles are consistent with matter falling towards the stellar surface at large velocities. Furthermore, the locations of hotspots on the surfaces of stars inferred from Doppler Imaging maps to produce maps of Ca II IRT excess emission imply that accretion is chanelled by magnetic fields onto the stellar surface (Donati et al. 2010a; Donati et al. 2011a; Donati et al. 2011b).

Early magnetospheric accretion models generally assumed that the star's magnetic field was a pure axisymmetric dipole. If this was the case, accreting material would flow along large dipolar field lines and impact the stellar surface at high latitudes in axisymmetric bands extending around the entire star. However, in most cases, the magnetic fields for CTTSs tend to be significantly more complex than axisymmetric dipoles, and have dipole components that are tilted with respect to the star's axis-of-rotation.

Romanova et al. (2003) and Romanova et al. (2004) used full 3D MHD accretion simulations to investigate accretion onto stars with inclined dipole fields. They found that the structure of the inner edge of the accretion disc, the trajectories of the accretion streams, and the distribution of accretion footpoints can be significantly affected by the tilt in the dipole component of the field (even for inclination angles of $\sim 5°$). This non-axisymmetric accretion has several observational consequences, such as introducing rotational modulation in a star's lightcurve due to the complex distribution of hotspots on the stellar surface. They also confirmed the earlier suggestion by Terquem & Papaloizou (2000) that a tilted dipole component

can cause a warped inner disc, similar to what is seen on the CTTS AA Tau (Bouvier et al. 1999).

As discussed in Section 1.3.2, there is now a sample of CTTSs with published ZDI magnetograms. This has made it possible to study accretion onto stars with real magnetic field geometries. Gregory et al. (2006b) and Gregory et al. (2008) used a simple accretion model and potential field extrapolations of realistic magnetic fields based on ZDI magnetograms to show that more complex field structures can have a significant effect on magnetospheric accretion. They found that when the field is not a simple dipole, accretion footpoints can be distributed at a range of latitudes and in complex patterns. Long et al. (2011) performed 3D MHD simulations of accretion onto the CTTS BP Tau. BP Tau's magnetic field can be approximated as the sum of a 1.2 kG dipole, and a 1.6 kG octupole, both tilted with respect to the star's axis-of-rotation. They found that the disc is disrupted several stellar radii from the stellar surface, and accreting material falls in two streams towards each of the star's poles along large dipolar field lines. Closer to the star, the octupole component dominates over the dipole component, and material falls along octupolar field lines to high latitudes. Due to the presence of the octupole component of the field, the latitudes at which accretion impacts the stellar surface in this case are higher than what would be expected for the pure dipole case. Romanova et al. (2011) presented similar simulations for the magnetic field of V2129 Oph. V2129 Oph's magnetic field can be approximated as the sum of a 0.35 kG tilted dipole and a 1.2 kG octupole (Donati et al. 2007). Romanova et al. (2011) found that as accreting material left the disc, it would fall along large dipolar field lines towards high latitudes. However, as material gets closer to the star, the octupole component begins to dominate over the dipole component and each accretion stream is broken into two streams, with one heading towards high latitudes (higher than if the field was a pure dipole), and the other heading towards mid-latitudes. These simulations are discussed in more detail in Section 3.5.

1.3.2 CTTS magnetic fields

Before magnetic fields were detected on TTSs, several studies attempted to estimate their strengths based on magnetospheric accretion models (Koenigl 1991; Collier Cameron & Campbell 1993; Shu et al. 1994). The first detection of a magnetic field on a TTS was given by Basri et al. (1992) who observed increases in the equivalent widths of photospheric Zeeman-sensitive absorption lines which were not present in Zeeman-insensitive lines for the WTTS

TAP 35. The enhanced equivalent widths, which were a result of Zeeman-splitting, were consistent with field strengths of ∼1 kG. The next direct detection of a magnetic field on a WTTS came from Donati et al. (1997) who used spectropolarimetric observations to detect fields on V410 Tau and HD 283572. The first detection of a field on CTTSs came from Guenther et al. (1999) who detected fields on three CTTSs, and one WTTS. They found surface averaged field strengths of 2.35 kG and 1.1 kG for the CTTSs T Tau and LkCa 15 respectively. Johns-Krull et al. (1999b) were the first to successfully apply the Zeeman broadening technique to a CTTS. They presented optical and IR spectra for BP Tau and observed significant broadening in the Ti I (2.22 μm) photospheric absorption line which they could only account for by Zeeman broadening consistent with surface averaged field strengths of 2.5 kG. Johns-Krull (2007) presented magnetic field measurements for 14 CTTSs (including AA Tau, BP Tau, and TW Hya) and found surface average field strengths of between ∼1 kG and ∼3 kG. The measured field strengths were found to be significantly larger than the predictions of magnetospheric accretion models, which is unsurprising given that these accretion models assume dipole geometries. Further unresolved measurements of magnetic fields on CTTSs showed that they indeed possess strong kG fields (Yang et al. 2005; Yang et al. 2008; Yang & Johns-Krull 2011). These results are summarized by Reiners (2012).

It is often necessary to be able to resolve the field structures of CTTSs. For instance, in order to estimate the distance from the star at which the disc is truncated by the magnetic field, it is necessary to know the strength of the dipole component of the field, and this cannot be inferred from surface averaged field strengths. In recent years, a large number of ZDI magnetograms have been published for CTTSs as part of the Magnetic Protostars and Planets project (MaPP). In Section 1.1, I review some of the results of ZDI studies for main-sequence stars which have shown that the strength and structure of a star's magnetic field is a function of the star's internal structure. Similar results are seen in the sample of CTTSs, though the situation is complicated by the fact that the internal structure of pre-main sequence stars is determined by both mass and age. Pre-main sequence stars of all masses are initially fully convective, and develop radiative cores as they age. The age at which this happens is a strong function of stellar mass, with higher mass stars developing radiative cores at much earlier ages than lower mass stars. There are currently ten such stars with published ZDI magnetograms (Donati et al. 2010a; Donati et al. 2008a; Hussain et al. 2009; Hussain et al. 2009; Skelly et al. 2012; Donati et al. 2011b; Donati et al. 2007; Donati et al. 2011a; Donati et al. 2010b;

Donati et al. 2011c). Of these ten stars, only one (V2247 Oph; ∼0.36 $M_\odot$) is of such a low mass that it will never develop a radiative core, and this star possesses a weak, highly complex, non-axisymmetric field. Two of the other nine stars (AA Tau and BP Tau) have yet to develop radiative cores, both of which have fields that are dominated by strong axisymmetric dipole and octupole components. The other stars in the sample (including MT Ori which may have developed a radiative core, or may be very close to developing a radiative core) generally show much weaker dipoles and much more complex, non-axisymmetric fields. These results are summarised by Gregory et al. (2012) who proposes that the magnetic topology of a star can be predicted by its position on the Hertzsprung-Russell diagram.

1.3.3 X-ray emission

Using *Einstein* observations of the Orion Nebula Cluster, Ku & Chanan (1979) suggested that some of their X-ray sources may be TTSs. Feigelson & Decampli (1981) observed several TTSs with *Einstein* and estimated X-ray luminosities of $\sim 10^{30} - 10^{31}$ erg s^{-1}, a factor of $\sim 10^5$ greater than what is observed on the Sun. Since then, several large X-ray surveys, most specifically the *ROSAT* All-Sky Survey (RASS; Neuhaeuser et al. 1995), the *Chandra* Orion Ultradeep Project (COUP; Preibisch et al. 2005), and the XMM-Newton extended survey of the Taurus molecular cloud (XEST; Güdel et al. 2007), have significantly increased our knowledge of X-ray emission processes on CTTSs.

X-ray emission from CTTSs comes from a variety of mechanisms, the most important of which is emission from hot magnetically confined coronal plasma in most cases. Whereas plasma temperatures in the solar corona are typically a few MK, the plasma temperatures responsible for X-ray emission from TTSs can be as high as 50 MK and are typically above 10 MK. On the main sequence, the level of X-ray emission observed is strongly correlated with rotation rate (see Fig. 1.9), with the fastest rotators showing the strongest X-ray emission, up until rotation periods of a few days, at which point, the X-ray emission saturates. TTSs show no correlation between X-ray emission and rotation rate. Instead, X-ray emission is strongly correlated with stellar mass and stellar luminosity, as shown in Fig. 1.12. X-ray emission is also correlated with stellar surface area, however, not as strongly as it is with stellar mass (Güdel et al. 2007). This suggests that the L_x dependence on mass is more fundamental than the dependance on stellar surface area. By assuming that all X-ray emission originates in isothermal magnetically confined coronae in hydrostatic equilibrium, Jardine et al. (2006)

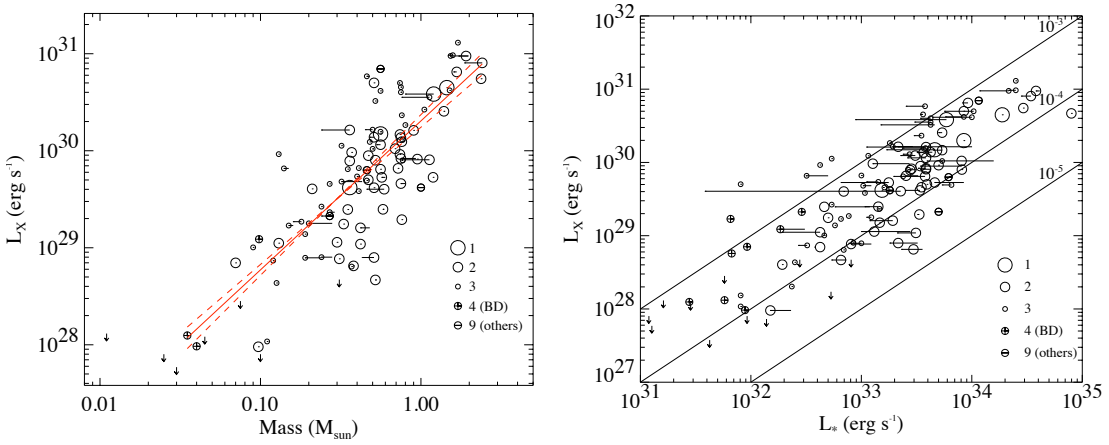

Figure 1.12: Reproduced from Güdel et al. (2007). X-ray luminosity as a function of stellar mass (left panel) and stellar luminosity (right panel) for the sample of pre-main sequence stars observed as part of the XEST project.

showed that this mass dependence can arise naturally from variations in surface gravities and coronal sizes (see Fig. 1.13).

By considering the magnetic flux and X-ray emission observed from the quiet Sun, solar active regions, the entire solar disc, dwarf stars, and T Tauri stars, Fisher et al. (1998) and Pevtsov et al. (2003) showed that the relationship between total unsigned magnetic flux and X-ray emission is almost linear over 12 orders of magnitude. This is shown in Fig. 1.8. Johns-Krull (2007) presented magnetic field measurements for 14 CTTSs using the broadening of Zeeman-sensitive spectral lines. Using these measurements, and the relation of Pevtsov et al. (2003), they predicted X-ray luminosities for their stars and compared these predictions to observed values from the literature. They found that the observed X-ray luminosities are typically an order of magnitude below the predicted values. A similar result was found by Yang & Johns-Krull (2011) for a larger sample of TTSs, and is shown Fig. 1.14. They suggest that this may be due to the strong fields of TTSs suppressing convection over much of the stellar surface.

One peculiar feature of X-ray emission from TTSs is the fact that the X-ray luminosities are on average slightly lower for CTTSs than for WTTSs. This effect was identified in the Taurus-Auriga star forming region by Neuhaeuser et al. (1995) who found median X-ray luminosities of $\approx 10^{29.7}$ erg s^{-1} for WTTSs and $\approx 10^{29.1}$ erg s^{-1} for CTTSs. This result was initially controversial because it was not found in other star-forming regions, but the contradictory results were probably caused by the use of different indicators to classify CTTSs (i.e. accretion proxies or disc proxies) and the result has since been confirmed (Flaccomio et al.

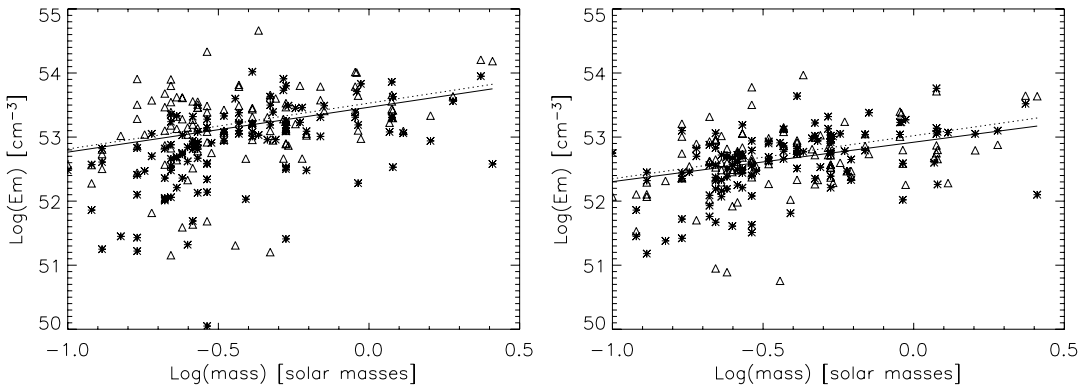

Figure 1.13: Reproduced from Jardine et al. (2006). Mass dependence of observed (crosses) and predicted (triangles) coronal X-ray emission measures for stars observed as part of the *Chandra* Orion Ultradeep Project (COUP; Preibisch et al. 2005) for high-temperatures (left panel) and low temperatures (right panel). Predicted emission measures come from assuming isothermal coronae in hydrostatic equilibrium (see the model presented in Section 2.5 of this thesis) and show that the observed mass dependence of X-ray emission can arise naturally from variations in surface gravities and coronal sizes.

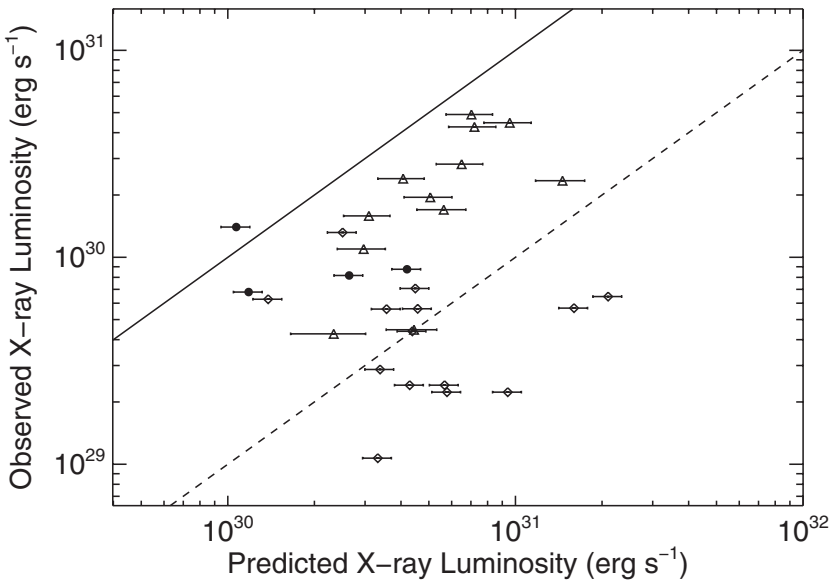

Figure 1.14: Reproduced from Yang & Johns-Krull (2011). Observed X-ray luminosities against values predicted based on the measured field strengths and the relation between X-ray emission and magnetic flux of Pevtsov et al. (2003) for a sample of TTSs. The solid line represents the line of equality and the dashed line is an order-of-magnitude below the solid line.

2003; Getman et al. 2005b; Güdel et al. 2007). Several mechanisms might be responsible for this effect, such as X-ray absorption by circumstellar discs in CTTSs, absorption by dense material in accretion columns, the inhibition of magnetic activity by accretion, and decreased activity in CTTSs due to their lower rotation rate.

One source of X-ray emission in CTTSs is accretion shocks where accreting material impacts the stellar surface. Accreting material should impact the stellar surface at approximately free-fall velocities, thus heating chromospheric plasma to several MK, causing it to emit a soft X-ray spectrum. Using data from the COUP sample, Preibisch et al. (2005) found no evidence of a correlation between X-ray emission and mass accretion rate (in fact, they found a weak, statistically insignificant anti-correlation). Although this does not prove that accretion shocks are not responsible for some X-ray emission in CTTSs, it does show that X-ray emission is not primarily generated in accretion shocks. Further evidence that accretion shocks are not the primary mechanism of X-ray emission in CTTSs comes from the plasma temperatures derived from the X-ray spectra of these stars, which are usually of the order ~ 10 MK (Getman et al. 2005b; Güdel et al. 2007) whereas accretion is unlikely to be able to deposit enough energy on the surfaces of accreting stars to heat the plasma to temperatures above a few MK (Preibisch et al. 2005). One star where this appears not to be the case is the close-by CTTS TW Hya. Analysis of the X-ray spectrum of this star shows that its X-ray emission is dominated by emission from a low-temperature (~ 3 MK) and high density ($\sim 10^{12}$ cm^{-3}) plasma. This star is discussed in more detail in Section 4.1.6.

2

Methods in modelling stellar coronae

In Chapters 3, 4, and 5, I use magnetic field extrapolations of stellar surface magnetograms to model the 3D coronal field structures of hypothetical and real stars. Using these extrapolations, I model closed X-ray emitting coronae and magnetospheric accretion. In this chapter, I describe the models used in the next three chapters. This chapter is set out as follows: in Section 2.1, I describe the surface flux transport model used to generate the simulated surface magnetograms used in Chapter 3; in Section 2.2, I give a brief introduction to spherical harmonics; in Section 2.3, I describe how spherical harmonics are used to describe the 2D magnetic fields over the surfaces of stars; in Section 2.4, I describe the potential field model used to extrapolate surface fields to higher radii; in Section 2.5, I explain the model used to predict coronal plasma pressures from magnetic field structures; in Section 2.6, I explain the magnetospheric accretion model used to predict circumstellar disc truncation radii and model accretion onto CTTSs.

2.1 Magnetic flux transport models

The solar magnetic field can roughly be broken down into two parts: the strong small scale field found within active regions, and the weak large scale general field found over the rest of the surface[1]. The strong small scale field probably originates in the transition region between the Sun's radiative core and its convective outer envelope, known as the tachocline. Due to the rapid radial variation in rotation rate in the tachocline, strong magnetic fields are generated, and through magnetic buoyancy, the field rises through the convection zone and emerges onto the solar surface in the form of bipolar active regions which can be seen in visible light as dark sunspots (for a review of solar dynamo models, see Charbonneau 2010). The weak large scale field is a product of the time evolution of the strong small scale field.

The number of bipolar active regions, and therefore the number of sunspots, on the solar surface varies periodically over 11-year activity cycles (Schwabe 1844). The latitudes at which sunspots are visible starts high at the beginning of each cycle and decreases slowly over the course of the cycle. Sunspots come in pairs, with the leading spot at lower latitudes to the trailing spot (this is known as 'Joy's law'). Hale et al. (1919) showed that the two spots in each pair had opposite magnetic polarities, with all of the leading spots in a given hemisphere having the same polarity, which is opposite to the polarities of the leading spots in the other hemisphere. Furthermore, they discovered that the polarities reverse between sunspot cycles (collectively this is known as 'Hale's polarity law'). Babcock (1959) discovered that the Sun's polar magnetic field also reverses polarity during solar maximum, as can be seen in the magnetic butterfly diagram shown in Fig. 2.1. Therefore, the 11-year sunspot cycle is in fact a 22-year magnetic cycle.

Leighton (1964) showed that the weak large scale solar field could be generated by the transport over the solar surface of magnetic flux from active regions. This was based on the discovery of supergranulation which is a rapidly evolving pattern in the velocity field over the solar surface. The pattern consists of cells with typical diameters of $\sim$30 Mm and horizontal velocities directed towards the edges of each supergranule of $\sim$200 m s^{-1} (Rieutord & Rincon 2010). The supergranular pattern evolves rapidly on the timescale of a few days. Due to the

[1]This is a simplification as the general solar surface is covered in highly complex field structures on very small scales, known as the solar magnetic carpet. At any time, the amount of magnetic flux emerging onto the solar surface is dominated by these very small scale fields. However, as these fields have much shorter lives than the larger field structures seen in active regions, at any time, the magnetic flux on the surface is dominated by magnetic flux that has emerged as larger active regions.

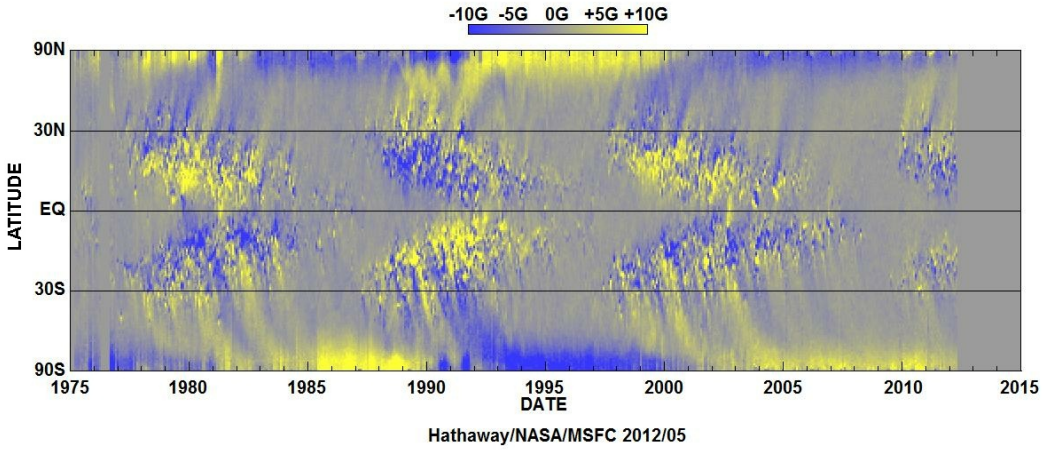

Figure 2.1: Solar magnetic butterfly diagram. Image credit: NASA/MSFC/David Hathaway.

horizontal motions, magnetic flux is expelled to the boundaries of each supergranular cell, and as the supergranual pattern evolves, magnetic flux is moved over the solar surface in what can be approximated as a random walk. Leighton (1964) modelled this random walk as a diffusion of magnetic flux over the surface of the Sun, described by diffusion constant D. In this model, when magnetic fluxes of opposite polarity overlap, they cancel each other out, leaving a weaker field given by the sum of the original opposite polarity fields. Coupled with Joy's law and Hale's polarity law, this model is able to explain several aspects of the solar activity cycle. Since the trailing spots in each sunspot pair emerges onto the solar surface closer to the poles than the leading spot, as magnetic flux spreads out, the flux from the trailing spots reach the poles before the flux from the leading spots. As the trailing spots of each sunspot pair have the same polarity, and the opposite polarity to what they had in the previous sunspot cycle, the combined flux from the large number of trailing spots cancels out the polar field from the previous cycle, and causes the observed polar polarity reversal half way through the cycle. Similarly, the flux from the lower latitude leading spots diffuses across the equator and overlaps with the opposite polarity flux from the leading spots in the opposite hemisphere.

Previously, Babcock & Babcock (1955) and Babcock (1961) had suggested that a poleward flow of magnetic flux from the trailing spots could cause the polarity reversal of the polar field in the middle of each sunspot cycle. In their model, this is a result of a large scale meridional surface flow towards the poles, and not a result of diffusion. Using Doppler shift measurements, this meridional flow was discovered, and measured to have a velocity of ~ 10

m s^{-1} (Duvall 1979).

It turns out that both supergranular diffusion and meridional flow are necessary to properly account for the Sun's polar field. Devore et al. (1984) showed that without meridional flow, the flux transport model is only able to produce a dipole-like field distribution at the poles, and not the 'topknot' structure that is seen, i.e. where the field is more concentrated at the poles than would be expected for a pure dipole field. However, assuming a meridional flow of 10 m s^{-1} over the entire surface leads to the magnetic flux being too concentrated at the poles, with field strengths of several tens of Gauss. Combining these two processes such that the evolution of the field is a result of diffusion and a latitude-dependent meridional flow which peaks at low latitude and then reduces to zero at higher latitudes leads to a larger polar cap with more reasonable field strengths. This model is also able to explain the 'surges' of magnetic flux towards the poles seen in magnetic butterfly diagrams (Wang et al. 1989).

For a historical review of the development and use of the flux transport model, see Sheeley (2005). The flux transport model in its modern form, as described by van Ballegooijen et al. (1998) and Mackay et al. (2004)[2], includes the effects of the emergence of bipolar active regions, meridional flow, differential rotation, and supergranular diffusion to evolve the radial component of the magnetic field forward in time according to the differential equation[3]

$$\frac{\partial B_r}{\partial t} = \frac{1}{\sin\theta}\frac{\partial}{\partial\theta}\left[\sin\theta\left(-u(\theta)B_r + D\frac{\partial B_r}{\partial\theta}\right)\right] + \frac{D}{\sin^2\theta}\frac{\partial^2 B_r}{\partial\phi^2} - \Omega(\theta)\frac{\partial B_r}{\partial\phi} + Q \qquad (2.1)$$

where θ is the colatitude, $u(\theta)$ is the latitude dependent meridional flow, $\Omega(\theta)$ is the differential rotation, and Q is a source term describing the emergence of field onto the solar surface. Typically, the photospheric diffusion constant is taken to be ~ 450 km^2 s^{-1}. For the Sun, the meridional flow is approximately given by

[2]The description of the flux transport model given here is primarily based on the description given in Mackay et al. (2004). Although the model has been described in several papers, I concentrate on Mackay et al. (2004) because I use the surface magnetograms from their two simulated stars in Chapter 3.

[3]Baumann et al. (2006) argues that as the current flux transport model only considers diffusion in two dimensions (i.e. over the stellar surface), the rate at which fields decay are underestimated, and it is necessary to account for diffusion in the radial direction. This addition to the model corresponds to an extra diffusion term in Eqn. 2.1.

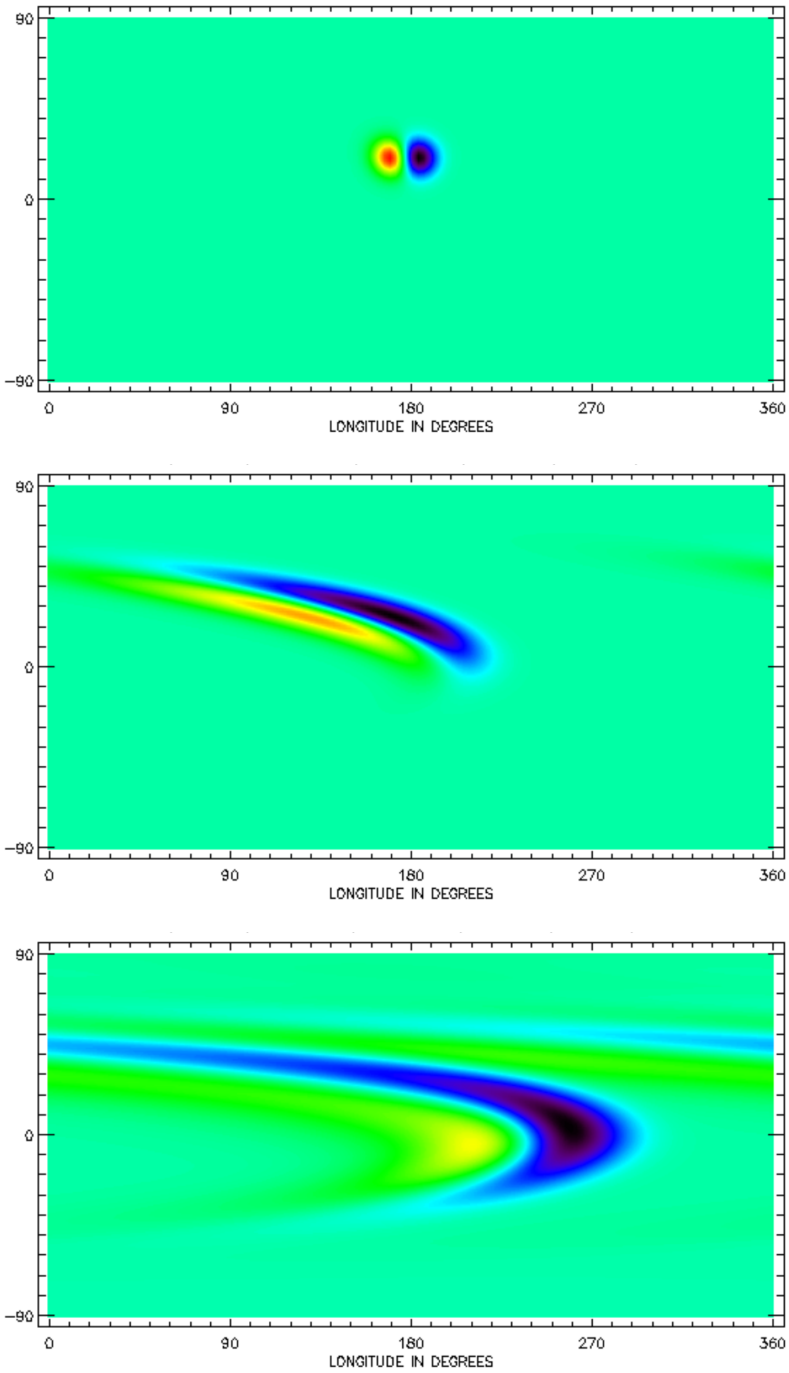

Figure 2.2: Images courtesy of Joe Llama. Magnetograms showing the time evolution of a single bipolar active region over one year using the flux transport model and solar values of diffusion, differential rotation, and meridional flow. The evolution results in a significant reduction in the field strengths that cannot be seen in these magnetograms. From top to bottom, the magnetograms have maximum field strengths of 300 G, 22 G, and 0.5 G.

$$u(\theta) = \begin{cases} -u_0 \sin(\pi\lambda/\lambda_0), & |\lambda| < \lambda_0, \\ 0, & |\lambda| > \lambda_0. \end{cases}$$

where λ is the latitude (defined by $\lambda = \pi/2 - \theta$) and λ_0 is the latitude at which the meridional flow vanishes. Solar values for u_0 and λ_0 of ~ 11 m s^{-1} and $\sim 75^\circ$ are determined observationally. The solar differential rotation was determined by Snodgrass (1983), and is given by

$$\Omega(\theta) = \left[13.38 - 2.30\cos^2\theta - 1.62\cos^4\theta\right] \text{deg day}^{-1} \tag{2.2}$$

The solar meridional flow and differential rotation profiles are shown in Fig. 2.3.

The surface flux transport model has not only been used to investigate the evolution of the magnetic field over the surface of the Sun, but has also been used to explore magnetic activity on other stars. Schrijver & Title (2001) used flux transport models to show that active stars with enhanced magnetic cycles are able to form polar caps with fields comparable in strength to those found in sunspots. Such strong polar fields have been observed on young stars, such as the CTTS AA Tau discussed in Chapter 4. Mackay et al. (2004) showed that the solar parameters are not able to reproduce the complex multi-polarity polar field structures seen at high latitudes in the ZDI magnetogram of AB Dor produced by Donati & Collier Cameron (1997). Instead, they found that such patterns can be reproduced if magnetic flux is emerged at higher latitudes and an enhanced meridional flow of ~ 100 m s^{-1} is assumed. The magnetograms produced by flux transport models are also useful because they contain a large amount of magnetic flux in small scale active regions that are not reproduced in ZDI magnetograms. Based on the magnetograms of Mackay et al. (2004), I studied how this missing flux affects our ability to model stellar coronae and magnetospheric accretion (Johnstone et al. 2010; Chapter 3 of this thesis). Similarly, Llama et al. (2012) used different simulated magnetic cycles to explore what can be learned about stellar activity cycles by photometric observations of planetary transits over starspots.

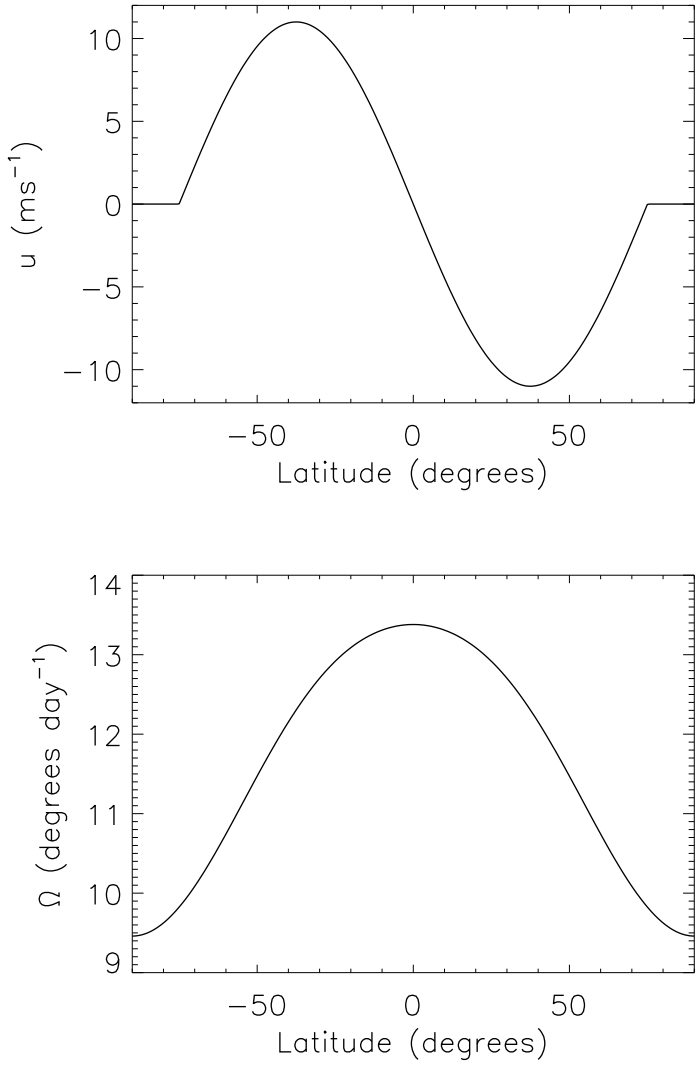

Figure 2.3: Solar meridional flow (upper panel) and differential rotation (lower panel) profiles as a function of latitude. The meridional flow is defined such that negative values correspond to flows towards the pole with a latitude of 90°.

2.2 Spherical harmonics

Spherical harmonics is a method for describing 3D functions that satisfy Laplace's equation in spherical polar coordinates. It can also be used to describe 2D functions defined over the surfaces of spheres. The following is an outline of the standard derivation of the spherical harmonic solution of Laplace's equation that can be found in most textbooks.

Consider a 3D function, f, which satisfies Laplace's equation[4]

$$\nabla^2 f(r,\theta,\phi) = 0 \tag{2.3}$$

which, in spherical polar coordinates, can be written

$$\frac{1}{r^2}\frac{\partial}{\partial r}\left(r^2\frac{\partial f}{\partial r}\right) + \frac{1}{r^2\sin\theta}\frac{\partial}{\partial\theta}\left(\sin\theta\frac{\partial f}{\partial\theta}\right) + \frac{1}{r^2\sin^2\theta}\frac{\partial^2 f}{\partial\phi^2} = 0 \tag{2.4}$$

A separable solution to this equation is of the form $f(r,\theta,\phi) = R(r)\Theta(\theta)\Phi(\phi)$. Substituting this into Eqn. 2.4, and multiplying by $r^2/R(r)\Theta(\theta)\Phi(\phi)$ gives

$$\frac{1}{R(r)}\frac{d}{dr}\left(r^2\frac{dR(r)}{dr}\right) + \frac{1}{\Theta(\theta)\sin\theta}\frac{d}{d\theta}\left(\sin\theta\frac{d\Theta(\theta)}{d\theta}\right) + \frac{1}{\Phi(\phi)\sin^2\theta}\frac{d^2\Phi(\phi)}{d\phi^2} = 0 \tag{2.5}$$

Let us now define λ and m such that

$$\lambda = \frac{1}{R(r)}\frac{d}{dr}\left(r^2\frac{dR(r)}{dr}\right) \tag{2.6}$$

$$-m^2 = \frac{1}{\Phi(\phi)}\frac{d^2\Phi(\phi)}{d\phi^2} \tag{2.7}$$

It can be seen that neither λ nor m can be functions of the coordinates r, θ, or ϕ [5]. Substi-

[4] Magnetic fields satisfy Laplace's equation in any volume of space where electric currents are not present.

[5]
$$\lambda = \frac{1}{R}\frac{d}{dr}\left(r^2\frac{dR(r)}{dr}\right) = -\frac{1}{\Theta\sin\theta}\frac{d}{d\theta}\left(\sin\theta\frac{d\Theta}{d\theta}\right) + \frac{1}{\Phi\sin^2\theta}\frac{d^2\Phi}{d\phi^2}$$
As the LHS is a function of r only, and the RHS is a function of θ and ϕ only, and as this equation must hold for

tuting these into Eqn. 2.5 in different ways gives[6]

$$\frac{d}{dr}\left(r^2\frac{dR(r)}{dr}\right) = \lambda R(r) \tag{2.8}$$

$$\frac{d^2\Phi(\phi)}{d\phi^2} = -m^2\Phi(\phi) \tag{2.9}$$

$$\sin\theta\frac{d}{d\theta}\left(\sin\theta\frac{d\Theta(\theta)}{d\theta}\right) + \left(\lambda\sin^2\theta - m^2\right)\Theta(\theta) = 0 \tag{2.10}$$

Finding the solutions to these three equations leads to an expression for the function f.

Eqn. 2.9 is trivial to solve and has the solution

$$\Phi(\phi) = Ae^{im\phi} \tag{2.11}$$

where A is a constant. As the function $f(r,\theta,\phi)$ must be single valued at every point

$$\Phi(\phi) = \Phi(\phi + 2\pi) \tag{2.12}$$

---

all values of r, θ, and ϕ, λ cannot be a function of these three variables. Similarly for m, where

$$-m^2 = \frac{1}{\Phi(\phi)}\frac{d^2\Phi(\phi)}{d\phi^2} = -\frac{1}{\Theta(\theta)}\sin\theta\frac{d}{d\theta}\left(\sin\theta\frac{d\Theta(\theta)}{d\theta}\right) - \lambda\sin^2\theta$$

[6]Eqn. 2.8 and Eqn. 2.9 are true by the definitions of λ and m given in Eqn. 2.6 and Eqn. 2.7. For Eqn. 2.10 substitute Eqn. 2.6 into Eqn. 2.5 to get

$$\underbrace{\lambda\sin^2\theta + \frac{1}{\Theta(\theta)}\sin\theta\frac{d}{d\theta}\left(\sin\theta\frac{d\Theta(\theta)}{d\theta}\right)}_{m^2} + \underbrace{\frac{1}{\Phi(\phi)}\frac{d^2\Phi(\phi)}{d\phi^2}}_{-m^2} = 0$$

Thus

$$\lambda\sin^2\theta + \frac{\sin\theta}{\Theta}\frac{d}{d\theta}\left(\sin\theta\frac{d\Theta(\theta)}{d\theta}\right) = m^2$$

Rearranging gives

$$\sin\theta\frac{d}{d\theta}\left(\sin\theta\frac{d\Theta(\theta)}{d\theta}\right) + \left(\lambda\sin^2\theta - m^2\right)\Theta(\theta) = 0$$

and therefore, m must be an integer.

Eqn. 2.10 is much less trivial to solve. It is the well known Legendre's associated equation (or the general Legendre equation) with $x = \cos\theta$, the solutions of which are the associated Legendre polynomials[7]. In order for the solutions of Eqn. 2.10 to be finite at $\theta = 0$ and at $\theta = \pi$, the function λ must be of the form $l(l+1)$ where l is an integer, and the associated Legendre polynomials of the second kind, $Q_{lm}(\cos\theta)$, must be dismissed. The associated Legendre polynomials of the first kind are given by

$$P_{lm}(x) = (1-x^2)^{m/2}\frac{d^m}{dx^m}P_l(x) \tag{2.13}$$

where $P_l(x)$ are the Legendre polynomials, equivalent to $P_{l0}(x)$, and are given by

$$P_l(x) = \frac{1}{2^l l!}\frac{d^l}{dx^l}(x^2-1)^l \tag{2.14}$$

Putting these two together gives

[7]For example, if we set $m = 0$, then Legendre's associated equation becomes the Legendre equation

$$\frac{d}{dx}\left[(1-x^2)\frac{df}{dx}\right] + \lambda f = 0$$

the solutions of which are the Legendre polynomials. This equation can be solved using Frobenius' method by assuming a solution of the form

$$f = \sum_{j=0}^{\infty} a_j x^{j+\alpha}$$

It can be shown that

$$a_{j+2} = \left[\frac{(\alpha+j)(\alpha+j+1)-\lambda}{(\alpha+j+1)(\alpha+j+2)}\right]a_j$$

In order for this series solution to be finite at $x = \pm 1$, it must terminate (i.e. have a finite number of terms). This can only happen if either a_0, or a_1 is zero, and if λ is of the form $l(l+1)$, where l is an integer. Depending on the value of l, and the arbitrary choice of α as either -1, 0, or 1, the series terminates at even or odd values of j. If at an even value, then a_1 must vanish, and thus all odd terms of j must vanish, and if at an odd value, then a_0 must vanish, and thus all even terms of j must vanish. This leads to the Legendre polynomials of the first kind (Legendre polynomials of the second kind corresponds to the cases where the series does not terminate) being made up of either all even or all odd powers of x, which alternate depending on whether l is even or odd. When it comes to the spherical harmonic description of a magnetic field, this means that the axisymmetric components of the field (i.e. the $m = 0$ components) are antisymmetric about the equator for components with odd values of l, and symmetric for components with even values of l.

$$P_{lm}(x) = \frac{1}{2^l l!}(1-x^2)^{m/2}\frac{d^{l+m}}{dx^{l+m}}(x^2-1)^l \tag{2.15}$$

The term $(x^2-1)^l$ expands into a polynomial with the highest power of x being $2l$. As this polynomial is differentiated $l+m$ times with respect to x, if $m > l$ the associated Legendre polynomials vanish. Therefore there are no terms in the solution to Laplace's equation where $m > l$. It is important to note here that the above equations do not include the Condon-Shortley phase, which is a $(-1)^m$ term that is often included at the beginning of Eqns. 2.13 and 2.15. The first few associated Legendre polynomials, in terms of $\cos\theta$, are given by

$$P_{00} = 1 \tag{2.16}$$

$$P_{10} = \cos\theta \tag{2.17}$$

$$P_{11} = -\sin\theta \tag{2.18}$$

$$P_{20} = \frac{1}{2}(3\cos^2\theta - 1) \tag{2.19}$$

$$P_{21} = -3\cos\theta\sin\theta \tag{2.20}$$

$$P_{22} = 3\sin^2\theta \tag{2.21}$$

$$P_{30} = \frac{1}{2}(5\cos^3\theta - 3\cos\theta) \tag{2.22}$$

$$P_{31} = -\frac{3}{2}(5\cos^2\theta - 1)\sin\theta \tag{2.23}$$

$$P_{32} = 15\cos\theta\sin^2\theta \tag{2.24}$$

$$P_{33} = -15\sin^3\theta \tag{2.25}$$

$$\tag{2.26}$$

With $\lambda = l(l+1)$, Eqn. 2.8 becomes

$$\frac{d}{dr}\left(r^2\frac{dR(r)}{dr}\right) = l(l+1)R(r) \tag{2.27}$$

This has two solutions given by

$$R_1(r) = Ar^l \tag{2.28}$$

$$R_2(r) = Br^{-(l+1)} \tag{2.29}$$

Given that the weighted sum of solutions to a differential equation is itself a solution, we can finally write the full solution to Laplace's equation as

$$f(r,\theta,\phi) = \sum_{l=0}^{\infty}\sum_{m=-l}^{l}\left[a_{lm}r^{l} + b_{lm}r^{-(l+1)}\right]P_{lm}(\cos\theta)e^{im\phi} \tag{2.30}$$

2.3 Stellar surface magnetic fields

Although the description of 3D functions using Eqn. 2.30 is limited to functions that satisfy Laplace's equation, any 2D function defined over the surface of a sphere can be described in polar coordinates as a spherical harmonic expansion[8]. In this section, I outline how the magnetic fields over the surfaces of stars are described using spherical harmonics.

2.3.1 The B_r, B_θ, and B_ϕ magnetic components

In Section 2.4, I show that a potential magnetic field can be described using a scalar potential Ψ, such that $\nabla^2\Psi = 0$, and therefore

$$\Psi(r,\theta,\phi) = \sum_{l=0}^{\infty}\sum_{m=-l}^{l}\left[a_{lm}r^{l} + b_{lm}r^{-(l+1)}\right]P_{lm}(\cos\theta)e^{im\phi} \tag{2.31}$$

The magnetic field is given by $\mathbf{B} = -\nabla\Psi$, and assuming that it falls off to zero at $r = \infty$, the a_{lm} coefficients vanish and the three components of the magnetic field over the surface of a star can be written

$$B_r(\theta,\phi) = \sum_{l=0}^{\infty}\sum_{m=-l}^{l} c_{lm}P_{lm}(\cos\theta)e^{im\phi} \tag{2.32}$$

[8]This can be seen by considering that any 2D function defined over the surface of a sphere can be considered as part of a 3D function that varies in the radial direction in such a way that it satisfies Laplace's equation, i.e.

$$\frac{1}{r^2}\frac{\partial}{\partial r}\left(r^2\frac{\partial f}{\partial r}\right) = -\frac{1}{r^2\sin\theta}\frac{\partial}{\partial\theta}\left(\sin\theta\frac{\partial f}{\partial\theta}\right) - \frac{1}{r^2\sin^2\theta}\frac{\partial^2 f}{\partial\phi^2} = 0$$

$$B_\theta(\theta,\phi) = -\sum_{l=0}^{\infty}\sum_{m=-l}^{l}\frac{c_{lm}}{l+1}\frac{dP_{lm}(\cos\theta)}{d\theta}e^{im\phi} \tag{2.33}$$

$$B_\phi(\theta,\phi) = -\sum_{l=0}^{\infty}\sum_{m=-l}^{l}\frac{c_{lm}}{l+1}P_{lm}(\cos\theta)\frac{im}{\sin\theta}e^{im\phi} \tag{2.34}$$

where $c_{lm} = b_{lm}(l+1)R_*^{-(l+2)}$. Alternatively, if the field is not assumed to be zero at $r=\infty$, but instead is assumed to become completely radial at some radius R_{ss}, it can be written as

$$B_r(\theta,\phi) = \sum_{l=0}^{\infty}\sum_{m=-l}^{l}B_{lm}P_{lm}(\cos\theta)e^{im\phi} \tag{2.35}$$

$$B_\theta(\theta,\phi) = \sum_{l=0}^{\infty}\sum_{m=-l}^{l}B_{lm}f_{lm}\frac{dP_{lm}(\cos\theta)}{d\theta}e^{im\phi} \tag{2.36}$$

$$B_\phi(\theta,\phi) = \sum_{l=0}^{\infty}\sum_{m=-l}^{l}B_{lm}f_{lm}P_{lm}(\cos\theta)\frac{im}{\sin\theta}e^{im\phi} \tag{2.37}$$

where

$$f_{lm} = \frac{(R_{ss}/R_*)^{-(2l+1)} - 1}{l(R_{ss}/R_*)^{-(2l+1)} + l + 1} \tag{2.38}$$

and the coefficients B_{lm} are given by

$$B_{lm} = -a_{lm}R_*^{l-1} + b_{lm}(l+1)R_*^{-(2l+1)} \tag{2.39}$$

This is the potential-field source-surface model derived in Section 2.4.

Surface fields can also be represented in a non-potential way. Donati et al. (2006b) and many subsequent ZDI studies represent the field as the sum of potential and non-potential components using

$$B_r(\theta,\phi) = -\sum_{l=0}^{\infty}\sum_{m=0}^{l}\alpha_{lm}Y_{lm}(\theta,\phi) \tag{2.40}$$

$$B_\theta(\theta,\phi) = -\sum_{l=0}^{\infty}\sum_{m=0}^{l}\left[\beta_{lm}Z_{lm}(\theta,\phi) - \gamma_{lm}X_{lm}(\theta,\phi)\right] \tag{2.41}$$

$$B_\phi(\theta,\phi) = -\sum_{l=0}^{\infty}\sum_{m=0}^{l}\left[\beta_{lm}X_{lm}(\theta,\phi) + \gamma_{lm}Z_{lm}(\theta,\phi)\right] \tag{2.42}$$

where $Y_{lm}(\theta,\phi)$ are the spherical harmonics and are given by

$$Y_{lm}(\theta,\phi) = \sqrt{\frac{(2l+1)}{4\pi}\frac{(l-m)!}{(l+m)!}}P_{lm}(\cos\theta)e^{im\phi} \tag{2.43}$$

and

$$Z_{lm}(\theta,\phi) = \frac{1}{l+1}\sqrt{\frac{(2l+1)}{4\pi}\frac{(l-m)!}{(l+m)!}}\frac{dP_{lm}(\cos\theta)}{d\theta}e^{im\phi} \tag{2.44}$$

$$X_{lm}(\theta,\phi) = \frac{1}{l+1}\sqrt{\frac{(2l+1)}{4\pi}\frac{(l-m)!}{(l+m)!}}\frac{im}{\sin\theta}P_{lm}(\cos\theta)e^{im\phi} \tag{2.45}$$

where $\gamma_{lm} = 0$ and $\beta_{lm} = -\alpha_{lm} = c_{lm}$ for the case of a potential field. Eqn. 2.43 is common in spherical harmonics, and often contains the Condon-Shortly phase term.

2.3.2 The determination of the c_{lm} and B_{lm} coefficients

In this section, I will prove that the coefficients c_{lm}, or equivalently B_{lm} in the potential-field source-surface (PFSS) model, are given by

$$c_{lm} = \frac{(2l+1)[(l-m)!]}{4\pi[(l+m)!]}\int_0^{2\pi}\int_0^{\pi}B_r(\theta,\phi)P_{lm}(\cos\theta)e^{-im\phi}\sin\theta\,d\theta\,d\phi \tag{2.46}$$

Consider the following expression

$$\int_0^{2\pi}\int_0^{\pi}B_r(\theta,\phi)P_{l'm'}(\cos\theta)e^{-im'\phi}\sin\theta\,d\theta\,d\phi \tag{2.47}$$

Substituting Eqn. 2.32 into this gives

$$\sum_{l=0}^{\infty}\sum_{m=-l}^{l} c_{lm}\int_0^{2\pi} e^{im\phi}e^{-im'\phi}\,d\phi\int_0^{\pi} P_{lm}(\cos\theta)P_{l'm'}(\cos\theta)\sin\theta\,d\theta \tag{2.48}$$

All the terms in this expression can be broken down into three types satisfying the following conditions

Type A. $m = m'$, and $l = l'$ (this corresponds to a single term in the sum)

Type B. $l \neq l'$ and $m = m'$

Type C. $m \neq m'$

I will now show that all of the Type B and Type C terms vanish, leaving the only term that satisfies the Type A conditions.

Consider the Type B terms first. When $m = m'$, the following orthogonality condition applies

$$\int_0^{\pi} P_{lm}(\cos\theta)P_{l'm'}(\cos\theta)\sin\theta\,d\theta = \frac{2[(l+m)!]}{(2l+1)[(l-m)!]}\delta_{l',l} \tag{2.49}$$

where $\delta_{l',l}$ is the Kronecker delta function. As $l \neq l'$ for Type B terms, the integral over latitude in Eqn. 2.48 vanishes, and therefore all Type B terms vanish.

For the Type C terms, consider the integral over longitude in Eqn. 2.48

$$\begin{aligned}
\int_0^{2\pi} e^{i(m-m')!\phi} &= \int_0^{2\pi}\cos[(m-m')\phi]d\phi + i\int_0^{2\pi}\sin[(m-m')\phi]d\phi && (2.50)\\
&= \frac{\sin[(m-m')2\pi]}{m-m'} - \frac{i\cos[(m-m')2\pi]}{m-m'} + \frac{i}{m-m'} && (2.51)\\
&= \frac{i}{m-m'} - \frac{i}{m-m'} && (2.52)\\
&= 0 && (2.53)
\end{aligned}$$

and therefore, all Type C terms vanish[9].

The only term that does not vanish is the Type A term. Eqn. 2.48 then reduces to

[9]The third step is due to the fact that both m and m' are integers, which means that $m - m'$ must be a non-zero integer when $m \neq m'$. Therefore, $\sin[(m-m')2\pi] = 0$ and $\cos[(m-m')2\pi] = 1$.

$$c_{lm}\int_0^{2\pi} e^{i(m-m')\phi}d\phi\int_0^{\pi} P_{lm}(\cos\theta)P_{l'm'}(\cos\theta)\sin\theta d\theta \tag{2.54}$$

As $m = m'$, the inegral over ϕ becomes 2π, and the integral over θ is given by the orthogonality condition in Eqn. 2.49. Equating the above to the original expression given in Eqn. 2.47 gives

$$c_{lm} = \frac{(2l+1)[(l-m)!]}{4\pi[(l+m)!]}\int_0^{2\pi}\int_0^{\pi} B_r(\theta,\phi)P_{lm}(\cos\theta)e^{-im\phi}\sin\theta d\theta d\phi \tag{2.55}$$

Or equivalently, B_{lm} in the PFSS model is given by

$$B_{lm} = \frac{(2l+1)[(l-m)!]}{4\pi[(l+m)!]}\int_0^{2\pi}\int_0^{\pi} B_r(\theta,\phi)P_{lm}(\cos\theta)e^{-im\phi}\sin\theta d\theta d\phi \tag{2.56}$$

2.3.3 The negative m components

In this section, I show how the spherical harmonic components with negative values of m are related to the positive m value components, and I show that the negative m value components can be neglected by doubling the strengths of the positive non-zero m value components.

Eqn. 2.55 shows that the real and imaginary parts of c_{lm} are given by

$$Re\{c_{lm}\} = \frac{(2l+1)[(l-m)!]}{4\pi[(l+m)!]}\int_0^{2\pi}\int_0^{\pi} B_r(\theta,\phi)P_{lm}(\cos\theta)\sin\theta\cos(m\phi)d\theta d\phi \tag{2.57}$$

$$Im\{c_{lm}\} = -\frac{(2l+1)[(l-m)!]}{4\pi[(l+m)!]}\int_0^{2\pi}\int_0^{\pi} B_r(\theta,\phi)P_{lm}(\cos\theta)\sin\theta\sin(m\phi)d\theta d\phi \tag{2.58}$$

Rewriting Eqn. 2.55 in terms of $-m$ gives

$$c_{l,-m} = \frac{(2l+1)[(l+m)!]}{4\pi[(l-m)!]}\int_0^{2\pi}\int_0^{\pi} B_r(\theta,\phi)P_{l,-m}(\cos\theta)e^{im\phi}\sin\theta d\theta d\phi \tag{2.59}$$

The associated Legendre polynomials for the positive and negative m value components are related by

$$P_{l,-m}(\cos\theta) = (-1)^m \frac{(l-m)!}{(l+m)!} P_{lm}(\cos\theta) \tag{2.60}$$

Substituting this into Eqn. 2.59 gives

$$c_{l,-m} = (-1)^m \frac{(2l+1)}{4\pi} \int_0^{2\pi} \int_0^{\pi} B_r(\theta,\phi) P_{lm}(\cos\theta) e^{im\phi} \sin\theta \, d\theta \, d\phi \tag{2.61}$$

where the real and imaginary parts of $c_{l,-m}$ are given by

$$Re\{c_{l,-m}\} = (-1)^m \frac{(2l+1)}{4\pi} \int_0^{2\pi} \int_0^{\pi} B_r(\theta,\phi) P_{lm}(\cos\theta) \sin\theta \cos(m\phi) d\theta \, d\phi \tag{2.62}$$

$$Im\{c_{l,-m}\} = (-1)^m \frac{(2l+1)}{4\pi} \int_0^{2\pi} \int_0^{\pi} B_r(\theta,\phi) P_{lm}(\cos\theta) \sin\theta \sin(m\phi) d\theta \, d\phi \tag{2.63}$$

Combining these with Eqn. 2.57 and Eqn. 2.58 gives

$$Re\{c_{l,-m}\} = (-1)^m \frac{(l+m)!}{(l-m)!} Re\{c_{lm}\} \tag{2.64}$$

$$Im\{c_{l,-m}\} = (-1)^{m+1} \frac{(l+m)!}{(l-m)!} Im\{c_{lm}\} \tag{2.65}$$

I now show that

$$B_r(\theta,\phi) = \sum_{l=0}^{\infty} \sum_{m=-l}^{l} c_{lm} P_{lm}(\cos\theta) e^{im\phi} \tag{2.66}$$

$$= \sum_{l=0}^{\infty} \sum_{m=0}^{l} (2 - \delta_{m,0}) c_{lm} P_{lm}(\cos\theta) e^{im\phi} \tag{2.67}$$

where $\delta_{m,0}$ is the Kronecker delta function. This effectively means that the negative m value components can be disregarded by doubling the strengths of the non-zero positive m value components. The sums over all of the l and m components in the spherical harmonic expansion of $B_r(\theta,\phi)$ can be broken down into sums over all terms with $m=0$, $m>0$, or $m<0$. Writing it in this way gives

$$B_r(\theta,\phi)=\sum_{l=0}^{\infty}c_{l0}P_l(\cos\theta)+\sum_{l=0}^{\infty}\sum_{m=1}^{l}c_{lm}P_{lm}(\cos\theta)e^{im\phi}+\sum_{l=0}^{\infty}\sum_{m=-l}^{-1}c_{lm}P_{lm}(\cos\theta)e^{im\phi} \quad (2.68)$$

The third sum in this equation can be rewritten in terms of positive m values such that

$$\sum_{l=0}^{\infty}\sum_{m=-l}^{-1}c_{lm}P_{lm}(\cos\theta)e^{im\phi}=\sum_{l=0}^{\infty}\sum_{m=1}^{l}c_{l,-m}P_{l,-m}(\cos\theta)e^{-im\phi} \quad (2.69)$$

Expanding the expression inside the sum out into its real and imaginary parts and substituting in expressions for $P_{l,-m}$, $Re\{c_{l,-m}\}$, and $Im\{c_{l,-m}\}$ gives[10]

$$Re\{c_{l,-m}P_{l,-m}(\cos\theta)e^{-im\phi}\}=Re\{c_{lm}P_{lm}(\cos\theta)e^{im\phi}\} \quad (2.70)$$

$$Im\{c_{l,-m}P_{l,-m}(\cos\theta)e^{-im\phi}\}=-Im\{c_{lm}P_{lm}(\cos\theta)e^{im\phi}\} \quad (2.71)$$

and therefore Eqn. 2.68 becomes

$$B_r(\theta,\phi)=\sum_{l=0}^{\infty}c_{l0}P_l(\cos\theta)+2\sum_{l=0}^{\infty}\sum_{m=1}^{l}c_{lm}P_{lm}(\cos\theta)e^{im\phi} \quad (2.77)$$

[10]

$$\begin{aligned}
&Re\{c_{l,-m}P_{l,-m}(\cos\theta)e^{-im\phi}\} && (2.72)\\
&=(-1)^m\frac{(l+m)!}{(l-m)!}\left[Re\{c_{lm}\}-iIm\{c_{lm}\}\right]\left[\cos m\phi-i\sin m\phi\right] && (2.73)\\
&\times(-1)^m\frac{(l-m)!}{(l+m)!}P_{lm}(\cos\theta) && (2.74)\\
&=\left[Re\{c_{lm}\}\cos m\phi-Im\{c_{lm}\}\sin m\phi\right]P_{lm}(\cos\theta) && (2.75)\\
&=Re\{c_{lm}P_{lm}(\cos\theta)e^{im\phi}\} && (2.76)
\end{aligned}$$

Similar reasoning leads to the expression for the imaginary components.

which can be rewritten as

$$B_r(\theta,\phi) = \sum_{l=0}^{\infty}\sum_{m=0}^{l}(2-\delta_{m,0})c_{lm}P_{lm}(\cos\theta)e^{im\phi} \tag{2.78}$$

It is important to note that the above equation is actually only true for the real part of B_r. In the spherical harmonic expansion of a function that considers both the positive and negative m value components, the resulting function is real because the imaginary parts of the positive m value components cancel out with the imaginary parts of the negative m value components, due to the result given in Eqn. 2.71. However, in the above equation, this cancellation does not happen, and the resulting function is complex.

2.3.4 The 'complexity' of a magnetic field

It is often useful to discuss the fraction of magnetic energy held within each spherical harmonic component near the stellar surface. This can be used as a measure of the dominance of each component. In general, the energy held in the magnetic field is calculated by integrating the magnetic energy density, otherwise known as the magnetic pressure, over the stellar surface. Since the magnetic energy density is an energy per unit volume, this does not actually give an energy. If the energy density is also integrated radially outwards from the surface by a small distance Δr, the field can be assumed to be uniform over this distance and the energy in this volume is given by

$$E_B = R_*^2\Delta r\int_0^{2\pi}\int_0^{\pi}\frac{B^2}{8\pi}\sin\theta\, d\theta\, d\phi \tag{2.79}$$

It is important to remember that when the magnetic energy held within a surface field is discussed, what is really meant is the energy held within a small volume surrounding the star.

When a field is the superposition of two fields, it is not generally the case that the energy of the total field is the sum of the energies held within each component. However, when the field is described as a spherical harmonic expansion, *the magnetic energy in the field is the sum of the magnetic energies held within each spherical harmonic component*. This can be expressed as

$$E_B = \sum_{l=0}^{\infty} \sum_{m=-l}^{l} E_{lm} \tag{2.80}$$

where E_{lm} is the energy held within each spherical harmonic component.

At several points in this thesis, I refer to the 'complexity' of a star's magnetic field. In general, this term refers to the fraction of magnetic flux held in small scales structures, such as the active regions seen on the solar surface at times of strong activity. It is often desirable to represent the complexity of a magnetic field as a single parameter. In this thesis, I use the energy weighted average l value that describes the field. This is given by

$$< l >= \frac{\sum_{l=0}^{\infty} E_l l}{\sum_{l=0}^{\infty} E_l} \tag{2.81}$$

where $E_l = \sum_{m=-l}^{l} E_{lm}$.

2.4 Modelling 3D coronal field structures

In the absence of electric currents, and ignoring electric fields, Ampère's circuit law states that

$$\nabla \times \boldsymbol{B} = 0 \tag{2.82}$$

Such a field is called a potential field (or current-free field) and can be described using the magnetic scalar potential Ψ by the following formula [11]

$$\boldsymbol{B} = -\nabla \Psi \tag{2.83}$$

Given that $\nabla \cdot \boldsymbol{B} = 0$, the magnetic scalar potential is a solution of Laplace's equation and can be described in spherical polar coordinates by

$$\Psi(r, \theta, \phi) = \sum_{l=1}^{\infty} \sum_{m=-l}^{l} \left[a_{lm} r^l + b_{lm} r^{-(l+1)} \right] P_{lm}(\cos\theta) e^{im\phi} \tag{2.84}$$

[11] Note that describing the magnetic field using a scalar potential only is only valid in the case of a potential field. This can be seen by the fact that $\nabla \times (\nabla A)$ vanishes for any scalar field A. Thus, if $\boldsymbol{B} = -\nabla\Psi$, then $\nabla \times \boldsymbol{B} = -\nabla \times (\nabla\Psi) = 0$

Thus, by Eqn. 2.83, we get

$$B_r(r,\theta,\phi) = -\frac{\partial \Psi}{\partial r} = -\sum_{l=1}^{\infty}\sum_{m=-l}^{l}\left[a_{lm} l r^{l-1} - b_{lm}(l+1)r^{-(l+2)}\right] P_{lm}(\cos\theta)e^{im\phi} \tag{2.85}$$

$$B_\theta(r,\theta,\phi) = -\frac{1}{r}\frac{\partial \Psi}{\partial r} = -\sum_{l=1}^{\infty}\sum_{m=-l}^{l}\left[a_{lm} r^{l-1} + b_{lm} r^{-(l+2)}\right] \frac{dP_{lm}(\cos\theta)}{d\theta} e^{im\phi} \tag{2.86}$$

$$B_\phi(r,\theta,\phi) = -\frac{1}{r\sin\theta}\frac{\partial \Psi}{\partial r} = -\sum_{l=1}^{\infty}\sum_{m=-l}^{l}\left[a_{lm} r^{l-1} + b_{lm} r^{-(l+2)}\right] P_{lm}(\cos\theta)\frac{im}{\sin\theta} e^{im\phi} \tag{2.87}$$

Assuming the field decreases to zero far from the star means that $a_{lm} = 0$ and therefore

$$B_r(r,\theta,\phi) = \sum_{l=1}^{\infty}\sum_{m=-l}^{l} c_{lm}\left(\frac{r}{R_*}\right)^{-(l+2)} P_{lm}(\cos\theta)e^{im\phi} \tag{2.88}$$

$$B_\theta(r,\theta,\phi) = -\sum_{l=1}^{\infty}\sum_{m=-l}^{l} \frac{c_{lm}}{l+1}\left(\frac{r}{R_*}\right)^{-(l+2)} \frac{dP_{lm}(\cos\theta)}{d\theta} e^{im\phi} \tag{2.89}$$

$$B_\phi(r,\theta,\phi) = -\sum_{l=1}^{\infty}\sum_{m=-l}^{l} \frac{c_{lm}}{l+1}\left(\frac{r}{R_*}\right)^{-(l+2)} P_{lm}(\cos\theta)\frac{im}{\sin\theta} e^{im\phi} \tag{2.90}$$

where $c_{lm} = b_{lm}(l+1)R_*^{-(l+2)}$.

On medium scales in the stellar corona, this model may be a good approximation. However, far from the star, coronal magnetic fields are blown open by coronal plasma and become approximately radial. We can simulate the effect of the opening up of field lines by hot coronal plasma on the magnetic field structure using the $a_{lm} r^{l-1}$ terms in Eqns. 2.85, 2.86, 2.87 by assuming that at a certain radius, called the source surface radius R_{ss}, the magnetic field is entirely radial, i.e. $B_\theta(R_{ss},\theta,\phi) = B_\phi(R_{ss},\theta,\phi) = 0$. This is the potential-field source-surface (PFSS) model, originally developed by Altschuler & Newkirk (1969). The effect of the source surface on the field structure is shown in Fig. 2.4. The source surface assumption implies that

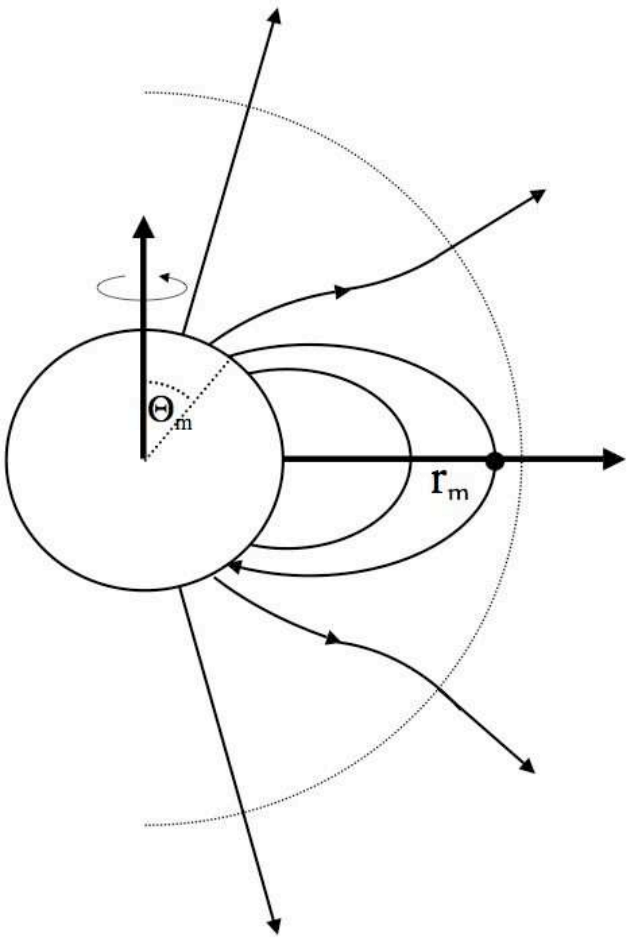

Figure 2.4: Reproduced from Jardine et al. (2006). The effect of the source surface assumption on the field structure of a simple dipole.

$$a_{lm}R_{ss}^{l-1} + b_{lm}R_{ss}^{-(l+2)} = 0 \tag{2.91}$$

and thus

$$\frac{a_{lm}}{b_{lm}} = -R_{ss}^{-(2l+1)} \tag{2.92}$$

We define B_{lm} as

$$B_{lm} = -a_{lm}lR_*^{l-1} + b_{lm}(l+1)R_*^{-(l+2)} \tag{2.93}$$

Substituting Eqn. 2.92 and Eqn. 2.93 into Eqn. 2.85 gives [12]

$$B_r(r,\theta,\phi) = \sum_{l=1}^{\infty}\sum_{m=-l}^{l} B_{lm}f_l(r)P_{lm}(\cos\theta)e^{im\phi} \tag{2.101}$$

$$B_\theta(r,\theta,\phi) = \sum_{l=1}^{\infty}\sum_{m=-l}^{l} B_{lm}g_l(r)\frac{dP_{lm}(\cos\theta)}{d\theta}e^{im\phi} \tag{2.102}$$

[12] *For B_r:*

$$-\left[a_{lm}lr^{l-1} - b_{lm}(l+1)r^{-(l+2)}\right] = B_{lm}(R_*)\left[\frac{b_{lm}(l+1)r^{-(l+2)} - a_{lm}lr^{l-1}}{b_{lm}(l+1)R_*^{-(l+2)} - a_{lm}lR_*^{l-1}}\right] \tag{2.94}$$

$$= B_{lm}(R_*)\left[\frac{b_{lm}(l+1)r^{-(l+2)} + b_{lm}lr^{l-1}R_{ss}^{-(2l+1)}}{b_{lm}(l+1)R_*^{-(l+2)} + b_{lm}lR_*^{l-1}R_{ss}^{-(2l+1)}}\right] \tag{2.95}$$

$$= B_{lm}(R_*)\left[\frac{(l+1)r^{-(l+2)}R_*^{-(l+2)} + lr^{l-1}R_{ss}^{-(2l+1)}R_*^{l+2}}{lR_*^{2l+1}R_{ss}^{-(2l+1)} + (l+1)}\right] \tag{2.96}$$

$$= B_{lm}(R_*)\left[\frac{l\left(\frac{R_{ss}}{R_*}\right)^{-(2l+1)}\left(\frac{r}{R_*}\right)^{l-1} + (l+1)\left(\frac{r}{R_*}\right)^{-(l+2)}}{l\left(\frac{R_{ss}}{R_*}\right)^{-(2l+1)} + l + 1}\right] \tag{2.97}$$

For B_θ and B_ϕ:

$$-\left[a_{lm}r^{l-1} + b_{lm}r^{-(l+2)}\right] = B_{lm}(R_*)\left[\frac{a_{lm}r^{l-1} + b_{lm}r^{-(l+2)}}{b_{lm}(l+1)R_*^{-(l+2)} - a_{lm}lR_*^{l-1}}\right] \tag{2.98}$$

$$= B_{lm}(R_*)\left[\frac{r^{l-1}R_{ss}^{-(2l+1)}R_*^{l+2} - r^{-(l+2)}R_*^{l+2}}{(l+1) + lR_*^{2l+1}R_{ss}^{-(2l+1)}}\right] \tag{2.99}$$

$$= B_{lm}(R_*)\left[\frac{\left(\frac{r}{R_*}\right)^{l-1}\left(\frac{R_{ss}}{R_*}\right)^{-(2l+1)} - \left(\frac{r}{R_*}\right)^{-(l+2)}}{l\left(\frac{R_{ss}}{R_*}\right)^{-(2l+1)} + l + 1}\right] \tag{2.100}$$

$$B_\phi(r,\theta,\phi) = \sum_{l=1}^{\infty}\sum_{m=-l}^{l} B_{lm} g_l(r) P_{lm}(\cos\theta)\frac{im}{\sin\theta}e^{im\phi} \tag{2.103}$$

where $f_l(r)$ and $g_l(r)$ are given by

$$f_l(r) = \left[\frac{(l+1)\left(\frac{r}{R_*}\right)^{-(l+2)} + l\left(\frac{R_{ss}}{R_*}\right)^{-(2l+1)}\left(\frac{r}{R_*}\right)^{l-1}}{l\left(\frac{R_{ss}}{R_*}\right)^{-(2l+1)} + l + 1}\right] \tag{2.104}$$

$$g_l(r) = \left[\frac{\left(\frac{r}{R_*}\right)^{l-1}\left(\frac{R_{ss}}{R_*}\right)^{-(2l+1)} - \left(\frac{r}{R_*}\right)^{-(l+2)}}{l\left(\frac{R_{ss}}{R_*}\right)^{-(2l+1)} + l + 1}\right] \tag{2.105}$$

At the source surface, $g_{lm}(R_{ss}) = 0$, causing the field to become completely radial. Beyond the source surface, the $f_{lm}(r)$ function increases with distance from the star, which is physically unrealistic, and therefore the PFSS model does not apply for $r > R_{ss}$. If the source surface radius is set to the stellar radius, $g_{lm}(R_*) = 0$, and therefore the field becomes completely radial at the stellar surface. At the stellar surface, these functions are given by

$$f_l(R_*) = \left[\frac{l\left(\frac{R_{ss}}{R_*}\right)^{-(2l+1)} + l + 1}{l\left(\frac{R_{ss}}{R_*}\right)^{-(2l+1)} + l + 1}\right] = 1 \tag{2.106}$$

$$g_l(R_*) = \left[\frac{\left(\frac{R_{ss}}{R_*}\right)^{-(2l+1)} - 1}{l\left(\frac{R_{ss}}{R_*}\right)^{-(2l+1)} + l + 1}\right] \tag{2.107}$$

If the source surface is set very far from the star, it has a negligible effect on the surface field and $g_l(R_*) = -1/(l+1)$. In this case, the PFSS model reduces to the potential field model without a source surface. This can also be seen from the relationship between B_{lm}, a_{lm}, and b_{lm}. The parameters a_{lm} and b_{lm} are related to B_{lm} by [13]

[13] By definition

$$B_{lm} = b_{lm}(l+1)R_*^{-(l+2)} - a_{lm} l R_*^{l-1}$$

As above, since the field becomes radial at the source surface

$$\frac{a_{lm}}{b_{lm}} = -R_{ss}^{-(2l+1)}$$

Substituting seperately for a_{lm} and b_{lm} gives

$$a_{lm} = -\frac{R_*^{-(l-1)}}{(l+1)\left(R_{ss}/R_*\right)^{2l+1} + l} B_{lm} \tag{2.108}$$

$$b_{lm} = \frac{R_*^{l+2}}{l\left(R_{ss}/R_*\right)^{-(2l+1)} + l + 1} B_{lm} \tag{2.109}$$

When $R_{ss} = \infty$, we get $a_{lm} = 0$ and $b_{lm} = (l+1)^{-1} R_*^{l+2} B_{lm}$ as in the potential field model without a source surface.

In Section 2.3.2, I prove that the parameter B_{lm} can be calculated from $B_r(R_*, \theta, \phi)$ using

$$B_{lm} = \frac{(2l+1)[(l-m)!]}{2\pi[(l+m)!]} \int_0^{2\pi} \int_0^{\pi} B_r(R_*, \theta, \phi) P_{lm}(\cos\theta) \sin\theta e^{-im\phi} d\theta d\phi \tag{2.110}$$

Since all three components of $\boldsymbol{B}$ between the stellar surface and the source surface are defined entirely by the values of B_{lm}, this is sufficient to prove that the 3D structure of $\boldsymbol{B}$ is defined entirely by the B_r component at the stellar surface in the potential field model and in the PFSS model.

Throughout this thesis, I extrapolate fields using the field extrapolation code developed by van Ballegooijen et al. (1998).

$$B_{lm} = -a_{lm}(l+1)R_{ss}^{2l+1}R_*^{-(l+2)} - a_{lm}lR_*^{l-1}$$

$$B_{lm} = b_{lm}(l+1)R_*^{-(l+2)} + b_{lm}lR_{ss}^{-(2l+1)}R_*^{l-1}$$

Rearranging gives

$$a_{lm} = -\frac{B_{lm}}{lR_*^{l-1} + (l+1)R_{ss}^{2l+1}R_*^{-(l+2)}}$$

$$b_{lm} = \frac{B_{lm}}{lR_*^{l-1}R_{ss}^{-(2l+1)} + (l+1)R_*^{-(l+2)}}$$

2.5 Modelling the closed X-ray emitting corona

2.5.1 Coronal plasma from magnetic fields

It is desirable to use coronal magnetic fields to make predictions about the structure of coronal plasma. In this section, I introduce the coronal plasma model used in Chapters 3 and 4. This model has previously been used by Jardine & Unruh (1999), Jardine et al. (2002), Jardine et al. (2006), Gregory et al. (2006a), Hussain et al. (2007), Johnstone et al. (2010), and Arzoumanian et al. (2011). In this model, the following assumptions are made

- *The corona is isothermal, in hydrostatic equilibrium along each field line, and corotating with the stellar surface.* This is based on the solar analogy where both the isothermal and hydrostatic equilibrium assumptions are reasonable (Aschwanden & Nitta 2000). The hydrostatic equilibrium assumption implies that along a magnetic field line, the plasma pressure is given by

$$p = p_0 \exp\left(\frac{m}{k_B T}\int g_s ds\right) \tag{2.111}$$

  where p_0 is the plasma pressure at the base of the field line, m is the average molecular mass, T is the coronal temperature, and g_s is the component of the effective gravity parallel to the field line and is given by

$$g_s = \frac{\mathbf{g}.\mathbf{B}}{|\mathbf{B}|} \tag{2.112}$$

  where

$$\mathbf{g} = \left(-GM_*/r^2 + \omega^2 r \sin^2\theta\right)\mathbf{e_r} + \left(\omega^2 r \sin\theta\cos\theta\right)\mathbf{e}_\theta \tag{2.113}$$

  where M_* is the stellar mass, r is the distance from the centre of the star, ω is the stellar surface angular velocity, θ is the colatitude (ranging between 0 and π radians), and $\mathbf{e_r}$ and $\mathbf{e}_\theta$ are unit vectors.

- *The plasma pressure at the base of the corona is proportional to the magnetic pressure, such that*

$$p_0(\theta, \phi) = KB_0(\theta, \phi)^2 \tag{2.114}$$

This is similar to the result of Wang et al. (1997) who modelled the solar corona using field extrapolations of synodic magnetograms and fit their model to green light observations of the corona by assuming that the plasma electron density varies as $n_e \propto B_0^n$. They found that $n \sim 0.9$ gave the best agreement between their models and the observations. Their models and the green light observations are reproduced here in Fig. 2.5. This assumption leads to much greater plasma densities in active regions where the magnetic field is strong, similar to what is seen in the solar corona ($\sim 10^9 - 10^{10}$ cm^{-3} in active regions and $\sim 10^7 - 10^8$ cm^{-3} in the quiet sun; Aschwanden 2001).

- *Magnetic field lines are blown open if the plasma β becomes greater than unity at any point along the magnetic loop.* Based on the analogy with the solar corona where coronal holes are dark in X-rays, *the plasma pressure in regions of open field is set to zero*. The dominance of the closed corona over the open corona in X-ray emission is mostly due to the large difference in plasma densities between the open and closed regions, and not to the differences in temperatures between the two (e.g. Munro & Jackson 1977).

Using this model, plasma pressures throughout the coronal volume can be predicted, and this can give an estimate of the total coronal emission measure. The coronal emission measure is defined as

$$EM = \int n_e^2 dV = \int \left(\frac{p}{2kT}\right)^2 dV \tag{2.115}$$

where n_e is the electron number density, the factor of 2 is a result of the assumption that half of the particles in the plasma are electrons, and the integral is over the entire coronal volume.

The free parameters in this model are the values of the proportionality constant K and the coronal temperature. In Chapter 4, I determine these parameters for a sample of classical T Tauri stars by using published temperatures and emission measures that have been fitted to observed X-ray spectra. For each star, the value of K is scaled to fit the observed emission measure. Typical values of $\log K \sim -7$ to -5 are necessary to reproduce the observed emission measures. This is similar to the values found by Jardine et al. (2006) who applied the model described here to the sample of pre-main sequence stars observed as part of the *Chandra* Orion

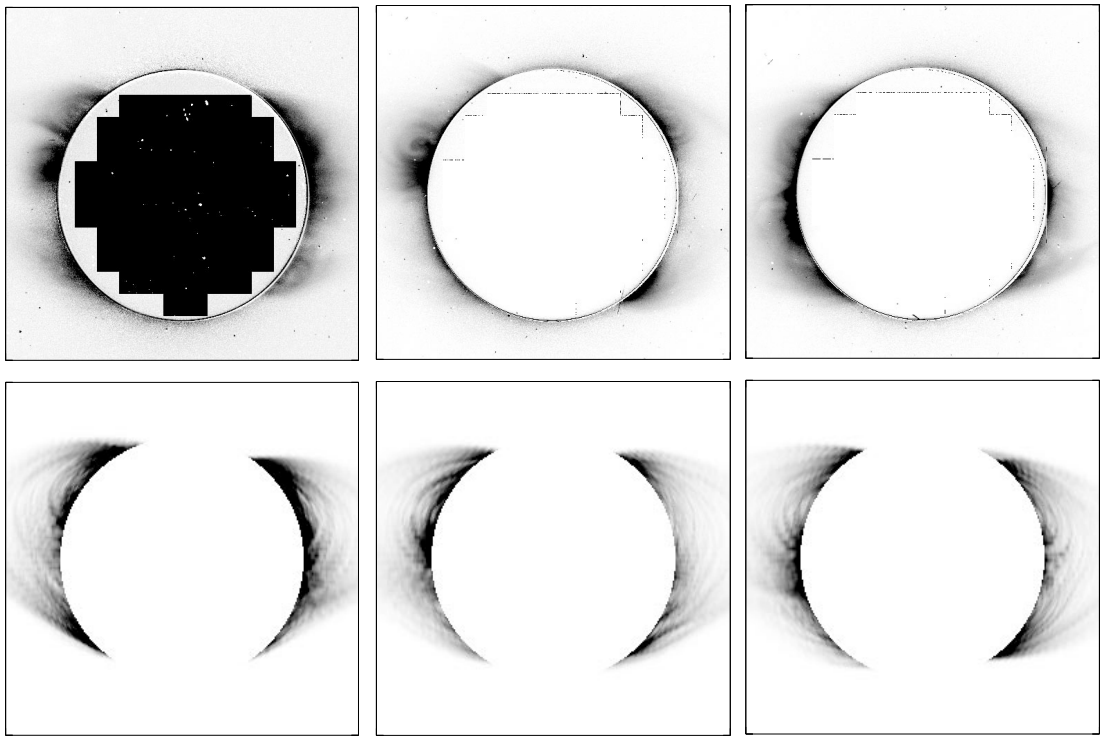

Figure 2.5: Reproduced from Wang et al. (1997). *Upper panels*: green light observations of the solar corona with the LASCO C1 coronagraph on *SOHO* from February 1996 (left), April 1996 (middle), and May 1998 (right). *Lower panels*: simulations based on potential field extrapolations of simultaneous synodic magnetograms and the assumption that at the base of the corona, the electron density scales with the magnetic field strength as $n_e = B_0^{0.9}$.

Ultradeep Project. They found that values of $\log K \sim -6$ to -4 gave good fits to the observed emission measures.

One feature of the coronal model is that there is a maximum amount of material that can be held in the closed corona (although the observed emission measures for the sample of classical T Tauri stars considered in Chapter 4 are all significantly below the maximum value that can be held by their fields). This is due to the assumption that magnetic field lines are blown open if the plasma β becomes greater than unity at any point along the magnetic loop. At low values of K, as K increases, the plasma densities increase, leading to an increase in the total emission measure. However, this also corresponds to a decrease in the size of the closed corona, as the higher densities mean the plasma pressure is able to overcome the magnetic pressure at smaller distances from the star. At some point, the effect of the decrease in the size of the corona overcomes the effect of the increase in the plasma densities, leading to a rapid drop off in emission measure. This is shown in Fig. 2.6. One consequence is the fact that any observed emission measure below the maximum can actually be reproduced by two values of K. However, the coronae that are predicted by the higher K values have unrealistically high densities ($n_e \sim 10^{13}$ cm^{-3}) and unrealistically small coronae. Thus, the higher values of K should be disregarded.

Throughout this thesis, I apply the coronal plasma model described above using code written by Jardine & Unruh (1999).

2.5.2 The extent of the closed corona

To first approximation, the closed corona exists in regions where the magnetic pressure dominates over the plasma pressure. In order for there to be a closed corona at all, at the base of the corona the magnetic pressure must far exceed the plasma pressure. As magnetic pressure falls off with radius faster than plasma pressure in hydrostatic equilibrium, at some point above the star, the plasma pressure will dominate the magnetic pressure. The point where the two pressures balance is approximately the point where the closed corona is truncated. This is where

$$p_T = p_B \tag{2.116}$$

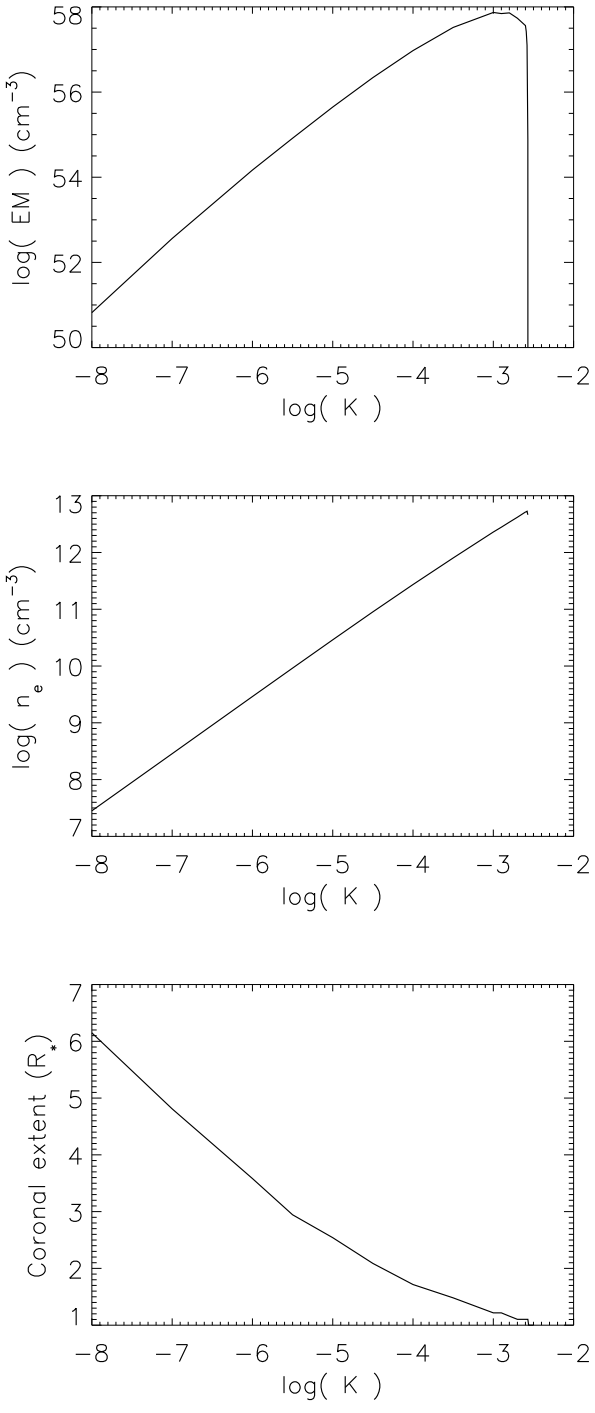

Figure 2.6: Predicted emission measures (upper panel), average electron densities (middle panel), and coronal extents (lower panel) as a function of the proportionality constant K from Eqn. 2.170 for the PFSS extrapolation of the observed magnetic field of AA Tau with a source surface set at 7.63 R_*.

where p_B is the magnetic pressure and p_T is the thermal pressure. The plasma pressure as a function of radius is given by Eqn. 2.111, which if integrated in radius from the stellar surface to a radius r gives

$$p_t(r) = KB_0^2 \exp\left(\frac{GM_* m_H}{kT}(r^{-1} - R_*^{-1}) - \frac{\omega^2 \sin^2\theta m_H}{2kT}(r^2 - R_*^2)\right) \tag{2.117}$$

The rate at which magnetic pressure falls off with radius depends on the complexity of the field. In general, the field strength of the l spherical harmonic component of a field falls of with radius as $(r/R_*)^{-(l+2)}$ if no source surface is assumed. In reality, the field is made up of several spherical harmonic components and near the star approximately falls of as $(r/R_*)^{-(<l>+2)}$, where $< l >$ is the field complexity parameter described in Section 2.3.4[14]. For potential field extrapolations of two CTTSs, Fig. 2.7 shows that this assumption is reasonable. However, this assumption is only reasonable relatively close to the star and if energy is only distributed over a few spherical harmonic components (as it is in low resolution ZDI magnetograms). Under this assumption, the magnetic pressure is given by

$$p_B = \frac{10^{-8}}{2\mu_0} B_0^2 \left(\frac{r}{R_*}\right)^{-2(<l>+2)} \tag{2.118}$$

where B_0 is in G and p_B is in Pa. Eqn. 2.116 becomes

$$K \exp\left(\frac{GM_* m_H}{kT}(r_{max}^{-1} - R_*^{-1}) - \frac{\omega^2 \sin^2\theta m_H}{2kT}(r_{max}^2 - R_*^2)\right) = \frac{10^{-8}}{2\mu_0}\left(\frac{r_{max}}{R_*}\right)^{-2(<l>+2)} \tag{2.119}$$

where r_{max} is the radius at which the closed corona is truncated.

One of the unexpected results of this analysis is the fact that the coronal truncation radius is not a function of the strength of the magnetic field. This is a result of the assumption in the coronal plasma model that the plasma pressure at the base of the corona is proportional to the magnetic pressure ($p_0 = KB_0^2$). A different assumption will be that plasma pressure is proportional to the magnetic field strength raised to a different power, i.e. $p_0 = KB_0^n$, where

[14]This is only a good assumption at a small range of radii near the star. Very close to the star, this underestimates the rate at which the field strength falls off with radius. Very far from the star, the field fall off with r^{-3}, and this assumption drastically overestimates the rate at which the field falls off with radius. Luckily, it appears that in most cases the corona is truncated within the range of radii where this is a good approximation.

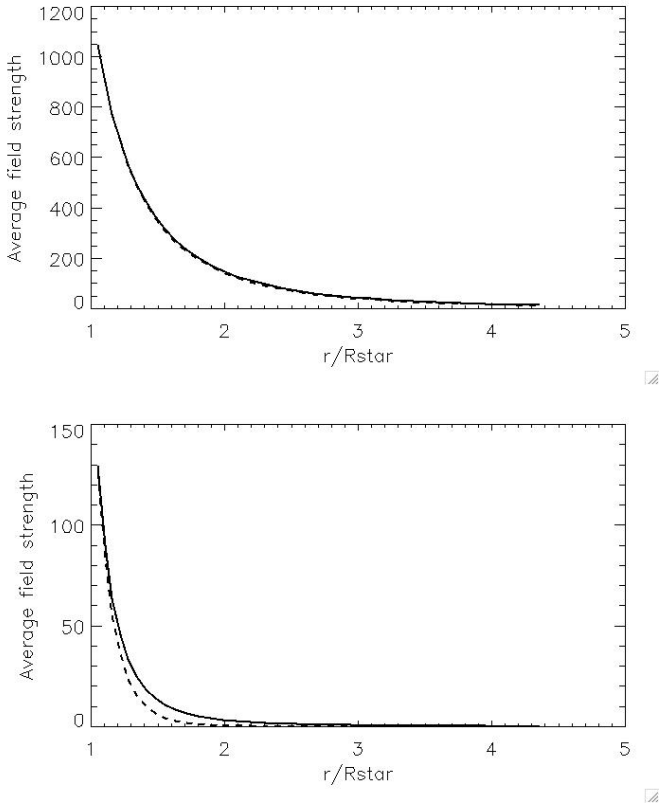

Figure 2.7: Radial dependance of field strength for AA Tau (upper panel) and CV Cha (lower panel), with values of $< l >$ of 1.11 and 6.54 respectively. The full lines show the numerical calculations using a potential field with a massive source surface radius. The dashed lines show the analytical prediction assuming $B = B_* r^{-(<l>+2)}$.

$n \neq 2$. In that case, if $n < 2$ (as in Wang et al. 1997) the coronal plasma model will predict that stronger magnetic fields are able to hold onto the coronal plasma to higher radii than weaker fields. On the other hand, if $n > 2$, then stronger fields will be able to hold onto the closed corona less far from the star than weaker fields.

2.6 Modelling magnetospheric accretion

Strong magnetic fields on CTTSs are able to truncate circumstellar discs several stellar radii from the star and channel accreting material onto the stellar surface along magnetic field lines. In Chapter 5, I use potential field extrapolations from a sample of CTTSs to estimate the disc truncation radii, and the trajectories of accreting material. In this section, I describe the model used in Chapter 5.

2.6.1 The disc truncation radius

Several methods for calculating the disc truncation radius are given in the literature. A simple method for estimating the disc truncation radius is to assume that the disc is truncated at the Alfvén surface where the energy density of the star's magnetic field is balanced by the kinetic energy density of the disc. Alternatively, an upper limit for the radius at which accretion can occur is the radius at which the magnetic torque balances the internal viscous torque in the disc (Bessolaz et al. 2008). In this model, I assume accretion from the disc occurs between the Alfvén surface radius and the torque balance radius.

The Alfvén surface radius for spherical accretion

In this section, I consider the case of 'spherical accretion' where spherically symmetric accretion occurs onto the star by material that free-falls from infinity under the force of gravity. I repeat the derivation of the Alfvén surface radius as a function of mass accretion rate and magnetic field strength given by Elsner & Lamb (1977).

The material is assumed to have zero kinetic energy at infinity, and therefore at any radius, the material has a velocity of

$$v(r) = \sqrt{\frac{2GM_*}{r}} \tag{2.120}$$

Take a sphere with radius r centered on the centre of the star: assuming mass conservation, the mass accretion rate onto the star, $\dot{M}_a$, is the rate at which mass passes through the surface of this sphere. This is given by

$$\dot{M}_\mathrm{a} = 4\pi r^2 \rho(r) v(r) \tag{2.121}$$

where $\rho(r)$ is the mass density.

For a dipole magnetic field, the strength of the field depends on radius as

$$B = B_* \left(\frac{r}{R_*}\right)^{-3} = \mu_1 r^{-3} \tag{2.122}$$

where B_* is the magnetic field strength at the stellar surface[15]and μ_1 is the magnetic moment, given by $\mu_1 = B_* R_*^3$.

For the case of spherical accretion, Elsner & Lamb (1977) presented an expression for the Alfvén surface radius, r_A, at which the magnetic energy density balances the kinetic energy density of infalling material[16]. This is where

$$\frac{1}{2}\rho v^2 = \frac{B^2}{8\pi} \tag{2.123}$$

Substituting Eqns. 2.120, 2.121, and 2.122 into this gives

$$r_A = \left(2GM_*\right)^{-\frac{1}{7}} \dot{M}_a^{-\frac{2}{7}} \mu_1^{\frac{4}{7}} \tag{2.124}$$

It is important to note that this equation has been derived using the definition of magnetic energy density, $B^2/8\pi$, that assumes cgs units. If the derivation had been in SI units, the Alfvén surface radius would be

$$r_A = 2^{\frac{3}{7}} \left(\frac{\mu_0}{\pi}\right)^{-\frac{2}{7}} \left(GM_*\right)^{-\frac{1}{7}} \dot{M}_a^{-\frac{2}{7}} \mu_1^{\frac{4}{7}} \tag{2.125}$$

where μ_0 is the permeability of free space.

The Alfvén surface radius for accretion from a disc

Although Eqn. 2.124 gives the radius of the Alfvén surface for the case of spherical accretion, the value of r_A for the case of magnetospheric accretion from a disc scales with the stellar mass, mass accretion rate, and the strength of the magnetic field in the same way. Thus the Alfvén surface radius for the case of magnetospheric accretion from a disc can be written as

$$r_A = k\left(GM_*\right)^{-\frac{1}{7}} \dot{M}^{-\frac{2}{7}} \mu_1^{\frac{4}{7}} \tag{2.126}$$

where k is a factor that accounts for the difference between magnetospheric accretion from

[15]Elsner & Lamb (1977) do not define at which point on the stellar surface is the magnetic field strength equal to B_*. When I consider the case of accretion form a disc, B_* is the field strength at the stellar equator.

[16]This is not the 'Alfvén radius' used when studying stellar winds which is the radius at which the wind speed is equal to the speed of Alfvén waves though the wind.

a disc and spherical accretion. Long et al. (2005) used values of r_A calculated from MHD accretion simulations to estimate that $k \sim 0.5$ for magnetospheric accretion. In this equation, $\mu_1 = B_* R_*^3$, where B_* is the equatorial magnetic field strength of the dipole component of the field.

Eqn. 2.124 is derived by assuming that the field is an axisymmetric dipole. However, the magnetic fields of real accreting stars are rarely completely dipolar. In most cases, the disc will be truncated far from the star, such that only the dipole component of the field needs to be taken into account. However, in cases where the dipole component is very weak and the disc is truncated close to the star, or where the dipole component is highly non-axisymmetric, it may be necessary to take into account realistic field geometries when calculating r_A.

For a field that is described entirely by a single spherical harmonic component of order l, the value of the field strength is given by

$$B = B_* \left(\frac{r}{R_*} \right)^{-(l+2)} = \mu_l r^{-(l+2)} \tag{2.127}$$

where $\mu_l = B_* R_*^{l+2}$. Repeating the derivation presented in the last section, the Alfvén surface radius is given by

$$r_A = A^{\frac{2}{4l+3}} (2GM_*)^{-\frac{1}{4l+3}} \dot{M}_a^{-\frac{2}{4l+3}} \mu_l^{\frac{4}{4l+3}} \tag{2.128}$$

where A is a factor, similar to k in Eqn. 2.126, that accounts for the difference between magnetospheric accretion from a disc and spherical accretion, and $A = 2^{-7/2}$ is equivalent to taking $k = 0.5$. However, this is not useful when the field is described by multiple spherical harmonic components. Instead, consider Eqn. 2.123 again

$$\frac{1}{2} \rho v^2 = \frac{B^2}{8\pi} \tag{2.129}$$

Substituting Eqns. 2.120 and 2.122 into this, but making no assumption about the magnetic field structure, gives the Alfvén surface radius at the point where

$$B^2 = C (GM_*)^{\frac{1}{2}} \dot{M}_a r_A^{-\frac{5}{2}} \tag{2.130}$$

where once again, C is a factor that accounts for the difference between magnetospheric accretion from a disc and spherical accretion, and $C = 16$ is a equivalent to taking $k = 0.5$. Using an extrapolated field, the Alfvén surface can then be found by taking B^2 at each radius to be the average value of B^2 over all longitudes in the equatorial plane and finding the point at which B^2 equals the RHS of this equation.

The torque balance radius

Star-disc magnetic interactions are capable of transferring angular momentum between the star and the disc. As the magnetic field lines anchored on the stellar surface will tend to corotate with the star, whether the magnetic field exerts a positive or negative torque on any part of the disc depends on whether that part of the disc is rotating faster or slower than the central star. Outside the corotation radius, the magnetic field exerts a positive torque on the disc, and inside the corotation radius, it exerts a negative torque. The differential magnetic torque is given by

$$\frac{d\tau_m}{dr} = B_\phi B_z r^2 \tag{2.131}$$

where B_z is the z component of the magnetic field in cylindrical coordinates, and B_ϕ is the ϕ component of the field in spherical polar coordinates and can be generated by differential rotation between the star and the disc (Clarke et al. 1995). Due to the difference in rotation rate between the disc and the star (except for at the corotation radius), the magnetic field lines connecting the star and the disc become twisted. As in Gregory et al. (2008), we estimate that this twist is 45°, and therefore $|B_z| = |B_\phi|$, and as $B_z = B_\theta$ in the equatorial plane, the differential torque is given by

$$\frac{d\tau_m}{dr} = B_\theta^2 r^2 \tag{2.132}$$

The magnetic torque is not the only torque that acts on the material in the disc: an internal viscous torque is also present. Through internal viscosity, an annulus of the disc will exert a spin-up torque on a neighbouring annulus if the neighbouring annulus has a lower orbital angular velocity. Thus, in a Keplerian accretion disc, as the angular velocity, $\Omega = (GM_*/r^3)^{1/2}$, decreases with increasing radius, angular momentum will be transported through the disc

away from the central star. At the same time, material is moving inwards through the disc. Assuming that the rate at which mass is transfered through the disc, $\dot{M}_a$, is uniform at all radii, i.e. the disc is in a steady state, the differential viscous torque is given by

$$\frac{d\tau_\nu}{dr} = \dot{M}_a \frac{d}{dr}\left(\Omega r^2\right) \tag{2.133}$$

Close to the star, the magnetic torque dominates over the viscous torque. However, the differential magnetic torque falls off with radius rapidly and the differential viscous torque increases with radius, therefore there will be a point where the two torques balance. Inside of this point, the magnetic torque dominates over the viscous torque. If this point is inside the corotation radius, the disc material will be slowed down by the magnetic torque and will fall towards the star. Substituting $\Omega = (GM_*/r^3)^{1/2}$ into Eqn. 2.133 and equating the differential torques gives

$$B_\theta^2 r_t^2 = \frac{1}{2}\dot{M}_a \left(\frac{GM_*}{r_t}\right)^{\frac{1}{2}} \tag{2.134}$$

where r_t is the torque balance radius. As in Gregory et al. (2008), I locate this point by using B_θ^2 averaged over all longitudes in the equatorial plane and finding the radius at which the LHS of this equation equals the RHS.

If the magnetic field is assumed to be an axisymmetric dipole, in the equatorial plane $B_r = B_\phi = 0$ and the field can be written $B_\theta = B_*(r/R_*)^{-3}$. Substituting this into Eqn. 2.134 gives

$$r_t = \left(\frac{2B_*^2 R_*^6}{(GM_*)^{1/2}\dot{M}_a}\right)^{\frac{2}{7}} \tag{2.135}$$

The tilted dipole field

The method given by Elsner & Lamb (1977) for calculating the Alfvén surface radius assumes that the field is a simple dipole that is aligned with the rotation axis. However, ZDI studies have shown that CTTSs often have field structures that depart significantly from simple axisymmetric dipoles (see Chapters 4 and 5). In the previous sections, I give the Elsner & Lamb (1977) expression for the Alfvén surface radius without making any assumptions about

the field structure. Here I explore the effect that having tilted dipole fields has on the Alfvén surface radius and the torque balance radius.

To explore the effect of the dipole tilt angle, I take a fictitious star of mass 1 $M_\odot$, radius 1 $R_\odot$, mass accretion rate of 10^{-9} $M_\odot$ yr^{-1}, and a dipole field with a strength of 1000 G at the magnetic poles. When the dipole field is not tilted, the Alfvén surface radius is found to be 2.53 R_*, and the torque balance radius is 6.78 R_*. As shown in the upper panel of Fig. 2.8, as the dipole tilt angle is increased, the Alfvén surface radius increases and the torque balance radius decreases. The Alfvén surface radius for the aligned dipole case is 2.53 R_*, and for the perpendicular case is 3.31 R_*. The increase in the Alfvén surface radius as the dipole is tilted is due to an increase in the average field strength in the equatorial plane, as shown in the middle panel of Fig. 2.8. This increase in the field strength causes the magnetic energy density to dominate over the kinetic energy density of the disc further from the star. Similarly, the decrease in the torque balance radius as the dipole is tilted is due to the decrease in B_θ in the equatorial plane. When the dipole is tilted at 90°, B_θ becomes zero in the equatorial plane and the torque balance radius, as predicted using Eqn. 2.134, is no longer outside of the star. This is due to the fact that as the dipole tilt angle increases, the assumptions made in deriving the equation for the torque balance radius become less valid, and the torque balance radius argument is not physically realistic for dipoles that are significantly tilted.

The dipole+octupole field

I will now explore the effect of adding an axisymmetric octupole component to an axisymmetric dipole field. This is important as a large number of the ZDI magnetograms for CTTSs have dominant dipole and octupole components (especially BP Tau, TW Hya, and V2129 Oph discussed in Chapter 4). Assuming the same stellar parameters as in the last section and an axisymmetric field that is the sum of an octupole of strength 1000 G and a dipole, I investigate the effects of varying the strength of the dipole component from 2000 G, where it is aligned with the octupole component, to -2000 G, where it is anti-aligned.

The dependences of the Alfvén surface radius and the torque balance radius on the strength of the dipole component in the dipole+octupole field is shown in Fig. 2.9. When the dipole and octupole components are aligned, they add up constructively at the poles, and destructively at the equator. Thus, the addition of a strong octupole component that is aligned with the dipole component causes the field to be weaker in the equatorial plane, which causes the

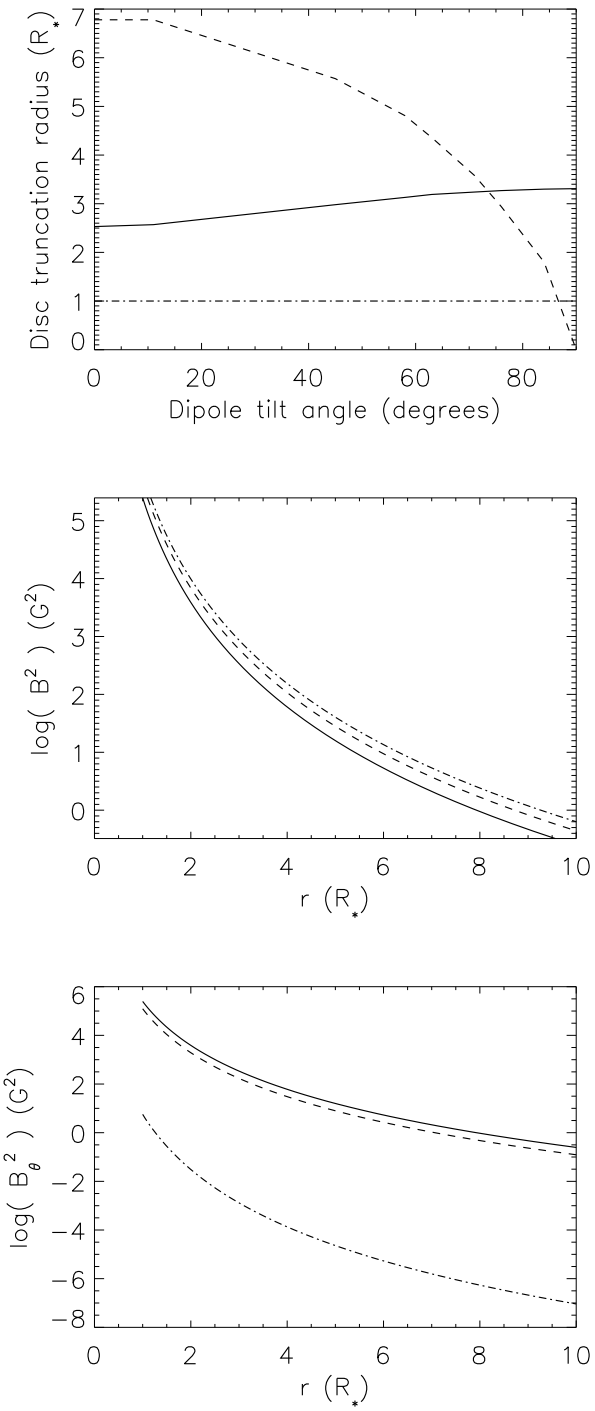

Figure 2.8: *Upper panel*: the dependence of the predicted Alfvén surface radius (solid line) and torque balance radius (dashed line) on the dipole tilt angle. The dot-dashed line shows the radius of the stellar surface. *Middle panel*: the dependence on radius of the value of B^2 averaged over all longitude in the equatorial plane for dipoles with tilt angles 0° (full line), 45° (dashed line), and 90° (dot-dashed line). *Lower panel*: the dependence on radius of the value of B_θ^2 averaged over all longitude in the equatorial plane for dipoles with tilt angles 0° (full line), 45° (dashed line), and 90° (dot-dashed line).

Alfvén surface radius to move closer to the star. For the 1000 G aligned dipole discussed in the last section, the Alfvén surface radius was 2.53 R_*. For the case of a 1000 G dipole and a 1000 G octupole, the Alfvén surface radius is 2.30 R_*. On the other hand, when the dipole and the octupole are anti-aligned, they add up constructively at the equator which pushes the Alfvén surface radius away from the star. The case of a -1000 G dipole gives an Alfvén surface radius of 2.69 R_*.

When the dipole component is 2000 G, it dominates at all radii. Thus, as the dipole is weakened, the Alfvén surface radius moves towards the star. However, when the dipole becomes weaker than the octupole, the radius dependence of the field at the equator becomes more complicated. The solid line in the lower panel of Fig. 2.9 shows how B^2 varies with radius for an 800 G dipole. In this case, the octupole field is stronger at the poles than the dipole, but still weaker than the dipole at the equator. Close to the star, the dipole dominates over the octupole in the equatorial plane, but the octupole significantly decreases the strength of the dipole field. As the distance from the star is increased, the octupole falls off with radius faster than the dipole, and thus the amount by which the octupole cancels out the dipole decreases, which leads to an initial increase in the field strength with radius. However, further from the star, the decrease in strength of the dipole with radius begins to dominate and the overall field strength begins to decreases with increasing radius. This means that in some situations, there might be two solutions to the Alfvén surface radius equation, in which case the larger solution should be taken as the disc truncation radius. For the case of the 300 G dipole, shown as the dashed line in the lower panel of Fig. 2.9, the situation is even more complicated. Near the star, the octupole component is stronger than the dipole component in the equatorial plane. Thus, as the distance from the star increases, the decrease in the strength of the octupole dominates over the decrease in the amount by which the octupole and dipole cancel each other out, and thus the field strength decreases. However, further from the star, the dipole component begins to dominate and the field strength increases with increasing radius for the same reason as in the 800 G dipole case, and then decreases again at large distances from the star.

When the dipole component is strong, as it decreases in strength, the Alfvén surface radius moves towards the star, due to the fact that the field strength in the equatorial plane decreases. However, as the dipole weakens, while it is still aligned with the octupole component, the two components cancel each other out close to the star, as described above. Thus, with a dipole

of ∼700 G, the dipole and the octupole cancel each other out near the star so strongly that the magnetic field is too weak at all radii to truncate the disc outside of the star. This can be seen in Fig. 2.9. However, as the dipole component weakens further, the octupole component begins to dominate close to the star and the Alfvén surface radius begins to increase again. When the dipole vanishes, the disc is truncated entirely by the octupole at ∼1.5 R_*. As the dipole component becomes anti-aligned with the octupole, the two components add up constructively in the equatorial plane, and thus the Alfvén surface radius is pushed away from the star as the dipole component increases in strength.

A similar behavior can be seen in Fig. 2.9 for the torque balance radius, however, the torque balance radius begins to increase with decreasing dipole strength at a lower value of the dipole field strength than for the Alfvén surface radius. This is due to the fact that the torque balance radius is always further from the star than the Alfvén surface radius where the dipole component is more dominant.

2.6.2 Accretion columns

When the inner and outer radii of the disc at which accretion can occur has been estimated, it is possible to use a field extrapolation to model accretion onto the star. I assume that accretion occurs along every field line that connects the star to the disc between the inner and outer radii at which accretion can occur. I then use a field extrapolation to estimate the trajectories of accretion streams.

Assuming that the magnetic flux is uniform along the accretion column gives for some point s along the accretion column

$$B(s)A(s) = B_d A_d \tag{2.136}$$

where B_d and A_d are the magnetic field strength and the area of the accretion column at the inner edge of the disc, and $B(s)$ and $A(s)$ are similar values for the point s along the field line. Similarly, assuming mass conservation along the accretion column gives

$$\rho(s)v(s)A(s) = \rho_d v_d A_d \tag{2.137}$$

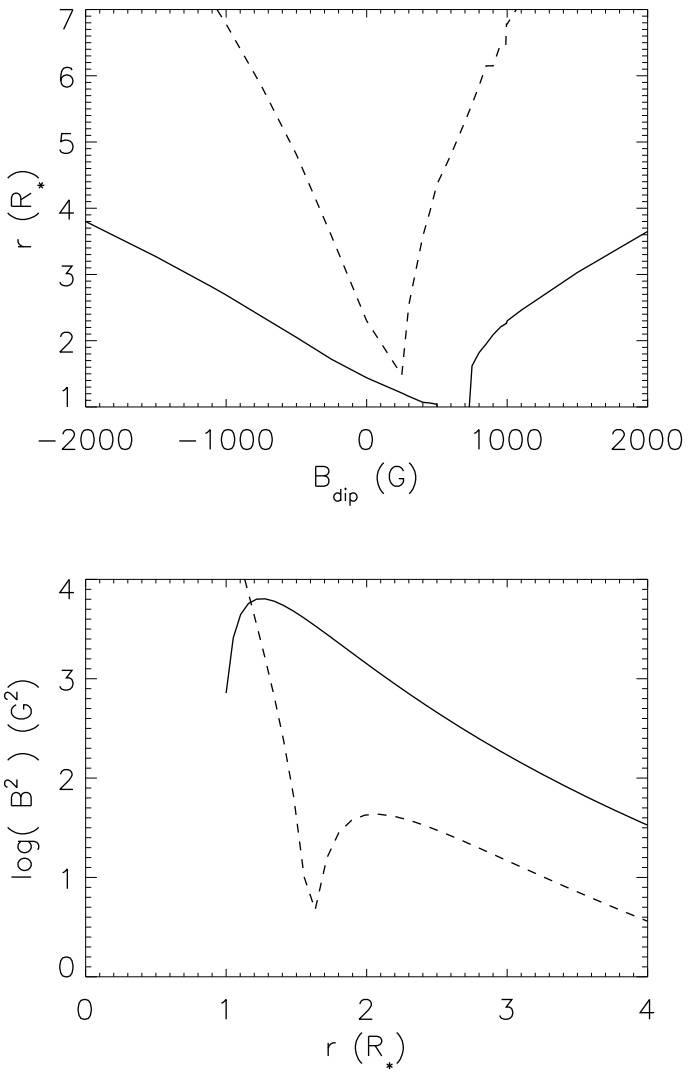

Figure 2.9: *Upper panel*: the dependance of the Alfvén surface radius (solid line) and torque balance radius (dashed line) on the strength of the dipole component in the dipole+octupole field, where the octupole component has a strength of 1000 G at the magnetic pole and is aligned with the dipole component when the dipole component has a positive strength. *Lower panel*: the dependence on distance from the star for a dipole+octupole field in the equatorial plane with a dipole component of 800 G (solid line) and 300 G (dashed line).

where ρ_d and v_d are the mass density and velocity at inner edge of the disc. Putting these two equations together gives

$$\frac{\rho(s)v(s)}{B(s)} = \frac{\rho_d v_d}{B_d} \tag{2.138}$$

As the accreting material is approximately in free fall, the infall velocity is given by

$$v(s) = \sqrt{2GM_* \left(\frac{1}{r(s)} - \frac{1}{r_d}\right) + v_d} \tag{2.139}$$

where in this equation, the v_d term is negligible, except for close to the disc. Since the value of $\rho_d v_d$ is unknown, Eqn. 2.138 can be expressed in terms of the mass accretion rate, which can be taken as an input parameter to this model. Assuming that the inner edge of the disc is at a uniform density and that material is leaving the disc at a uniform rate over the inner edge of the disc, the mass accretion rate is given by

$$\dot{M}_a = \rho_d v_d A_{d,\text{total}} \tag{2.140}$$

where $A_{d,\text{total}}$ is the total area of the disc over which accretion is occurring. Thus, Eqn. 2.138 becomes

$$\frac{\rho(s)v(s)}{B(s)} = \frac{\dot{M}_a}{A_{d,\text{total}} B_d} \tag{2.141}$$

Assuming that accretion is coming entirely from between radii r_{in} and r_{out}, and that at any point accretion is leaving the disc in a single direction, the area over which accretion is occurring is

$$A_{d,\text{total}} = \pi(r_{out}^2 - r_{in}^2) \tag{2.142}$$

2.7 Summary

The following is a summary of the key points from this chapter.

- The time evolution of the magnetic field over the surface of the Sun can be modelled using the effects of the emergence of bipolar active regions, meridional flow, differential rotation, and supergranular diffusion according to the differential equation

$$\frac{\partial B_r}{\partial t} = \frac{1}{\sin\theta}\frac{\partial}{\partial\theta}\left[\sin\theta\left(-u(\theta)B_r + D\frac{\partial B_r}{\partial\theta}\right)\right] + \frac{D}{\sin^2\theta}\frac{\partial^2 B_r}{\partial\phi^2} - \Omega(\theta)\frac{\partial B_r}{\partial\phi} + Q \quad (2.143)$$

- The magnetic field at the surface of a star can be described as a spherical harmonic expansion. If the field is assumed to fall off to zero far from the star, the three components of the field in spherical polar coordinates are

$$B_r(\theta,\phi) = \sum_{l=0}^{\infty}\sum_{m=-l}^{l} c_{lm}P_{lm}(\cos\theta)e^{im\phi} \quad (2.144)$$

$$B_\theta(\theta,\phi) = -\sum_{l=0}^{\infty}\sum_{m=-l}^{l} \frac{c_{lm}}{l+1}\frac{dP_{lm}(\cos\theta)}{d\theta}e^{im\phi} \quad (2.145)$$

$$B_\phi(\theta,\phi) = -\sum_{l=0}^{\infty}\sum_{m=-l}^{l} \frac{c_{lm}}{l+1}P_{lm}(\cos\theta)\frac{im}{\sin\theta}e^{im\phi} \quad (2.146)$$

or, if a source-surface of radius R_{ss} is assumed

$$B_r(\theta,\phi) = \sum_{l=0}^{\infty}\sum_{m=-l}^{l} B_{lm}P_{lm}(\cos\theta)e^{im\phi} \quad (2.147)$$

$$B_\theta(\theta,\phi) = \sum_{l=0}^{\infty}\sum_{m=-l}^{l} B_{lm}f_{lm}\frac{dP_{lm}(\cos\theta)}{d\theta}e^{im\phi} \quad (2.148)$$

$$B_\phi(\theta,\phi) = \sum_{l=0}^{\infty}\sum_{m=-l}^{l} B_{lm}f_{lm}P_{lm}(\cos\theta)\frac{im}{\sin\theta}e^{im\phi} \quad (2.149)$$

where

$$f_{lm} = \frac{(R_{ss}/R_*)^{-(2l+1)} - 1}{l(R_{ss}/R_*)^{-(2l+1)} + l + 1} \quad (2.150)$$

- The values of c_{lm}, or B_{lm}, in the above equations can be calculated from the radial component of the surface field according to

$$c_{lm} = \frac{(2l+1)[(l-m)!]}{4\pi[(l+m)!]} \int_0^{2\pi} \int_0^{\pi} B_r(\theta,\phi) P_{lm}(\cos\theta) e^{-im\phi} \sin\theta d\theta d\phi \tag{2.151}$$

$$B_{lm} = \frac{(2l+1)[(l-m)!]}{4\pi[(l+m)!]} \int_0^{2\pi} \int_0^{\pi} B_r(\theta,\phi) P_{lm}(\cos\theta) e^{-im\phi} \sin\theta d\theta d\phi \tag{2.152}$$

- The associated Legendre polynomials with negative m values are related to those with positive m values using

$$P_{l,-m}(\cos\theta) = (-1)^m \frac{(l-m)!}{(l+m)!} P_{lm}(\cos\theta) \tag{2.153}$$

The real and imaginary parts of $c_{l,-m}$ are related to the real and imaginary parts of c_{lm} by

$$Re\{c_{l,-m}\} = (-1)^m \frac{(l+m)!}{(l-m)!} Re\{c_{lm}\} \tag{2.154}$$

$$Im\{c_{l,-m}\} = (-1)^{m+1} \frac{(l+m)!}{(l-m)!} Im\{c_{lm}\} \tag{2.155}$$

and the negative m value components can be ignored in any spherical harmonic expansion by doubling the strengths of the positive non-zero m value components. This is because

$$B_r(\theta,\phi) = \sum_{l=0}^{\infty} \sum_{m=-l}^{l} c_{lm} P_{lm}(\cos\theta) e^{im\phi} \tag{2.156}$$

$$= \sum_{l=0}^{\infty} \sum_{m=0}^{l} (2-\delta_{m,0}) c_{lm} P_{lm}(\cos\theta) e^{im\phi} \tag{2.157}$$

- The energy of a surface magnetic field can be defined as the integral of B^2 over the stellar surface, and is the sum of the energies of each spherical harmonic component. The 'complexity' of a magnetic field can be quantified in a simple way as the energy weighted average l value that described the field. This is given by

$$< l >= \frac{\sum_{l=0}^{\infty} E_l l}{\sum_{l=0}^{\infty} E_l} \tag{2.158}$$

where $E_l = \sum_{m=-l}^{l} E_{lm}$.

- Assuming a star's potential magnetic field falls off to zero far from the star gives the 3D field as

$$B_r(r,\theta,\phi) = \sum_{l=1}^{\infty}\sum_{m=-l}^{l} c_{lm}\left(\frac{r}{R_*}\right)^{-(l+2)} P_{lm}(\cos\theta)e^{im\phi} \tag{2.159}$$

$$B_\theta(r,\theta,\phi) = -\sum_{l=1}^{\infty}\sum_{m=-l}^{l} \frac{c_{lm}}{l+1}\left(\frac{r}{R_*}\right)^{-(l+2)} \frac{dP_{lm}(\cos\theta)}{d\theta}e^{im\phi} \tag{2.160}$$

$$B_\phi(r,\theta,\phi) = -\sum_{l=1}^{\infty}\sum_{m=-l}^{l} \frac{c_{lm}}{l+1}\left(\frac{r}{R_*}\right)^{-(l+2)} P_{lm}(\cos\theta)\frac{im}{\sin\theta}e^{im\phi} \tag{2.161}$$

or alternatively, assuming the field becomes completely radial at some radius R_{ss} gives

$$B_r(r,\theta,\phi) = \sum_{l=1}^{\infty}\sum_{m=-l}^{l} B_{lm} f_l(r) P_{lm}(\cos\theta)e^{im\phi} \tag{2.162}$$

$$B_\theta(r,\theta,\phi) = \sum_{l=1}^{\infty}\sum_{m=-l}^{l} B_{lm} g_l(r) \frac{dP_{lm}(\cos\theta)}{d\theta}e^{im\phi} \tag{2.163}$$

$$B_\phi(r,\theta,\phi) = \sum_{l=1}^{\infty}\sum_{m=-l}^{l} B_{lm} g_l(r) P_{lm}(\cos\theta)\frac{im}{\sin\theta}e^{im\phi} \tag{2.164}$$

where $f_l(r)$ and $g_l(r)$ are given by

$$f_l(r) = \left[\frac{(l+1)\left(\frac{r}{R_*}\right)^{-(l+2)} + l\left(\frac{R_{ss}}{R_*}\right)^{-(2l+1)}\left(\frac{r}{R_*}\right)^{l-1}}{l\left(\frac{R_{ss}}{R_*}\right)^{-(2l+1)} + l + 1}\right] \tag{2.165}$$

$$g_l(r) = \left[\frac{\left(\frac{r}{R_*}\right)^{l-1}\left(\frac{R_{ss}}{R_*}\right)^{-(2l+1)} - \left(\frac{r}{R_*}\right)^{-(l+2)}}{l\left(\frac{R_{ss}}{R_*}\right)^{-(2l+1)} + l + 1}\right] \tag{2.166}$$

- The coronal plasma pressure can be modelled using the magnetic field structure, and by assuming that the corona is in hydrostatic equilibrium, and at the base of the corona, the plasma pressure is proportional to the magnetic pressure. This gives

$$p = p_0 \exp\left(\frac{m}{k_B T}\int g_s ds\right) \tag{2.167}$$

$$g_s = \frac{\mathbf{g}.\mathbf{B}}{|\mathbf{B}|} \tag{2.168}$$

$$\mathbf{g} = \left(-GM_*/r^2 + \omega^2 r\sin^2\theta\right)\mathbf{e_r} + \left(\omega^2 r\sin\theta\cos\theta\right)\mathbf{e}_\theta \tag{2.169}$$

$$p_0(\theta,\phi) = KB_0(\theta,\phi)^2 \tag{2.170}$$

- Assuming that magnetic field lines are blown open by coronal plasma when the plasma β becomes greater than unity at any point along the field line means that there is a maximum radius to which the magnetic field can hold onto the closed corona. This radius, r_{max}, is approximately where

$$K\exp\left(\frac{GM_* m_H}{kT}(r_{max}^{-1} - R_*^{-1}) - \frac{\omega^2\sin^2\theta\, m_H}{2kT}(r_{max}^2 - R_*^2)\right) = \frac{10^{-8}}{2\mu_0}\left(\frac{r_{max}}{R_*}\right)^{-2(<l>+2)} \tag{2.171}$$

- Circumstellar discs are truncated by stellar magnetic fields approximately at the Alfvén surface radius where the magnetic energy density becomes equal to the kinetic energy density in the disc. For an axisymmetric dipole field of strength μ_1, where $\mu_1 = B_* R_*^3$ and B_* is the field strength in the equatorial plane, the Alfvén surface radius is given by

$$r_A = k\left(GM_*\right)^{-\frac{1}{7}}\dot{M}^{-\frac{2}{7}}\mu_1^{\frac{4}{7}} \tag{2.172}$$

where $k \sim 0.5$. For an arbitrary field geometry, the Alfvén surface is at the point where

$$B^2 = C(GM_*)^{\frac{1}{2}}\dot{M}_a r^{-\frac{5}{2}} \tag{2.173}$$

where $C \sim 16$.

- The maximum radius at which accretion can occur is the radius at which the magnetic torque on the disc is balanced by the internal viscous torques, which is at the radius where

$$B_\theta^2 r_t^2 = \frac{1}{2}\dot{M}_a \left(\frac{GM_*}{r_t}\right)^{\frac{1}{2}} \tag{2.174}$$

- Accretion stream trajectories can be modelled using field extrapolations by assuming that all field lines that connect the stellar surface to the inner edge of the disc between the radii r_A and r_t are accreting. The velocity and density of accreting material that left the disc at a radius r_d as it impacts the stellar surface is approximately

$$v_* = \sqrt{2GM_* \left(\frac{1}{R_*} - \frac{1}{r_d}\right)} \tag{2.175}$$

$$\rho_* = \frac{B_*}{B_d} \frac{\dot{M}_a}{v_d A_{d,\text{total}}} \tag{2.176}$$

where B_* and B_d are the magnetic field strengths at the base of the accretion stream and the point where the material leaves the disc respectively, and $A_{d,\text{total}}$ is the area of the inner edge of the disc from which accretion can occur.

3

The role of missing magnetic flux in stellar surface magnetograms

As described in the previous chapter, ZDI magnetograms can be used to infer the 3D structures of coronal magnetic fields. These structures can be used to model stellar coronae and star-disc interactions, instead of relying on arbitrary assumptions about the field geometries. However, the ZDI technique is unable to recover some or most of the magnetic flux at the stellar surface for several reasons.

1. Starspots are the stellar analogue of sunspots, and are present on a large number of observed stars (for a review, see Berdyugina 2005 and Strassmeier 2009). In some cases, Doppler Imaging of stellar surfaces has shown massive dark spots covering significant fractions of the stellar surface. For instance, Donati et al. (2011a) found that the classical T Tauri star V2129 Oph possessed a large dark polar starspot covering ∼6.5% of the stellar surface. The suppression of the Zeeman signature in photospheric absorption lines from regions of the stellar photosphere covered in dark spots is likely to cause

magnetic field strengths in these regions to be underestimated. Berdyugina (2005) argues that the differences between observed starspot filling factors and magnetic filling factors, along with the fact that regions of intermediate brightness have been observed to contain the strongest magnetic fields on ZDI magnetograms, indicates that the fields from starspot umbrae have yet to be detected.

2. In order for the ZDI technique to work, the stellar axis of rotation must be inclined relative to our line-of-sight by an amount that means we are not observing the star pole-on or equator-on. As the technique relies on the Doppler shift of different parts of a star's surface due to the star's rotation, ZDI does not work for stars being viewed purely pole-on as no Doppler shift would be seen. On the other hand, if a star is being viewed equator-on, the effect that a magnetic feature has on Zeeman-sensitive spectral lines would not depend on which hemisphere the feature is in (for example, a feature 20° above the equator would be indistinguishable from a feature 20° below the equator) and therefore, the ZDI technique is not able to determine in which hemisphere a feature lies. Therefore, it is necessary for the star's rotation axis to be inclined with respect to our line-of-sight by amount less than 90°[1]. The ZDI technique suffers from the fundamental limitation that it will never be able to map magnetic fields over the entire surface of a star because it is not possible for the technique to be applied to stars where the entire surface is visible.

3. Magnetic detection techniques that are based on detecting circular polarisation signatures in stellar spectra suffer from missing magnetic flux due to the finite resolution of ZDI magnetograms. This is due to the fact that the circular polarisation signature from an unresolved area is only sensitive to the average magnetic field in that area. If an area of the stellar surface containing a mixture of opposite polarity regions is unresolved, the circular polarization signals from these regions will cancel each other out, causing only weak fields to be measured. As ZDI relies on fitting magnetograms to circular polarisation signatures, it suffers from missing magnetic flux. As ZDI magnetograms are generally produced by fitting a series of spherical harmonic components, the resolution of a magnetogram can be expressed as the highest order spherical harmonic component that can be measured with any accuracy. This is given by

[1]Throughout this thesis, the stars 'inclination angle' is defined as the angle between our line-of-sight and the stellar rotation axis, such that if we are viewing a star from directly above its pole, it will have an inclination angle of 0°.

Star	$v \sin i$ (km s^{-1})	l_{max}	Reference
V374 Peg	36.5	10	Morin et al. (2008a)
GJ 51	12.0	5	Morin et al. (2010)
GJ 1156	17.0	6	Morin et al. (2010)
GJ 1245	7.0	4	Morin et al. (2010)
WX UMa	5.0	4	Morin et al. (2010)
DX Cnc	13.0	6	Morin et al. (2010)
GJ 3622	3.0	2	Morin et al. (2010)
V2129 Oph	14.5	8	Donati et al. (2011a)
TW Hya	4.0	5	Donati et al. (2011b)
τ Boo	15.9	8	Fares et al. (2009)
AA Tau	11.3	5	Donati et al. (2010a)
ξ Bootis A	3.0	5	Morgenthaler et al. (2011)

Table 3.1: Compilation of values of l_{max} for several stars that have been studies using the ZDI technique.

$$l_{max} \sim 2\pi \frac{v \sin i}{FWHM} \tag{3.1}$$

where $v \sin i$ is the projected rotational velocity, and $FWHM$ is the full-width half-maximum (expressed as a velocity), a measure of the width of the unpolarised line (Morin et al. 2010). The value of $FWHM$ is a function of the stellar photospheric temperature, with larger temperatures giving broader lines, and is typically ~ 9 km s^{-1} for inactive M dwarfs (Morin et al. 2008a). Quickly rotating stars with low photospheric temperatures have the highest resolutions. Table 3.1 gives values of l_{max} for some of the stars that have had the ZDI technique applied to them. Typically l_{max} is between 4 and 8, with the best resolution on the rapid rotator V374 Peg. It should be noted that the ZDI magnetogram for V374 Peg shows a very simple, almost pure dipole configuration, despite its high resolution (Morin et al. 2008a).

Since we use ZDI magnetograms to model stellar magnetic processes, it is important to understand how missing magnetic flux limits our ability to model stellar coronae and star-disc interactions. This is especially important for modelling X-ray emitting coronal plasma, which on the Sun is dominated by small scale active regions as shown in Fig. 3.1. In this chapter, I explore these limitations using surface magnetograms for two simulated stars. These stars have been simulated using the surface flux transport model described in Section 2.1. Since all of the information about these magnetic fields is known, I simulate the effects of missing magnetic flux on these magnetograms.

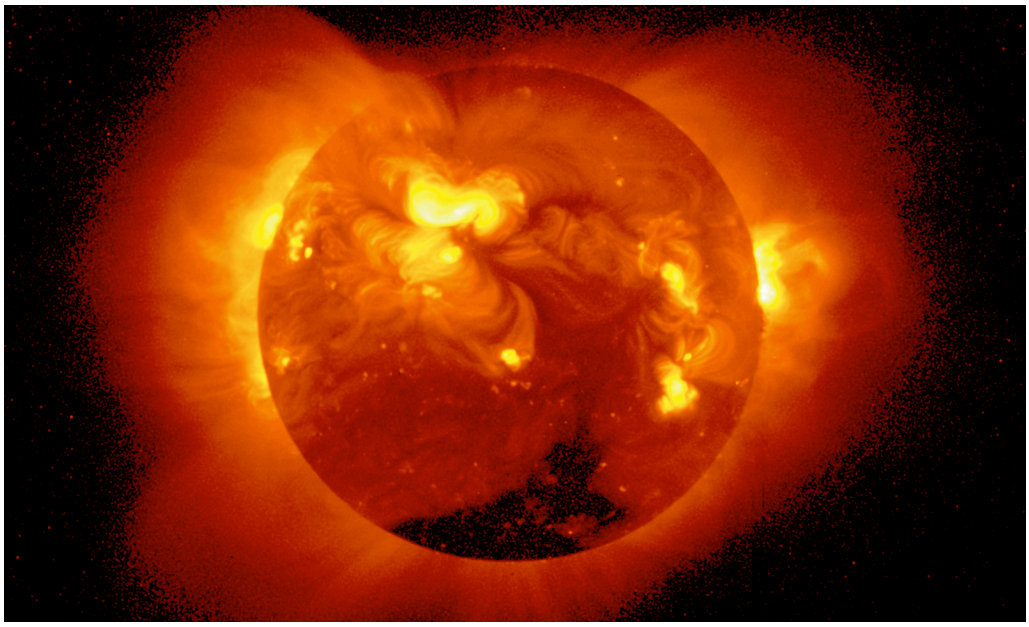

Figure 3.1: The Sun's X-ray emitting corona at a time of maximum activity in 1992. The corona is dominated by emission from small-scale field structures that would not be reproduced on most ZDI magnetograms. The solar X-ray image is from the Yohkoh mission of ISAS, Japan. The X-ray telescope was prepared by the Lockheed-Martin Solar and Astrophysics Laboratory, the National Astronomical Observatory of Japan, and the University of Tokyo with the support of NASA and ISAS.

3.1 Simulating surface magnetograms

The surface radial field magnetograms for the two simulated stars that I use in this chapter were produced by Mackay et al. (2004). These stars are designated the 'active star' and the 'inactive star' based on the fact that they are analogous to the relatively active star AB Dor, and the relatively inactive star, the Sun, respectively. Both stars are assumed to have diffusion constants D of 450 km^2 s^{-1} and are simulated to have periodic variations over 11-year activity cycles, with the latitudes at which magnetic flux is emerged started high at the beginning of each cycle and moving towards the equator as the cycle progresses. The stars have also been simulated to show polarity reversals between each cycle. The two stars differ only in the range of latitudes at which flux is emerged, and the speed of the meridional flow. For the active star, flux is emerged between latitudes 10° and 70°, and a meridional flow of 100 m s^{-1} is taken. For the inactive star, flux is emerged between latitudes 10° and 40°, and a meridional flow of 11 m s^{-1} is taken.

Butterfly diagrams showing the activity cycles for both of these stars are given in Fig. 3.2. For the inactive star, the polar field reversals are seen in the middle of each cycle, as seen on the solar surface (see Fig. 2.1), and for the inactive star, due to the high latitudes of flux

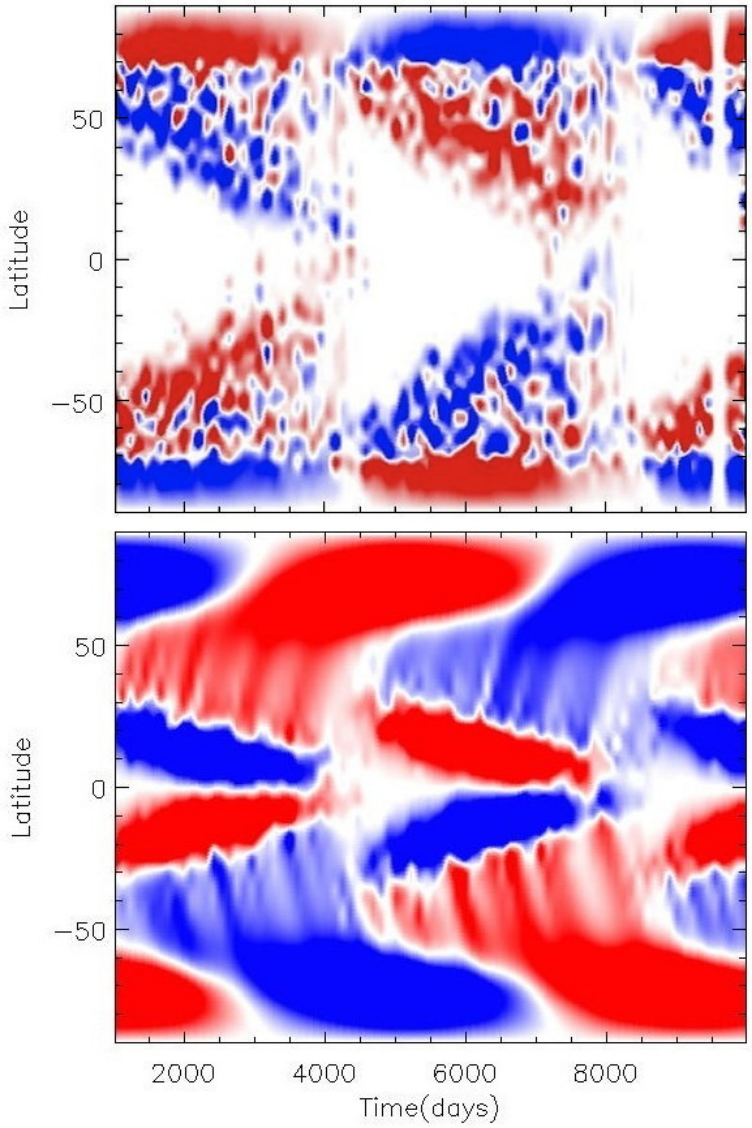

Figure 3.2: Butterfly diagram showing the latitudes of magnetic flux over two 11-year activity cycles for the active star (upper panel) and inactive star (lower panel).

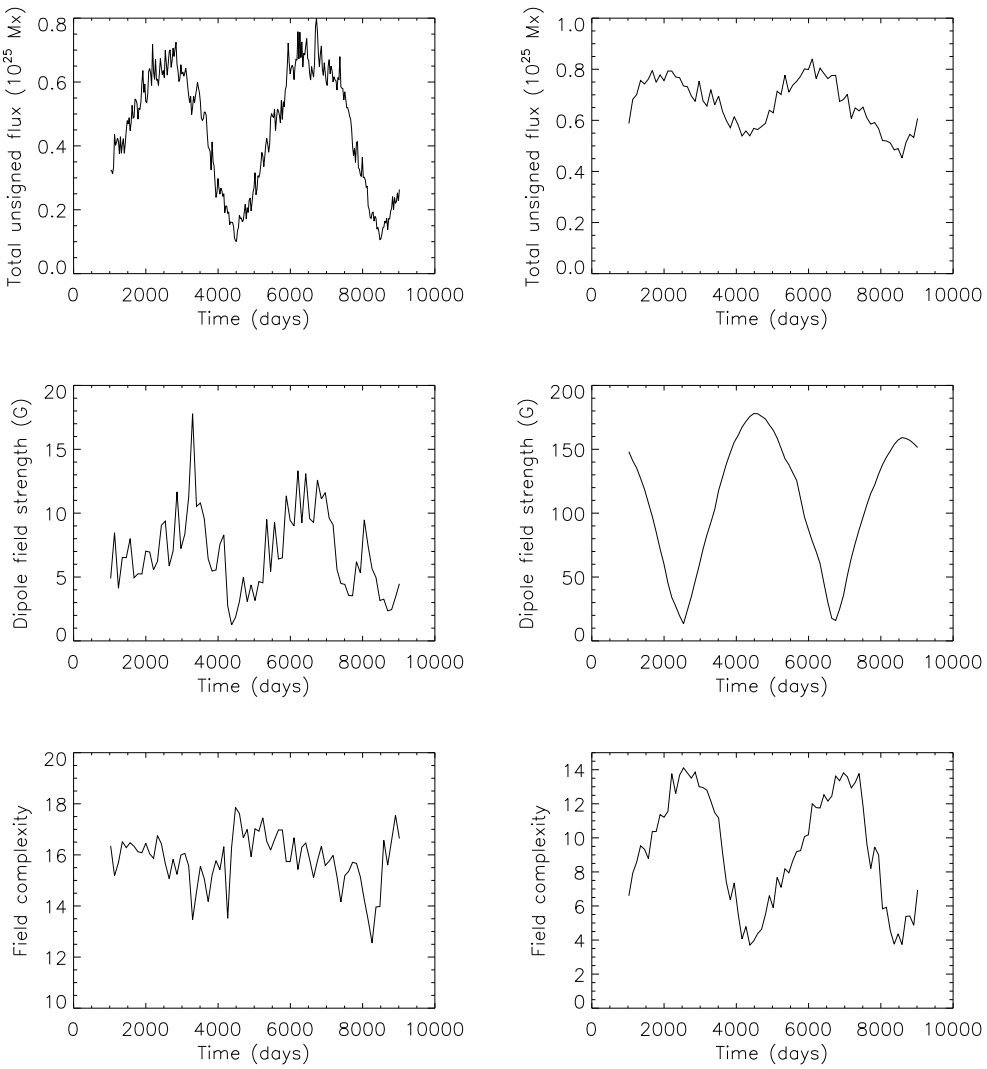

Figure 3.3: Plots showing the variations of total unsigned magnetic flux (upper row), the strength of the dipole component of the field (middle row), and field complexity defined as the energy weighted average l value that describes the field (lower row) for the active star (left column) and the inactive star (right column).

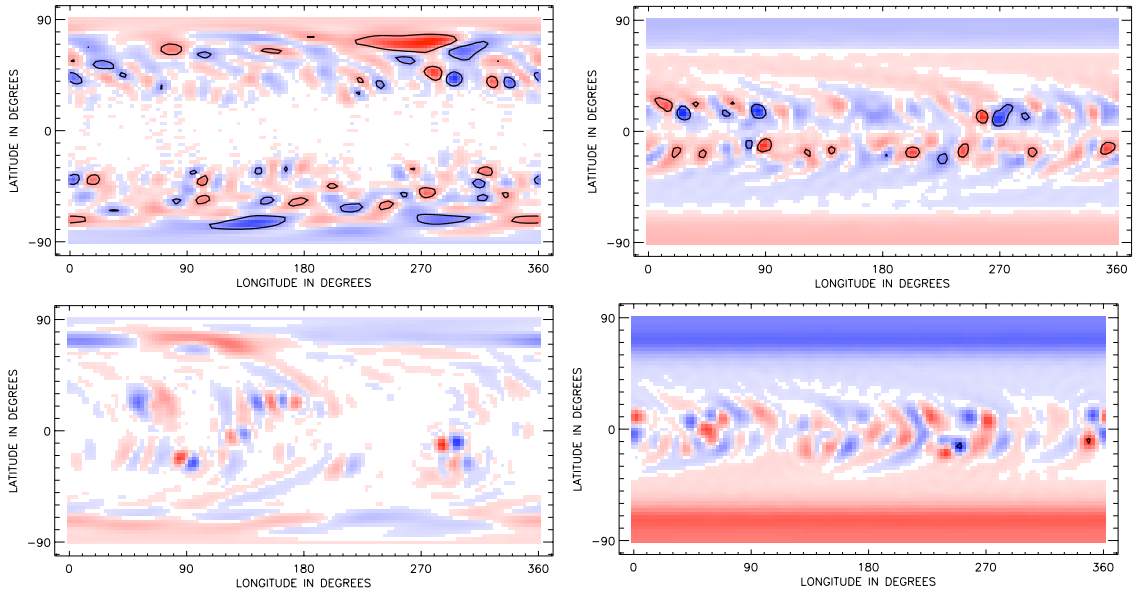

Figure 3.4: Surface radial field magnetograms for the active star (left column) and the inactive star (right column) at a time of a relative maximum in magnetic activity (upper row) and relative minimum in magnetic activity (lower row). The black contour lines indicate where the field strengths are above 500 G.

emergence and the strong meridional flow, polar field reversals occur approximately between cycles. Fig. 3.3 shows the variations in the total unsigned magnetic flux, the dipole field strength, and the field complexity over the course of a simulated cycle for both stars. For the active star, the total unsigned magnetic flux varies by a factor of five over the cycle and is well correlated with the strength of the dipole component of the field. However, the complexities of the magnetograms, as measured by the energy weighted average l value, does not vary by much over the course of the cycle. For the inactive star, there are much smaller variations in the total unsigned flux, but much larger variations in the dipole field strength and the field complexity. Interestingly, for the active star, the field is always so complex that the value of $< l >$ is significantly above what could be reproduced using the ZDI technique, whereas for the inactive star, during times of activity minimum, the field complexity is low enough that it could be fully reproduced by high resolution ZDI magnetograms. Examples of magnetograms at maximum and minimum times in the cycle for both stars are shown in Fig. 3.4.

3.2 Simulating missing magnetic flux

Based on the solar analogy, I assume that starspots exist in regions of strong magnetic field and I simulate the presence of starspots by setting the field strengths to zero in all areas of the surface magnetograms where the radial component of the field is stronger than 500 G. The

locations of these regions are indicated by the black contour lines in Fig. 3.4.

The obscuration of a portion of the star's surface due to a tilt in its rotation axis is simulated by setting to zero the field strength in an entire hemisphere. This corresponds to a limiting case where the star's rotation axis is parallel with our line-of-sight and we can only see one hemisphere. If a star actually had this tilt angle, the features on its surface would not be Doppler shifted as the star rotates, and stellar magnetograms would be impossible to produce. Even though this does not correspond to a physically realistic situation, I consider it as it provides the most severe limitation on the fraction of the stellar surface that is visible. It is worth noting that while the very early ZDI maps were produced by reconstructing the radial component, or all three vector components, of the field at each point on the surface independently (Brown et al. 1991, Donati et al. 1999), the more recent reconstructions (Donati et al. 2001, Donati et al. 2006b, Morin et al. 2008a) describe the field in terms of spherical harmonics whose amplitudes are fitted to the line profiles. This allows the reconstruction of magnetic modes that are symmetric or antisymmetric about the equator and therefore some indication of the global symmetry of the field can be obtained by comparing the fit to the data of the modes, even if some portion of one hemisphere is out of view.

I simulate the effect of limited resolution in two different ways, approximately corresponding to the two techniques used for fitting ZDI magnetograms mentioned above. In the first method, I simulate low resolution by smearing the surface field such that the original maps, with a latitudinal resolution of just over 1° and an equal longitudinal resolution at the equator, are replaced by maps with latitudinal resolution of around 11° degrees and a longitudinal resolution of around 8° at the equator. Each new surface grid element contains a field with a strength that is the area weighted mean of the field strengths in the old elements contained within it. This simulates the low resolution magnetograms produced by the first ZDI technique. In the second method, I cut all spherical harmonic components with l greater than some cutoff value l_{max}. Fig. 3.5 shows magnetograms that have been degraded using the two methods.

In the next section, I discuss the effects of simulating missing magnetic flux due to starspots, a hemisphere out-of-view, and a limited resolution based on the first method discussed above. The effects of a limited resolution based on the second method is discussed separately in Section 3.4.

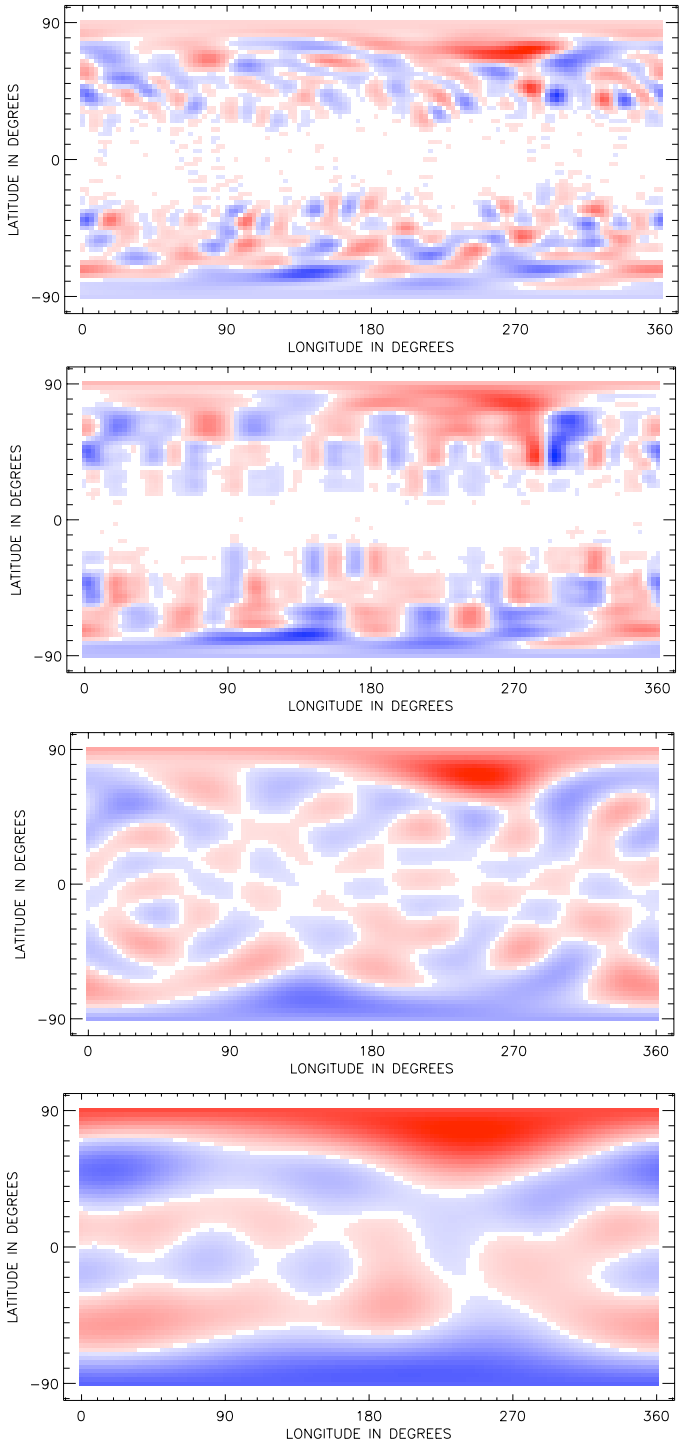

Figure 3.5: Magnetograms showing the effects of the simulated low resolution on surface magnetograms for the active star at a time of maximum activity. From top to bottom, these magnetograms correspond to the original magnetogram, the smeared magnetogram, the magnetogram with only the spherical harmonic components below $l = 10$ considered, and the magnetogram with only the spherical-harmonic components below $l = 5$ considered. From top to bottom, the maximum field strengths for each of these magnetograms are 1214 G, 731 G, 403 G, and 161 G.

Star	$\Delta\Phi_{spots}$ (%)	$\Delta\Phi_{hemisphere}$ (%)	$\Delta\Phi_{smeared}$ (%)
Active	19	52	17
Inactive	11	51	10

Table 3.2: Percentage drop, averaged over one activity cycle, in total magnetic flux, Φ, over the stellar surface for both stars. This drop is due to the suppression of magnetic field in dark starspots and an entire hemisphere out of view and the cancellation of opposite polarity magnetic fields due to the smearing of the stellar surface magnetogram.

3.3 Results I[2]

3.3.1 The surface magnetograms

I now discuss the effects of applying the degrading techniques discussed in the last section on the magnetograms themselves.

One way of visualising the effect of degrading the surface magnetograms is by looking at the strengths of each spherical harmonic component. This is shown in Fig. 3.6 for periods of maximum activity during the magnetic cycles. The first column shows the distribution of power across the modes for both the active star (upper panel) and the inactive star (lower panel). The magnetic field of the active star has power distributed across a much greater range of modes than the inactive star, corresponding to its more complex field. The second column, illustrating the effect of dark star spots, shows the influence on the field structure of cutting out all regions of field above 500 G. This clearly has a greater effect on the field of the more active star since it has a greater coverage of these strong-field regions. While some power is removed from all of the modes, it is the high-order modes that are most strongly suppressed, while the dominant low-order modes are largely unaffected. The third column illustrates the effect of removing field from the unobserved hemisphere. This has a significant effect on the field structures of both stars. It allows power to be distributed more evenly over the different modes, giving the effect of blurring the plot. The fourth column illustrates the effect of smearing the original magnetogram. This removes power from some of the higher order components while leaving the lower order components unchanged. As the strength of higher order components decreases with increasing distance from the star faster than lower order components, this affects the field on smaller scales more than on larger scales.

Table 3.2 shows the percentage drop (averaged over the stellar activity cycle) in the total unsigned surface magnetic flux for both the active and inactive stars. The case where an entire

[2]This section is based on Johnstone et al. (2010).

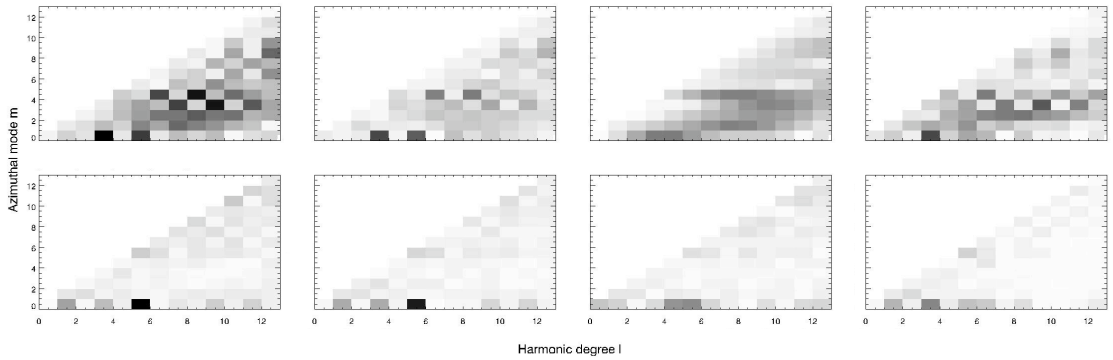

Figure 3.6: Plots showing the strengths of each spherical harmonic component. Results are shown for the full data case (first column), the field cutoff above 500 G (second column), the field cutoff in an entire hemisphere (third column), and the field smeared (forth column) for both the active star (upper row) and the inactive star (lower row).

hemisphere is cut from the surface magnetograms presents the largest drop in magnetic flux of about 50% on average. For the active star, the case where the surface magnetogram is smeared gives a large drop in magnetic flux due to cancellation of opposite polarity field.

Although these stars show large unsigned magnetic fluxes over their entire magnetograms, according to Gauss' law for the magnetic field ($\oint \mathbf{B}.d\mathbf{S} = 0$) the total signed flux must always be zero (in the absence of magnetic monopoles). However, when regions of the magnetograms are suppressed, if more flux of one polarity is lost, this condition will not be satisfied. This is the case when the fields stronger than 500 G and when the field in an entire hemisphere is suppressed, although in both cases, the total signed flux is usually smaller than 2% of the total unsigned flux. In these calculations, the surface magnetograms are represented as the sum over many spherical-harmonic components. The total signed flux for each individual component is zero and thus for the spherical-harmonic expansion of the surface magnetograms is also zero. The extrapolated magnetic fields, in most cases, cannot perfectly represent the original surface magnetograms when regions of the magnetograms are suppressed. Instead of being zero, the total unsigned flux in the hemisphere that is suppressed after the extrapolation is usually around 5 - 10% of its original (unsuppressed) value.

3.3.2 The magnetic field structure, accretion and open flux

Extrapolated magnetic fields for both stars are given in Fig. 3.7. These diagrams show the field structure at a time of maximum activity. For the active star, the strong octupolar component of the field is very clear in all cases except where the field in the lower hemisphere is suppressed.

One of the reasons why understanding the structure of stellar magnetic fields is important

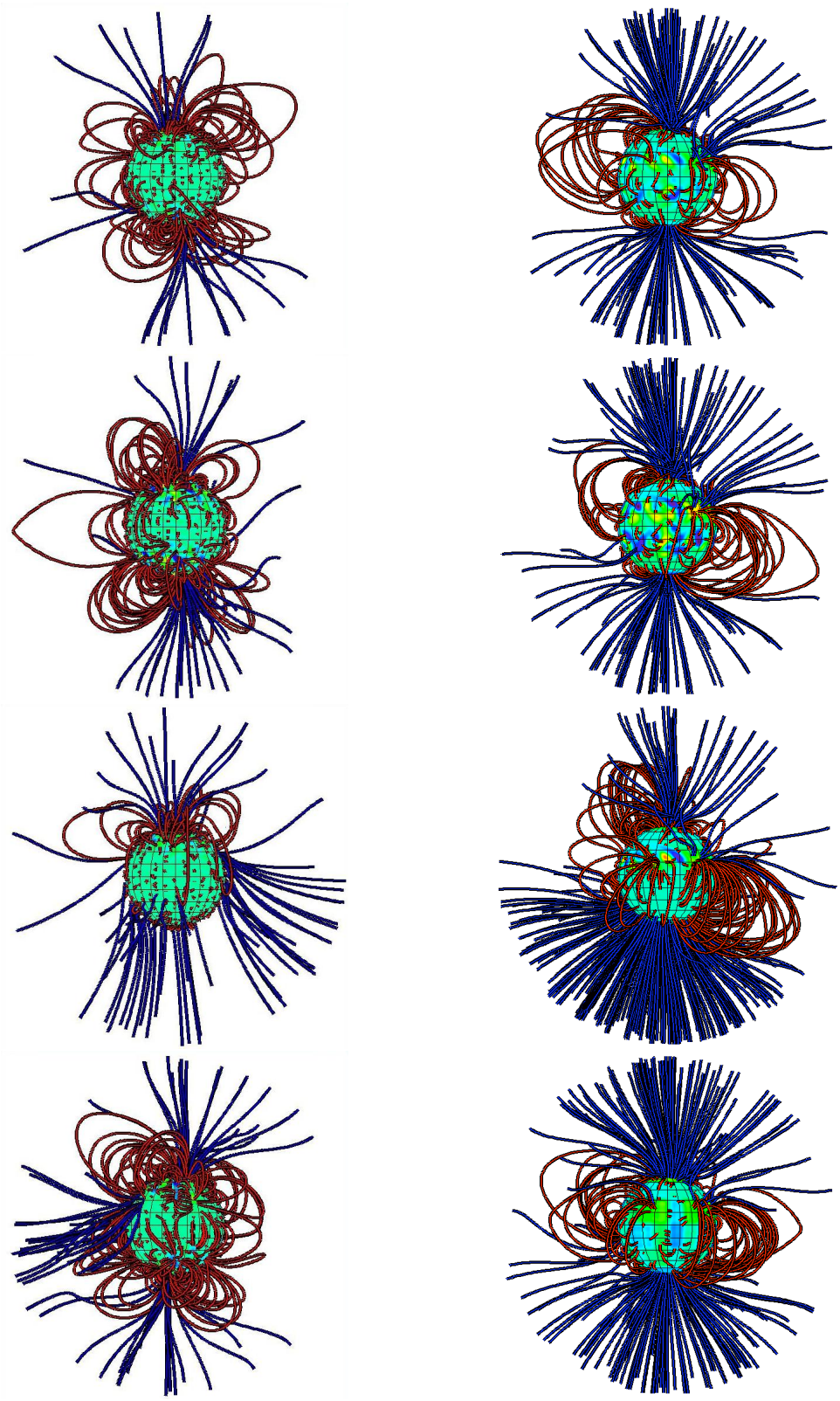

Figure 3.7: Extrapolated coronal fields for the active star (right) and the inactive star (left). Presented for the full data (first row), the field cut off above 500 G (second row), the field cutoff in an entire hemisphere (third row), and the field smeared (fourth row). Open field lines are plotted in blue and closed field lines in red.

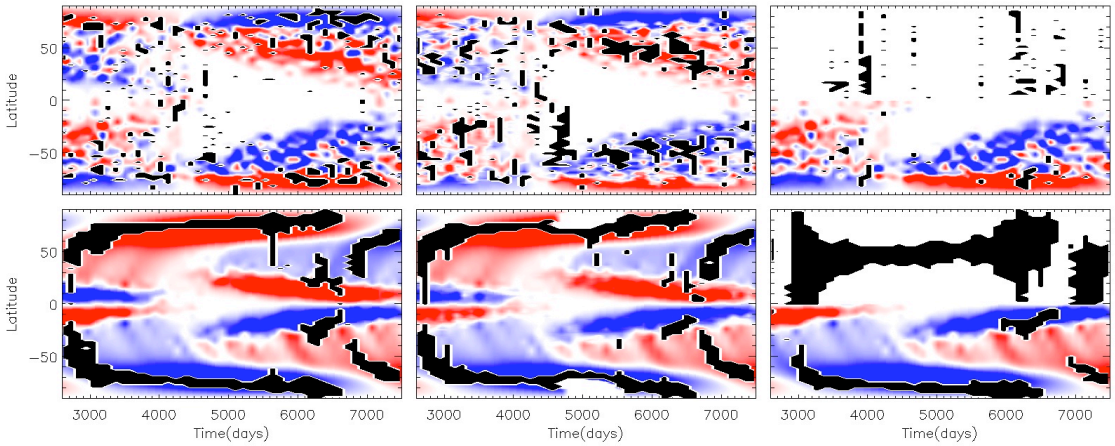

Figure 3.8: Butterfly diagrams for the active star (top row) and inactive star (bottom row) for the full case (left column), suppression of the field stronger than 500 G (middle column) and suppression of the field in an entire hemisphere (right column). The black regions show the latitudinal locations where field lines able to support accretion from a circumstellar disc attach to the stellar surface.

is that it will help to understand magnetospheric accretion onto pre-main sequence stars from their circumstellar discs. In this section, I discuss the effects of missing information in on calculated accretion filling factors and the latitudes at which accreting field lines attach to the stellar surface. For both stars and at all times, the effect of lowering the resolution of the surface magnetograms is insignificant and will not be discussed here.

The locations on the stellar surface where accretion can take place are calculated by tracing field lines from every grid point on the stellar surface. For these calculations, the global magnetic fields are extrapolated assuming a source radius of 10 R_*. All field lines that cross the equator and extend to radii between $0.5R_{co}$ and $1.0R_{co}$, where R_{co} is the equatorial corotation radius, are assumed to be able to support accretion. In this case, R_{co} is calculated assuming the star has solar mass and radius and a rotation period of 2.5 days. Thus, R_{co} has a value of approximately 8 R_*.

Fig. 3.8 shows the latitudes at which field lines that can support accretion connect with the stellar surface over an entire activity cycle superimposed on magnetic butterfly diagrams. When the fields with strengths above 500 G are suppressed, there is only a small effect on the accretion filling factors for the inactive star. The active star shows small increases at some times during the cycle with an increase in the number of low latitude regions contributing to accretion at most times in the cycle. The most significant effect on the accretion filling factors and latitudes comes in the case where the field is suppressed in an entire hemisphere. This is clear for both stars and is due to the fact that without regions of stronger and weaker field

Star	Δf_{spots} (%)	$\Delta f_{\text{hemisphere}}$ (%)	$\Delta f_{\text{smeared}}$ (%)
Active	15	26	48
Inactive	9	-2	20

Table 3.3: Percentage increase, averaged over one activity cycle, in the fraction of open flux to total flux, $f = \Delta(\Phi_{open}/\Phi_{total})$, for fields with missing information due to starspots, an entire hemisphere out of view, and a limited resolution for both active and inactive stars.

in the invisible hemisphere, field lines that are being traced from the visible hemisphere can connect to anywhere with no preferred location. However, when an entire hemisphere is out of view, the accretion pattern in the visible hemisphere tends to remain the same.

Another important aspect of the magnetic structure and accretion is the magnetic pressure in the equatorial plane, which determines the field's ability to disrupt the circumstellar disc. Fortunately the missing information causes no significant change in the strength of the magnetic field in the equatorial plane, and its variation as a function of distance from the surface.

Finally, I briefly explore the effect that the missing information has on calculated open magnetic fluxes. The two important aspects are the fraction of open flux to total flux, and the latitudinal distribution of open field. These are important as they can affect the rate at which stars lose angular momentum through stellar winds. In every case, the missing information causes a large drop in the total open flux due to the drop in total unsigned flux. Table 3.3 gives the average percentage drop in the fraction of open flux to total flux for each case. In almost every case the missing information causes an increase in the fraction of open flux to total flux. The effect of the missing information not only decreases the open flux and the total flux, but also changes the nature of that flux. Typically the flux that is lost is closed such that the loss of information leads to a greater fraction of the flux through the stellar surface being open.

For both the active and inactive stars, the open flux tends to be located at the stars' poles. The latitudinal distribution of the open flux is not generally affected by the missing information for both stars. An exception to this is the case of the suppression of the field stronger than 500 G on the active star. In this case, the open flux is generally located at slightly lower latitudes.

Star	$\Delta n_{e,\mathrm{spots}}$ (%)	$\Delta n_{e,\mathrm{hemisphere}}$ (%)	$\Delta n_{e,\mathrm{smear}}$ (%)
Active	-81	15	-35
Inactive	-68	-1	-45

Table 3.4: Percentage increase, averaged over one activity cycle, in coronal electron density, n_e, averaged over the volume of plasma in closed magnetic loops. Results given for both stars due to the absence of magnetic fields in starspots, a hemisphere out of view, and the effects of having a surface magnetogram with a reduced resolution.

3.3.3 The coronal density and emission measure

The coronal plasma model used here is described in Section 2.5. The density at each point in the corona is determined by assuming isothermal, hydrostatic balance along the field line through that point. The one free parameter in this process is the pressure at the base of each field line. Since this is assumed to be proportional to the magnetic pressure, any degrading of the surface magnetic map will affect the modelled coronal pressure and hence the modelled density. This can be seen clearly in Fig. 3.9 which shows histograms of the number of volume elements in the coronal model at specific electron densities for a time close to cycle maximum. The results are presented for both stars and all cases under consideration. The most significant impact on the distribution of pressures, and hence densities, in the corona is for the case where the strongest fields are removed. Since this cuts out the regions of strongest field, it also cuts out the highest density values, as can be seen by the loss of the high-density tail in the second column of Fig. 3.9. This could be detected observationally as an enhancement of the densities derived from X-ray lines (e.g. Testa et al. 2004) compared to the model values for the same emission measures. The fraction by which the models would underestimate the densities as a result of the loss of information in the magnetograms is shown in Table 3.4. In the cases of missing information due to starspots and a limited resolution, large decreases in the average electron densities are seen. In the case of missing information in an entire hemisphere, there is no large decrease in the electron densities with little change in the inactive star and the active star showing a small increase.

The alterations of the modelled coronal densities are a response to changes in the surface magnetograms and are also apparent when the emission measures are calculated. Fig. 3.10 shows the variations of emission measures and the rotational modulation of the emission measures for just over one 11-year activity cycle for both stars. In all cases, the variation in emission measure closely follows the variation in total magnetic flux over the activity cycle. For the active star, predicted emission measures are fairly robust and are only significantly

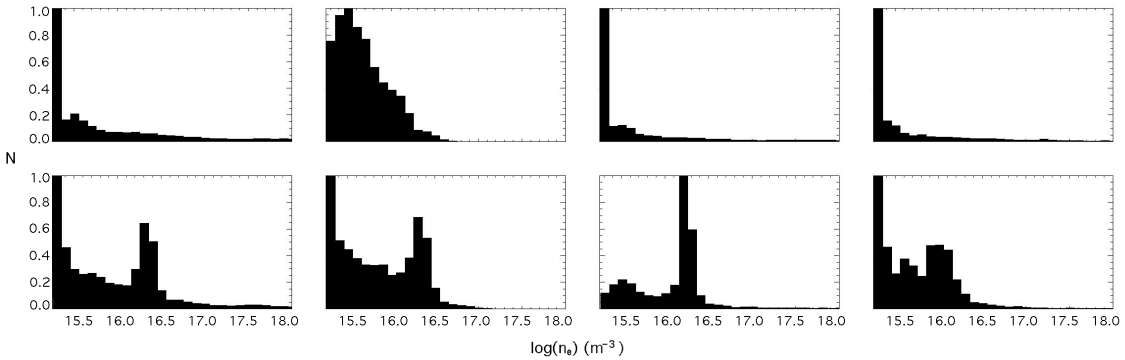

Figure 3.9: Histograms showing the number of grid points (normalised to a peak of unity) in the corona with specific electron densities for the active star (top row) and the inactive star (bottom row). The cases of the full data case (first column), the field cutoff above 500 G (second column), the field cutoff in an entire hemisphere (third column), and the field smeared (forth column) are given.

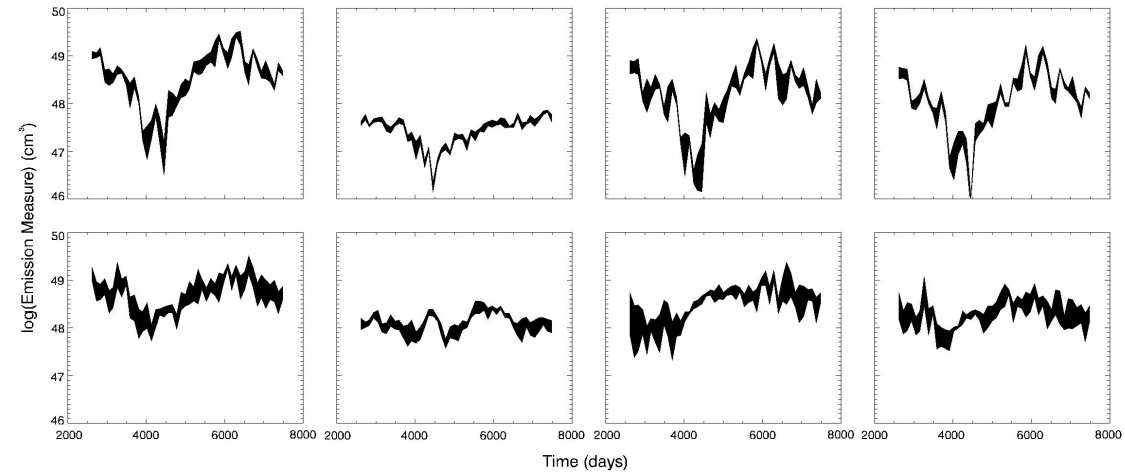

Figure 3.10: Emission measures over one 11-year activity cycle for the active star (upper row) and inactive star (lower row). Results are shown for the full data case (first column), the field cutoff above 500 G (second column), the field cutoff in an entire hemisphere (third column), and the field smeared (forth column). The thickness of the lines show the rotational modulation with the tops of the lines corresponding to the maximum and the bottoms of the lines corresponding to the minimum in visible emission measures as the stars rotate.

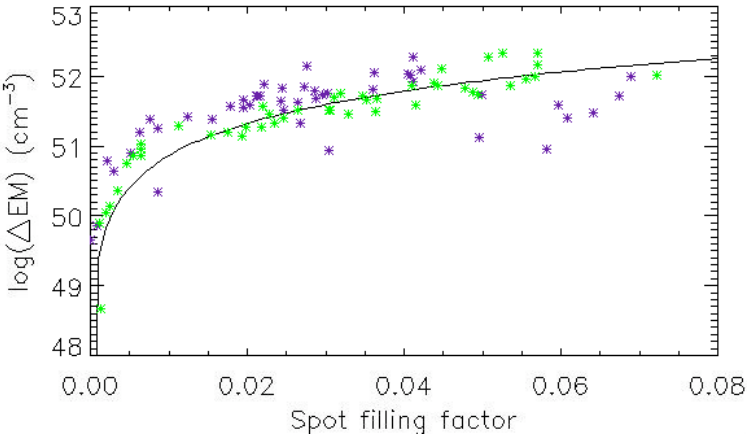

Figure 3.11: Drop in calculated emission measure for both active and inactive stars against the spot filling factor (fraction of stellar surface area with field above 500 G) for the active star (green) and inactive star (purple). The thin black line shows the equation $\log \Delta EM = 54 f_s^{0.013}$.

affected by the removal of the field in the spots. The very large drop in the emission measure is due to the large fraction of the surface covered in fields greater than 500 G. The inactive star has many fewer strong field regions and consequently a much larger rotational modulation. It is also much more severely affected by both the removal of the spot fields and also by the removal of the field in the lower hemisphere. In both these cases, the form of the variation is changed (indeed the cyclic nature of the variation is all but lost when the spot fields are removed). For both the active and inactive stars, the smearing of the maps has the least effect, while the removal of the spot fields has the greatest effect. It is only for the inactive star, however, that the form of the cycle is changed. This suggests that calculating stellar coronal emission measures from ZDI magnetograms may fail to reproduce the cyclic variations in emission measures for some stars even if magnetic cycles are present.

The large drops in the modelled emission measures due to the suppression of the strongest fields from the surface magnetograms clearly depends on the spot filling factors. This is shown in Fig. 3.11 for both stars. The dependance on spot filling factors is approximately the same for both stars.

3.4 Results II: the effects of missing high-order spherical-harmonic components[3]

[3]This section is based on a talk that I gave at the Bcool collaboration meeting in Toulouse in December 2011. The calculations presented here are not included in Johnstone et al. (2010) and are thus presented separately.

In this section, I investigate the effects of degrading the simulated magnetograms by cutting all spherical harmonic components above $l_{max} = 10$ and $l_{max} = 5$ separately. This simulates the effects of finite resolution in ZDI magnetograms that have been produced by fitting the strengths of spherical harmonic components directly to line profiles. I only consider the active star in this section.

Fig. 3.5 shows the effect of degrading a single magnetogram. Butterfly diagrams showing the effects over an entire cycle are given in Fig. 3.12. The degraded magnetograms in Fig. 3.5 are missing all of the small scale field structures seen in the original field. The $l_{max} = 10$ magnetogram contains some small scale structures, but these do not resemble the structures seen in the original. The $l_{max} = 5$ magnetogram contains no small scale field, and looks similar to a typical ZDI magnetogram. The maximum field strengths for the degraded magnetograms are significantly reduced. The original magnetogram has fields of ∼1200 G in the mid latitude active regions, and fields of ∼ 200 G near the poles. The polar field strengths of the degraded magnetograms are not affected, but the field strengths in the mid-latitude active belts are dramatically reduced, with fields of only a few hundred G remaining. This is shown in Fig. 3.13. The total unsigned magnetic fluxes over two activity cycles for the degraded magnetograms are shown in Fig. 3.14. For the $l_{max} = 10$ case, the flux is typically 60-80% of the original value[4]. For the $l_{max} = 5$ case, the flux is typically 30-50% of the original value. In both cases, a larger fraction of flux is lost at times of high activity.

Using the PFSS model, I have extrapolated these field to all radii within the corona by assuming a source surface at a radius of 2.5 R_*. Fig. 3.15 shows how the total unsigned magnetic flux depends on the distance from the stellar surface (here I define the total unsigned magnetic flux at a specific radius as the unsigned flux integrated over a spherical shell centered around the star at that radius). As shown above, at the stellar surface the flux is significantly lower in the degraded magnetograms. However, in the original case, where the higher order spherical-harmonic components dominate the field at the stellar surface, the field strength falls off with radius much faster than in the other two cases. By about a quarter of a stellar radius from the surface, the fields in these three cases are almost indistinguishable, in both

[4]For the $l_{max} = 10$ case, at one time during the minimum between the two activity cycles, the total unsigned flux is actually increased by the degrading of the maps. It is possible for the addition of a higher order spherical harmonic component to decrease the total unsigned flux. This can be demonstrated by considering a simple case: take two surface magnetograms, one of which is an axisymmetric dipole with a polar field strength of 1 G, and the other is an axisymmetric octupole with a polar field strength of 0.5 G, where the positive polarity poles for both these fields coincide. If you make a magnetogram that is the composite of these two maps, the total unsigned flux for this case is less than the total unsigned flux for the pure dipole case.

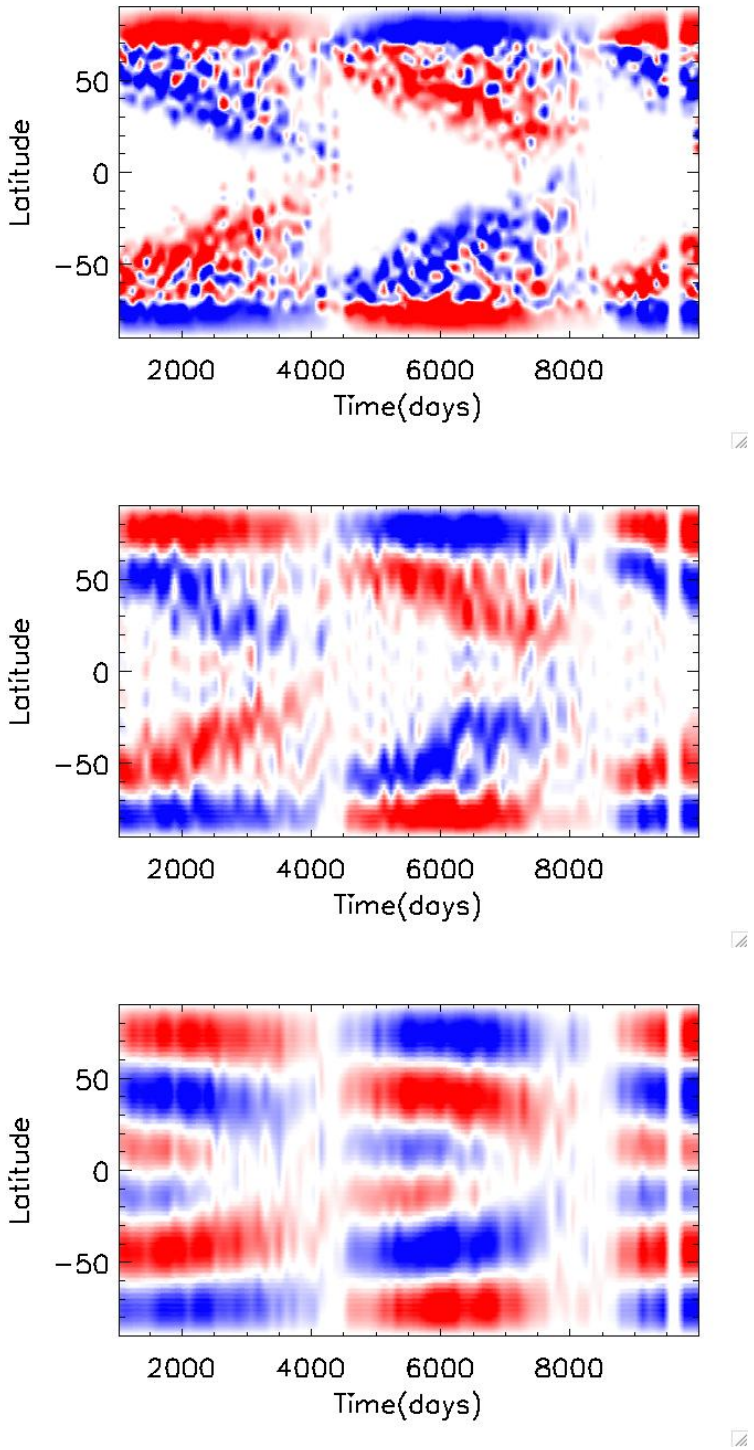

Figure 3.12: Butterfly diagrams showing the effects of degrading the magnetograms corresponding to the original case (upper panel), the $l_{max} = 10$ case (middle panel), and the $l_{max} = 5$ case (lower panel).

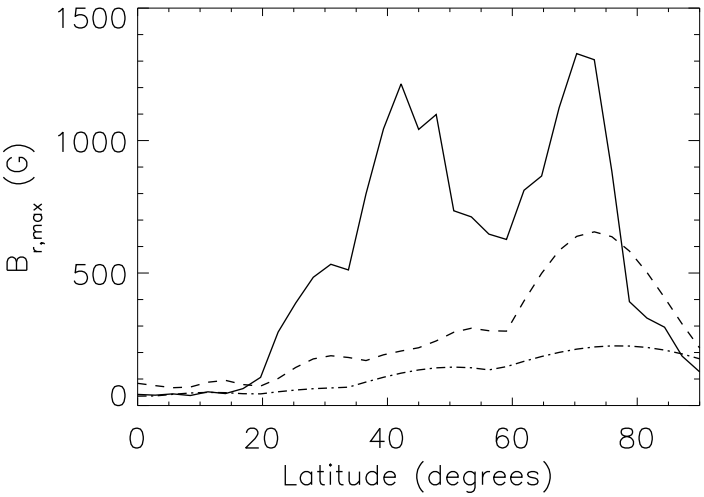

Figure 3.13: Diagram showing the maximum radial field strengths as a function of latitude, over an entire hemisphere for the magnetograms given in Fig. 3.5. The full line corresponds to the original case, the dashed line corresponds to the $l_{max} = 10$ case, and the dash-dot line corresponds to the $l_{max} = 5$ case.

strength and structure.

Using the coronal plasma model described in Section 2.5, I calculate the global coronal emission measures at each point in the activity cycles for each case. These can be seen in Fig. 3.16. As is shown in the last section for the case where the high field strengths in active regions were cut from the magnetograms, the degrading of the magnetograms correspond to a large decrease in the predicted coronal emission measures. For the $l_{max} = 10$ case, the emission measures are typically reduced by an order of magnitude. For the $l_{max} = 5$ case, they are reduced by up to three orders of magnitude. This is due to the fact that the plasma pressure at the base of the corona is assumed to be proportional to the magnetic pressure. In the degraded cases, the surface field strengths are significantly lower, giving much lower coronal pressures.

It is interesting to look at the sizes of the coronal X-ray emitting structures. Fig. 3.17 shows how much of the total emission measure is contained within magnetic loops of different lengths for the original case and for the $l_{max} = 5$ case. In the original case, the emission is dominated by contributions from closed field lines smaller than 0.7 R_*, with negligible contributions from larger structures. However, in the $l_{max} = 5$ case, as the small scale field structures are missing, the emission comes equally from field lines of all sizes betwen 0.2 R_* and 1.9 R_*. Interestingly, in the $l_{max} = 5$ case, there is a large increase in the amount of

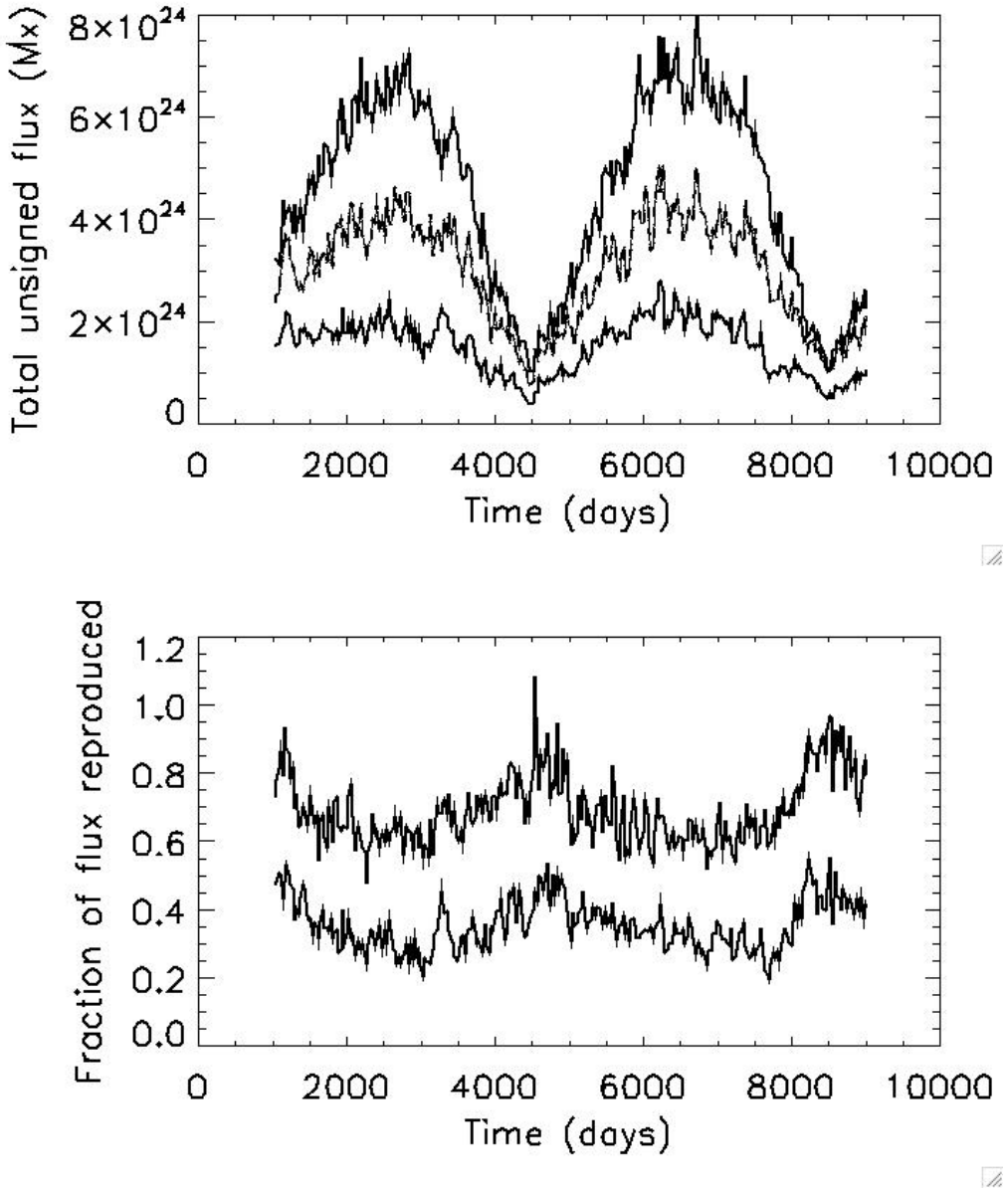

Figure 3.14: *Upper panel*: the total unsigned fluxes over two activity cycles for original case (upper line), the $l_{max} = 10$ case (middle line), and the $l_{max} = 5$ case (lower line). *Lower panel*: the fraction of the flux in the original magnetograms held in the degraded magnetograms over two activity cycles for the $l_{max} = 10$ case (upper line) and the $l_{max} = 5$ case (lower line).

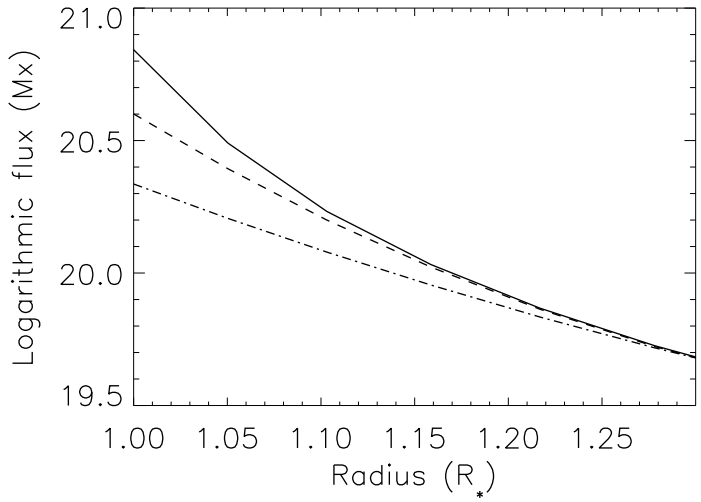

Figure 3.15: Total magnetic flux as a function of the distance from the star for the original field (solid line), the $l_{max} = 10$ field (dashed line), and the $l_{max} = 5$ field (dash-dot line).

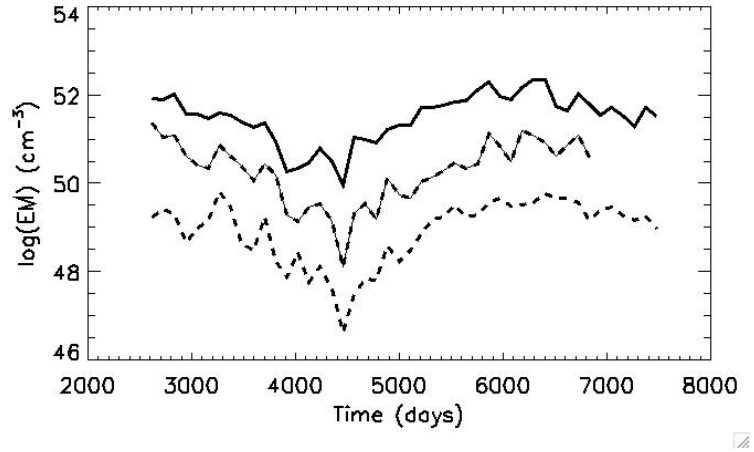

Figure 3.16: The total coronal emission measure over almost two activity cycles. The full line corresponds to the original case, the dash-dot line corresponds to the $l_{max} = 10$ case, and the dashed line corresponds to the $l_{max} = 5$ case.

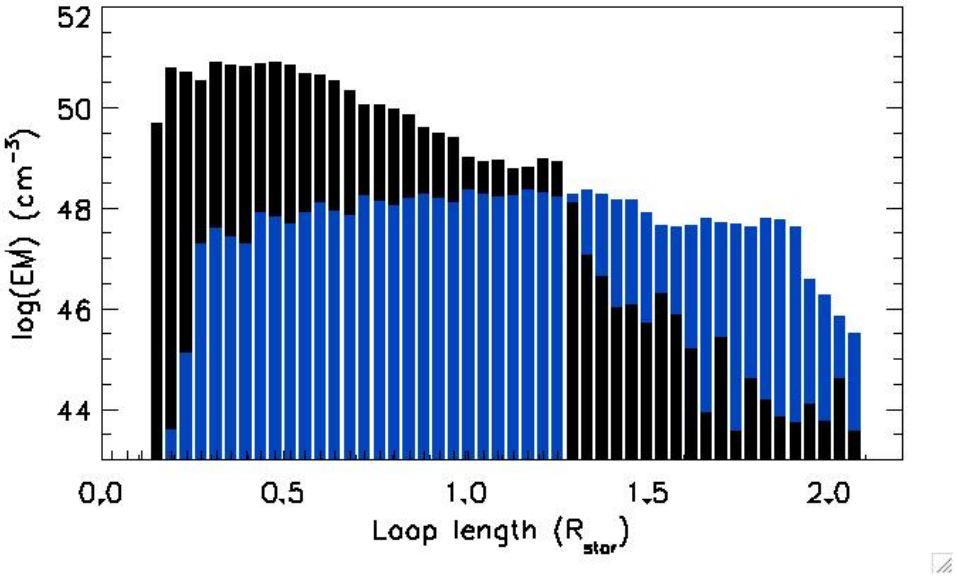

Figure 3.17: Bar chart showing the contribution to the total emission measure from closed magnetic loops of different lengths for the original case (black bars), and the $l_{max} = 5$ case (blue bars).

emission coming from larger field lines as the removal of the small scale field structures allow long field lines to connect to stronger field in the low latitude activity belts.

3.5 Reconstructing missing flux in starspots and the curious case of V2129 Oph

It may be possible to correct for the underestimation of magnetic field strengths in dark regions of the stellar surface. This can be done using Doppler Imaging brightness maps to predict the locations of these dark regions and add magnetic flux back into the ZDI magnetograms. Arzoumanian et al. (2011) explored this possibility for the two rapidly rotating low mass stars V374 Peg and AB Dor[5]. Based on Doppler Imaging brightness maps, they added magnetic flux of different strengths and randomly chosen polarities into the observed ZDI magnetograms. They found that since both stars have very complex brightness maps, with many low latitude dark spots, adding flux into the magnetograms in this way increases the complexity of the magnetic fields on small scales. Using the same coronal plasma model that I use in this thesis, they found that this has a large effect on the predicted coronal plasma structures. This can be seen by comparing the predicted rotational modulations of X-ray emission from the altered fields with those of the original fields. This is shown in Fig. 3.18 for the case of V374 Peg. They repeated the calculations for a large number of different combinations of randomly cho-

sen spot polarities and showed that different combinations of polarities lead to significantly different coronal plasma structures.

One young accreting CTTS that has been extensively studied is V2129 Oph (see Section 4.1). Donati et al. (2007) and Donati et al. (2011a) produced ZDI magnetograms for V2129 Oph based on observations taken in June 2005 and July 2009. They found that the star's magnetic field is dominated by a strong tilted octupole and a weaker tilted dipole of strengths 1.2 kG and 0.35 kG respectively. Donati et al. (2007) also produced a Doppler Imaging surface brightness map and a Ca II IRT excess emission map. The radial field, surface brightness, and Ca II IRT excess emission maps are shown in Fig. 3.19. They found that V2129 Oph possesses a large dark polar starspot which coincides spacially with a region of strong radial field and Ca II IRT excess emission.

Ca II IRT excess emission likely originates in accretion shocks so the Doppler Imaging map shows that accretion is impacting the stellar surface primarily at high latitudes. By extrapolating the June 2005 ZDI magnetogram, and assuming a simplified accretion model to calculate which field lines are accreting, Donati et al. (2007) and Jardine et al. (2008) showed that V2129 Oph's magnetosphere must extend to at least 7 R_* from the star's centre for their predicted accretion footpoints to coincide with the areas of high Ca II IRT excess emission. Romanova et al. (2011) carried out 3D MHD simulations of accretion onto V2129 Oph. The simulations used, as their initial magnetic field, a superposition of a tilted dipole and a tilted octupole of strengths 0.35 kG and 1.2 kG respectively. They found that using these field strengths, they were only able to reproduce the observed accretion rate of $10^{-8.4}$ $M_\odot$ yr^{-1} (Donati et al. 2007) if the disc is truncated close to the stellar surface, at about 3.4 R_*. However, this would lead to a significant component of accretion impacting the stellar surface at low latitudes contrary to what is indicated by the Ca II IRT excess emission map. They were able to produce simulations where the disc was truncated at 6.8 R_*, and thus the polar accretion spots dominate over the low-latitude accretion spots. However, this lead to mass accretion rates that are an order of magnitude below the observed value. They found that this problem could be resolved if the dipole component was made twice as strong as the June 2005 observations suggest.

In this section, I explore the possibility that the dipole component of V2129 Oph's mag-

[5]They used ZDI magnetograms and Dopper imaging maps from Donati et al. (2006a) for V374 Peg, and from Hussain et al. (2007) for AB Dor.

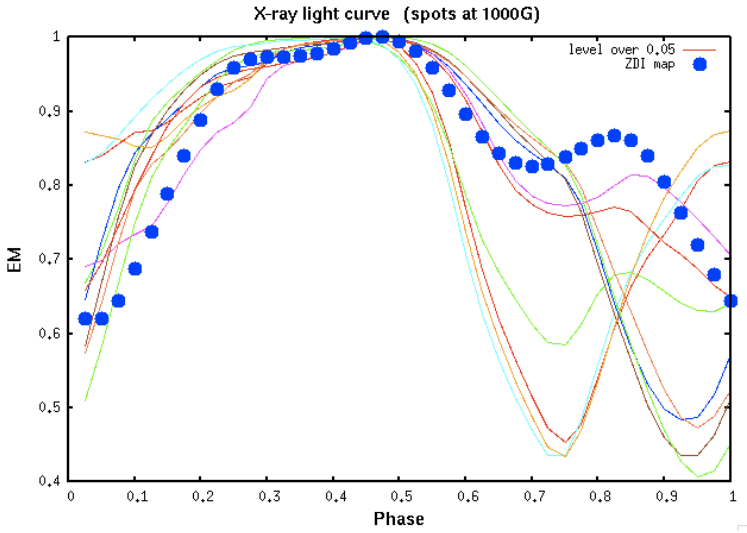

Figure 3.18: Reproduced from Arzoumanian et al. (2011). The rotation modulation of the coronal X-ray emission measure for the observed ZDI magnetogram of V374 Peg (blue dots), and for the magnetograms that have been altered by the addition of 1 kG strength field into dark photospheric regions of the original ZDI magnetogram (other lines).

netic field may not have been fully reproduced in the ZDI magnetogram due to the suppression of the Zeeman signature within the large polar starspot. One problem with this interpretation is the fact that the ZDI magnetogram was not only fit to photospheric absorption lines, but was also fit to circular polarization signals in accretion related emission lines. As the location of the accretion hotspot appears to coincide with the dark polar spot, it is possible that this compensates for the suppression of the circular polarization signal in photospheric absorption lines. Based on the surface brightness map, I add magnetic field into the original ZDI magnetogram and show that this gives a large increase in the strength of V2129 Oph's large scale dipole, while having little effect on other parameters.

3.5.1 Reconstructing the polar field

In this section, I propose a simple model for adding magnetic field to V2129 Oph's ZDI magnetogram based on the Doppler imaging brightness map. I assume that the actual large-scale magnetic field of V2129 Oph (i.e. the field that would have been observed had there not been a polar starspot) can be described as the sum of the observed field, $B_{r,0}(\theta,\phi)$, and an additional field $B_{r,+}(\theta,\phi)$, such that

$$B_r(\theta,\phi) = B_{r,0}(\theta,\phi) + B_{r,+}(\theta,\phi) \tag{3.2}$$

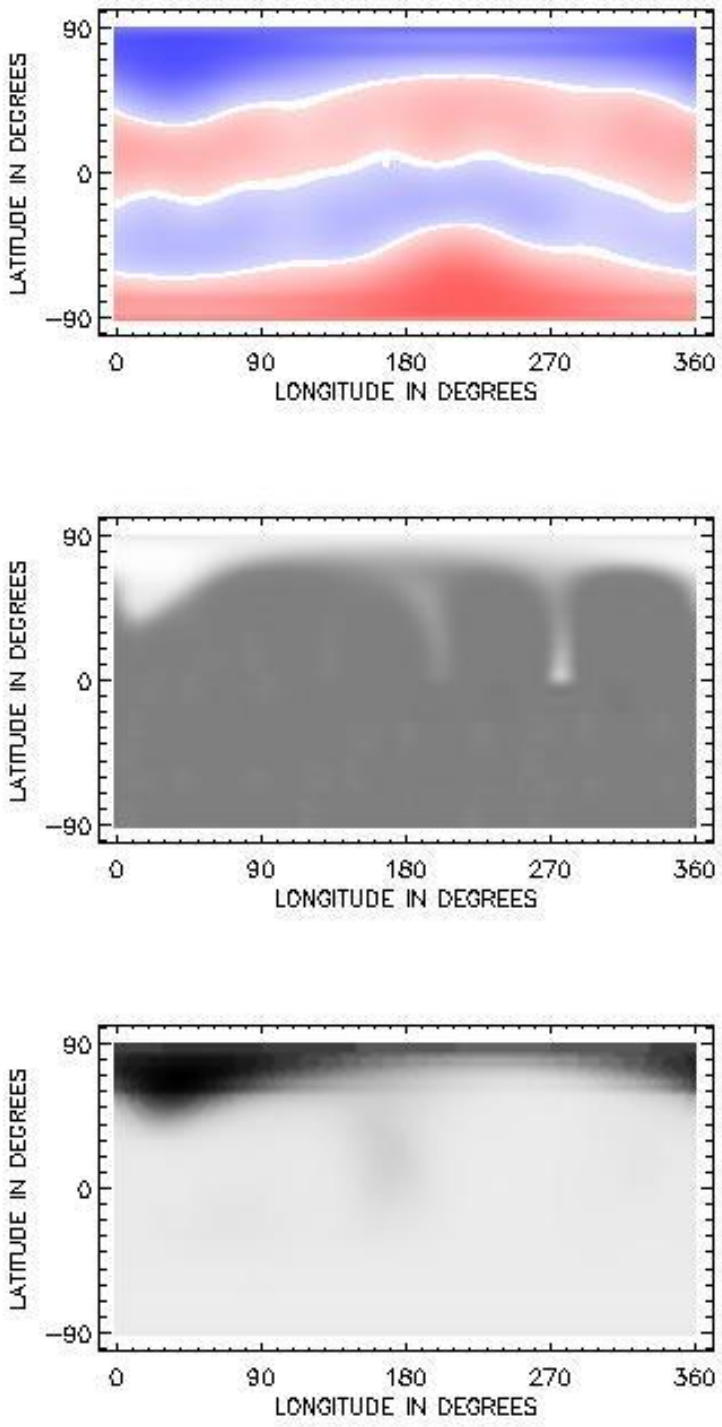

Figure 3.19: The surface of V2129 Oph (Donati et al. 2007). *Upper panel*: ZDI magnetogram for the radial component of the magnetic field. *Middle panel*: Doppler Imaging brightness map. *Lower panel*: Ca II IRT excess emission map. .

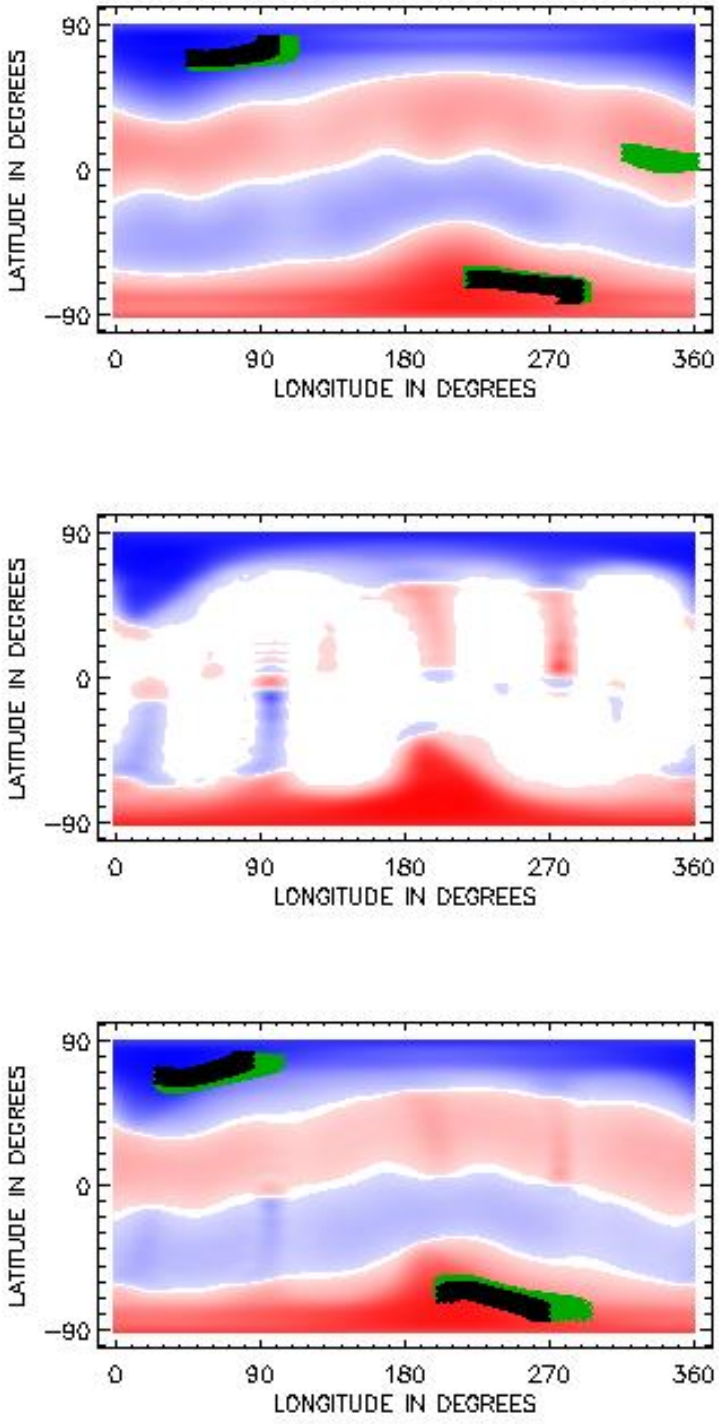

Figure 3.20: *Upper panel*: the original surface magnetogram for V2129 Oph. *Middle panel*: the additional field to be added to the original field. *Lower panel*: the sum of the above two fields. The black and green regions show the predicted locations of accretion footpoints assuming disc truncation radii of 6.8 R_* and 3.4 R_* respectively.

In order to calculate the addition map, it is necessary to assume a plausible relation between the stellar surface brightness and the magnetic field strength that is to be added. As a first approximation, I assume that the strength of the additional component of the radial surface field is linearly proportional to the brightness. I further assume that the field polarities of the additional magnetogram are the same as those in the observed ZDI magnetogram. This can be expressed as

$$B_{r,+}(\theta,\phi) = C\left(\frac{B_{r,0}(\theta,\phi)}{|B_{r,0}(\theta,\phi)|}\right)A(\theta,\phi) \tag{3.3}$$

where $A(\theta,\phi)$ represents the surface brightness and ranges from 0 for maximally bright and 1 for minimally bright, and C is the constant of proportionality.

It is necessary for the signed magnetic flux integrated over the entire stellar surface to be zero. Given that the observed surface brightness map contains a dark polar spot in only the visible hemisphere, flux balance will not be maintained when field is added based on this brightness map. Therefore, I add a spot into the invisible hemisphere of the brightness map that is identical to the spot in the visible hemisphere but shifted in longitude so that it coincides with the magnetic pole on the other hemisphere. This configuration has some plausibility based on the configuration of the magnetic field in the invisible hemisphere. If the dark polar spot in the visible hemisphere is a result of the suppression of convection by the strong polar magnetic field, it is possible that there may also be a spot on the opposite pole, if such strong field strengths are present there too.

Given this model, I find that a value of the proportionality constant in Eqn. 3.3 of ∼1400 G is necessary to double the strength of the dipole component of V2129 Oph's field.

3.5.2 Results

Fig. 3.20 shows the observed ZDI magnetogram, the additional magnetogram, and the final composite magnetogram. Table 3.5 tabulates some of the properties of these magnetograms.

The predicted locations of accretion footpoints are shown in Fig. 3.20 for disc truncation radii of 3.4 R_* and 6.8 R_*. In the composite magnetogram, due to the strong polar field strengths, even with the small disc truncation radius, accretion primarily impacts the stellar surface at high latitudes. This may be surprising given that the addition of field into the

Magnetogram	E_d (%) (1)	B_{dip} (G) (2)	B_{quad} (3)	B_{oct} (4)	$< l >$ (5)	θ_{dip} (6)	Φ_{tot} (10^{25} Mx) (7)
Observed	15.2	284	146	1625	2.96	24°	12.2
Addition	21.7	258	9	511	3.62	21°	3.14
Total	9.6	527	154	2127	3.02	18°	15.3

Table 3.5: Parameters for the three surface magnetograms shown in Fig. 3.20. From left to right, the columns correspond to the percentage of magnetic energy in the dipole component, the strength of the dipole component, the strength of the quadrupole component, the strength of the octupole component, the field complexity parameter <l>, the tilt angle of the dipole component, and the total unsigned magnetic flux.

observed magnetogram actually increases the strength of the octupole component more than the dipole component. However, this is due to the increase in the polar field strengths and not an increase in the field strengths at lower latitudes. Thus, accretion can still be expected to be directed towards high latitudes. The fraction of energy held within the dipole component of the field is actually reduced in the composite map. The other parameters which charactarise the magnetograms are little effected by the addition of flux into the observed magnetogram.

3.6 Summary and conclusions

In this chapter, I have analysed the effects of missing magnetic flux in ZDI magnetograms on the magnetograms themselves, and on our ability to model coronal magnetic fields, coronal X-ray emitting plasma, and magnetospheric accretion. I used surface magnetograms for two simulated stars over solar-like 11-year activity cycles where all of the information about the fields was known. I used the potential-field source-surface model to extrapolate the surface radial fields to all radii, and the coronal plasma model to calculate the coronal emission measures and rotational modulations for these simulated stars. The calculations were repeated for several cases to simulate the absence of information due to starspots, limited spatial resolution and limited surface visibility due to a tilt in a star's rotation axis. The results were compared in order to understand the limitations of reconstructing coronal magnetic fields in the absence of this information. In all cases, the field structures and emission measures are affected to various degrees.

In the presence of the simulated starspots, the global flux levels calculated from the surface magnetograms are reduced, but the field structure is not drastically affected on large scales. The largest change in the field comes on a smaller scale from the loss of the mid-latitude active regions. These results suggest that the presence of starspots does not significantly affect the extrapolation of large scale coronal fields but is relevant for studying smaller scale field

structures. This does however lead to the largest decrease in the emission measure from the original case of the three effects studied, hinting that missing magnetic flux in starspots may be one of the largest problems when modelling stellar X-ray emission. The rotational modulation of emission measures are also significantly affected when the strongest field regions are lost. The loss of field measurements in dark spotted regions has the greatest impact on the gas pressures inferred from the magnetic field extrapolations. In particular, it reduces the maximum gas pressures (and hence densities) that can be predicted.

Using the Doppler Imaging technique, it is possible to determine the positions and sizes of starspots of sufficient sizes on the surfaces of stars. One possible solution to the problems that starspots introduce may be to artificially impose field into the surface magnetograms. This has been explored by Arzoumanian et al. (2011). Another possible solution may be to detect the fields within starspots directly. Using molecular lines that are only formed in starspot umbrae, Berdyugina (2002) and Berdyugina et al. (2008) were able to detect Stokes V signals on at least four M dwarfs.

The missing information due to a lack of visibility of an entire hemisphere has a greater effect on the final field structure than that of the loss of high field strength regions. In this case, it appeares that the magnetic energy is weaker and more spread out over different spherical harmonic components. The estimated coronal gas pressures and emission measures are not significantly affected, though on average half of the high pressure regions of the stellar corona are preserved. However, the emission measures drop significantly on the rare occasions during the stellar cycle when most of the magnetic flux happens to be in the hemisphere out of view. This is a problem for estimating the emission measure from real stars as one will not be able to know how much magnetic flux covers the missing regions of the observed star.

The observed drop in emission measure for both these cases is due to a loss of the highest pressure coronal gas that fills the volume above the high field strength regions. The modelled gas pressures depend on the assumption that the pressure at the base of closed field lines is proportional to the magnetic pressure ($p_0 \propto B_0^2$). Due to this assumption the variations in gas pressures and emission measures for both stars closely follow the total magnetic flux. If a weaker dependance on the magnetic pressure is taken ($p_0 \propto B_0^\alpha$ where $\alpha < 2$), then the dependance of the emission measure on the regions of high field strength would be reduced, and a stronger dependance ($\alpha > 2$) would have the opposite effect.

The final case of taking into account the finite resolution limitation on observational reconstructions of surface magnetic fields has a simplifying effect on the extrapolated field. This suggests that the resolution is only an issue when studying highly complex fields, such as those seen during epochs of maximum activity in the solar cycle. Cutting the high-order spherical harmonic components from the magnetograms, has a significant effect on the field structure close to the stellar surface and the coronal plasma structure. Close to the star, this causes all of the small scale active regions to be lost. As these are most likely responsible for most of the coronal X-ray emission, this may limit our ability to model coronal plasma structures based on ZDI magnetograms. It is worth pointing out that it is not clear that ZDI magnetograms are always missing small scale field. The two young main-sequence stars AB Dor and V374 Peg are useful examples. Both stars are rapid rotators ($P_{rot} \approx 0.5$ days in both cases) and yet the ZDI magnetograms for AB Dor show highly complex small-scale structures, similar in scale to what can be seen in the simulated magnetograms considered in this chapter (Donati & Collier Cameron 1997; Donati et al. 2003), whereas V374 Peg has a simple, dipolar field structure (Morin et al. 2008a). However, the missing small scale structures do not affect magnetic field structures on large scales. This implies that the limited resolution of ZDI magnetograms does not limit our ability to model large scale coronal structures, stellar winds, or magnetic star-disc interactions.

Calculations involving field lines that cross the equator and extend to a radius that could coincide with the inner region of a circumstellar disc can be affected in various ways. When the field in an entire hemisphere is suppressed, the modelled locations of accretion hotspots are largely unaffected in the visible hemisphere. However, we are unable to reproduce the location of hotspots in the invisible hemisphere leading to an increase in the calculated accretion filling factors. In order to study accretion onto stars using field structures extrapolated from ZDI maps, these results suggest that it is better to reproduce plausible field configurations in the hemisphere out of view (as in Gregory et al. 2006b) although it is possible to reproduce the location and distribution of accretion hotspots in the visible hemisphere, even with incomplete surface magnetograms.

Finally, I have attempted to reconstruct the missing magnetic flux in a ZDI magnetogram of the classical T Tauri star V2129 Oph. Doppler Imaging of V2129 Oph shows that it possesses a large dark polar spot that could cause the magnetic flux to be underestimated in that region. If this is the case, it could be that the strength of the dipole component has been underestimated,

making it difficult to model accretion from the star's circumstellar disc, as models that are able to reproduce the observed accretion rates show a disc that is truncated too close to the star with the weakened dipole.

4

The magnetic fields and coronae of classical T Tauri stars

In the last few years, fourteen ZDI magnetograms have been produced for ten classical T Tauri stars as part of the Magnetic Protostars and Planets (MaPP) project. The stars in the sample are AA Tau (Donati et al. 2010a), BP Tau (Donati et al. 2008a), CR Cha (Hussain et al. 2009), CV Cha (Hussain et al. 2009), MT Ori (Skelly et al. 2012), TW Hya (Donati et al. 2011b), V2129 Oph (Donati et al. 2007; Donati et al. 2011a), V2247 Oph (Donati et al. 2010b), and both stars in the binary system V4046 Sgr (Donati et al. 2011c)[1]. For AA Tau, BP Tau, TW Hya, and V2129 Oph, maps exist from multiple epochs. The main results from this project are summarized in Section 1.3.

In this chapter, I analyse the sample of magnetograms and model the 3D magnetic fields

[1]Since this thesis was originally written, two ZDI magnetic maps for the CTTS GQ Lup have been published by Donati et al. (2012). GQ Lup is a slowly rotating 1.05 $M_{\odot}$ star which has recently developed a radiative core. The star hosts a magnetic field that is simple and poloidal, with a dominant octupole component. The large scale magnetic field strengths seen on the stellar surface are stronger than the field strengths for any of the stars in the sample discussed in this chapter.

and coronal plasma structures for all of these stars except the two in the V4046 Sgr binary system. In Section 4.1, I discuss each of the stars in the sample in detail; in Section 4.2, I present and analyse the ZDI magnetograms for the stars; in Section 4.3, I present the of results the coronal modelling; in Section 4.4, I summarise and discuss the results. In the next chapter, I use field extrapolations for most of the stars in the sample to model magnetospheric accretion processes on each of the stars.

4.1 Stellar sample

4.1.1 AA Tau

AA Tau is one of the most extensively studied stars in the sample. The star has a spectral type K7 and a photospheric temperature of 4000 K (Cohen & Kuhi 1979; Vrba et al. 1989; Kenyon & Hartmann 1995; Bouvier et al. 1999). Using the pre-main sequence stellar evolution tracks of Siess et al. (2000), and the bolometric luminosity of 1 $L_{\odot}$, Donati et al. (2010a) estimates that AA Tau has a radius of 2 $R_{\odot}$, a mass of 0.7 $M_{\odot}$, and an age of 1.5 Myr. Given its young age, the star is unlikely to have developed a radiative core. These values are in close agreement with earlier estimates from evolutionary models (Bouvier et al. 1999) and spectral energy distribution fits (Chiang et al. 2001; O'Sullivan et al. 2005). Several studies have given estimates for AA Tau's projected rotational velocity of 11 km s^{-1} (Hartmann & Stauffer 1989; Bouvier et al. 1999; Bouvier et al. 2003; Nguyen et al. 2009) and a rotation period of 8.2 days (Vrba et al. 1989; Bouvier et al. 1995; Smith et al. 1999; Bouvier et al. 2007). The projected rotational velocity, rotation period, and stellar radius are consistent with an inclination angle of $\sim 70°$.

AA Tau shows strong Hα emission, indicating that it is currently undergoing accretion from its circumstellar disc. For instance, Cohen & Kuhi (1979) measured a Hα EW of 37.1 Å. Smith et al. (1999) found that the star's Hα EW varies rapidly over several days, with values measured in the range 10-35 Å. Similar results were found by Bouvier et al. (1999), Bouvier et al. (2003), and Bouvier et al. (2007) who also found weak veiling, indicating weak but ongoing accretion. Using excess continuum emission to calculate the accretion rates for a sample of CTTSs, Gullbring et al. (1998) and Valenti et al. (1993) measured a mass accretion rate of $10^{-8.48}$ $M_{\odot}$ yr^{-1} and $10^{-8.15}$ $M_{\odot}$ yr^{-1} respectively. In both cases, AA Tau's accretion rate was low in comparison to the other stars in the sample. Large variations in the measured

accretion rates over several days have been observed by Bouvier et al. (2003) and Donati et al. (2010a). Bouvier et al. (2003) found that the Hα and Hβ profiles are consistent with accretion rates of 10^{-9} to 10^{-8} $M_\odot$ yr^{-1}. Donati et al. (2010a) measured the accretion rate using the strengths of several emission lines formed in accretion shocks. During their December 2008 observations, the mass accretion rate was found to vary by an order of magnitude, with an average value of $10^{-9.2}$ $M_\odot$ yr^{-1}.

The rotation axis of AA Tau has a large inclination angle ($\sim 70°$; see Section 4.3 of Bouvier et al. 1999) with respect to our line-of-sight, which means that it is viewed almost equator-on. Bouvier et al. (1999) observed AA Tau for a month and found that the star's visible lightcurve showed periodic decreases in magnitude of up to $\sim$1.4 mags in all observed wavelength bands. The period of this variability was found to be approximately 8.22 days with each dip in magnitude lasting several days. Between each dip, the star's lightcurve showed little significant variations. They concluded that the central star is being periodically eclipsed by a warp in the inner edge of its circumstellar disc at the equatorial corotation radius. The duration of each dip suggests that the warp extends π radians in longitude. They also noticed that the observed polarization level was at a maximum during periods of minimum brightness, consistent with this interpretation. During the eclipse of the central star, unpolarized light from AA Tau's photosphere is blocked, whereas polarized light produced by scattering from the disc is less affected. Follow up studies by Ménard et al. (2003), Bouvier et al. (2003), and Bouvier et al. (2007) have shown that the shapes of the dips are highly variable, indicating large changes in the geometries of the eclipsing region on timescales as short as a few days. Bouvier et al. (2003) even found that the optical eclipse disappeared for a few days in December 1999. Terquem & Papaloizou (2000) and Romanova et al. (2003) showed that a warp at the inner edge of an accretion disc can be created if the central star has a large-scale dipole that is tilted with respect to the stellar rotation axis.

AA Tau hosts a strong magnetic field, first measured by Johns-Krull & Valenti (2000) who gave a surface averaged field strength of 2.9 kG. Johns-Krull (2007) measured a similar value of 2.78 kG. Using spectropolarimetric observations taken in December 2008, and again in January 2009, Donati et al. (2010a) produced ZDI magnetograms for both epochs. Due to the star's slow rotation, the magnetograms could only be fit up to the $l = 5$ spherical harmonic component. However, both of the magnetograms have most of their magnetic energies in the dipole component such that AA Tau's large scale magnetic field is a simple tilted dipole with

polar field strengths of $\sim$ 1.6 kG. In the visible hemisphere, the magnetic pole of AA Tau's large scale dipole coincides well with regions of low surface brightness and Ca II IRT excess emission, both mapped using Doppler Imaging (see Fig. 5 of Donati et al. 2010a). The latter quantity is a proxy for the locations of accretion footpoints and indicates that accretion is taking place along large scale dipolar field lines, and impacting the surface at high latitudes.

Several X-ray observations of AA Tau are available in the literature and show that the star is a highly variable X-ray emitter. It was first observed in X-rays in March 1980 and then again in February 1981 using the *Einstein* observatory (Walter & Kuhi 1981; Walter & Kuhi 1984). In the March 1980 observations, AA Tau was found to be one of the strongest X-ray emitters in the sample of twenty-five T Tauri stars, with an X-ray luminosity of $10^{30.29}$ erg s^{-1}. Remarkably, the February 1981 observations failed to yield a detection corresponding to a decrease in flux by more than a factor of 7.5. The star was later detected by the ROSAT All-Sky Survey (RASS; Neuhaeuser et al. 1995) which found that it was one of the weakest X-ray sources in their sample. Grosso et al. (2007) observed AA Tau with XMM-Newton over two rotation periods along with simultaneous UV and optical monitoring and noticed that it X-ray emission was highly variable. Although they were able to identify the optical eclipse of the star from the warped inner edge of the disc, they found no corresponding eclipse in the X-ray data, indicating that the X-ray emitting regions are located at high latitudes. The high X-ray variability was interpreted as being a result of a flare temporarily dominating the star's X-ray emission. However, they did find that the X-ray absorption peaked during the second optical eclipse of the star, which they interpreted as being the result of obscuration from low-density accretion funnels. Using the same X-ray and UV data (though without the optical data), Schmitt & Robrade (2007) gave a different interpretation. They suggested that the X-ray emitting regions must be located at low latitudes to account for the peak in X-ray absorption. An X-ray luminosity of $10^{30.09}$ erg s^{-1} was given as part of the XMM-Newton extended survey of the Taurus molecular cloud (XEST; Güdel et al. 2007; once again using the data from Grosso et al. 2007). Using a single temperature fit to the star's X-ray spectrum, they derived a plasma temperature of $10^{7.4}$ K and an emission measure of $10^{52.46}$ cm^{-3}.

4.1.2 BP Tau

BP Tau is a K7-type star in the Taurus−Auriga star forming region with a photospheric temperature of 4000 K (Johns-Krull et al. 1999b). Johns-Krull et al. (1999b) estimated that BP

Tau has a radius of 1.95 $R_\odot$ and a mass of 0.65 $M_\odot$. Using the pre-main sequence stellar evolution tracks of Siess et al. (2000), Donati et al. (2008a) estimated that the star has a mass of 2.0 $M_\odot$, and an age of 1.5 Myr. Given its young age, BP Tau is likely to still be fully convective. Johns-Krull et al. (1999b) and Donati et al. (2008a) gave similar projected rotational velocities of approximately 9 km s^{-1}. A slightly higher value of 13.1 km s^{-1} was estimated by Nguyen et al. (2009)[2]. Vrba et al. (1986) used optical photometric monitoring of BP Tau to derive a rotation period of 7.64 days. Given these parameters, the star's axis-of-rotation is inclined at $\sim 45^\circ$ to our line-of-sight.

BP Tau shows signs of ongoing accretion from its circumstellar disc. Gullbring (1994) and Gullbring et al. (1996) presented optical photometry of the star and showed that it has almost constant brightness in the observed wavebands. However, they found slow variations in the star's brightness which they assumed was the result of non-steady accretion. Various accretion rate estimates have been derived in the literature. Using excess continuum emission to calculate the accretion rates for a samples of CTTSs, Gullbring et al. (1998) and Valenti et al. (1993) measured a mass accretion rate for BP Tau of $10^{-7.54}$ $M_\odot$ yr^{-1} and $10^{-7.6}$ $M_\odot$ yr^{-1} respectively. Schmitt et al. (2005) used XMM-Newton observations to derive a significantly lower value of $10^{-9.05}$ $M_\odot$ yr^{-1}. From the EWs of the Hα, Hβ, and He I D_3 emission lines, Donati et al. (2010b) calculates a value of $10^{-8.6}$ $M_\odot$ yr^{-1}. Curran et al. (2011) derived mass accretion rates from several optical emission lines ranging between $10^{-8.88}$ and $10^{-7.86}$ $M_\odot$ yr^{-1} depending on which line was used, with an average value of $10^{-8.34}$ $M_\odot$ yr^{-1}.

BP Tau was the first CTTS star to have its magnetic field detected unambiguously. Johns-Krull et al. (1999b) presented optical and IR spectra and found significant broadening in the Ti I (2.2233 μm) photospheric absorption line, which, due to the stars small photospheric temperature, they could only account for by Zeeman broadening by a field with an average surface strength of 2.5 kG. However, Johns-Krull et al. (1999a) was unable to detect a net polarization in photospheric absorption lines, putting an upper limit on the average longitudinal field of BP Tau of $\pm$200 G. This discrepancy indicates that BP Tau's field deviates from a simple dipole configuration. They were able to detect a polarisation signal in the He I (5876 Å) emission line which indicated that the emission was coming from a region of strong kG field, probably accretion shocks at the magnetic poles. Using fits to unpolarized photo-

[2]Given the rotation period of 7.64 days, and the stellar radius of 1.95 $R_\odot$, the rotational velocity of BP Tau is 12.6 km s^{-1}, which is lower than the value for the projected rotational velocity of 13.1 km s^{-1} estimated by Nguyen et al. (2009), and thus this combination of parameters is not possible.

spheric absorption lines (mostly K band Ti I lines), Johns-Krull (2007) reported a surface averaged field strength of 2.17 kG. Using spectropolarimetric observations from February and December 2006, Donati et al. (2008a) measured strong fields of several kG. Based on these observations, they produced ZDI magnetograms for each observational epoch. These magnetogram are both quite similar, being dominated by strong dipole and octupole components. They were also able to detect strong circular polarization in emission lines associated with accretion, such as the Ca II IRT lines. The circular polarization signatures in these lines differed significantly from what was seen in photospheric absorption lines, indicating that they are formed over different regions of the stellar surface, i.e. accretion footpoints.

BP Tau was first observed in X-rays by Walter & Kuhi (1981) who observed the star in March 1980 using the Einstein observatory and found that it had a moderate level of X-ray emission, with a luminosity of $10^{30.06}$ ergs s^{-1}. Neuhaeuser et al. (1995) observed the star with ROSAT, measuring an X-ray luminosity of $10^{29.85}$ ergs s^{-1}. They found that the a two temperature model describes the star's spectra well, with a low-temperature component of 2.3 MK and a high-temperature component 14 MK. The star was detected by the ROSAT All-Sky Survey (RASS; Neuhaeuser et al. 1995) which measured an X-ray luminosity of $10^{29.85}$ ergs s^{-1}. Gullbring et al. (1997) observed BP Tau with ROSAT and found that the star's X-ray emission varied from night to night, but simultaneous optical photometry showed that the variations in the star's optical brightness did not correlate with X-ray luminosity, indicating that the X-ray emission was not primarily originating in accretion shocks. X-ray observations using XMM-Newton were presented by Schmitt et al. (2005) and Robrade & Schmitt (2006). Schmitt et al. (2005) showed that a component of the star's X-ray emission must be coming from a high-density, low-temperature plasma, most likely from the base of an accretion shock. Using a multi-temperature model, Robrade & Schmitt (2006) showed that BP Tau's X-ray spectra can be well described by emission from a plasma with a low temperature ($\sim$ 2.3 MK) component, and two high temperature components ($\sim$7 MK and $\sim$25 MK). The high temperature components dominate over the low temperature component in X-ray emission. This three temperature fit can be seen in Table 4.3. The same X-ray data was incorporated into the XEST project (Güdel et al. 2007) where a two temperature component model with temperatures of 4.8 MK and 22.3 MK, was fitted to the spectrum, with the low-temperature component slightly dominating[3]. Based on the same X-ray data, Telleschi et al. (2007) derived electron densities from the O VII triplet emission lines, which are produced in low temperature

(∼2 MK) plasma, and showed that it predominantly originates in a high density ($n_e = 10^{11.53}$ cm^{-3}), low temperature plasma, likely to be produced by the accretion shock.

4.1.3 CR Cha

CR Cha is a K2-type CTTS in the Chameleon molecular cloud (Appenzeller & Wagner 1989) with an effective temperature of 4900 K (Schegerer et al. 2006). Using the pre-main sequence stellar evolution tracks of Siess et al. (2000), Hussain et al. (2009) estimates that the star has a radius of 2.5 $R_\odot$, a mass of 1.9 $M_\odot$, and an age of 3 Myr. This implies that the star has developed a significant radiative core corresponding to 62% of the star's mass and 57% of the star's radius. Nguyen et al. (2009) derived a projected rotational velocity of 35 km s^{-1}, and Bouvier et al. (1986) (called 'LHα 332-20') gives a rotation period of 2.3 days. The rotation period, projected rotational velocity, and stellar radius are consistent with an inclination angle of the star's rotation axis of $\sim 40^\circ$. This is similar to the inclination angle of $\sim 50^\circ$ derived using Doppler Imaging parameter optimization by Hussain et al. (2009).

Strong emission in Hα and other accretion sensitive emission lines shows that CR Cha is actively accreting. Analysis of spectropolarimetric observations of the star by Hussain et al. (2009) failed to detect a circular polarization signal in accretion related emission lines, possibly indicating that the inner edge of the disc is truncated close to the stellar surface with accretion footpoints distributed over the stellar surface in regions of opposite polarity magnetic field. A mass accretion rate for CR Cha of $10^{-9.0}$ $M_\odot$ yr^{-1} was estimated by Hussain et al. (2009) using the width of the Hα emission line at 10% maximum.

Using spectropolarimetric observations of CR Cha and CV Cha (see below) taken in April 2006, Hussain et al. (2009) clearly detected circular polarization signatures from magnetic fields. They produced a Doppler Imaging brightness map and a ZDI magnetogram for the star. The brightness map showed a complex pattern of low latitude spots and a large polar spot. Due to bad weather and phase coverage, their derived magnetogram has a relatively poor spatial resolution given its fast rotation rate. Despite the poor spatial resolution, the ZDI

[3]It may seem here that the two different multi-temperature component spectral fits to the same XMM-Newton data given by Robrade & Schmitt (2006) and by Güdel et al. (2007) contradict each other. However, this is not actually the case. The fit from Robrade & Schmitt (2006) has three components with temperatures of 2.3, 7.2, and 25.1 MK, and emission measures of 3.4, 5.3, and 10.3 $\times 10^{52}$ cm^{-3}. If we combine the two low-temperature components, using the relation $log(T) = (EM_1 logT_1 + EM_2 logT_2)/(EM_1 + EM_2)$, we get a single component of temperature 4.6 MK, and emission measure of 8.7×10^{52} cm^{-3}. This is in approximate agreement with the values given by Güdel et al. (2007).

magnetogram shows surface magnetic fields of up to 400 G covering a large part of the visible surface in a highly complex pattern of opposite polarity regions. The lack of any polarization signal in accretion related emission lines is consistent with the star's weak field truncating the disc close to the stellar surface, and the star's highly complex field causing accretion to occur along non-dipolar field lines and impacting the stellar surface in several regions of opposite polarity magnetic field, thus causing cancelations in the circular polarization signals from accretion-related emission.

Feigelson & Kriss (1989) observed CR Cha (called 'CHX 3') in X-rays with *Einstein* and derived a luminosity of $10^{30.65}$ ergs s^{-1}. Using ROSAT, Feigelson et al. (1993) detected CR Cha (called 'Lk 332-20') and derived a value of $10^{30.1}$ ergs s^{-1}. Ingleby et al. (2011) presented *Chandra* observations of CR Cha, giving a similar value of $10^{30.3}$ ergs s^{-1}. Using XMM-Newton observations, Robrade & Schmitt (2006) fitted a three temperature component model to CR Cha's X-ray spectrum. This fit can be seen in Table 4.3. They found that, similar to their results for BP Tau (discussed above), CR Cha's X-ray emission is dominated by a high temperature component, presumable from a magnetically confined corona, but that the star also has a clear low-temperature component. Analysis of the O VII triplet emission line showed that the emission line was formed in a high-density plasma ($n_e = 10^{11.20}$ cm^{-3}) probably within an accretion shock.

4.1.4 CV Cha

CV Cha is a G8-K0 type CTTS in the Chameleon molecular cloud (Appenzeller & Wagner 1989; Hussain et al. 2009) with a photospheric temperature of 4500 K (Stempels & Piskunov 2003). Using the pre-main sequence stellar evolution tracks of Siess et al. (2000), Hussain et al. (2009) estimates that the star has a radius of 2.5 $R_\odot$, a mass of 2.0 $M_\odot$, and an age of 5 Myr. They also estimate that the star has developed a significant radiative core corresponding to 92% of the star's mass and 75% of the star's radius. Stempels & Piskunov (2003) derived a projected rotational velocity of 28 km s^{-1}, and Bouvier et al. (1986) gives a rotation period of 4.4 days. This is quite similar to the value of 25 km s^{-1} derived using Doppler Imaging parameter optimization by Hussain et al. (2009). The rotation period, projected rotational velocity, and stellar radius is consistent with an inclination angle of the star's rotation axis of $\sim 60°$. This is quite different to the angle of $\sim 35°$ derived using Doppler Imaging parameter optimization by Hussain et al. (2009). CV Cha has a binary companion (CW Cha) at a distance

of ∼1500 AU (Reipurth & Zinnecker 1993).

Strong emission in Hα and other accretion sensitive emission lines shows that CV Cha is actively accreting. As with CR Cha, analysis of spectropolarimetric observations of the star by Hussain et al. (2009) failed to detect a circular polarization signal in accretion related emission lines, possibly indicating that the inner edge of the disc is truncated close to the stellar surface with accretion footpoints distributed over the stellar surface in regions of opposite polarity magnetic field. A mass accretion rate for CV Cha of $10^{-7.5}$ $M_{\odot}$ yr^{-1} was estimated by Hussain et al. (2009) using the width of the Hα emission line at 10% maximum.

Spectropolarimetric circular polarization signatures of magnetic fields were detected for CV Cha by Hussain et al. (2009). As with CR Cha discussed above, they produced a Doppler Imaging brightness map and a ZDI magnetogram for the star. The brightness map showed a complex pattern of low latitude spots and a large polar spot. The ZDI magnetogram showed surface magnetic fields of up to 500 G covering a large part of the visible surface in a highly complex pattern of opposite polarity regions.

Unfortunately, very few X-ray observations of CV Cha are available in the literature. Feigelson & Kriss (1989) observed CV Cha (called 'CHX 19') in X-rays with *Einstein* and derived a luminosity of $10^{30.1}$ ergs s^{-1}. Using ROSAT, Feigelson et al. (1993) detected CR Cha (called 'Lk 332-21') and derived a value of $10^{30.0}$ ergs s^{-1}.

4.1.5 MT Ori

MT Ori is a K2-type star in the Orion Nebula Cluster with an effective temperature of 4580 K (Hillenbrand 1997). Hillenbrand (1997) estimated that the star (called 'Source 567') has a radius of 8.2 $R_{\odot}$, a mass of 1.0 $M_{\odot}$. However, using the pre-main sequence stellar evolution tracks of Siess et al. (2000), Skelly et al. (2012) estimates that the star has a larger mass of 2.6 $M_{\odot}$, and an age of 0.23 Myr. Based on this result, they estimate that the star hosts a small radiative core which contains 34% of the star's mass within 10% of the star's radius. It is worth noting that there is some doubt over the precise evolutionary status of MT Ori as the pre-main sequence evolutionary tracks of Tognelli et al. (2011) suggest that it has yet to develop a radiative core (Gregory et al. 2012) though its relatively large mass means that it will develop a radiative core at a much earlier age than the other stars in the sample. Rhode et al. (2001) gave a projected rotational velocity of 22.2 km s^{-1} and a rotation period of 8.53

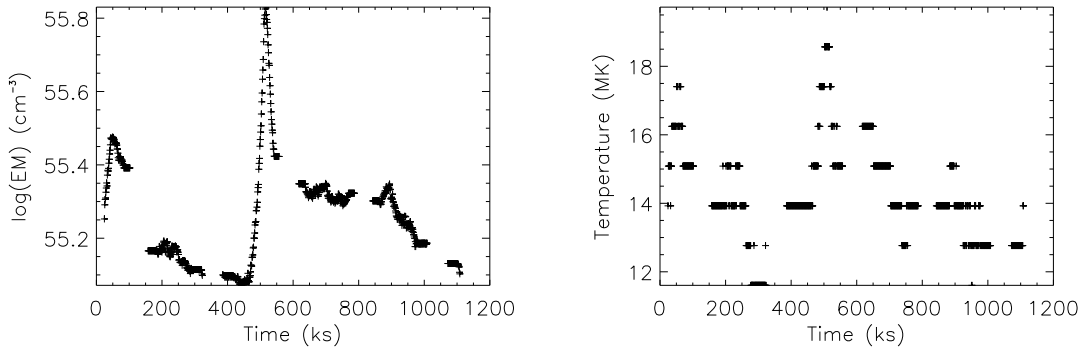

Figure 4.1: Emission measure vs time (left panel) and plasma temperature vs time (right panel) for MT Ori during the *Chandra* Orion Ultradeep Project (COUP; Getman et al. 2005b).

days. A similar period was found in the star's X-ray lightcurve due to rotational modulation (Flaccomio et al. 2005). These parameters give an inclination angle of $\sim 27°$, which is similar to the value of $\sim 30°$ derived from Doppler Imaging parameter optimization given by Skelly et al. (2012).

MT Ori is undergoing active accretion. Using the equivalent width of the Ca II IRT line, Skelly et al. (2012) estimates that it has a mass accretion rate of $10^{-9.1}$ $M_\odot$ yr^{-1}, with variations between $10^{-9.3}$ and $10^{-9.0}$ $M_\odot$ yr^{-1} during their observations.

Spectropolarimetric circular polarization signatures of magnetic fields were detected for MT Ori by Skelly et al. (2012). They produced a ZDI magnetogram and found that the field is moderately axisymmetric and highly complex, with average field strengths of ∼500 G. The complexity of the field is probably due to the fact that the star has recently developed a radiative core.

Unfortunately, very few X-ray observations of MT Ori are available in the literature. Feigelson et al. (2002) observed the star (called '626') as part of a survey of 1075 sources in the Orion Nebula Cluster and found an X-ray luminosity of $10^{31.7}$ erg s^{-1}. It was observed as part of the *Chandra* Orion Ultradeep Project (COUP; Getman et al. 2005b) as 'COUP Source 932' and found to have an X-ray luminosity of $10^{31.9}$ erg s^{-1}. Getman et al. (2005b) provided a two-temperature component fit to the star's X-ray spectrum, which is given in Table 4.3. Both Feigelson et al. (2002) and Getman et al. (2005b) observed flares on the star, with the COUP flare reaching a peak luminosity of $10^{32.77}$ erg s^{-1}, an order of magnitude above the quiet value. The COUP flare is shown in Fig. 4.1.

4.1.6 TW Hya

TW Hya is a K6-K8 type star in the near-by (∼50 pc) TW Hydrae association and has an effective temperature of 4000 K (Torres et al. 2003). The association has an age of ∼10 Myr (Barrado Y Navascués 2006). Yang et al. (2005) estimated the radius and mass of TW Hya to be 0.93 $M_\odot$ and 0.96 $R_\odot$. Using the pre-main sequence stellar evolution tracks of Siess et al. (2000), Donati et al. (2011b) estimated that the star has a mass of 0.8 $M_\odot$, and a radius of 1.1 $R_\odot$. Based on this result, they estimated that the star hosts a radiative core with a radius of 0.35 R_*. Due to its large inclination angle, the star has a low $v \sin i$ (literature values range from $4 - 15$ km s^{-1} as reviewed by Torres et al. 2003). Using Doppler Imaging parameter optimization, Donati et al. (2011b) derived a $v \sin i$ of 4 km s^{-1}. Weise et al. (2010) derived a similar value of 6.2 km s^{-1} and an age of 8 Myr. TW Hya's rotation period has been measured through periodic variations in radial velocity to be 3.56 days (Huélamo et al. 2008). These give an inclination angle of $\sim 15°$.

TW Hya is actively accreting from its circumstellar disc and several estimates for the accretion rate can be found in the literature. Modelling the star's Hα emission profile, Muzerolle et al. (2000) derived an accretion rate of $10^{-9.3}$ $M_\odot$ yr^{-1}. Given that the X-ray emission of TW Hya is dominated by emission from a dense, low-temperature accretion shock, Kastner et al. (2002) used high resolution X-ray spectra to estimate a mass accretion rate of 10^{-8} $M_\odot$ yr^{-1}. This is significantly different from the value of 10^{-11} $M_\odot$ yr^{-1} computed from its X-ray spectrum by Stelzer & Schmitt (2004). Donati et al. (2011b) used the equivalent widths of several optical emission lines formed as a result of accretion to estimate an accretion rate of $10^{-8.9}$ $M_\odot$ yr^{-1}. Curran et al. (2011) derived mass accretion rates from several optical emission lines ranging between $10^{-9.82}$ and $10^{-8.38}$ $M_\odot$ yr^{-1} depending on which line was used. They got an average value of $10^{-9.17}$ $M_\odot$ yr^{-1}.

Yang et al. (2005) observed Zeeman broadening in photospheric absorption lines consistent with a field strength of ∼2.6 kG averaged over the visible surface. Yang et al. (2007) used high resolution spectropolarimetry to measure an average longitudinal field strength on TW Hya of 149 G. Assuming a dipole of strength 2.6 kG, they showed that they should expect to observe an average longitudinal field strength of ∼1 kG. This is significantly greater than their measured value, which indicates that a large fraction of the stars magnetic flux is held in small scale field structures that are not observable using spectropolarimetry. They

also detected significant circular polarization signatures in emission lines formed primarily in accretion shocks. Donati et al. (2011b) used spectropolarimetric observations from two epochs (March 2008 and Feb/March 2010) to produce ZDI magnetograms for TW Hya. For both epochs, strong kG magnetic fields were reconstructed, with an average strength of ∼1.5 kG, and a maximum strength of ∼3 kG in the 2008 magnetogram. In both cases, the field is dominated by axisymmetric octupole components (∼2.5 kG), and weaker dipole components (∼0.5 kG). The dipole and the octupole components are aligned anti-parallel (such that the positive polarity magnetic pole of the dipole component approximately coincides with the negative polarity pole of the octupole).

Of the sample of CTTSs considered in this chapter, TW Hya is the most extensively studied in X-rays. This is due to several factors which make it ideal for studying X-ray emission processes. The star is located at a distance of only ∼50 pc and is surrounded by little ambient cloud material, which means that it has a much larger X-ray flux than most CTTSs (Kastner et al. 2002). Furthermore, the fact that it is being viewed pole-on (i.e. with an inclination angle $i \sim 0°$), makes it ideal for studying emission from accretion shocks. The star's X-ray spectrum is dominated by emission from a low temperature, high density plasma. Kastner et al. (1999) presented ASCA and ROSAT X-ray observations for TW Hya, and derived an X-ray luminosity of $10^{30.3}$ erg s^{-1}. Kastner et al. (2002) presented a high-resolution sprectum of TW Hya from *Chandra* and produced differential emission measure (DEM) fits to selected emission lines[4]. They found that their best fit DEM, shown in Fig. 4.2, is dominated by a low temperature component at $10^{6.5}$ K and that the lack of O VII emission implies that the emission is coming from regions of high density (10^{13} cm^{-3}). This suggests that the low temperature emission component probably originates in a high density accretion shock. A similar result was obtained by Stelzer & Schmitt (2004) and independently by Robrade & Schmitt (2006) using the same XMM-Newton data. Robrade & Schmitt (2006) fitted a three temperature component model to the star's X-ray spectrum, which showed a dominant low temperature (∼3 MK) component. This fit can be seen in Table 4.3. For the other three stars in their sample, BP Tau, CR Cha, and SU Aur, they found that the X-ray hardness ratio (defined as $HR = (H-S)/(H+S)$, where H and S are the magnitudes in hard and soft X-rays respectively) is positively correlated with X-ray brightness, a result consistent with the interpretation that the variability in these stars comes primarily from the observed flares. However, for TW Hya, the hardness ratio is negatively correlated with X-ray brightness, indicating that the star's X-ray

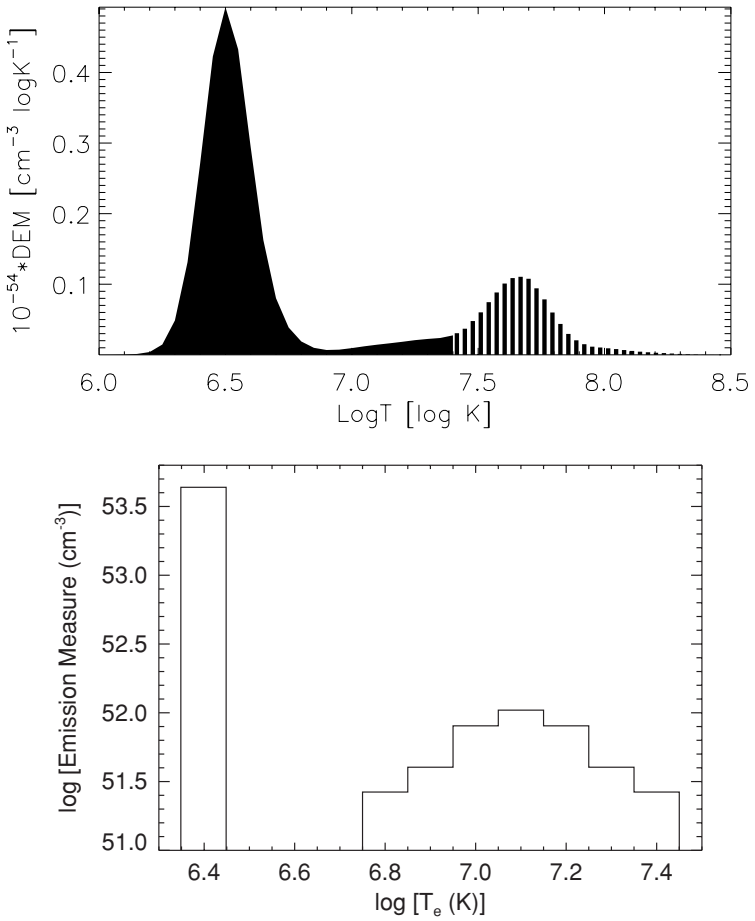

Figure 4.2: *Upper panel*: Reproduced from Kastner et al. (2002) showing a differential emission measure fit to the high-resolution *Chandra* spectrum of TW Hya. *Lower panel*: Reproduced from Brickhouse et al. (2010) showing an emission measure distribution fit to a 489 ks *Chandra* observation.

brightness variability is a result of variable accretion. Brickhouse et al. (2010) observed TW Hya with *Chandra* for 489 ks and gave an emission measure distribution spectral fit, shown in Fig. 4.2, confirming that the star's emission is dominated by a low temperature plasma. Using emission lines formed at lower temperatures, they derived an electron temperature of 2.5 MK and a density of 3×10^{12} cm^{-3}.

4.1.7 V2129 Oph

V2129 Oph is a K2-type star in the ρ Oph star-forming region and has an effective temperature of 4500 K (Padgett 1996; Bouvier & Appenzeller 1992; Donati et al. 2007). The star forming region has an age of ∼2-3 Myr and a distance of ∼120 pc (Loinard et al. 2008). Using this distance, and the star's luminosity, Donati et al. (2011a) estimated that it has a radius of 2.0

[4]This was actually the first high-resolution X-ray spectrum to be obtained for any classical T Tauri star (and probably any pre-main sequence star).

$R_\odot$, and using the pre-main sequence stellar evolution tracks of Siess et al. (2000), a mass of 2.45 $M_\odot$ and an age of 2-3 Myr. They also find that V2129 Oph most likely has a radiative core of mass 0.3 $M_\odot$ and radius 0.3 $R_\odot$. Donati et al. (2007) derived a projected rotational velocity of 14.5 km s^{-1}, consistent with previous estimates. Weise et al. (2010) derived a similar value of 13.5 km s^{-1} and an age of 3 Myr. V2129 Oph (called 'SR 9') has been monitored since 1986 as part of the long term photometric program ROTOR. Grankin et al. (2008) estimated rotation periods at ten epochs between 1986 and 2002 using periodic photometric variability and derived values between 6.29 and 6.68 days, with an average value of 6.55 days. The star's rotation period and radius imply that it has an equatorial rotational velocity of 15.5 km s^{-1}, which coupled with the stars projected rotational velocity implies an inclination angle of $\sim 69°$. Using parameter optimization with tomographic imaging, Donati et al. (2007) and Donati et al. (2011a) derived a smaller value of $\sim 60°$. The star also has a faint low mass companion at a distance of 60-120 AU (Geoffray & Monin 2001).

V2129 Oph is actively accreting from its circumstellar disc. Eisner et al. (2005) estimated a mass accretion rate of $10^{-7.5}$ $M_\odot$ yr^{-1}. From the flux in the Ca II 866 nm line in observations taken in 2005, Donati et al. (2007) obtained a much smaller value of $10^{-8.4}$ $M_\odot$ yr^{-1}. Based on the same observations, and observations at a different epoch in 2009, Donati et al. (2011a) estimated an even smaller value of $10^{-9.2}$ $M_\odot$ yr^{-1} for both epochs. Using the same 2009 data, Alencar et al. (2012) used the equivalent widths of the He I (5876 Å) emission line to derive mass accretion rates at various points over four rotations of the star. They found that the accretion rate was generally quite steady at a value of $10^{-8.8}$ $M_\odot$ yr^{-1}, but it did show two sudden bursts where the accretion rate increased by approximately a factor of three. *Chandra* X-ray observations that were taken simultaneously with the 2009 epoch gave a much smaller value of $10^{-10.2}$ $M_\odot$ yr^{-1}. Curran et al. (2011) derived mass accretion rates from several optical emission lines ranging between $10^{-10.23}$ and $10^{-9.19}$ $M_\odot$ yr^{-1} depending on which line was used. They obtained an average value of $10^{-9.64}$ $M_\odot$ yr^{-1}.

V2129 Oph's magnetic field has been measured using spectropolarimetric observations taken in 2005 by Donati et al. (2007). Donati et al. (2011a) provided further spectropolarimetric observations from 2009 and a reanalysis of the 2005 observations. They find clear signatures of strong kG magnetic fields and produce ZDI magnetograms for both epochs. In both cases, the star's magnetic field is predominantly poloidal (5% of the magnetic energy was found to be in the toroidal component) and axisymmetric with strong dipole and oc-

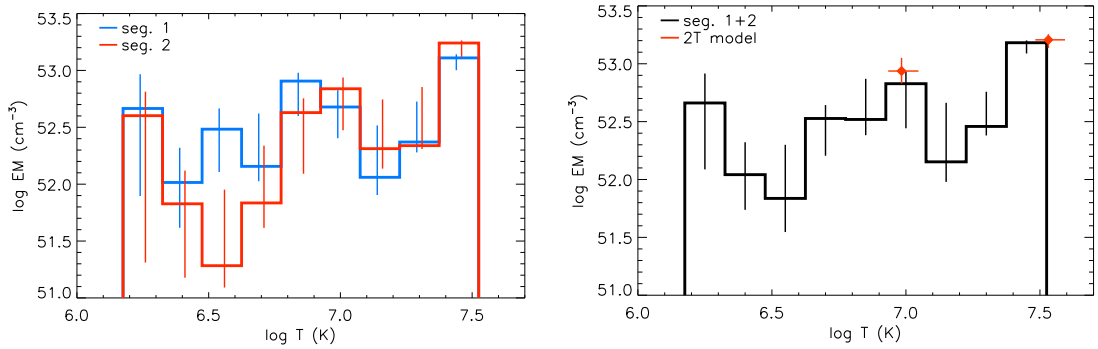

Figure 4.3: Reproduced from Argiroffi et al. (2011). Emission measure distributions for V2129 Oph derived from *Chandra* observations from 2009. *Left panel*: EMDs for both the first observing segment (blue) and the second segment (red). *Right panel*: EMD from both segments together and the results of a two temperature component fit (red points).

tupole components. They also found that the topologies of the magnetic fields from both epochs are similar, but the strengths of the dipole and octupole components both increase significantly between 2005 and 2009.

V2129 Oph is a typical X-ray emitter, with an X-ray luminosity of $10^{30.4}$ ergs s^{-1} (Casanova et al. 1995). During the 2009 spectropolarimetric observations of V2129 Oph discussed above, Argiroffi et al. (2011) simultaneously observed the star in X-rays with *Chandra* over two separate 100 ks segments. They fitted a nine temperature component EMD model to both observing segments and found a drop in emission from low temperature plasma between the segments. This drop was attributed to variable obscuration of a large high latitude accretion shock by the accretion column. This interpretation is supported by the simultaneous magnetic and accretion study of Donati et al. (2011a), which showed that at the rotation phase of the second segment of X-ray observations, the geometry of the system will be such that the accretion shock will probably have been viewed through the accretion column.

4.1.8 V2247 Oph

V2247 Oph is an M2.5 type star in the ρ Oph star-forming region, and has an effective temperature of 3500 K (Gras-Velázquez & Ray 2005). The star forming region has an age of ∼2-3 Myr and a distance of ∼120 pc (Loinard et al. 2008). Gras-Velázquez & Ray (2005) estimated that the star has a mass of 0.2-0.4 $M_\odot$ and a radius of 2.7 $R_\odot$. Using the pre-main sequence stellar evolution tracks of Siess et al. (2000), Donati et al. (2010b) estimated that the star has a mass of 0.36 $M_\odot$, a radius of 2.0 $R_\odot$, and an age of 1 Myr. Thus, V2247 Oph is the lowest mass star in the sample, and is the only one that is unlikely to develop a radiative core as it

evolves. V2247 Oph has a projected rotational velocity of 20.5 km s^{-1} (Bouvier et al. 1986; Donati et al. 2010b). The star (called 'SR 12') has been monitored as part of the long term photometric program ROTOR. Grankin et al. (2008) estimated rotation periods at five epochs between 1989 and 1994 using periodic photometric variability and derived values between 3.40 and 3.58 days, with an average value of 3.52 days. The star's rotation period and radius imply that it has an equatorial rotational velocity of 18.7 km s^{-1}, which coupled with the star's projected rotational velocity implies an inclination angle of $\sim 35°$. Using parameter optimization with tomographic imaging, Donati et al. (2010b) derived a smaller value of $\sim 45° \pm 10°$. The star also has a faint low mass companion (Gras-Velázquez & Ray 2005).

V2247 Oph has a very small Hα equivalent width: Cohen & Kuhi (1979) found a value of 3.6 Å; Bouvier & Appenzeller 1992 found large variations in the Hα EW, with a minimum value of 4.5 Å, and a maximum value of 8.8 Å. Due to its low Hα EW, the star has often been classified as a WTTS (e.g. Gras-Velázquez & Ray 2005; Grankin et al. 2008). However, Gras-Velázquez & Ray (2005) found that the star's SED showed excess IR emission, consistent with the presence of a disc and observations taken in January 2002 showed that the star's Hα EW had increased to approximately 17.6 Å (Littlefair et al. 2004). From the EWs of the Hα, Hβ, and He I D_3 emission lines, Donati et al. (2010b) calculates a value of $10^{-9.8}$ $M_\odot$ yr^{-1}. This indicates that V2247 Oph probably has the lowest level of accretion in the sample of CTTSs. This is consistent with the star's weak accretion related emission lines.

Donati et al. (2010b) provided spectropolarimetric observations from July 2008 and found clear signatures of magnetic fields in photospheric absorption lines. They produced a ZDI magnetogram for the star and found that its magnetic field is highly complex and non-axisymmetric, with approximately 60% of the magnetic energy held in the toroidal component. The magnetic field has a weak ∼100 G dipole component tilted at ∼45° to the axis-of-rotation.

V2247 Oph (called 'BF-46') was observed by Imanishi et al. (2003) using *Chandra* and was found to have a quiet X-ray luminosity of $10^{30.2}$ erg s^{-1}. The star (called 'SR12A-B' or 'ROXN-36') was observed in X-rays using XMM-Newton by Ozawa et al. (2005). They found that the star had a typical X-ray luminosity of $10^{30.3}$ erg s^{-1}, with a slightly higher luminosity of $10^{30.4}$ erg s^{-1} during a flare. They were unable to describe the star's X-ray spectrum with single or two temperature component models, but found that a three temperature component

Star	M_* ($M_\odot$)	R_* ($R_\odot$)	P_{rot} (days)	Age (Myr)	R_{co} (R_*)	$v \sin i$ (km s^{-1})	$\log \dot{M}_a$ ($M_\odot$ yr^{-1})
AA Tau	0.7	2.0	8.22	1.5	7.62	12.3	-9.2
BP Tau	0.7	1.95	7.6	1.5	6.04	9.0	-8.5
CR Cha	1.9	2.5	2.3	3	3.63	35.0	-9.0
CV Cha	2.0	2.5	4.4	5.0	5.7	25.0	-7.5
MT Ori	2.6	8.2	8.53	0.23	2.95	22.0	-9.1
TW Hya	0.8	1.1	3.56	8.0	8.3	5.0	-8.9
V2129 Oph	1.35	2.0	6.53	2.3	8.13	14.5	-9.2
V2247 Oph	0.36	2.0	3.5	1.0	3.42	20.5	-9.8

Table 4.1: Stellar parameters taken from the literature for all of the stars in the sample. From left to right, the columns correspond to stellar mass, radius, rotation period, age, corotation radius, projected rotational velocity, and mass accretion rate. For references, see the text of Section 4.1.

model provided an acceptable fit[5]. V2247 Oph was observed as part of the Deep Rho Oph XMM-Newton Observation project (DROXO; Pillitteri et al. 2010; as 'src 53' and 'SR 12A') and was found to be one of the brightest sources in their sample with an X-ray luminosity of $10^{30.1}$ erg s^{-1}. They found that the star's spectrum was well fit with a three temperature component thermal emission model[6]. This fit can be seen in Table 4.3. A strong low-temperature component of this fit is at ~ 5 MK.

4.2 Results: surface magnetograms

In this section, I analyse the sample of ZDI magnetograms. Although Donati et al. (2010a) presented magnetograms for AA Tau at two separate epochs, the two fields are almost identical in their structures and strengths and so I only consider the 2009 field here. It is important to note that I am only considering the potential components of the fields based on the radial components of the ZDI fits (i.e. for each field I calculate the B_θ and B_ϕ components from the B_r component using the potential field assumption). This means that the field strengths will be underestimated in cases where they have significantly toroidal components.

Due to the method that was used to fit the ZDI magnetograms to CR Cha and CV Cha (Hussain et al. 2009), the published fields do not contain any magnetic flux in the hemisphere that is out of view. As was shown in Chapter 3, one cannot reproduce reasonable coronal magnetic field structures when the flux in an entire hemisphere is missing. Thus, for both of

[5]Fitting to V2247 Oph's quiet spectrum, they obtained temperatures for the three components of 2.9 MK, 11.3 MK, and 40.6 MK, respectively, with corresponding emission measures of 18.2, 18.6, and 5.6 $\times 10^{52}$ cm^{-3}.

[6]They actually fitted a three temperature component model to V2247 Oph in order to take account of the fact that the star's light was contaminated by light from the fainter source IRS 42/GY 252 (src. 54) which they fitted with a single temperature model.

these stars I impose field on the invisible hemisphere by reflecting the magnetograms about the equator and reverse the polarity of the field.

The radial components of the magnetic fields for the stars in the sample are shown in Fig. 4.4. The magnetograms show significant variations in the field complexities, ranging from a simple dipole for AA Tau, to a simple octupole for TW Hya, to very complex distributions of regions of opposite polarity field on V2247 Oph. The field complexities, as measured by the energy weighted average l value that describes the field are given in Table 4.2. AA Tau has the simplest field, with a value of $< l >$ of 1.1, which is consistent with its dipolar configuration. The most complex fields are CR Cha and CV Cha, with values of 6.6 and 6.5 respectively . It is worth remembering that small scale field structures are likely to be missing from these magnetograms. If these structures were present, the values of $< l >$ would be much larger[7].

The strengths of the dipole, quadrupole, and octupole components for each of the fields are given in Table 4.2. Other than in the cases of the weak, complex fields of CR Cha, and CV Cha, all of the fields have dominant even l value components, and weak odd l value components. This is a result of the ZDI fitting technique which favors solutions that have a larger fraction of the magnetic energy in the even l modes, therefore forcing the magnetograms to be approximately anti-symmetric about the equator. Some justification for this for the CTTS sample comes from the fact that Doppler Imaging Ca II IRT excess emission maps show dominant accretion spots at high latitudes. This would only be expected if accretion occurs along large dipole-like field lines extending from the pole in the visible hemisphere through the accretion disc to the pole in the opposite hemisphere. Thus, one would expect the polarity of the fields on the two poles to be opposite, as is seen on the Sun.

[7]In the simulated stellar magnetograms considered in Chapter 3, the values of $< l >$ are typically $\sim$15 for the active AB Dor-like star and vary between 4 and 14 for the inactive solar-like star (see Fig. 3.3).

Star	Φ_{total} (10^{25} Mx)	$< B >$ (G)	B_{dip} (G)	B_{oct} (G)	θ_{dip} (degrees)	$< l >$
AA Tau 2009	22.4	1218.0	1720.7	503.8	174	1.1
BP Tau Feb 2006	15.9	1005.8	1219.1	1597.6	11	2.3
BP Tau Dec 2006	15.2	967.6	957.0	1801.0	25	2.6
CR Cha	4.9	195.0	91.2	38.8	180	6.6
CV Cha	4.8	122.1	24.0	60.4	180	6.5
MT Ori	88.1	312.6	147.0	514.9	93	5.2
TW Hya 2008	6.54	1289.5	374.4	2628.8	42	3.1
TW Hya 2010	8.3	1607.3	729.1	3103.2	6	2.9
V2129 Oph 2005	12.1	738.8	283.8	1624.9	24	3.0
V2129 Oph 2009	15.7	981.3	965.9	2155.6	13	2.7
V2247 Oph	3.5	216.0	111.2	233.5	42	4.6
V4046 Sgr A	0.53	102.4	102.1	125.6	63	2.50
V4046 Sgr B	0.67	149.2	77.6	244.1	83	3.05

Table 4.2: Results for the analysis of the ZDI magnetograms for all of the stars in the sample. From left to right, the columns correspond to the total magnetic flux, the surface averaged field strength, the strength of the dipole component, the strength of the quadrupole component, the strength of the octupole component, the tilt angle of the dipole component, and the field complexity parameter defined as the energy weighted average l value that describes the field.

The average surface field strengths on these stars vary between 0.1 kG and 1.6 kG. These values are lower than the typical values derived for CTTSs using the Zeeman effect in unpolarized line profiles. For instance, Johns-Krull (2007) derived field strengths averaged over the stellar surface for AA Tau and BP Tau of 2.78 kG and 2.17 kG respectively, in contrast to the value of ∼1 kG derived from the ZDI magnetograms. This discrepancy can be explained in two ways. Firstly, because I disregard the toroidal components of the field, the average surface field strengths that I calculate are underestimates of the true field strengths on these stars. However, neither AA Tau, nor BP Tau have significant toroidal components in their ZDI magnetograms. Secondly, as the ZDI magnetograms are primarily fit to circularly polarized line profiles, they suffer severely from the cancelation of unresolved small scale field structures. Reiners (2012) showed that the surface averaged field strengths derived from Stokes V measurements are typically much lower than those derived from Stokes I. Strong fields in unresolved active regions may be distributed over the surfaces of these stars, and may contribute to the strong field strengths derived from unpolarized line profiles, but not to the field strengths derived from spectropolarimetry.

Fig. 4.5 shows that the complexity of a surface field is correlated with the field strength averaged over the stellar surface, such that simple fields show the strongest field strengths. This may be related to the evolution of the internal structure of pre-main sequence stars and the dynamo processes responsible for the generation of these fields. Pre-main sequence stars are initially fully convective, and as they evolve, they grow radiative cores. This probably causes a change in the dynamo mechanisms that produce the large scale fields of these stars and this change might be visible in the field strengths and structures. I should point out that the oldest star in the sample, TW Hya, has a strong simple field. However, due to its relatively low mass, it probably has not developed as substantial a radiative core as some of the younger higher mass stars in the sample. Alternatively, this correlation might be a result of the finite resolution of the ZDI technique. If the differences in field the complexities are real, and not a resolution effect, fields with more complex ZDI magnetograms contain field structures on smaller scales, and therefore are more susceptible to the cancellation of magnetic flux from unresolved regions of opposite polarity, therefore making them appear weaker. However, this explanation is unable to account for the fact that the fields of the two stars in the binary system V4046 Sgr do not follow this correlation.

[7]The simulated magnetograms used in Chapter 3 that contained a large number of small-scale active regions that would not be produced in the ZDI magnetograms had values of $< l >$ of typically around 14-16.

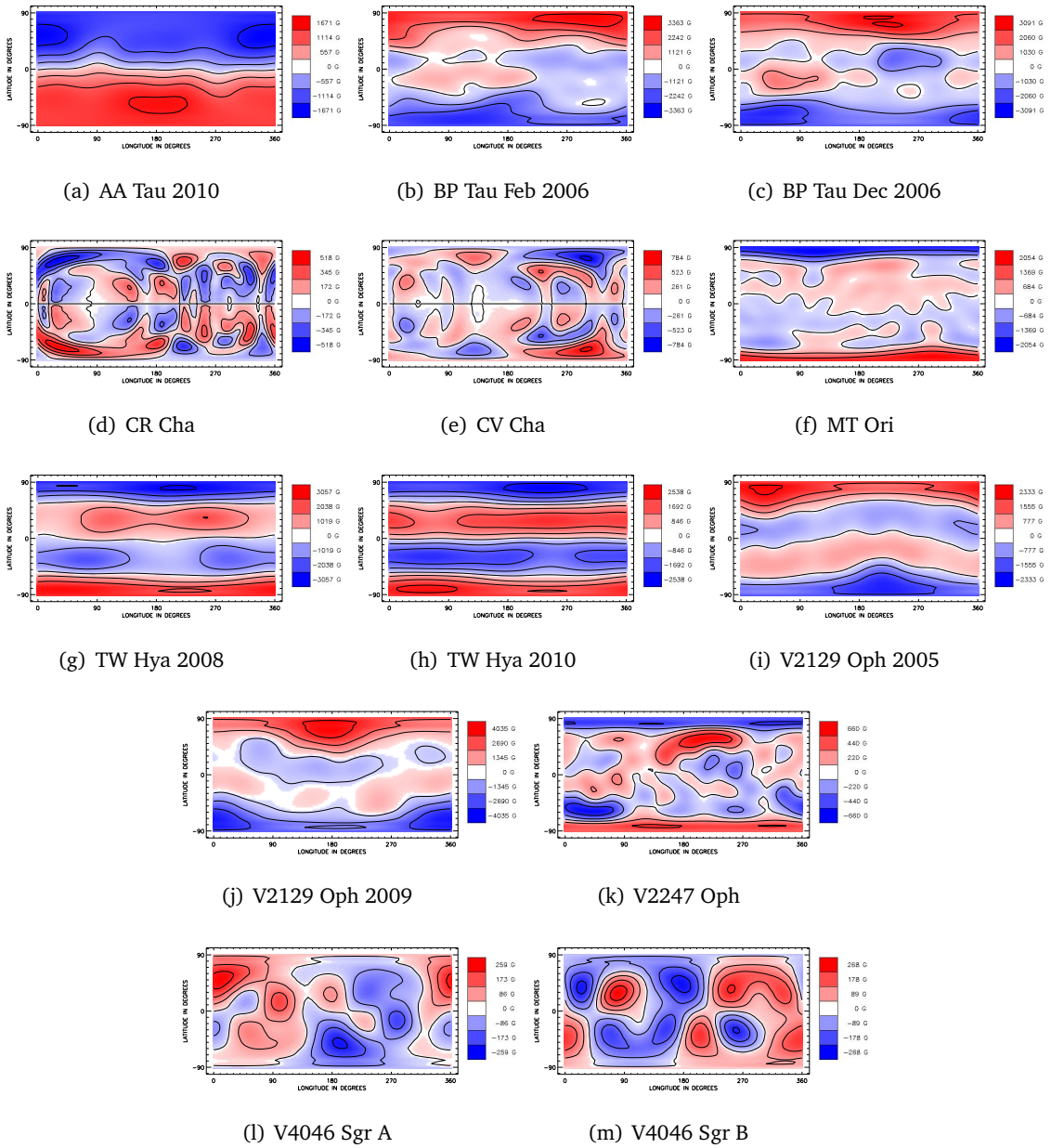

(a) AA Tau 2010 (b) BP Tau Feb 2006 (c) BP Tau Dec 2006

(d) CR Cha (e) CV Cha (f) MT Ori

(g) TW Hya 2008 (h) TW Hya 2010 (i) V2129 Oph 2005

(j) V2129 Oph 2009 (k) V2247 Oph

(l) V4046 Sgr A (m) V4046 Sgr B

Figure 4.4: The radial components of the ZDI magnetograms for all of the stars in the sample. These are reproduced from Donati et al. (2010a), Donati et al. (2008a), Donati et al. (2008a), Hussain et al. (2009), Hussain et al. (2009), Donati et al. (2011b), Donati et al. (2011b), Donati et al. (2011a), Donati et al. (2011a), and Donati et al. (2010b).

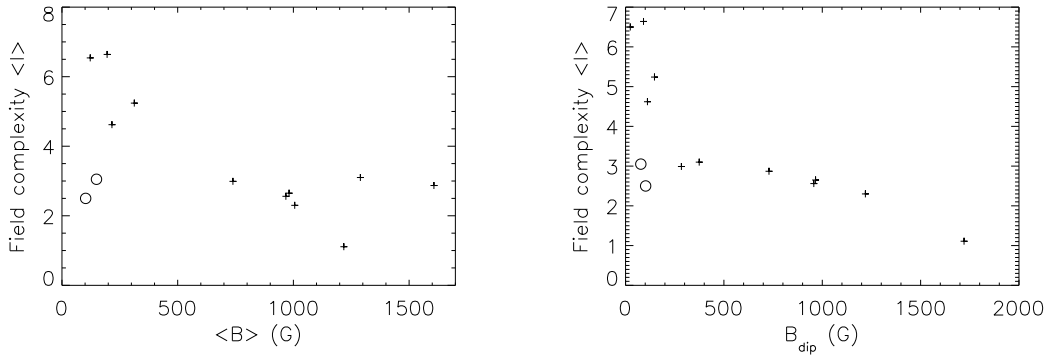

Figure 4.5: *Right-hand panel*: correlation between the field complexity parameter $< l >$ and the surface averaged field strength $< B >$ for the sample of ZDI magnetograms. *Left-hand panel*: correlation between the field complexity parameter $< l >$ and the strength of the dipole component of the field. The two stars in the binary system V4046 Sgr are shown as asterisks'.

As the finite ability to spatially resolve field structures is a significant factor in determining the complexities and strengths of measured fields, it is important to understand to what extent the differences in the field complexities and strengths between the stars are a result of different resolution. Fig. 4.6 shows that the complexities of the magnetograms is strongly correlated with stellar rotational $v \sin i$ with the faster rotators having more complex fields and the slower rotators having less complex fields. Since the resolution of the ZDI technique is directly proportional to the stellar $v \sin i$, the most obvious interpretation of this result is that it is a resolution effect. Thus, with the faster rotators, ZDI is able to resolve smaller scale field structures that remain unresolved on the slow rotators. However, if this interpretation is correct, it might be expected that the faster rotators will also have the strongest surface averaged fields as they will suffer less from the cancellation of flux in unresolved regions of the surface. Fig. 4.6 shows that this is not the case, with a very strong anti-correlation between field strength and projected rotational velocity.

The correlation between field complexity and rotation rate may be a result of star-disc interactions. TTSs that still possess circumstellar discs have been shown to be slower rotators than TTSs that do not possess discs. This is thought to be a result of disc-locking, where magnetic interactions between the star and the region of the circumstellar disc outside of the corotation radius, and magnetic interactions between the star and accreting material, exerts spin-down torques on the star, causing the star to rotate slower. Since the strength of the magnetic interactions between the star and the disc is primarily determined by the dipole component of the field, the disc-locking theory might predict that stars with stronger dipole components will be rotating slower as fields with stronger dipoles will be able to connect

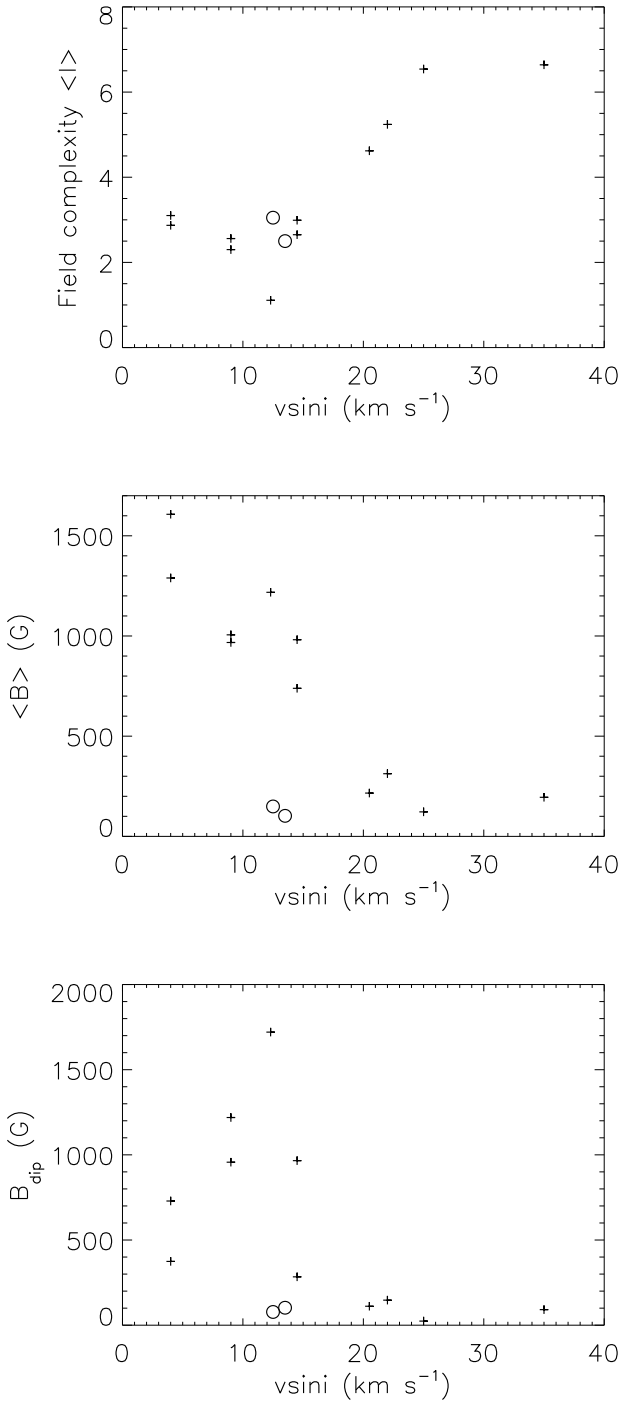

Figure 4.6: Correlations between projected rotational velocity and field complexity (upper panel), surface averaged field strength (middle panel), and the strength of the dipole component of the field (lower panel).

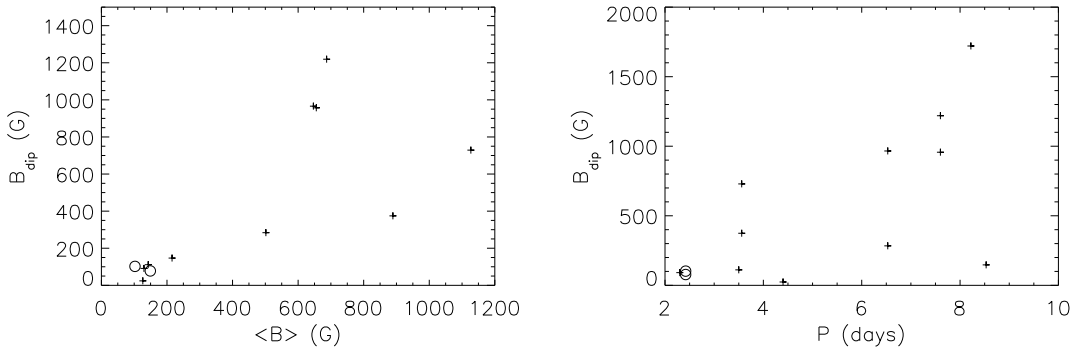

Figure 4.7: Strength of the dipole component of the field against surface averaged field strength (left panel) and rotation period (right panel).

with the disc outside the corotation radius better than fields with weaker dipoles[8]. This correlation is clearly visible in Fig. 4.7 which shows the strength of the dipole component against rotation period. The main outlier in this plot is the young star MT Ori which has a long rotation period and a small dipole component. As MT Ori is only ∼0.25 Myr old, and still has a radius of 8.2 R_*, it is likely that it is an outlier as it has undergone less spin-up due to contraction than the other stars in the sample. Due to its higher mass, it is likely to have developed a radiative core at this young age (as opposed to the much older lower mass stars AA Tau and BP Tau which have not developed radiative cores) and thus has a weak dipole component. As the strength of the dipole component is positively correlated with the field complexity and the average field strength, this can explain why the faster rotators appear to have more complex and stronger fields. In this interpretation, it is still not clear whether the correlation between field strength and complexity is a resolution effect. It may be that, due to disc-locking, the stars with the strongest fields are the slowest rotators, and thus, due to limited spatial resolution have the simplest ZDI magnetograms. On the other hand, it may be that the correlation between field strength and complexity is real, such that the strongest fields are the most dipolar, and thus, due to disc-locking, are the slower rotators. The analogy with the sample of M dwarfs that have been studied using the ZDI technique (see Section 1.1) would favor the latter interpretation.

[8]I should note here that this situation is not so simple as stronger dipole components will also lead to a better connection between the central star and the region of the disc inside the corotation radius which will exert a spin-up torque on the central star. There may also be another effect here that means that stronger dipole components lead to a larger spin-down torque on the central star. The distance between the star and the inner edge of the disc is largely determined by the strength of the dipole, such that stronger dipoles cause the inner edge of the disc to be further away from the stellar surface. Thus, if the strength of the dipole component of a field is increased, the size of the region of the disc inside of the corotation radius will be decreased. This can lead to less of a spin-up torque on the central star.

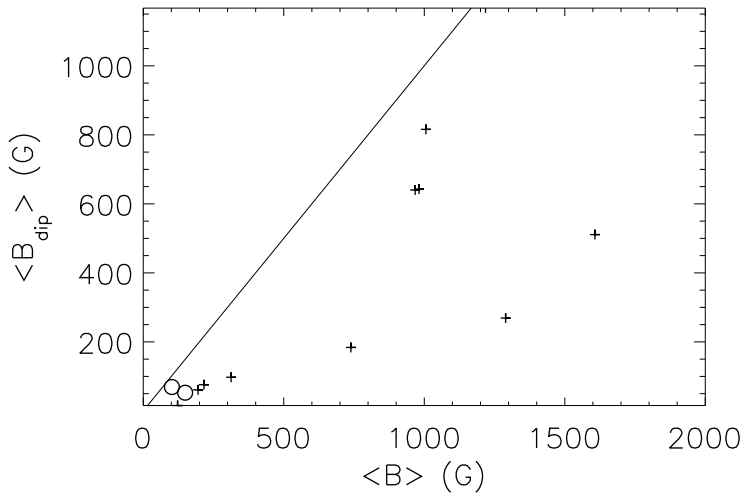

Figure 4.8: Surface averaged field strength of the dipole component of the field (i.e. the surface averaged field strength for a field that is made up of *just* the dipole component) against surface averaged field strength for the entire field.

The correlation between field complexity and rotation rate shown in Fig. 4.6 may be accounted for in another way that involves neither finite resolution nor disc-locking. It may be a result of the contraction and the evolution of the internal structure of these stars. As pre-main sequence stars contract, in order to conserve angular momentum, they spin-up. This means that older pre-main sequence stars will tend to be faster rotators than younger ones. At the same time, as they age, they develop radiative cores, which can change the dynamo processes responsible for the generation of these fields, and thus change the field strengths and structures. As these stars grow radiative cores, the field structures appear to become more complex with weaker dipole components. This can account for the correlations shown in Fig. 4.6.

Based on the above discussion, I tentatively conclude that the differences in the field strengths and complexities of the various ZDI magnetograms is due in part to a real difference in the magnetic field strengths and complexities, though the spatial resolution of the ZDI technique is also likely to be a factor. This interpretation is supported by the fact that two of the most complex magnetograms in the sample, CR Cha and CV Cha, were based on low quality data, due to bad weather conditions and low phase coverage. Thus, the resolutions of their magnetograms are lower than what would be expected given their high projected rotational velocities. Hussain et al. (2009) estimates that the resolution of the magnetograms for these two stars is similar to that of the slower rotator V2129 Oph, which shows a significantly

simpler field structure, thus indicating that the difference in complexity of these stars is not simply due to resolution. Hussain et al. (2009) used the magnetograms from CR Cha and CV Cha to simulate data using the stellar parameters of the slower rotators BP Tau and V2129 Oph (the only other two CTTSs that had been studied using the ZDI technique at the time) and reconstruct magnetograms for CR Cha and CV Cha based on this data. They found that the V2129 Oph parameters gave simpler reconstructed magnetic fields of similar complexity to the actual magnetic field of V2129 Oph. However, for the BP Tau parameters, their reconstructed magnetic fields were significantly more complex than what was seen on BP Tau. This indicates that the higher complexities of the CR Cha and CV Cha fields are real.

Fig. 4.8 gives the surface averaged field strength of the dipole component of the field (i.e. the surface averaged field strength for a field that is made up of *just* the dipole component) against surface averaged field strength for the entire field. Fig. 4.8 shows that the surface averaged field strength is not a good indicator of the strength of the dipole component of the field. This is significant as studies of magnetospheric accretion often use surface averaged field strengths measured from Zeeman broadening of unpolarized line profiles that give no information about the strength of the dipole component of the field.

4.3 Results: coronal modelling

Using the radial component of the surface magnetograms, I extrapolate the fields to all radii using the PFSS model and assuming that the source surface is at the corotation radius. Using the coronal field structures, I then apply the plasma model described in Section 2.5 to all of the stars in the sample.

4.3.1 Plasma model

The coronal plasma model that I use in this section assumes as input parameters the stellar radius, stellar mass, rotation rate, coronal plasma temperature, and coronal X-ray emission measure. These parameters are compiled in Tables 4.1 and 4.3 for each of the stars in the sample.

The first step in applying the model is to calculate the values of the proportionality constant K between the magnetic pressure and the plasma pressure at the base of the corona ($K = p_0/B_0^2$). For each star, the value of K is assumed to be uniform over the surface, but it

is assumed to vary from star to star. We scale K for each star so that the modelled coronal emission measure matched the observed values given in Table 4.3.

For the temperatures and X-ray emission measures, where several values are available in the literature, I use those given in Table 4.3. Using observed X-ray data to model the coronae of CTTSs presents several significant problems. One of these problems is that an unknown amount of the X-ray emission originates in accretion shocks. The X-ray emitting plasma in accretion shocks is likely to be at a low temperature (∼2-3 MK) whereas the coronal plasma is likely to be at a much higher temperature (∼5-20 MK). I solve this problem by disregarding the low temperature components when multi-temperature component fits to X-ray spectra are available. I combine the remaining temperature components using

$$EM_{\rm total} = \sum_i EM_i \tag{4.1}$$

$$\log T_{\rm total} = \frac{\sum_i EM_i \log T_i}{\sum_i EM_i} \tag{4.2}$$

The following are some notes regarding the use of the X-ray data compiled in Table. 4.3.

- *AA Tau*: I use the single temperature component fit given by Güdel et al. (2007). As this component is at a high temperature of 26.9 MK, I assume that this corresponds entirely to coronal emission and has no component from the accretion shock.

- *MT Ori*: For this star, I use a two temperature component fit. Both components are at temperatures above 10 MK and are unlikely to have formed in an accretion shock.

- *BP Tau, CR Cha*: For these two stars, the three temperature component fits given by Robrade & Schmitt (2006) both have a low temperature component at approximately 2 MK which could be a result of X-ray emission from accretion shocks and so they are disregarded. However, the contribution to the total emission measure from these components are only ≈18%, so this only makes a small difference to the coronal models.

- *TW Hya and V2247 Oph*: The three temperature component fits for these two stars have low temperature components at approximately 3 MK that represent a significant fraction of the total X-ray emission measures. This is especially true for TW Hya where

the low temperature component is a factor of four larger than the other two components combined. Assuming that these components are a result of X-ray emission from accretion shocks, I disregard them in the coronal model.

- *V2129 Oph*: This is the only star in the sample for which X-ray observations taken simultaneously with the spectropolarimetric observations from which one of the ZDI magnetograms is derived are available. Argiroffi et al. (2011) provides a nine temperature component fit to this data. I assume that the three lowest temperature components were produced in accretion shocks and disregard them. However, these components only correspond to 8% of the total emission measure, so this does not significantly affect the coronal model.

- *CV Cha*: No temperature and emission measure fits are available for this star, so I do not consider it in this section.

Probably the most significant problem with using X-ray data to model stellar coronae from ZDI magnetograms is the fact that the magnetic fields probably contain a large amount of strong small scale field structures that are not reproduced in the ZDI magnetograms. Such active regions are seen on the solar surface, and are responsible for small scale coronal magnetic structures that are responsible for most of the Sun's X-ray emission. In Chapter 3, I show that missing this flux has a significant effect on the predicted coronal plasma structures. In this chapter, I do not consider this problem.

The values of the K parameters are given in Table 4.4. Fig 4.9 shows how K correlates with observed emission measure, surface field strength, and field complexity. An unexpected result is the lack of any correlation between K and the observed coronal emission measures. This is due to the fact that other factors, such as field strength and coronal volume, are very important for determining K. For instance, Fig. 4.9 shows that K is strongly correlated with average surface field strength. This is due to the assumption in the coronal model that the plasma pressure at the base of the corona is proportional to the plasma pressure ($p_0 = KB^2$), such that stars with stronger surface fields can give the observed emission measures with smaller values of K. A strong correlation between K and the field complexity parameter $< l >$, is also present. This could be for two reasons. Firstly, $< l >$ is strongly correlated with field strength, with the simpler fields also being the stronger fields. Thus, the simpler fields need lower values of K to reproduce the observed emission measures. Alternatively, this

correlation might be due to the fact that the more complex fields tend to have coronae that do not extend very far from the stellar surface, and thus have lower volumes. On the other hand, simple fields tend to be much more extended and so simpler fields have much larger coronae, and can reproduce the observed emission measure with lower values of K.

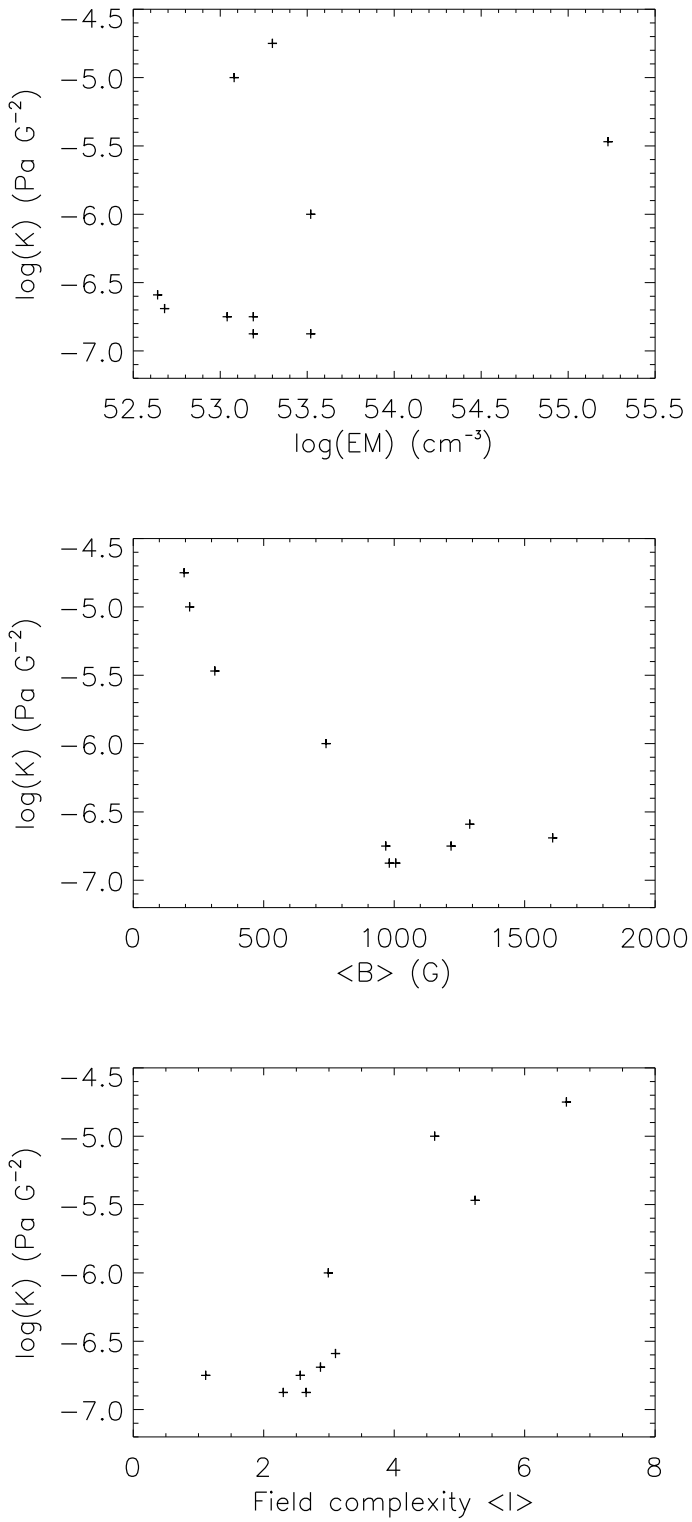

Figure 4.9: Values of the proportionality K between plasma pressure and magnetic pressure at the base of the corona that have been fit to observed X-ray emission measures against emission measure (upper panel), surface averaged field strength (middle panel), and the field complexity (lower panel) for most of the stars in the sample.

Star	$\log L_x$ (erg s^{-1})	$\log T_1$ (K)	$\log EM_1$ (cm^{-3})	$\log T_2$ (K)	$\log EM_2$ (cm^{-3})	$\log T_3$ (K)	$\log EM_3$ (cm^{-3})	$\log T$ (K)	$\log EM$ (cm^{-3})	Reference
AA Tau	30.09	7.43	52.951	-	-	-	-	7.43	52.951	1
BP Tau	30.11	6.37	52.542	6.86	52.723	7.40	53.013	7.22	53.193	2
CR Cha	30.12	6.29	52.695	6.88	53.028	7.35	52.967	7.10	53.300	2
MT Ori	31.90	7.03	55.229	7.28	55.05	-	-	7.16	55.230	3
TW Hya	30.18	6.46	53.282	6.90	52.090	7.19	52.494	7.11	52.638	2
V2129 Oph	30.43	-	-	-	-	-	-	7.19	53.517	4
V2247 Oph	30.10	6.68	52.98	7.02	52.940	7.61	52.50	7.18	53.075	5

Table 4.3: Multi-temperature component fits to observed X-ray spectra for the stars in the sample. References: (1) Güdel et al. (2007); (2) Robrade & Schmitt (2006); (3) Getman et al. (2005b); (4) Argiroffi et al. (2011); (5) Pillitteri et al. (2010).

Star/Magnetograms	$\log K$	$\log \bar{n}_e$ (cm^{-3})	r_{max} (R$_*$)	V (10^{35} cm^3)	Φ_{open} (10^{25} Mx)	f_{open}	$< B_{r,open} >$ (G)
AA Tau 2009	-6.65	8.72	4.36	3.71	5.33	0.17	1333.9
BP Tau Feb 2006	-6.88	8.98	3.76	2.01	4.34	0.11	1831.9
BP Tau Dec 2006	-6.75	9.06	3.95	1.82	3.95	0.16	959.0
CR Cha	-4.75	9.54	2.19	0.31	1.66	0.21	215.2
MT Ori	-5.60	9.83	2.30	14.69	26.21	0.21	307.8
TW Hya 2008	-6.59	9.31	3.25	0.21	0.68	0.06	1512.7
TW Hya 2010	-6.69	9.09	3.76	0.29	0.97	0.09	1535.8
V2129 Oph 2005	-6.00	9.49	2.42	0.35	2.00	0.08	1124.0
V2129 Oph 2009	-6.88	9.20	3.25	1.32	4.07	0.06	2810.3
V2247 Oph	-5.0	9.67	2.09	0.05	1.14	0.20	234.4

Table 4.4: Results from the coronal plasma model for each of the stars in the sample. From left to right, the columns correspond to the proportionality parameter K between the magnetic pressure and the plasma pressure at the base of the corona, the emission measure weighted average coronal electron density, the maximum radius at which the stellar magnetic field can hold onto the closed corona, the volume of the closed corona, the open flux, the fraction of the stellar surface covered in open field, and the average field strength in regions of the stellar surface covered in open field.

4.3.2 The coronal extent and the open magnetic flux

One of the features of the coronal plasma model is that if the plasma β becomes greater than unity at any point along a field line, that field line is assumed to be blown open by the hot coronal plasma. This means that there is a maximum radius at which the magnetic field can hold onto the closed corona. Table 4.4 gives this maximum radius for the sample of CTTSs as derived from the numerical model. The coronae generally extend several stellar radii from the surface with AA Tau being able to hold onto its corona out to 5 R_*. The coronal extents are correlated with several parameters, such as magnetic field strength and field complexity[9].

An alternative less accurate way to approximate the coronal extent is given in Section 2.5. The maximum radius of the closed corona is obtained by solving

$$K \exp\left(\frac{GM_* m_H}{kT}(r_{max}^{-1} - R_*^{-1}) - \frac{\omega^2 \sin^2\theta m_H}{2kT}(r_{max}^2 - R_*^2)\right) = \frac{10^{-8}}{2\mu_0}\left(\frac{r_{max}}{R_*}\right)^{-2(<l>+2)} \quad (4.3)$$

The values that are derived by solving this equation are plotted against the values from the numerical model in Fig. 4.10. The values from the two methods closely match the numerical results. Using this relation, it is possible to explore how important each factor is in determining the coronal extent. The most significant factor in this equation is the field complexity parameter $< l >$. In fact, I have found very similar results when holding all of the stellar parameters (i.e. M_*, R_*, T, and K) constant for all of the stars and only allowing $< l >$ to vary. Fig. 4.11 shows that the coronal extent is well correlated with field complexity. As this equation shows that the coronal extent does not depend on the magnetic field strength, the correlation between coronal extent and magnetic field strength is a secondary correlation, resulting from the correlation between field strength and complexity.

I should note that these calculations might underestimate the true coronal extents due to the fact that a large unknown amount of magnetic flux on small scales could be missing from

[9]The coronal extents results presented here are in disagreement with the results of a similar argument presented by Safier (1998) who modelled the magnetic fields of TTSs as the superposition of a small number of surface dipoles and showed that for an isothermal corona in hydrostatic equilibrium, the closed corona is only able to extend $\lesssim$3 R_*. Safier (1998) concludes that this is likely to be an upper limit to the coronal extent for TTSs. However, in the calculations presented here, I have not assumed that the magnetic field is dominated by small scale surface dipoles, but by large scale dipoles and octupoles. Such field structures allow the field to extend further than it would be able to if the field was dominated by small scale surface dipoles. The existence of such large scale field structures, with kG polar field strengths has been shown to exist on CTTSs using the ZDI technique.

the ZDI magnetograms. This will cause the value of K to be overestimated and the coronal extents to be underestimated[10].

Fig. 4.12 shows the locations of regions of open flux on the surfaces of each of the stars in the sample. The latitudinal distribution of open flux clearly depends strongly on field structure such that with the simplest fields the open flux is confined to high latitudes, whereas for the more complex fields the open flux is distributed over both high and low latitudes. None of the stars have regions of closed flux at the poles (even MT Ori, which has a dipole component that is tilted at 90°). The fields that do not show open flux at low latitudes are AA Tau, BP Tau (the February 2006 field more than the December 2006 field), and the V2129 Oph 2009 field. These are also the fields that have the lowest values of the field complexity parameter $< l >$. The TW Hya 2010 field has two low latitude bands of open flux at ±45°; this is due to this field being dominated by a large scale octupole component. The TW Hya 2008 and V2129 Oph 2009 fields have similar structures.

Table 4.4 gives the open fluxes derived for each of these stars. The open flux can be written as a function of two parameters: firstly, the average field strength at the stellar surface in regions of open field, $< B_{open} >$; secondly, the area of the stellar surface covered in open field, $4\pi R_*^2 f_{open}$, where f_{open} is the open flux filling factor, i.e. the fraction of the stellar surface covered in regions of open flux. This can be written as

$$\Phi_{open} = 4\pi R_*^2 f_{open} < B_{open} > \tag{4.4}$$

where $f_{open} < B_{open} >$ is the open field strength *averaged over the entire star*. The values of f_{open} and $< B_{open} >$ are given in Table 4.4. Despite the fact that MT Ori has the lowest value of $< B_{open} >$, it has a much larger open flux than any of the other stars in the sample due to its large open flux filling factor, and its large radius. The value of $f_{open} < B_{open} >$ is strongly correlated with the strength of the dipole component, as shown in Fig. 4.13. The best fit line shown in Fig. 4.13 represents the equation[11]

[10] I should also point out that if the small scale flux is included in the magnetograms, the values of $< l >$ will be much larger and it might be expected that the coronal extents will be much lower. However, if the small scale flux is included, magnetic energy will be distributed over many more spherical harmonic components, and the approximation that the field falls off with radius as $r^{-(<l>+2)}$ will be a bad approximation.

[11] A better fit to the data is found with the equation $f_{open} < B_{open} >= 1.46 \times 10^{-8} B_{dip}^3 - 7.62 \times 10^{-5} B_{dip}^2 + 0.20 B_{dip} + 24.21$.

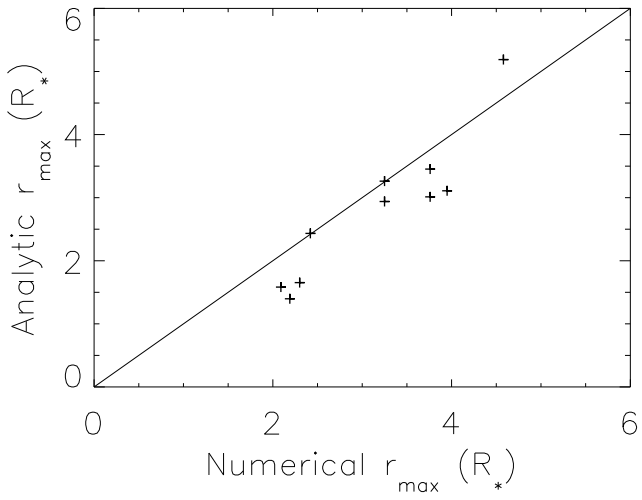

Figure 4.10: Values of the maximum radius at which the stellar magnetic field can hold onto the closed corona derived analytically from Eqn. 4.3 against the values derived using the numerical coronal pressure model.

$$f_{open} < B_{open} >= 0.12 B_{dip} + 41.30 \tag{4.5}$$

4.3.3 The closed coronae

Under the assumption that the X-ray emission from most stars is dominated by closed coronal plasma, it should be expected that the observed X-ray emission measures should correlate with stellar surface area. If the emission is dominated by small scale active regions, as it is on the Sun during times of maximum activity, then stars with large surface areas might be expected to have more X-ray emitting active regions, and thus greater levels of X-ray emission[12]. Similarly, if the emission is dominated by large scale field structures, then a correlation between X-ray emission and coronal volume would be expected. As coronal volume would probably be strongly correlated with stellar surface area, a correlation between X-ray emission and surface area would be expected. Although the number of CTTSs in the sample is small (7 stars with observed X-ray emission measures), there is a good correlation between stellar surface area and observed X-ray emission measures, as can be seen in Fig. 4.14. A similar correlation, albeit with a large scatter, is present in the sample of stars in the *Chandra* Orion Ultradeep Project (Getman et al. 2005b). Similar correlations have been seen by Wood et al. (1994), and Güdel et al. (2007) for both main-sequence and pre-main sequence stars. However, Güdel et al. (2007) found that although there was a strong correlation between stellar surface

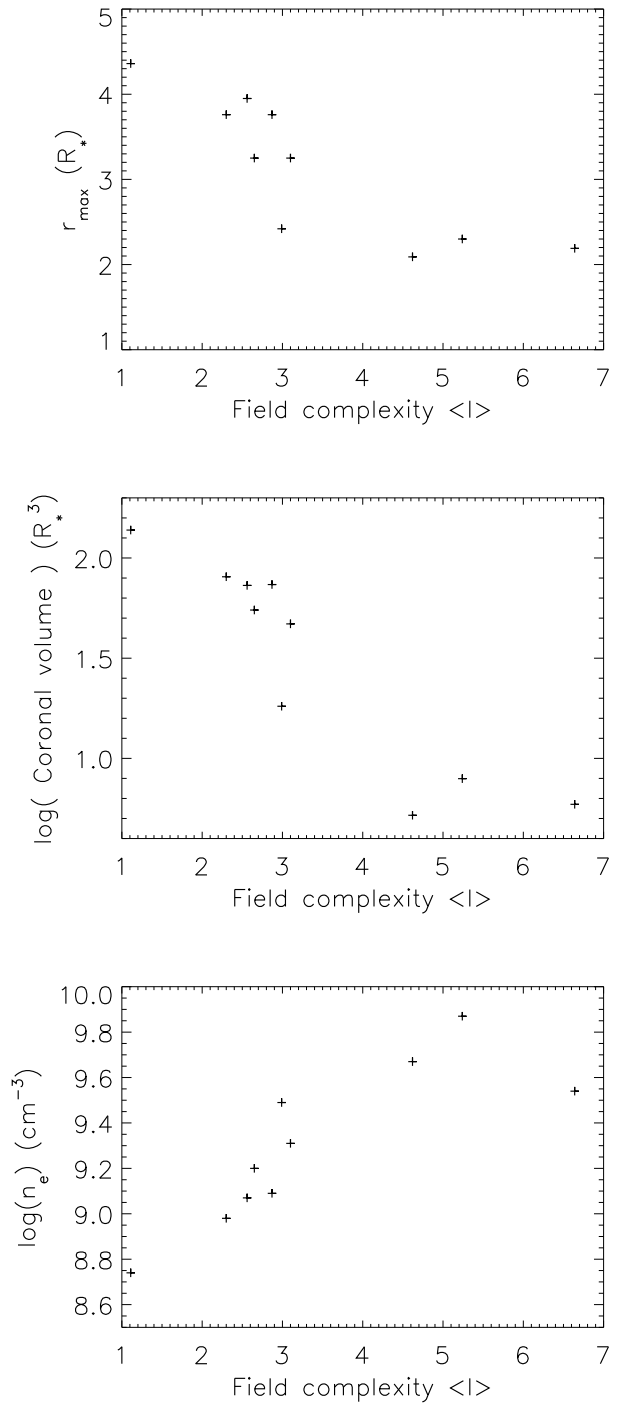

Figure 4.11: Results of the coronal X-ray emitting plasma model against field complexity. The plots show that the maximum radius at which the stellar magnetic field can hold onto the closed coronal plasma (left panel) and the coronal volume (middle panel) both decrease with increasing field complexity, and this corresponds to an increase in the emission measure weighted average coronal electron density (right panel). Therefore, simple magnetic fields lead to extended diffuse coronae, and complex fields lead to compact dense coronae.

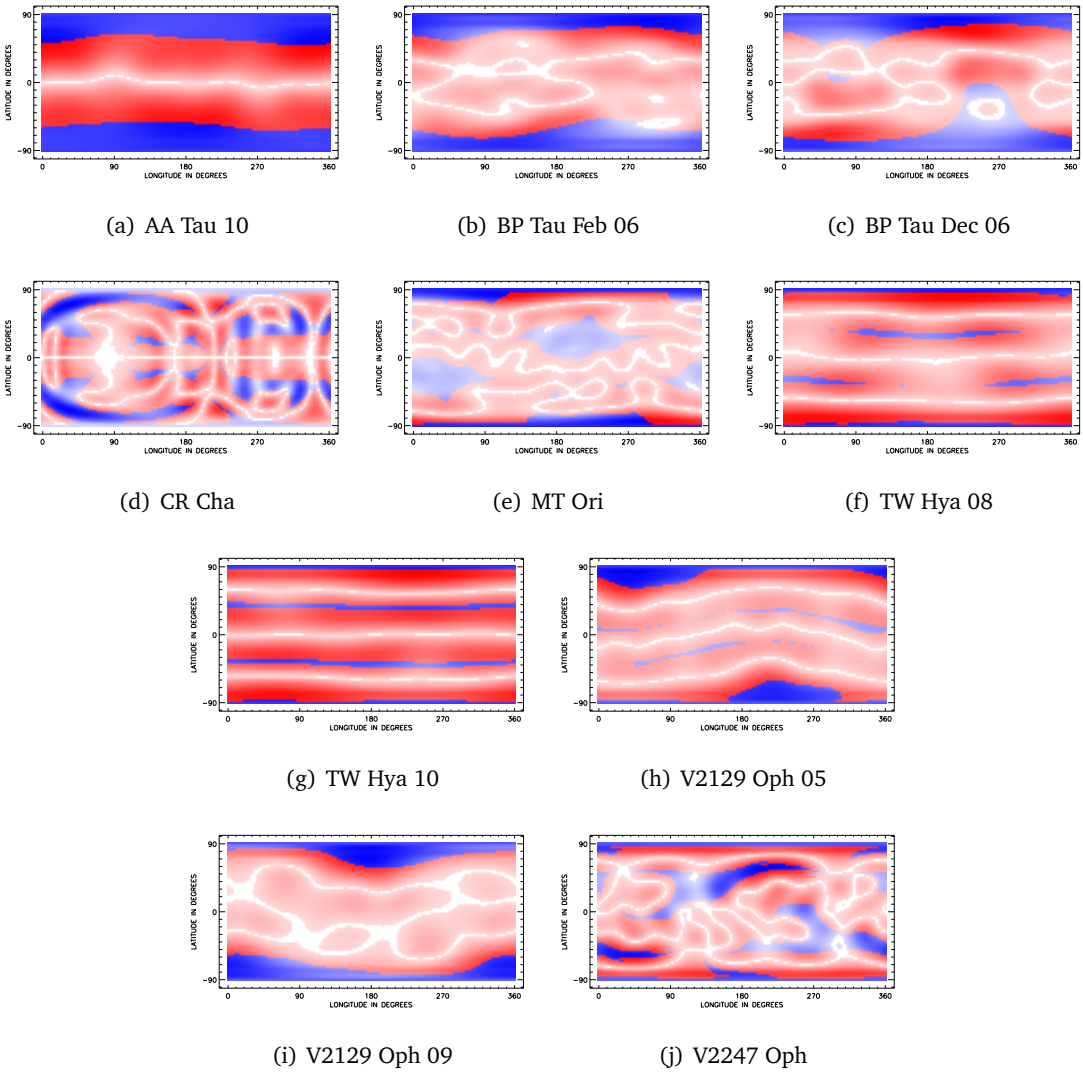

(a) AA Tau 10 (b) BP Tau Feb 06 (c) BP Tau Dec 06

(d) CR Cha (e) MT Ori (f) TW Hya 08

(g) TW Hya 10 (h) V2129 Oph 05

(i) V2129 Oph 09 (j) V2247 Oph

Figure 4.12: Magnetograms for most of the stars in the sample showing the predicted locations of open magnetic field (blue) and closed magnetic field (red).

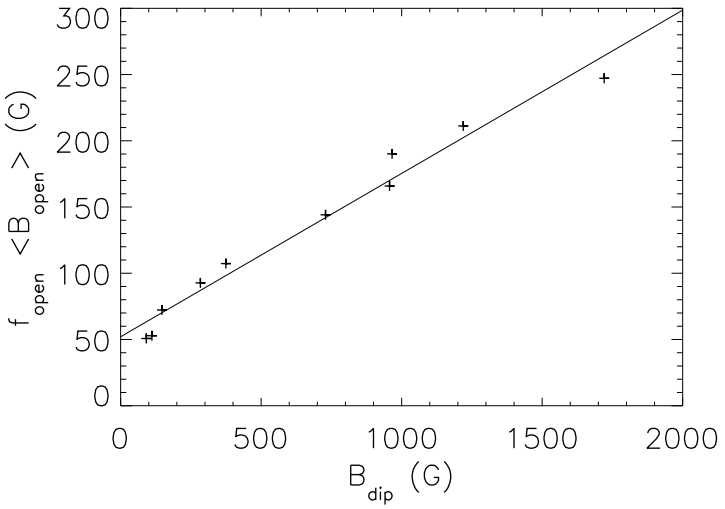

Figure 4.13: Correlation between open flux and the strength of the dipole component.

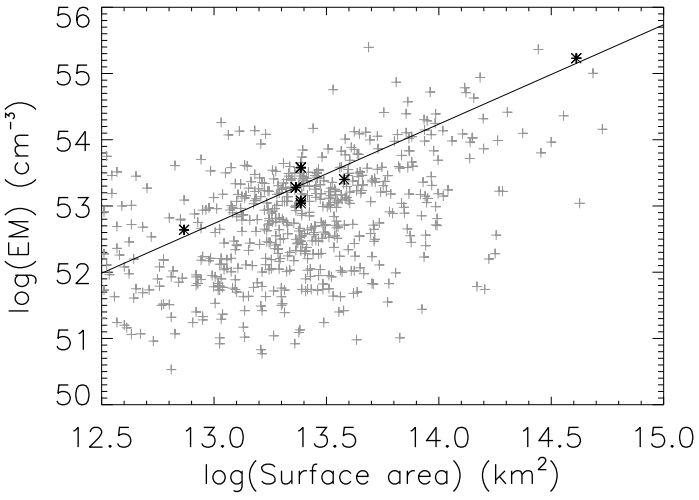

Figure 4.14: Correlation between observed X-ray emission measure and stellar surface area for the sample of CTTSs (black asterisks). The COUP sample of X-ray sources is plotted in the background (grey crosses). The COUP data has been taken from Getman et al. (2005b).

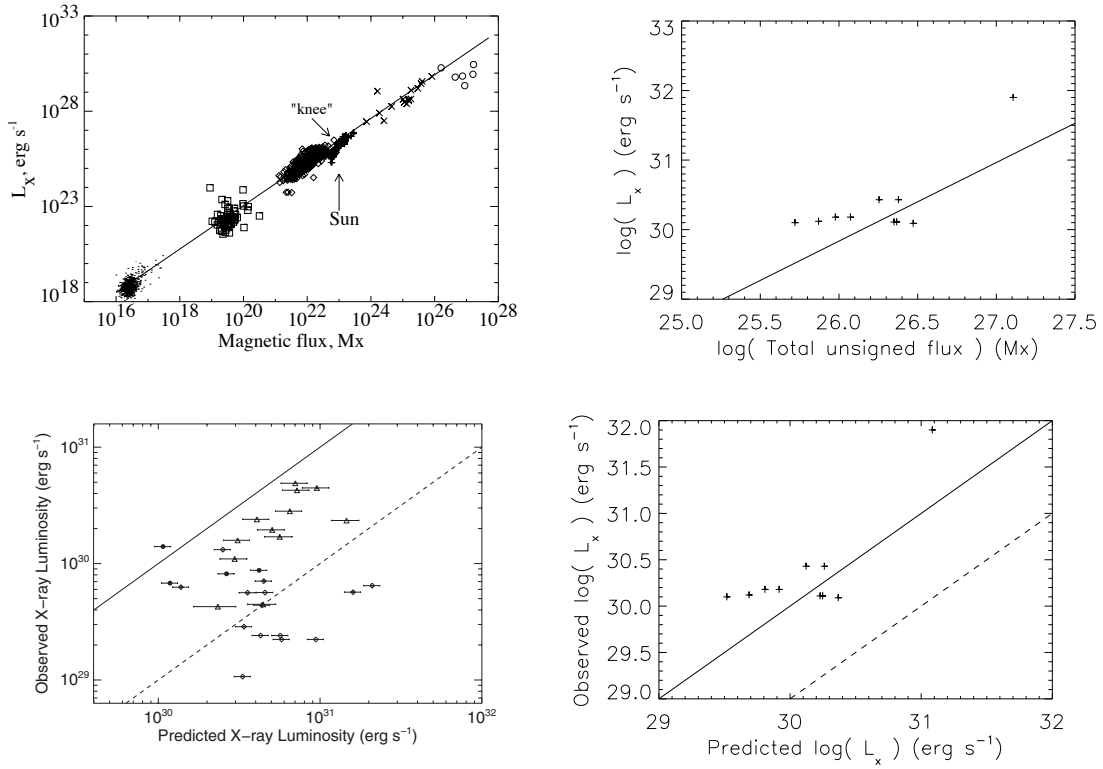

Figure 4.15: *Upper panels*: reproduced from Pevtsov et al. (2003) (left panel) showing the correlation between X-ray luminosity and magnetic flux for regions of the quiet Sun (dots), solar X-ray bright points (squares), solar active regions (diamonds), the entire solar disc (pluses), G, K, and M dwarfs (crosses), and T Tauri stars (circles), compared with a similar plot for the sample of CTTSs considered in this chapter based on the ZDI magnetograms (right panel). *Lower panels*: reproduced from Yang & Johns-Krull (2011) (left panel) showing observed X-ray luminosities against values predicted based on the measured field strengths and the relation between X-ray emission and magnetic flux of Pevtsov et al. (2003) for a sample of TTSs, compared with a similar plot for the sample of CTTSs considered in this chapter based on the ZDI magnetograms (right panel). The solid line represents the line of equality and the dashed line shows where the observed luminosities are an order of magnitude below the predicted values.

area and X-ray activity for the XEST sample of pre-main sequence stars, there was a stronger correlation between stellar mass and X-ray activity. This is possible because of the weak correlation between stellar mass and radius on the pre-main sequence.

By considering the magnetic flux and X-ray emission observed from the quiet Sun, solar active regions, the entire solar disc, dwarf stars, and T Tauri stars, Fisher et al. (1998) and Pevtsov et al. (2003) found that the relationship between total unsigned magnetic flux and X-ray emission is almost linear over 12 orders of magnitude. Fig. 4.15 shows the total unsigned magnetic flux as a function of X-ray luminosity. MT Ori is the outlier in this plot as it has an X-ray luminosity that is almost two orders of magnitude above the other stars. The solid lines in this figure shows the relation found by Pevtsov et al. (2003) of $L_x \propto \Phi_{\rm tot}^{1.13}$, where the constant of proportionality is $\sim$2.85 erg s^{-1} Mx$^{-1.13}$. The levels of X-ray emission from these stars are consistent with the magnetic fluxes and the relation given by Pevtsov et al. (2003). This is contrary to the results Johns-Krull (2007) and Yang & Johns-Krull (2011) who used field strengths derived from unpolarized line profiles to predict X-ray luminosities and found that they are typically an order of magnitude above observed values. This result is reproduced in Fig. 4.15 and compared with a similar analysis using the magnetic fluxes derived from ZDI magnetograms. As in Johns-Krull (2007) and Yang & Johns-Krull (2011), I define the magnetic flux as $4\pi R_* < B >$, and not $4\pi R_* < B_r >$. This discrepancy may be due to the underestimation of magnetic fluxes here due to the cancellation of unresolved opposite polarity features in the ZDI magnetograms causing smaller total unsigned fluxes, and therefore, smaller predicted X-ray luminosities. As Johns-Krull (2007) and Yang & Johns-Krull (2011) used Zeeman broadening to measure the magnetic field strengths, their values will suffer less from flux cancellation, and therefore have larger magnetic fluxes and larger predicted X-ray luminosities. However, analysis of the cases of AA Tau and BP Tau, which are in the sample of stars considered by Johns-Krull (2007) (they also include TW Hya) shows that flux cancellation in ZDI magnetograms is not entirely responsible for the discrepancy. For AA Tau, Johns-Krull (2007) finds a surface averaged field strength of 2.78 kG, which is larger than the value of 1.2 kG derived from the ZDI magnetogram. However, as Johns-Krull (2007) uses a slightly smaller stellar radius for AA Tau, he derives a magnetic flux that is only slightly larger than the value derived here. The main reason for the discrepancy for the case of AA

[12] It is worth pointing out here that if the solar surface was completely covered in solar-like active regions, it would only have an X-ray luminosity of $\sim 10^{29}$ erg s^{-1} (Wood et al. 1994), which is an order of magnitude below the least luminous X-ray source in the CTTS sample.

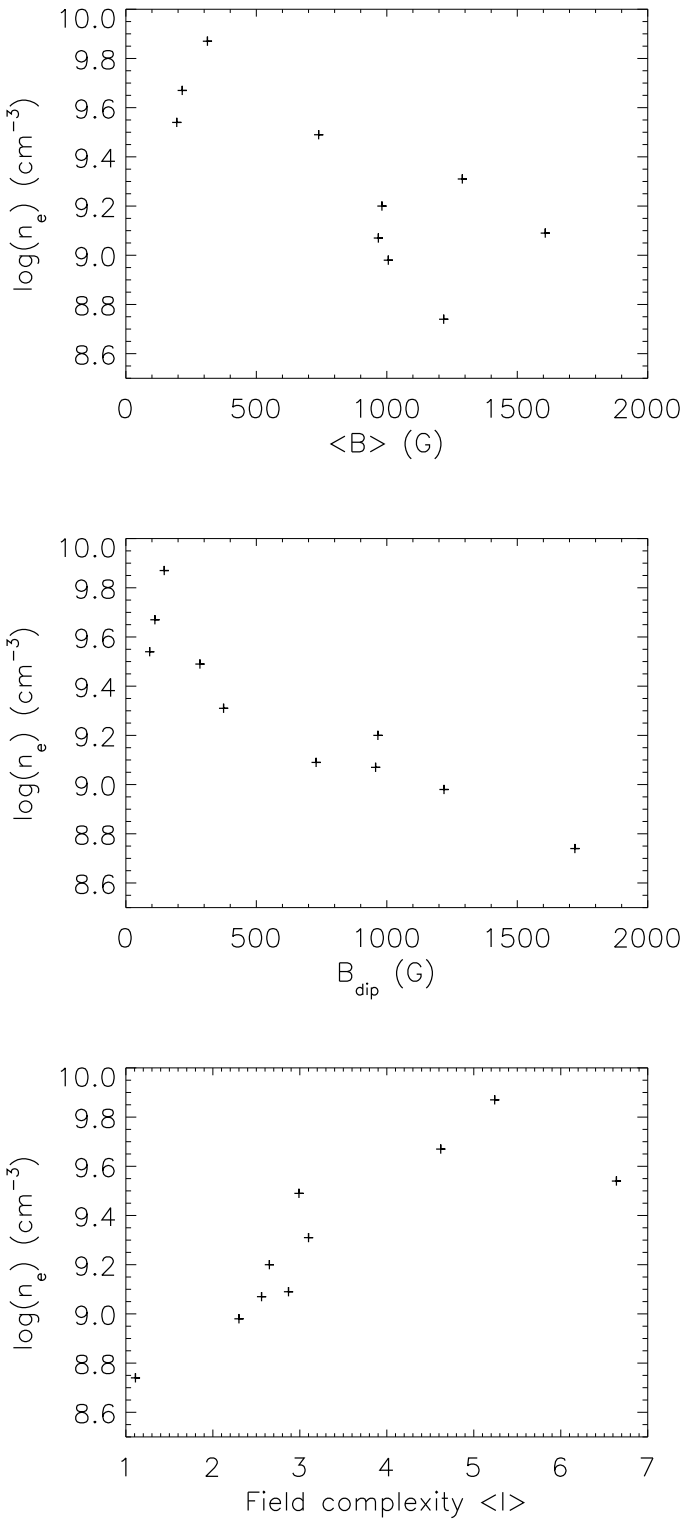

Figure 4.16: *Upper panel*: correlation between emission measure weighted average electron density and surface averaged field strength. *Middle panel*: correlation between emission measure weighted average electron density and the strength of the dipole component of the field. *Lower panel*: correlation between emission measure weighted average electron density and field complexity.

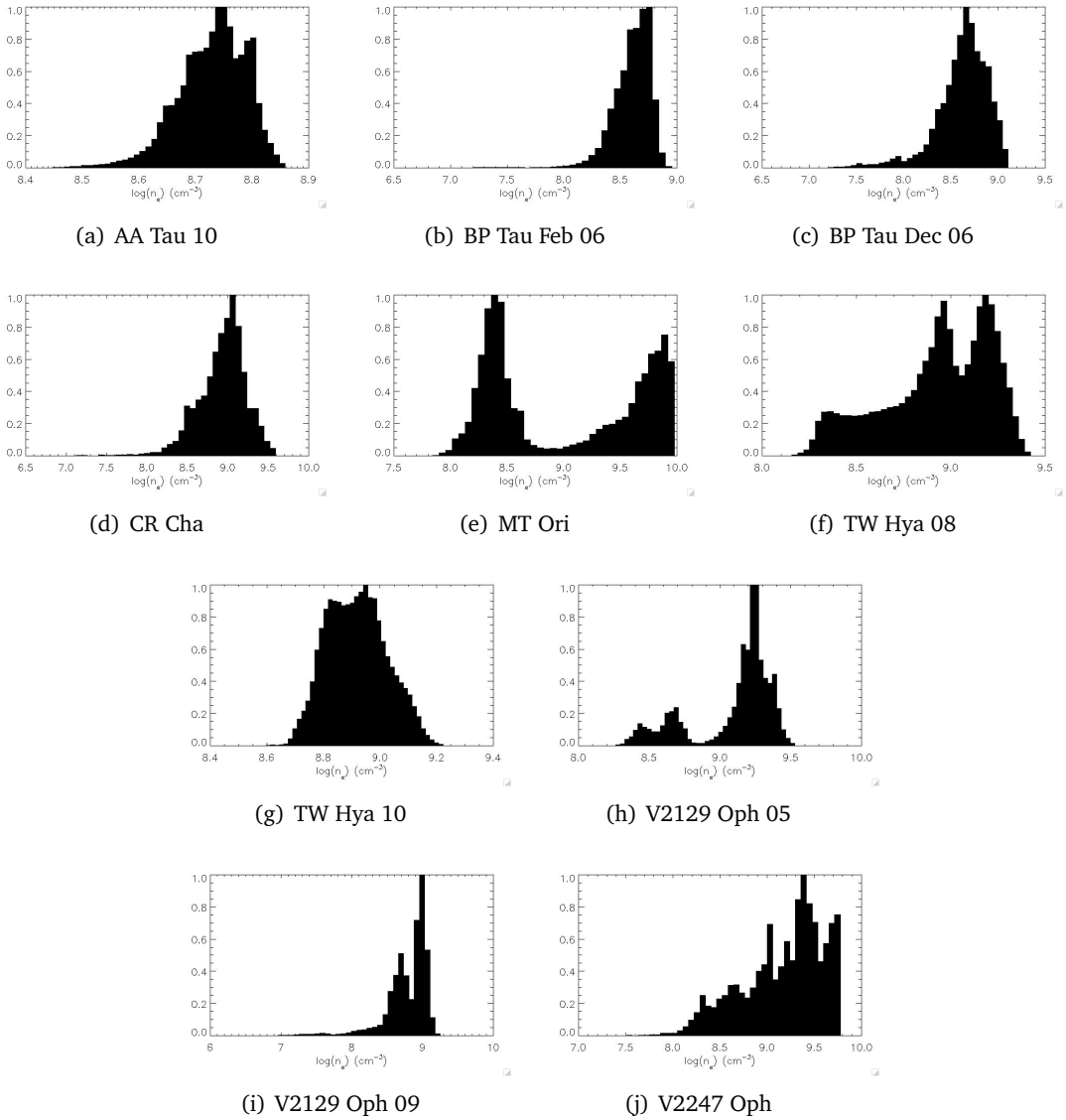

(a) AA Tau 10 (b) BP Tau Feb 06 (c) BP Tau Dec 06

(d) CR Cha (e) MT Ori (f) TW Hya 08

(g) TW Hya 10 (h) V2129 Oph 05

(i) V2129 Oph 09 (j) V2247 Oph

Figure 4.17: Histograms showing the number of grid elements in the coronal volume at specific electron densities for each of the fields considered here. MT Ori and V2129 Oph both show bimodal distributions in electron density.

Tau is that Johns-Krull (2007) takes a literature value for the star's X-ray luminosity that is significantly smaller than the value used here (AA Tau is well known to be highly variable in X-rays, as discusses in Section 4.1.1). The discrepancy for the case of BP Tau is for a similar reason.

Predicted emission measure weighted average electron densities for each of the stars are given in Table 4.4. The results show an order of magnitude variation between the stars in the sample, with values of the logarithmic electron density, $\bar{n}_e$, between $10^{8.7}$ and $10^{9.7}$ cm^{-3}. For each star, the distributions of electron densities throughout the closed corona are shown in

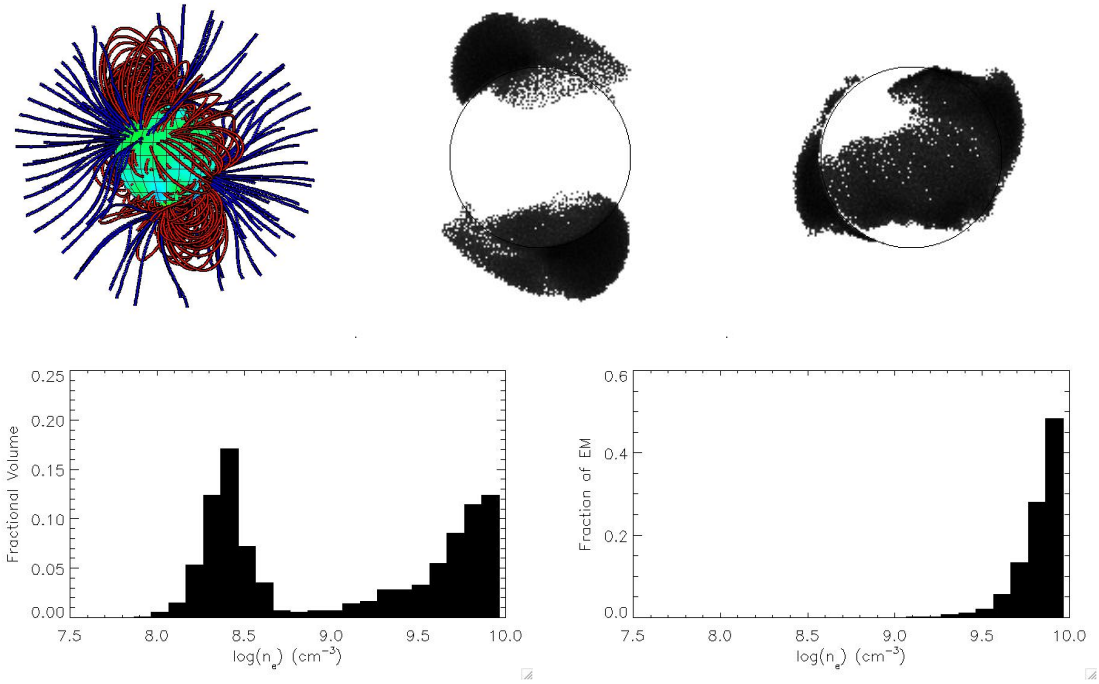

Figure 4.18: *Upper left*: structure of MT Ori's magnetic field with closed field lines in red and open field lines in blue. *Upper middle*: structure of MT Ori's high density corona. *Upper right*: structure of MT Ori's low density corona. *Lower left*: volume of corona at various densities. *Lower right*: contribution to total emission measure from regions of corona at various densities.

Fig. 4.17. Variations of more than an order of magnitude in the electron densities are present in all of the stars. However, as is shown below for the case of MT Ori, the low density coronal regions do not contribute to the X-ray emission significantly.

Given that in the coronal plasma model used here, the plasma pressures at the base of the corona are scaled with the magnetic pressure ($p_0 = KB_0^2$), one might expect that the stars with the strongest fields will have the highest electron densities. However, the opposite correlation can be seen in Fig. 4.16, with the highest electron densities being on the stars with weak complex fields. This is probably due to the fact that the strong fields are also simpler, such that their coronae extend further from the star. As electron density drops off with radius inside the corotation radius, the more extended coronae will have regions of low density far from the star, and thus a lower average electron density.

One of the most surprising results related to the coronal density is shown in Fig. 4.17. This shows a bimodal distribution in electron densities for MT Ori. Fig. 4.18 shows the locations in MT Ori's corona of the high and low density plasma. These two components are separated into two distinct regions of the corona, with the high density plasma located above both of the star's poles, and the low density plasma located at mid latitudes. This is due

to the assumption that the coronal gas pressure at the base of the corona is proportional to the magnetic pressure, so that regions of the surface that contain strong field will be below volumes of high density plasma. The ZDI magnetogram for MT Ori shows strong field at the poles and weak field near the equator. The switch between the strong polar field and the weak equatorial field is very sudden, thus leading to two distinct coronal density components. The bar charts presented in Fig. 4.18 show that a while the low density component of MT Ori's corona occupies approximately the same volume as the high density component, it is the high density component that dominates the X-ray emission. This is unsurprising given that the high density component is more than an order of magnitude more dense than the low density component. This result may be due to missing small scale flux in the ZDI magnetograms at mid latitudes. If the star's actual magnetic field consists of moderate polar flux and a large number of strong mid-latitude bipolar active regions, due to their finite resolution, the ZDI magnetograms would be expected to show moderate polar fields, but only weak field in the equatorial active belts (see Fig. 3.5 and Fig. 3.13).

4.4 Discussion

In recent years, ZDI magnetograms have become available for ten CTTSs. In this chapter, I analyse the poloidal components of the surface magnetic fields and model the coronae of most of the stars in the sample. In this section, I summarise the results.

- The magnetic fields of CTTSs vary in both strength and complexity, with some stars having very simple strong kG fields, and others having much weaker complex fields. The complexity of a magnetic field is a strong function of the star's rotation rate, with quickly rotating stars hosting highly complex fields, and slowly-rotating stars hosting significantly simpler fields. This could be a resolution effect as the resolution of the ZDI technique is strongly dependent on rotation rate. However, this interpretation is contradicted by the fact that the slower rotators also have stronger fields. Alternatively, the field complexity correlation with rotation rate could be a result of star-disc interactions. Stars with stronger fields might be expected to be slower rotators due to better coupling with their discs outside of the corotation radius. If the correlation between field complexity and rotation rate is a resolution effect, this could explain the simultaneous correlation between rotation rate and field strength. It would also imply that the correlation between field strength and complexity is only a result of disc-locking. Alter-

natively, if there is a correlation between field strength and complexity, then disc-locking could cause the correlation between complexity and rotation rate. An alternative cause for these correlations might be related to the contraction and evolution of the internal structure of pre-main sequence stars. As pre-main sequence stars contract, they spin up, and as they age, they develop radiative cores which is thought to lead to much weaker, more complex fields. Thus, the complexity-rotation correlation could be a secondary correlation, due to the fact that rotation rate and field complexity are both correlated with the evolution of pre-main sequence stars.

- The levels of X-ray emission in the sample are typical for CTTSs, with luminosities of around $10^{30} - 10^{32}$ ergs s^{-1}, and emission measures of 10^{53}-10^{55} cm^{-3}. Most of the stars in the sample have luminosities and emission measures on the low end of this range, with MT Ori being a large outlier due probably to its large radius and thus large surface area and magnetic flux. In all cases, it is possible to account for the large X-ray emission measures using magnetically confined coronae. The magnetic flux found in ZDI magnetograms is sufficient to confine enough plasma to give the observed emission measures and it is not necessary to invoke missing small scale magnetic flux in the magnetograms.

- The magnetic fields are able to hold onto the coronae of stars in the sample out to several stellar radii. The most important factor in determining the size of the closed corona is the complexity of the magnetic field. Simple dipole fields are able to dominate the coronal plasma pressure much further from the star than more complex fields. This is due to a difference in the rate at which the fields decrease in strength with increasing distance from the star.

- Typical logarithmic emission measure weighted average electron densities of between $10^{8.8}$ and 10^{10} cm^{-3} are present in the coronae of CTTSs. Despite the fact that the coronal plasma model used here assumes that the electron density at the base of the corona is proportional to the magnetic pressure, there is a negative correlation between electron density and surface magnetic field strength. This is consistent with the results of Jardine et al. (2006), who applied the same coronal plasma model to the set of X-ray emitting stars observed as part of the COUP project. They found that when they assumed a dipole field geometry, their calculated densities were an order of magnitude below the

values they obtained when they assumed complex field geometries. The closed coronae of MT Ori and V2129 Oph show bimodal distributions of electron densities. For MT Ori, the high density component is at high latitudes, and the low density component is closer to the equator. Although the two density components are comparable in volume, the high density component dominates over the low density component in X-ray coronal emission.

- The open magnetic flux is determined entirely by the strength of the dipole component of the field, and the stellar surface area. Stars with stronger dipoles and larger surface areas have larger open magnetic fluxes. The locations of open and closed field structures are a strong function of field complexity, with regions of open flux covering the magnetic poles on all stars. Simple axisymmetric dipole fields such as the one seen on AA Tau have regions of open flux predominantly at high latitudes, with all low latitude field structures being closed, and regions of open flux covering 10-20% of the stellar surface. More complex fields, such as those seen on MT Ori and V2247 Oph show open flux distributed over all latitudes, covering $\approx$ 20% of the stellar surface. Fields that are dominated by large scale octupole components, such as TW Hya and V2129 Oph, tend to have regions of open flux at mid-latitudes extending in bands around the star, with only 5-10% of the stellar surface covered in regions of open field.

Although there is still only a small number of stars in the sample, it is interesting to try to interpret these results in terms of the evolution of stars on the pre-main sequence. The main exception to the following interpretation is V2247 Oph, which due to its low mass is unlikely to develop a radiative core as it ages. Pre-main sequence stars are initially fully convective, and as they age, they develop radiative cores. When fully convective, they host strong fields with simple structures. As they develop radiative cores, the fields become weaker and significantly more complex. This should correspond to a decrease in the size of the coronae, with fully convective stars having large extended coronae and more evolved stars having much more compact coronae. Observationally, this might be seen as an increase in electron densities derived from X-ray emission lines formed primarily in hot coronal plasma (and not in accretion shocks). Since the level of open flux is primarily determined by the strength of the dipole component of the field and the stellar surface area, as pre-main sequence stars contract, and as they develop radiative cores, the rate at which angular momentum is lost due to stellar winds will decrease. This will also correspond to a change in the structure of these winds

as the latitudinal distributions of open flux is a strong function of field complexity. Fully convective stars will have winds originating from high latitudes, and more evolved stars will have winds originating from a range of latitudes.

5

Accretion onto classical T Tauri stars

In the previous chapter, I analyse the available ZDI magnetograms for the sample of CTTSs. I use potential field extrapolations to model the 3D coronal field and plasma structure for most of the stars in this sample. In this chapter, I use the same extrapolations to model magnetospheric accretion geometries onto these stars. In Section 5.1, I calculate the disc truncation radii; in Section 5.2, I use the disc truncation radii and the field extrapolations to predict the trajectories of accretion streams in all of these cases; in Section 5.3, I discuss some of the results in the context of the calculations from the previous chapter; and in Section 5.4, I give a summary of this chapter.

5.1 Disc truncation radii

In order to model accretion, it is necessary to know from where in the disc accretion can occur. I assume that accretion can occur along any field line that crosses the equator between the inner edge of the disc, r_{in}, and the outer radius at which accretion can occur, r_{out}. This means that it is necessary to estimate r_{in} and r_{out} for each of the CTTSs. One way of estimating the

radius at which accretion can occur is to calculate the radius at which the torque on the disc due to the magnetic field is balanced by the torque due to the internal disc viscosity. This is only an outer estimate of where accretion can occur as it is the radius at which the magnetic field can begin to disrupt the disc (Bessolaz et al. 2008). For this reason, I take r_{out} to be at this radius unless it is beyond the corotation radius, in which case I assume that it is at the corotation radius. The torque balance radius is where

$$B_\theta^2 r^2 = \frac{1}{2}\dot{M}_a \left(\frac{GM_*}{r}\right)^{\frac{1}{2}} \tag{5.1}$$

where I assume B_θ^2 is the value from the field extrapolations averaged over all longitudes in the equatorial plane.

I assume that the inner edge of the disc is approximately at the radius where the magnetic energy density balances the kinetic energy density of the disc. This is the Alfvén surface radius and should always be inside of the torque balance radius. Inside of this radius, the magnetic pressure dominates and the disc is not able to move inwards. If the Alfvén surface radius is outside of the corotation radius, then I assume that r_{in} is at 80% of the corotation radius. Elsner & Lamb (1977) gave the following expression (derived in Section 2.6.1) for the Alfvén surface radius

$$r_A = k\left(2GM_*\right)^{-\frac{1}{7}} \dot{M}_a^{-\frac{2}{7}} \mu_1^{\frac{4}{7}} \tag{5.2}$$

where $k \sim 0.5$ was estimated by Long et al. 2005 and accounts for the difference between spherical accretion and accretion from a disc. However, this expression only applies for a dipole field that is aligned with the stellar axis of rotation. In Section 2.6.1, I derive a similar expression for the case of arbitrary magnetic fields. The two pressures balance where

$$B^2 = C(GM_*)^{\frac{1}{2}} \dot{M}_a r^{-\frac{5}{2}} \tag{5.3}$$

where $C = 16$ is equivalent to $k = 0.5$ in Eqn. 5.2. In this expression, I assume B^2 is the value of B^2 averaged over all longitude in the equatorial plane.

In order to calculate r_{in} and r_{out}, Eqns. 5.1, 5.2, and 5.3 require mass accretion rates

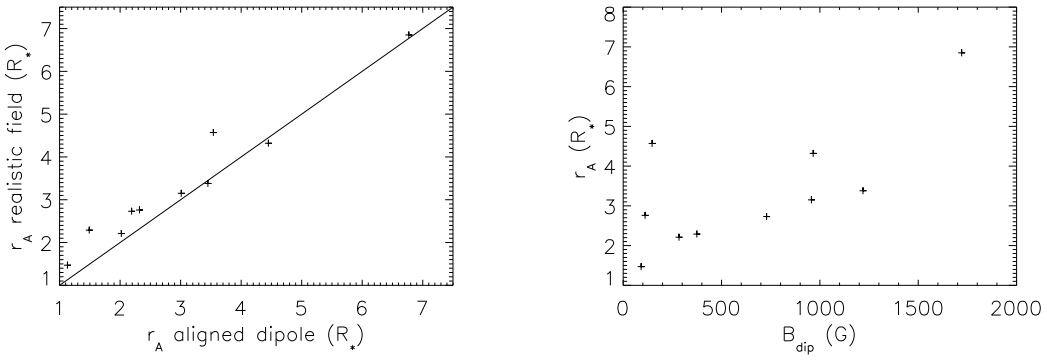

Figure 5.1: *Left panel*: Alfvén surface radius as calculated from Eqn. 5.3 and potential-field extrapolations of realistic fields against the value as calculated using Eqn. 5.2 which assumes that the field is a pure axisymmetric dipole. *Rght panel*: Alfvén surface radius against dipole field strength for the stars in the sample calculated using Eqn. 2.126.

for all of the stars which I take from the literature. These are given in Section 4.1. As most stars have several literature values, and the mass accretion rate is known to be highly time variable, where possible I take those that have been estimated based on the same observations from which the ZDI magnetograms are derived. These are given in Table 5.1, along with the estimated values of r_{in} and r_{out}.

For most of the stars, the Alfvén surface radius calculated using the Eqn. 5.2, which only takes into account the dipole component and assumes that it is axisymmetric, is lower than the values calculated using Eqn. 5.3. This is most significant for the case of the TW Hya 2008 field. The Alfvén surface radius determined using Eqn. 5.2 is 1.49 R_*, whereas using Eqn. 5.3, it is 2.29 R_*. This difference is partly due to the fact that the field is not a pure dipole but also has a strong octupole component. As the dipole and the octupole components are aligned, the effect of the octupole component is to move the Alfvén surface radius closer to the star. The fact that the Alfvén surface radius is further from the star than it would be if only the dipole component was considered is because of the large tilt ($\approx 45^\circ$) in the dipole component of the field. As I showed in Section 2.6.1, the tilting of the dipole component causes an increase in the field strength in the equatorial plane, and therefore a larger value for the Alfvén surface radius. Without this large tilt, the Alfvén surface radius would have had a value of 1.59 R_*, which is close to what would be expected if the field was a simple axisymmetric dipole. On the other hand, the octupole component does not cause the Alfvén surface radius to move further from the star. The differences in the two Alfvén surface radii calculated for the other fields can be explained in similar ways. For MT Ori, which has a dipole component that is tilted at 90° to the axis-of-rotation, the Alfvén surface is moved from 3.54 R_* to 4.57 R_*. The small

difference seen in the two Alfvén surface radii for the AA Tau field is due to both the tilt in the dipole component, and the anti-alignment of the dipole and octupole components increasing the field strength in the equatorial plane. Both the BP Tau February 2006 field, and the V2129 Oph 2009 field show Alfvén surface radii that are smaller than would be expected if the field was simply a dipole. This is due to the dipole and the octupole components being aligned, and thus adding up destructively in the equatorial plane, causing the Alfvén surface radii to move closer to the star. This dominates the effects of the small tilts in the dipole components.

One thing that can be seen from the results is the dependence of the Alfvén surface radius on the strength of the dipole component. The stars with the weakest dipole components, such as CR Cha, CV Cha, MT Ori, and V2247 Oph are also the stars with the smallest Alfvén radii.

Star	$\log \dot{M}_{acc}$ ($M_\odot$ yr^{-1})	B_{dip} (G)	θ_{dip} (degrees)	R_{co} (R_*)	r_A (R_*) Eqn. 5.2	r_A (R_*) Eqn. 5.3	r_t (R_*) Eqn. 5.1	r_{in}	r_{out}	r_{corona} (R_*)
AA Tau 2009	-9.2	1720.7	174	7.62	6.77	6.85	18.10	6.85	7.62	4.58
BP Tau Feb 2006	-8.5	1219.1	11	6.04	3.45	3.38	9.11	3.38	6.04	3.76
BP Tau Dec 2006	-8.5	957.0	25	6.04	3.01	3.15	7.48	3.15	6.04	3.95
CR Cha	-9.0	91.2	180	3.63	1.13	1.47	3.09	1.47	3.09	2.19
CV Cha	-7.5	24.0	180	5.7	0.20	-	1.22	-	-	-
MT Ori	-9.1	147.0	93	2.95	3.54	4.57	3.58	2.36	2.95	2.30
TW Hya 2008	-8.9	374.4	42	8.30	1.49	2.29	4.15	2.29	4.15	3.25
TW Hya 2010	-8.9	729.1	6	8.30	2.19	2.73	6.15	2.73	6.15	3.76
V2129 Oph 2005	-9.2	283.8	24	8.13	2.02	2.21	5.05	2.21	5.05	2.42
V2129 Oph 2009	-9.2	965.9	13	8.13	4.45	4.32	11.64	4.32	8.13	3.25
V2247 Oph	-9.8	111.2	42	3.42	2.32	2.76	5.31	2.76	3.42	2.09

Table 5.1: Information about the set of stars in the sample and estimations for the Alfvén surface radii and the torque balance radii.

5.2 Accretion

For AA Tau, BP Tau (February and December), the V2129 Oph 2009 field, and V2247 Oph, the torque balance radii are found to be outside of the corotation radii, thus I assume that r_{out} for these stars is at the corotation radius. For MT Ori, because its dipole component is tilted 90° to the star's rotation axis, the torque balance argument is not valid, and gives a value of r_{out} which is less than r_{in}. For MT Ori, I also take r_{out} to be at the corotation radius. For MT Ori, because it has a relatively strong dipole, and a small corotation radius, the value of r_{in} calculated using the pressure balance equation is outside of the corotation radius. Thus, for this star, I assume that r_{in} is 80% of the corotation radius. For CV Cha, the strength of the dipole component is so small that at no point outside of the star is the magnetic energy density balanced by the disc kinetic energy density, so this star is not considered in this section.

Using the estimates for r_{in} and r_{out}, I then trace field lines from every point in the disc between these two radii to the stellar surface and assume that accretion occurs along these field lines in one direction. The direction that accreting material leaves the disc is assumed to be the direction along the field line that is pointing inwards (e.g. if the radial component of the field at the point where the field line crosses the disc is positive, I assume that material accretes towards the positive polarity end of the field line) as this is the direction along the field line in which gravity points. Fig. 5.2 shows the locations of the predicted accretion footpoints for each of the stars in the sample. These locations are clearly highly dependent on magnetic field structure.

For the most dipolar fields, such as the AA Tau field, the two BP Tau fields, and the V2129 Oph 2009 field, the accretion footpoints are all at high latitudes. These are also the fields with the lowest values of the complexity parameter $< l >$. This is largely because the simple fields also have the strongest dipole components, and so have large disc truncation radii. Also, as the dipole components dominate close to the inner edge of the disc, accretion can be expected to take place along large dipolar field lines that connect with the stellar surface at high latitudes. The accreting field lines for AA Tau are shown in Fig. 5.3.

The two TW Hya fields are dominated by several kG strong octupole components and relatively weak dipole components. These fields have mid-latitude bands covered in regions of opposite polarity field, and thus their coronal field structures are dominated by field lines connecting these mid latitude bands close to the stellar surface, and large dipole field lines

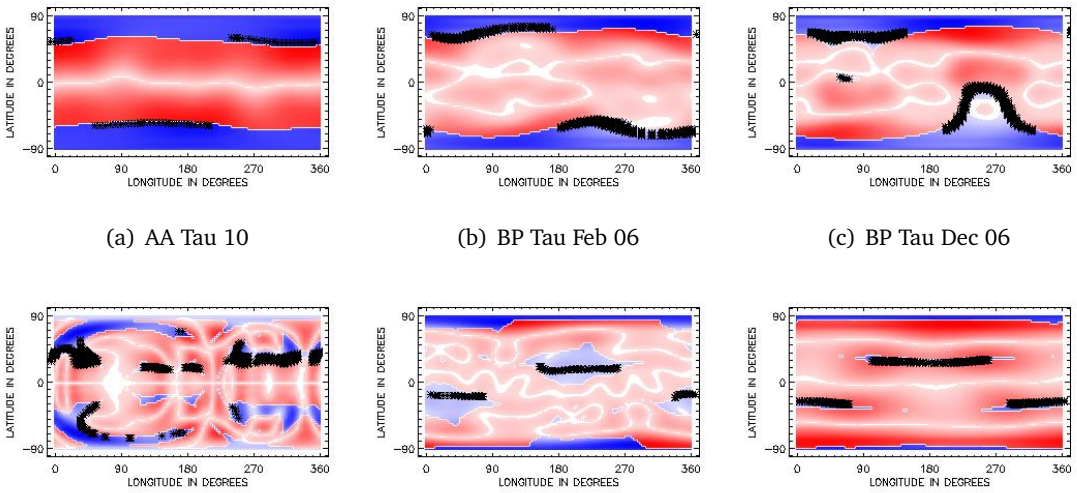

(a) AA Tau 10 (b) BP Tau Feb 06 (c) BP Tau Dec 06

(d) CR Cha (e) MT Ori (f) TW Hya 08

(g) TW Hya 10 (h) V2129 Oph 05

(i) V2129 Oph 09 (j) V2247 Oph

Figure 5.2: Magnetograms for most of the stars in the sample showing the predicted locations of open magnetic field (blue) and closed magnetic field (red). The predicted locations of accretion footpoints are shown in black.

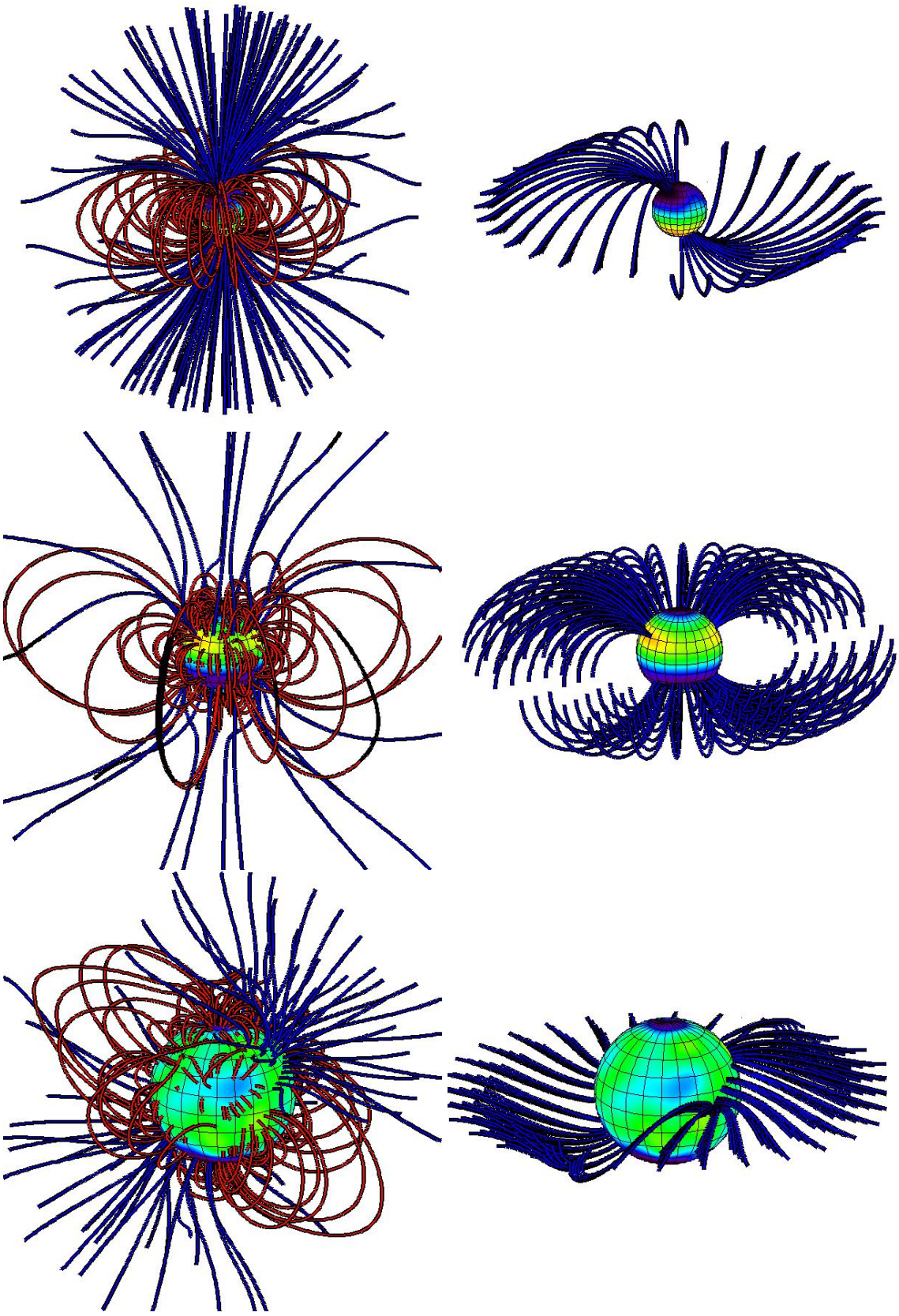

Figure 5.3: Potential field extrapolations for AA Tau (upper panels), the TW Hya 2010 field (middle panels), and the V2247 Oph field (lower panels) showing closed and open field lines (left) and accreting field lines (right).

connecting the two poles far from the surface. Since for both these fields the octupole component is significantly stronger than the dipole component at the stellar surface, the octupole component is able to dominate the field structure out to the inner edge of the disc, thus causing accretion to take place along octupolar field lines that connect with the stellar surface at mid-latitudes. The accreting field lines for the TW Hya 2010 field are shown in Fig. 5.3.

For the most complex fields, accretion impacts the surface at low latitudes and is distributed over the stellar surface in a much more complex pattern. This is especially true for CR Cha and V2247 Oph, both of which have highly complex fields. The field structure for the V2247 Oph field is shown in Fig. 5.3. As V2247 Oph has a weak dipole component, its disc is truncated close to the stellar surface despite its low mass accretion rate. Thus, the field is highly non-dipolar at the inner edge of the disc and accretion occurs along field lines that connect with the stellar surface at low latitudes and in a complex pattern.

The case of MT Ori is an interesting one. MT Ori has a highly complex field structure with a weak ($\sim$150 G) dipole component that is tilted 90° to the axis-of-rotation, such that the magnetic poles of the dipole component are at the equator. The two poles appear to approximately coincide with small regions of open magnetic field and active accretion.

5.3 Disc and coronal truncation radii

It is interesting to compare the Alfvén radii and the torque balance radii calculated in this chapter with the maximum radii that the stellar magnetic field can hold onto the closed corona calculated in Chapter 4. These are shown in Fig. 5.4. The stars are ordered from top to bottom by decreasing strength of the dipole component of the field and it can clearly be seen that as the dipole component weakens in strength, all of these radii move towards the star. Therefore, stars with strong dipole components have highly extended coronae, and discs that are truncated much further from the star. Stars with weak dipole components have very small coronae, and discs that are truncated much closer to the star.

Studies of magnetospheric accretion generally assume that the closed corona extends out to the inner edge of the accretion disc (upper panel of Fig. 5.5). Safier (1998) considered this assumption and argued that it is unlikely to be valid, having found that the closed corona is unlikely to extent further than $\lesssim 3\ R_*$, and as discs that are truncated several stellar radii from the surface they are likely to be embedded in regions of open field. However, Safier (1998)

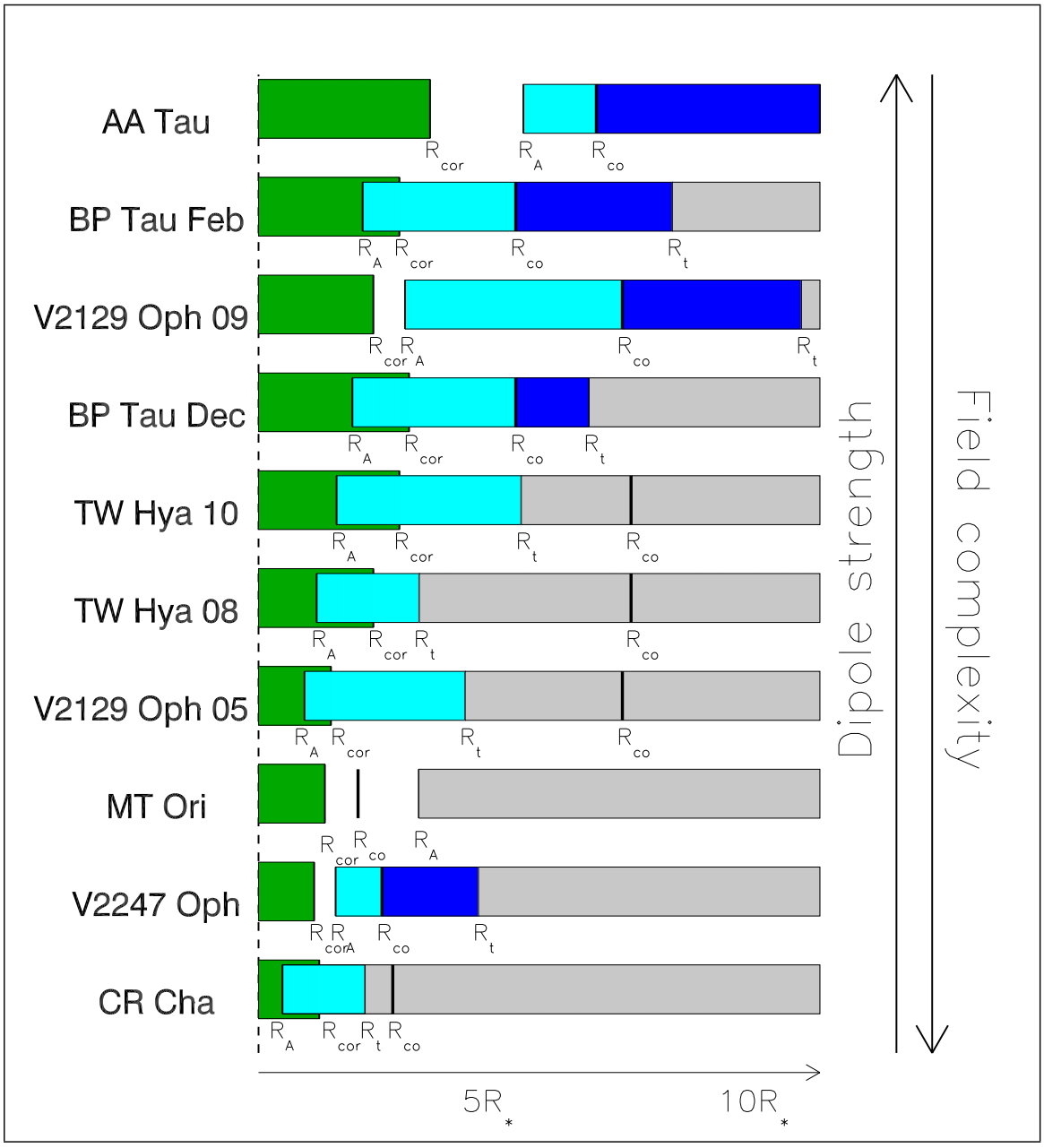

Figure 5.4: Cartoon showing, for most of the stars in the sample, the coronal extents and the disc truncation radii. The stars are ordered from top to bottom by decreasing strength of the dipole component of the field. The horizontal direction is measured in stellar radii from the stellar surface, marked by the dashed line, to approximately 12 R_*, with the torque balance radius for AA Tau lying off to the right of the plot at approximately 18 R_*. The extent of the closed corona is shown in green with the maximum radii to which the magnetic field can hold onto the closed corona defined as R_{cor}. For each star, the light blue bar shows the range of radii from which accretion can occur onto the star. This is between the inner edge of the disc, set to the Alfvén surface radius, and the torque balance radius, unless this lies outside the corotation radius, in which case it is taken as the corotation radius. For each star, the dark blue bar shows the range of radii that the magnetic field can disturb the disc outside the corotation radius. As the dipole component weakens, the outer edge of the corona and the inner edge of the disc moves inwards.

assumed that the stars magnetic field structure is dominated by small scale surface bipoles, and did not consider the effects that strong large scale dipoles and octupoles might have on the extent of the closed corona. More recent studies of CTTSs using the ZDI technique have shown that they possess strong dipole and octupole field structures which are able to hold onto the closed corona further out than small scale surface dipoles.

One result that can be seen in Fig. 5.2 is that in most cases, the predicted locations of accretion footpoints generally coincide with predicted regions of open field. This is because field lines that can support accretion tend to extend far from the stellar surface, so are also the most susceptible to being blown open by coronal plasma. Similarly, for some of the stars, the extent of the closed corona, as calculated in Chapter 4, is less than the Alfvén surface radius. This implies that for some of the stars, the closed coronae do not extent out to the inner edge of the disc. For stars where the disc truncation radius is outside the furthest radius at which the magnetic field can hold onto the closed corona (AA Tau; MT Ori; V2129 Oph 2009; V2247 Oph), the field lines that support accretion must all connect to the surface in regions of open field. Even for stars with closed coronae that extend out past the inner edge of the disc, accretion footpoints mostly lie in regions of open field.

For AA Tau, the corona appears to be truncated at $\sim$5 R_*, whereas the inner edge of the disc is truncated at $\sim$7 R_*. Similarly, the V2129 Oph 2009 field, and the V2247 Oph field show coronal truncation radii inside of the disc truncation radii. This raises an interesting question: what happens in the case where the coronal plasma pressure dominates over magnetic pressure at a distance from the star well inside the inner edge of the disc? Here, I propose three possible scenarios.

1. The disc is truncated well outside of the outer edge of the closed corona and is thus embedded in regions of radial magnetic field. The disc is still disrupted approximately at the Alfvén surface and disc material initially freefalls along radial magnetic field lines and is not lifted out of the equatorial plane until it reaches the outer edge of the closed corona.

2. The inner edge of the disc moves inwards along the open field lines until it reaches the outer edge of the closed corona. At this point, the disc material accretes along closed field lines in the usual way.

3. The field lines connecting the stellar surface with the inner edge of the circumstellar

disc are never blown open by the thermal pressure of closed coronal plasma as they only contain cold accreting material.

Another feature of the disc truncation radii results compared to the coronal truncation radii results is the fact that some of the coronae seem to extend past the inner edge of the disc. This may be physically unrealistic, as the inner edge of the disc might be expected to truncate the corona (Jardine et al. 2006; Getman et al. 2008b). However, as all of the coronae are truncated inside of the corotation radius, this may have little effect on the X-ray emission measures as the coronal emission will be dominated by plasma closer to the star, and thus the validity of the results is not affected.

5.4 Discussion

In this chapter, I predict the disc truncation radii and the trajectories of accreting material for most of the CTTSs in the sample. In this section, I summarise the results.

- Assuming that the inner-edges of circumstellar discs are truncated at the Alfvén radius, CTTS discs are typically truncated several stellar radii from the stellar surface. In most cases, the truncation radius is inside the corotation radius, allowing accretion to take place onto the star. The location of the Alfvén surface radius is not simply a function of the strength of large scale dipole component of the star's magnetic field, but also can be affected strongly by the tilt in the large scale dipole and the presence of an octupole component. For instance, the Alfvén radius for TW Hya is pushed further from the star by the tilt in the large scale dipole of $\sim 45^{\circ}$. The Alfvén surface radius for the BP Tau February 2006 field is closer to the star than would be expected if the field was a pure dipole due to the presence of the octupole component.

- The radius at which the torque exerted on the disc balances the torque due to viscosity is always outside of the Alfvén surface radius. In the case of MT Ori, where the dipole is tilted perpendicular to the star's axis-of-rotation, the method used for determining the torque balance radius is not valid. In several cases, especially for the two fully convective stars AA Tau and BP Tau, the torque balance radius is outside the corotation radius.

- The trajectories of accreting material, and the predicted locations of accretion footpoints

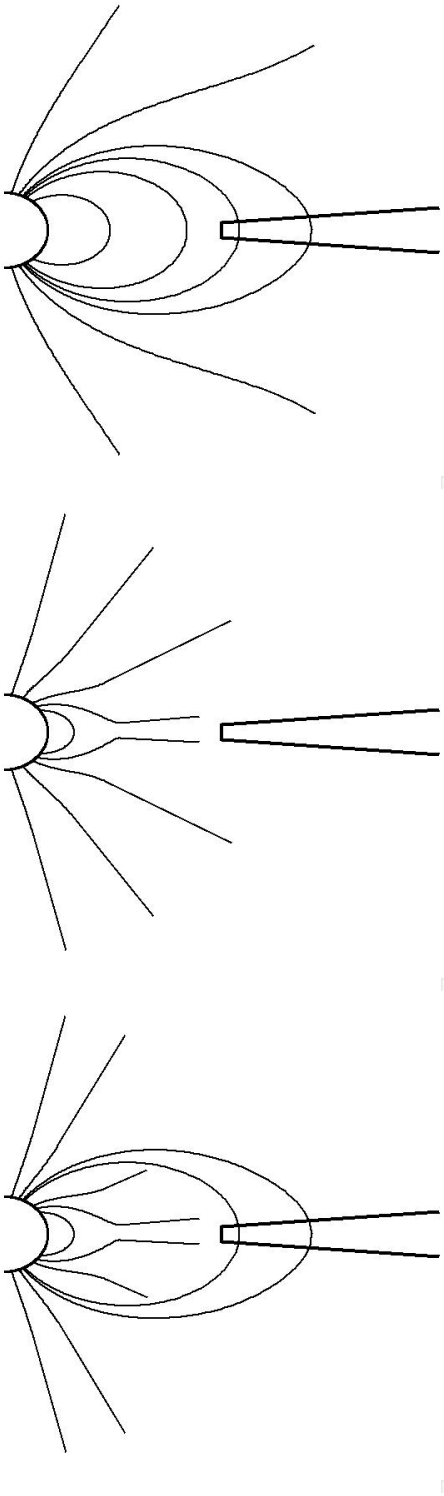

Figure 5.5: Cartoon showing different magnetic field configurations illustrating the possible situations described in the text. In the upper panel, the closed magnetic field extends all the way to the inner edge of the circumstellar disc. In the middle panel, the closed coronal plasma forces the field to become radial well inside the inner edge of the disc, such that the disc is embedded in open field. In the lower panel, the closed coronal plasma forces the field to become radial well inside the inner edge of the disc; however, field lines that connect the star to the disc are not forced open as they do not contain hot coronal plasma. This situation is possible if the system is not axisymmetric, allowing the open field lines to avoid crossing the closed field lines.

are strongly dependent on the complexity of the stars magnetic field. When the field is a simple dipole, accreting material falls along large dipolar magnetic loops and impacts the surface at high latitudes. Whereas, for more complex fields, accretion impacts the surface at a range of latitudes. The simplest fields tend also to be the strongest fields and have the strongest dipole components. This means that they have large disc truncation radii, allowing the inner edge of the disc to be threaded by dipolar field lines that exist further from the star and connect to the stellar surface at high latitudes. On the other hand, the complex fields tend to be relatively weak, which means that they truncate the discs at smaller radii, thus allowing them to be threaded by the more complex non-dipolar field lines that exist closer to the star and connect to the surface at a range of latitudes and in complex patterns.

- In some of the cases, it appears that the magnetic field is not able to hold onto the corona out to the inner edge of the disc. This means that the general assumption that the magnetic field structure is closed out to the inner edge of the star's accretion disc may not be justified in these cases.

6

Eclipsing of stellar flares

6.1 Introduction

Stellar flares are generally regarded as the stellar analogues of solar flares and their X-ray emission often only differs from their solar counterparts in magnitude and duration. Stellar flare peak temperatures and emission measures can be orders of magnitude greater than what is seen on the Sun. The durations of the longest lived stellar flares significantly exceed the longest durations seen in solar flares. For a detailed comparison between solar and stellar flares, see Aschwanden et al. (2008). They also differ in the fact that stellar flares are spatially unresolved, whereas this is only the case in the smallest of flare events on the Sun. Thus, it is not possible to observe directly where on its host star a flare is located, or whether parts of the flare are eclipsed by the host star. While the durations of all solar flares are very much less than the solar rotation period, this is not the case with most stellar flares. As a result, the likelihood that a stellar flare undergoes a rotational eclipse is much greater than that for solar flares. It is therefore natural to expect that although solar and stellar flares are probably

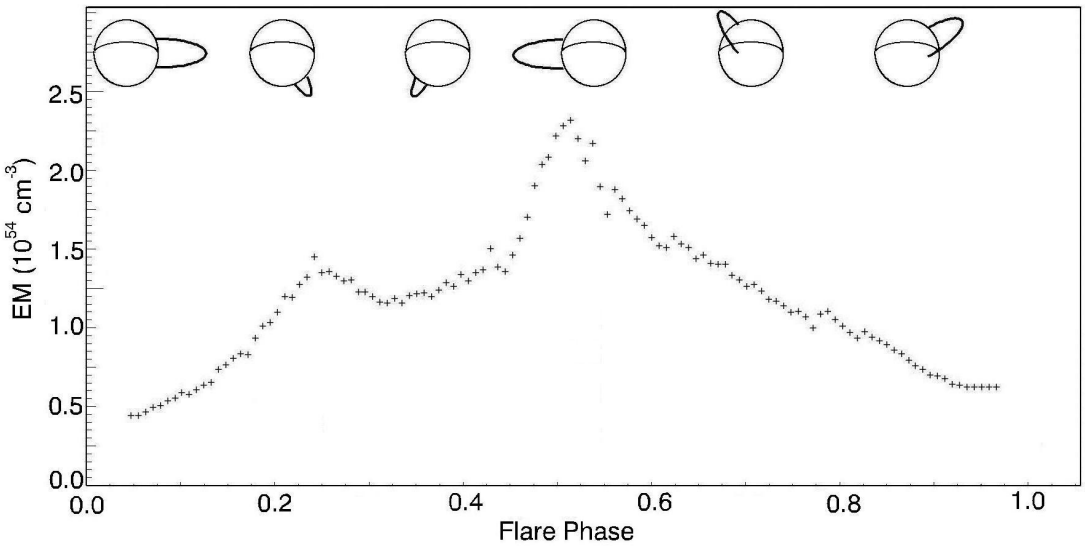

Figure 6.1: Example flare showing how eclipsing can cause an atypical flare morphology. The flare is assumed to be contained within a single magnetic loop with a uniform plasma density. The example emission measure curve is the flare on COUP source 649 given in Fig. 6.9. The images at the top show the position of the single magnetic loop containing the flaring plasma, the geometry of which has been determined from the best fit emission measure curve given in Fig. 6.9. Flare phase 0.0 and 1.0 represent the beginning and end of the flare respectively.

produced by similar processes, their observational signatures may differ.

For a review of the physical mechanisms in stellar flares, see Benz & Güdel (2010). A significant departure from a potential field configuration in a coronal magnetic field corresponds to a large amount of excess energy being held in that field. When reconnection events occur, the coronal magnetic field geometry is simplified (i.e. becomes closer to a potential field configuration) and the resulting field holds less magnetic energy. In this process, a large amount of the excess energy is converted into the non-thermal motions of electrons and ions which spiral down magnetic field lines and impact the stellar chromosphere. This can be seen at radio wavelengths as the charged particles emit gyrosychrotron radiation. As the energetic electrons impact the chromosphere, they emit non-thermal Bremsstrahlung radiation at hard X-ray wavelengths, as they become thermalised by random Coulomb interactions. This model is known as the “thick-target model" (Neupert 1968; Brown 1971; Lin & Hudson 1976). This causes chromospheric plasma to be heated and evaporated into the corona where it is contained within magnetic loop structures. Through a combination of mostly radiative losses and heat conduction back to the photosphere, the evaporated plasma cools (Antiochos & Sturrock 1978).

In this chapter, I consider the morphologies of the soft X-ray lightcurves of spatially unresolved stellar flares. In the majority of cases, the morphologies of typical flares can be broken down into two distinct phases. The first phase consists of a rapid increase in luminosity due to the heating and evaporation of chromospheric plasma. This is followed by a slow exponential decay due to cooling. However, a large number of stellar flares show more complex atypical morphologies (Getman et al. 2008a). Among these atypical morphologies are flares with longer rise phases and no clear peak and flares with multiple peaks or dips in their lightcurves. The interpretation of these events is important because large flares, especially on young pre-main sequence stars, can provide information about the extent of X-ray coronae (see for example, Mullan et al. 2006 and Getman et al. 2008b). Ionization by large X-ray flares can significantly influence the chemistry and turbulence (via the magneto-rotational instability) of circumstellar discs, which can have profound effects on accretion, dust settling, protoplanet migration and other physical processes (Ilgner & Nelson 2006, Feigelson et al. 2010)

Several interpretations of multiple peaked flares, often based on solar analogies, have been proposed. For example, Reale et al. (2004) observed an X-ray flare on Proxima Centauri that showed two distinct peaks in its lightcurve. They concluded that the second peak was probably produced through a similar event in a second loop system. Similarly, López-Santiago et al. (2010) reported the observation, by XMM-Newton, of the unusually long ($\sim$36ks) rise phase of a flare on a young star in the TW Hya association. They interpreted this rise phase as being a result of the superposition of multiple flares in separate loop systems. This interpretation of stellar flares with similar morphologies is common in the literature (see for example Pillitteri et al. 2005, Pandey & Singh 2008).

In this chapter, I consider an interesting geometric alternative to the explanations given above. In this alternative, atypical flare morphologies are not the result of multiple flare events, but are the result of the time variable eclipsing of the flaring coronal plasma caused by the rotation of the host star. Previous studies have used this interpretation to explain the morphologies of stellar flares using eclipsing by the flares' host stars (Skinner et al. 1997, Stelzer et al. 1999) or by a companion star in eclipsing binary systems (Schmitt & Favata 1999, Schmitt et al. 2003, Sanz-Forcada et al. 2006, Sanz-Forcada et al. 2007). In this chapter, I explore the eclipsing interpretation within the framework of a single loop model. Based on the solar analogy, it has recently been argued that it is unlikely that the large stellar flares

considered here take place within a single magnetic loop (Getman et al. 2011). However, the single loop assumption is often taken as a good approximation in situations where there is a single dominant loop within a complex loop system.

The way in which eclipsing can produce flares with atypical morphologies can be seen in the following hypothetical situation, shown in Fig. 6.1, in which a flare appears to show a double peaked morphology. In this example, the beginning of the rise phase (flare phase equal to 0.0) occurs when the flaring magnetic loop is on the limb of the stellar disc. Initially, as chromospheric plasma is evaporated into the corona, the visible emission measure increases. However, as the star rotates, flaring plasma is rotated out of view, resulting in a shallower rise from phases 0.0 to 0.25. As the rate at which flaring plasma is eclipsed becomes equal to and then exceeds the rate at which plasma is added to the corona, an initial peak is seen (flare phase equal to 0.23) followed by a gradual decay in the visible emission measure. However, the host star is at an inclination angle such that the flaring loop is never totally eclipsed. The flare's rise phase ends at flare phase equal to 0.3 and the decay phase begins. This, however, is not seen in the visible emission measure curve. As the eclipsed section of the flaring magnetic loop begins to rotate back into view, a second increase in the visible emission measure is seen. As the rate at which the flare's total emission measure decreases, equals, and then exceeds the rate at which eclipsed plasma is rotated back into view, a second peak followed by a second decay phase is seen in the flare's emission measure curve. Three observed eclipse candidate flares are shown in Fig. 6.2.

Although individual stellar flares have been studied in detail, in the last few years it has become possible to study large homogeneous samples of flares. One of the largest such study is the *Chandra* Orion-Ultradeep Project (COUP; Getman et al. 2005b). In 2003, the *Chandra X-Ray Observatory* provided 13 days of near-continuous observations of the members of the Orion Nebula Cluster. Using these observations, Getman et al. (2005b) identified 1616 X-ray sources, of which ∼1400 were confirmed as members of the Orion star forming region and the majority of the rest being background quasars seen through the molecular cloud (Getman et al. 2005a). Using the COUP data, Getman et al. (2008a) reported the detection of 216 bright flares on 161 of these stars using the condition that a 'bright flare' is any event that has a peak count rate above four times the characteristic (quiescent) count rate for the host star. This sample consists of the longest, brightest, and hottest flares detected during the COUP mission. Getman et al. (2008a) derived emission measures, flare durations, flare loop

lengths (using the hydrodynamic models of Reale et al. 1997) and other parameters which will be used extensively in this chapter. Getman et al. (2008a) gave a classification scheme for these flares based on their observed lightcurves. *Typical flares* are simples flares with a single impulsive rise phase followed by a short exponential decay, and correspond to 84 flares in the sample. *Step flares* are flares that look like typical flares, but with bumps in their decay phase, and correspond to 38 flares in the sample. *Double flares* are flares that show what appears to be multiple rise phases, and correspond to 8 flares in the sample. *Slow rise, top flat flares* are flares that have much slower impulsive rise phases, and either long lasting peaks or very long decay phases and correspond to 20 flares in the sample. The rest of the flares are classified as *incomplete flares* and *other flares*.

In this chapter, I consider the eclipsing interpretation of atypical stellar flare morphologies. More specifically, I ask whether such morphologies can be produced through the eclipsing of typical flares and to what extent the atypical COUP flares are likely to have been produced in this way. In Section 6.2 I describe the simple flare model that is used throughout this chapter. In Section 6.3, I use three examples of COUP flares to show that a range of atypical flare morphologies can be explained by eclipsing and I attempt to derive information about the geometries of these flares. In Section 6.4, I consider the distribution of atypical COUP morphologies and compare it to a similar modelled set of flares. In Section 6.5, I consider the effect that eclipsing of flares can have on the determination of flare loop lengths. Finally, in Section 6.6, the main results and conclusions from the chapter are summarised.

6.2 Flare model

The flare model that I use in this section involves the following assumptions

- The flare's emission is the result of a single event consisting of a rapid rise phase followed by a slow exponential decay of the flare's emission measure with time. When modelling the variation of emission measures with time, I do not consider the physical mechanisms that are responsible for triggering the flare.

- The flaring plasma is completely contained within a single static magnetic loop that is corotating with the stellar surface and has a uniform plasma density along its entire length.

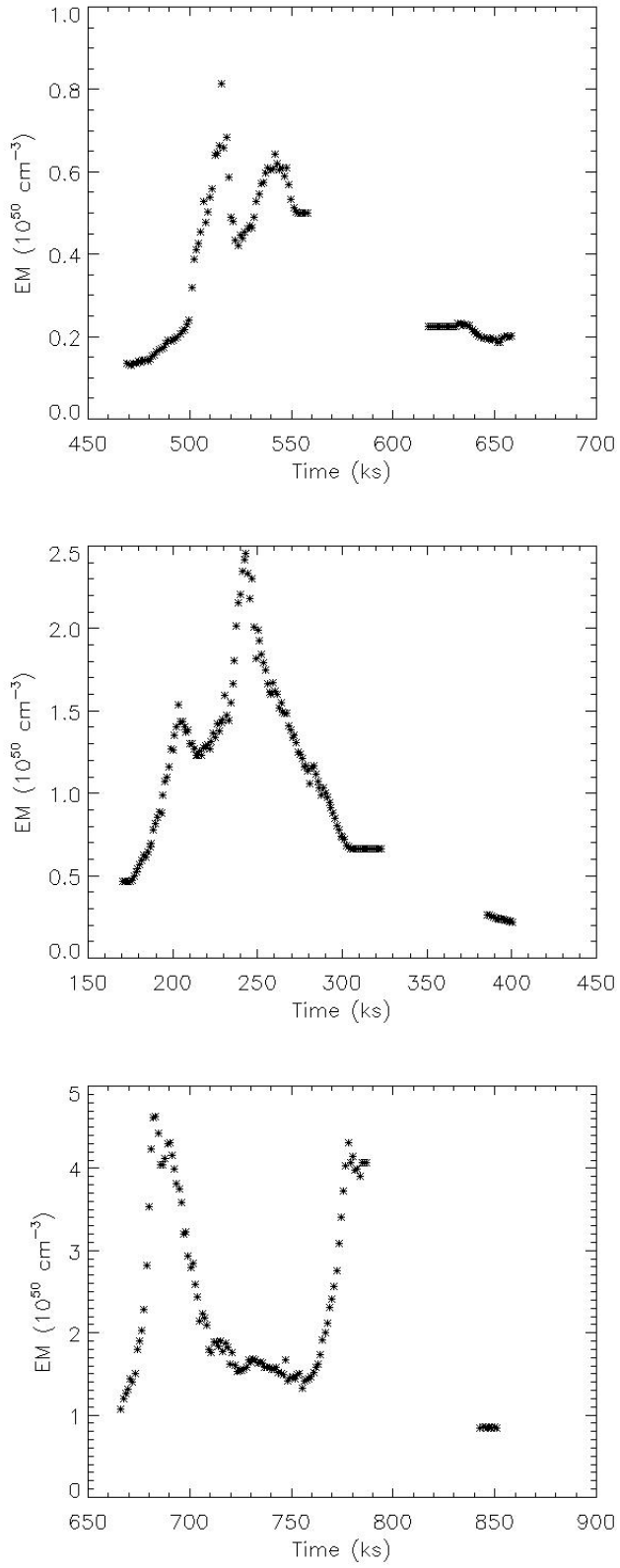

Figure 6.2: Emission measure vs time curves for three eclipse candidate COUP flares. The flares occurred on COUP sources 0066 (upper panel), 0649 (middle panel), and 0942 (lower panel).

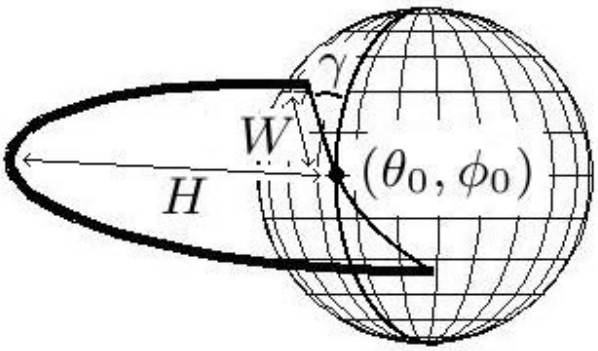

Figure 6.3: Example of an elliptical loop used to illustrate the parameters that define a flare's geometry. H is the loop height, W is the loop width, γ is the angle between the plane in which the loop is contained and the stellar rotation axis, and θ_0 and ϕ_0 are the latitude and longitude of the centre of the loop on the stellar surface.

- The geometry of the flaring loop is described by an ellipse with its centre located on, and its major axis perpendicular to, the stellar surface. The thickness of the flaring loop is assumed to be a negligible fraction of its length.

The first assumption, which is made throughout this chapter, means that any deviation from a simple flare lightcurve morphology in the modelled flares can only be a result of eclipsing of the flaring plasma.

The flaring loop geometry is characterized by the following five quantities: the height of the apex of the loop (i.e. the semi-major axis of the ellipse) (H), the width of the loop (i.e. the semi-minor axis of the ellipse) (W), the latitude and longitude of the centre of the ellipse (θ_0, ϕ_0), and the angle between the plane of the ellipse and the star's rotation axis (γ). These quantities can be seen in Fig. 6.3. It is worth emphasising that the term 'width' in this case refers to the length of the semi-minor axis of the ellipse and not the more common definition of the length between the two loop footpoints along the segment of the great circle that connects them. For the purposes of this model, the difference between these two definitions is not important. The other parameters that can determine the effects of eclipsing are the stellar inclination angle, the stellar rotation period, the flare's duration, and peak emission measure.

Under the assumption that the plasma density is uniform over the length of the flaring loop, the visible emission measure, $EM_{vis}(t)$, can be expressed as

$$EM_{vis}(t) = EM_{tot}(t)\left(\frac{V_{vis}(t)}{V_{tot}}\right) \tag{6.1}$$

where $EM_{tot}(t)$ is the flare emission measure curve that would be seen if the entire flaring loop is visible throughout the duration of the flare and $V_{vis}(t)/V_{tot}$ is the fraction of the volume of the flaring plasma that is visible at any given time t. The quantity $V_{vis}(t)/V_{tot}$ is calculated at each time t by considering a series of points equally spaced along the length of the flaring loop. Under the assumption that the loop thickness is small, the fraction of the flaring loop volume that is visible at this time is approximately equal to the fraction of these points that are visible. I give details of how to determine whether a point on a flaring loop is eclipsed or visible in Section 6.2.1. The methods used for chosing the function $EM_{tot}(t)$ is described in Paragraph 1 of Section 6.4.1.

The most obvious source of eclipsing of stellar flares comes from the host stars which I assume to be opaque spheres. However, other sources of eclipsing may be present. In pre-main sequence stars, these may be binary companions, circumstellar discs, accretion columns extending from a circumstellar disc to the stellar surface, planets at small radii, and flare associated prominences. In this chapter, the only sources of eclipsing that I consider are host stars, circumstellar discs, and flare associated prominences.

I model circumstellar discs as opaque discs with smooth inner edges located at the equatorial corotation radii ($R_{co} = \left(GM_*/\omega^2\right)^{1/3}$, where ω is the angular velocity of the stellar surface) of their host stars. The modelled discs are assumed to be flat and to lie in the equatorial plane. The possibility of more complex discs is not considered here although it should be noted that a warped circumstellar disc could have a significant effect on a flare's lightcurve, particularly if the stellar inclination is such that a warped inner disc periodically obscures the view to the star (e.g. Bouvier et al. 1999; Alencar et al. 2010).

I model prominences as opaque spheres that sit above the apex of flaring loops. Thus, a prominence is characterised by its height above the flaring loop and its radius. I take all prominences to be spheres of radius $0.5R_*$, the centres of which have heights above the apex of the flaring loops of $0.55R_*$. The prominences thus cover 25% of the stellar disc, which is similar to the estimated projected areas of prominences on AB Dor and Speedy Mic (Collier Cameron et al. 1990; Dunstone et al. 2006).

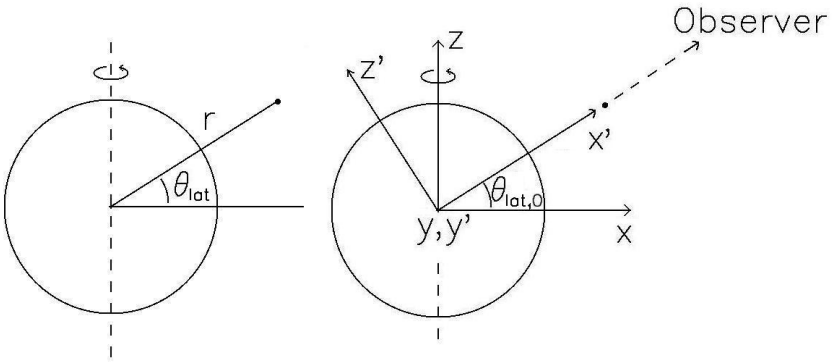

Figure 6.4: The various coordinate systems used to determine whether or not an object has been eclipsed. In this image, the y and y' axes are going into the page.

6.2.1 Conditions for eclipsing

I now, describe the method used in this chapter to determine whether or not a point is being eclipsed by either the host star, a circumstellar disc, or a prominence.

It is easiest to set up and evolve a stellar system in a spherical polar coordinate system (r, θ_{lat}, ϕ). However, the conditions for eclipsing are simplest when the system is represented in Cartesian coordinates with either one axis pointing along the line of zero longitude and latitude (x, y, z) or pointing towards the observer (x', y', z'). These three coordinate systems can be seen in Fig. 6.4. In all three coordinate systems, the origin is at the centre of the host star. The transformations between these three coordinate systems are as follows.

$$x = r \cos\phi \cos\theta_{lat} \tag{6.2}$$

$$y = r \sin\phi \cos\theta_{lat} \tag{6.3}$$

$$z = r \sin\theta_{lat} \tag{6.4}$$

$$x' = z \sin\theta_{lat,0} + x \cos\theta_{lat,0} \tag{6.5}$$

$$y' = y \tag{6.6}$$

$$z' = z \cos\theta_{lat,0} - x \sin\theta_{lat,0} \tag{6.7}$$

where θ_{lat} is the latitude and defined such that it has values between -90^o and 90^o and the observer is located at (r, θ_{lat}, ϕ) equal to $(\infty, \theta_{lat,0}, 0)$ and (x', y', z') equal to $(\infty, 0, 0)$.

Consider a point that does not lie within the star, the disc, or the prominence, and has coordinates (r, θ_{lat}, ϕ), (x, y, z), and (x', y', z') in the different coordinate systems. This point

is only visible if it is not eclipsed in all three of the following conditions.

Condition 1: The point is eclipsed by the host star with radius R_* if

$$x' < 0 \tag{6.8}$$

$$y'^2 + z'^2 < R_*^2 \tag{6.9}$$

The latter condition is only met if the point coincides with the disc of the host star in the plane of the sky and the former condition tests if the point is behind or in front of the host star.

Condition 2: The point is eclipsed by a circumstellar disc with an inner hole with a radius of R_{trunc}, which I assume to be the equatorial corotation radius, if

$$\theta_{lat} \times \theta_{lat,0} < 0 \tag{6.10}$$

$$\sin^2(\theta_{lat,0}) z'^2 + y'^2 > R_{trunc}^2 \tag{6.11}$$

As θ_{lat} and $\theta_{lat,0}$ are defined such that they are positive in one hemisphere and negative in the other, the first of these condition is only met if the point and the observer are in opposite hemispheres of the star. The second condition then tests if the point is visible through the inner hole of the disc as projected onto the plane of the sky.

Condition 3: The point is eclipsed by a prominence of radius R_p with its centre at $(r_p, \theta_{lat,p}, \phi_p)$, (x_p, y_p, z_p), and (x'_p, y'_p, z'_p) if

$$x' < x'_p \tag{6.12}$$

$$(y' - y'_p)^2 + (z' - z'_p)^2 < R_p^2 \tag{6.13}$$

These conditions are the same as the conditions for eclipsing by the host star above with

corrections for a sphere with a different radius and which is not centred at the origin of the coordinate system.

6.3 Modelling individual eclipsed flares

In this section [1], I consider two questions. Firstly, is it possible for flares with atypical X-ray lightcurves to be produced by the time-variable eclipsing of typical flares? Secondly, is it possible to learn anything about the geometries of these flares based on the shapes of their atypical lightcurves?

By fitting the geometric and temporal parameters listed in the last section to three observed atypical COUP flares, I show that such flares can be produced by the eclipsing of typical flares. However, by applying the same technique to modelled test flares, I show that it is not possible to learn anything useful about the geometries of these flares.

6.3.1 Fitting procedure

In the flare model presented in the last section, the visible emission measure curve of an eclipsed flare is determined by

- The emission measures that would have been seen had eclipsing not occurred as a function of time ($EM_{tot}(t)$ in Eqn. 6.1).
- The fraction of the flaring loop that is eclipsed as a function of time ($V_{vis}(t)/V_{tot}$ in Eqn. 6.1).

In order to model an eclipsed flare, I first estimate the $EM_{\rm tot}(t)$ function based on the flare's visible emission measure vs time curve. This is done by first estimating the times of the beginning and end of the eclipse based on the visible emission measure. Using this, the uneclipsed emission measure curve is fit to the visible emission measures at times outside of the eclipse by assuming that the uneclipsed emission measure curve can be described by the sum of a quadratic and a gaussian, according to the following equation[2]

$$\log EM(t) = A_1 e^{-\frac{(t-A_2)^2}{2A_3^2}} + A_4 + A_5 t + A_6 t^2 \tag{6.14}$$

[1] Unlike the rest of this chapter, this section was not included in Johnstone et al. (2012).
[2] I fit the coefficients using the IDL routine GAUSSFIT.

With an estimated uneclipsed emission measure curve, I then fit the set of geometric and temporal parameters that would cause this flare to be eclipsed in such a way that the observed emission measures are reproduced. This is done separately using two different methods: a search of a large grid of previously calculated models and a Markov-Chain Monte-Carlo (MCMC) search.

6.3.2 Test flares and the limitations of the fitting procedure

Before producing best fit sets of parameters to actual COUP flares, it is necessary to determine to what extent this method can be used to accurately model the geometries of unresolved flaring stellar systems. I do this by applying the fitting procedure to three eclipsed test flares. The results can then be compared with the known geometries of these modelled systems.

Each test flare is produced from the same original uneclipsed emission measure vs time curve. This can be seen as the full black lines in Fig. 6.5. I then produce each of the three test flares by eclipsing the flares in such a way that they have emission measure morphologies that resemble atypical observed flares. These eclipsed emission curves are assumed to be the observed emission measures. The geometric and temporal parameters that produced these flares are given in Table 6.1, Table 6.2, and Table 6.3 for Test Flare A, Test Flare B, and Test Flare C respectively. I then apply the fitting procedure to each of these eclipsed flares.

The first step in the fitting procedure is to estimate the flare's uneclipsed emission measures from the emission measures. These estimates for the three test flares are shown in Fig. 6.5 as dot-dash lines, and can be compared with the original uneclipsed emission measures, which are shown as full lines. The fitting procedure clearly underestimates the uneclipsed flare emission measures: this is particularly the case for Test Flare C. This is partly a result of the subjective determination of the starting and ending times of the eclipse systematically underestimating the durations of the eclipsing events. This represents a fundamental and significant limitation to this method and the effect that this underestimation has on the ability of the MCMC and grid fit methods to accurately estimate flare geometries is discussed below.

Using the estimated uneclipsed emission measure curves, sets of best fit geometric and temporal parameters are produced using the MCMC and grid fit methods separately for each test flare. The results are given in Tables 6.1, 6.2, and 6.3 for Test Flare A, Test Flare B, and Test Flare C respectively. The eclipsed emission measure curves corresponding to these fits are

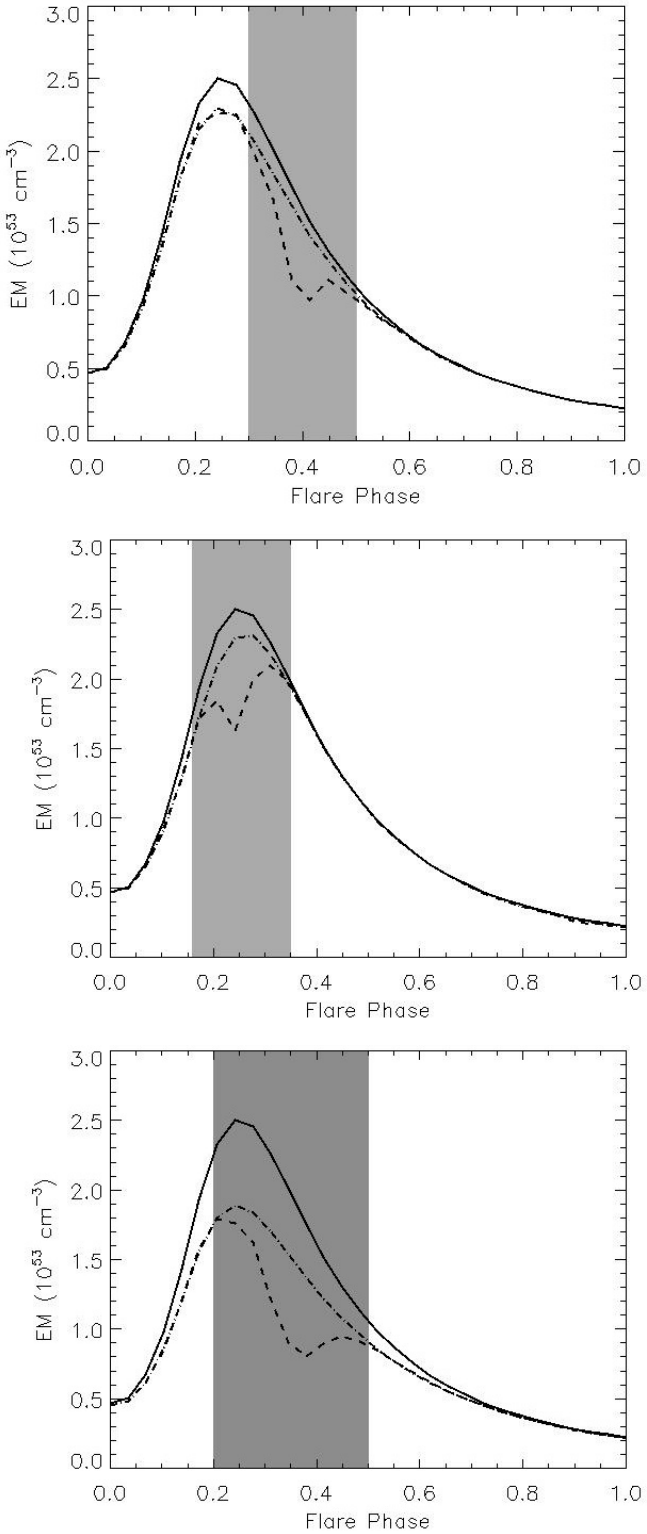

Figure 6.5: Emission measure vs time curves for Test flare A (upper panel), Test Flare B (middle panel), and Test Flare C (lower panel). The full lines gives original uneclipsed emission measure curves used to produce all three test flares. The dashed lines show the eclipsed emission measure curves: these are assumed to be the observed emission measure curves for each flare. The grey shaded areas show the parts of the eclipsed emission measure curves that were determined by a visual inspection to be times when the flare was eclipsed. The uneclipsed emission measure curves that have been fit to the eclipsed emission measures outside the grey shaded regions are shown as dot-dash lines.

shown in Fig. 6.6, 6.7, and 6.8 for Test Flares A, B, and C respectively.

The best fit emission measure curves produced by both the grid search and MCMC methods accurately reproduce the atypical morphologies of the 'observed' emission measure curves for all three test flares. However, the actual best fit parameters do not accurately reproduce the original parameters that were used to produce the modelled flares. In most cases, the fraction of the flare duration to host star rotation period, and the starting longitudes of the flares are accurately reproduced. However, the inclination angles of the stellar rotation axes and the latitudes of the flaring loops, do not correspond to their original values. The heights and widths of the flaring loops are also not well reproduced.

It appears that it may be possible to estimate some of the geometric and temporal parameters for eclipsed stellar flares from their visible emission measure curves. However, the parameters that can be estimated are those which are of little interest. The parameters that are of interest, i.e. the flaring loop latitudes, heights, widths and orientations, cannot be estimated.

Tables 6.1, 6.2, and 6.3 also give values of the goodness-of-fit parameter S for each of the fits. The tables also give values of S for the original sets of parameters. These are calculated by applying the original flare parameters to the estimated uneclipsed emission measure curves. If the estimated uneclipsed emission measures corresponded exactly to the original uneclipsed values, the goodness-of-fit parameter would be zero. However, due to the underestimation of the uneclipsed emission measures discussed above, the original flare parameters actually give worse fits than the best fit parameters that are calculated. Thus, the inaccuracies in the best fit parameters are not necessarily a result of the MCMC and grid searching methods.

It also must be pointed out that when applying the fitting procedure to these test flares, I have two significant advantages that I do not have when considering real stellar flares. In all three cases, the 'observed' emission measure data was taken to be perfectly accurate. The other advantage comes from the fact that the same physical model, presented in Section 6.2, was used to model the 'observed' emission measure curve as was used in the grid search and MCMC fitting methods. Even with these advantages, it is not possible to accurately determine interesting physical parameters about the flares, thus it is unlikely to be possible without these advantages.

Method	S (1)	ϕ_0 (deg) (2)	θ_{view} (deg) (3)	P_{flare}/P_{rot} (4)	θ_{loop} (deg) (5)	H (R_*) (6)	γ (deg) (7)	W (R_*) (8)
Original	0.09	0.49	47.94	1.26	-65.02	8.50	-120.20	0.03
MCMC	0.02	80.59	-0.78	0.69	-11.41	5.96	21.94	0.98
Grid	0.003	355.00	-48.00	1.30	42.00	10.00	225.00	0.75

Table 6.1: Original and best fit geometric and temporal parameters for Test Flare A. The columns correspond to: Col. (1): the goodness-of-fit parameter. Col. (2): the starting longitude of the centre of the flaring loop. Col. (3): the angle at which the star is being viewed, where 0° corresponds to a star that is being viewed equator-on. Col. (4): the ratio of the duration of the flare to the host star's rotation period. Col. (5): the latitude of the centre of the flaring loop, where 0° corresponds to a flaring loop with its centre on the star's equator. Col. (6): the height of the peak of the flaring loop. Col. (7): the orientation of the flaring loop (see Fig. 6.3). Col. (8): the width of the flaring loop.

Method	S (1)	ϕ_0 (deg) (2)	θ_{view} (deg) (3)	P_{flare}/P_{rot} (4)	θ_{loop} (deg) (5)	H (R_*) (6)	γ (deg) (7)	W (R_*) (8)
Original	0.05	55.12	-32.42	1.46	41.60	9.53	48.25	0.003
MCMC	0.009	57.30	-25.20	1.48	-59.88	0.007	49.34	0.19
Grid	0.009	45.00	-24.00	1.50	33.00	10.00	0.00	0.75

Table 6.2: Same as Table 6.1 for Test Flare B.

Method	S (1)	ϕ_0 (deg) (2)	θ_{view} (deg) (3)	P_{flare}/P_{rot} (4)	θ_{loop} (deg) (5)	H (R_*) (6)	γ (deg) (7)	W (R_*) (8)
Original	0.45	26.98	-59.88	1.18	73.66	3.83	23.76	0.46
MCMC	0.004	17.58	-9.14	1.24	-20.64	1.22	22.00	0.54
Grid	0.003	10.00	27.00	1.30	42.00	0.10	3.15	0.10

Table 6.3: Same as Table 6.1 for Test Flare C.

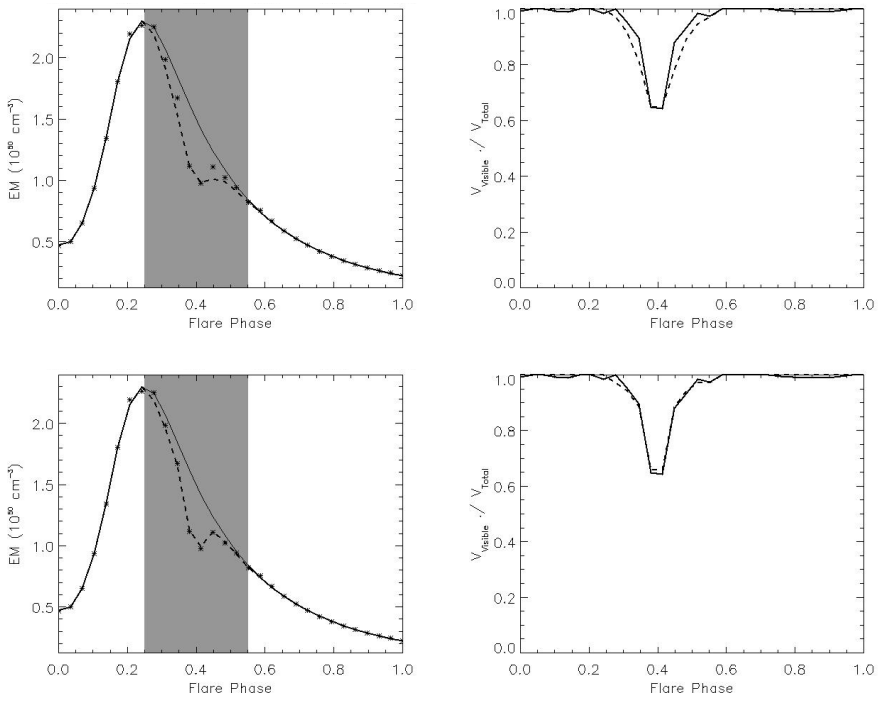

Figure 6.6: Best fit curves for Test Flare A using the grid fit method (upper panels) and the MCMC method (lower panels) showing the emission measure curves (left) and the fraction of the volume of the flaring loop that is visible over the flare's duration (right). In the emission measure plots, the original visible emission measures are shown as asterisks'. The modelled emission measure curves prior to any eclipsing, that are fit to the data using the emission measure values outside of the grey shaded area, are given by the full lines, and the final emission measure curves after being eclipsed using the best fit geometric parameters is given by the dashed line. In the plots showing the fractions of the flaring loops that are visible, the values given by the comparison of the modelled emission measure curves (full line on emission measure plots) with the original emission measures are given by the full lines and the values given by the best fit geometric parameters are given by the dashed lines.

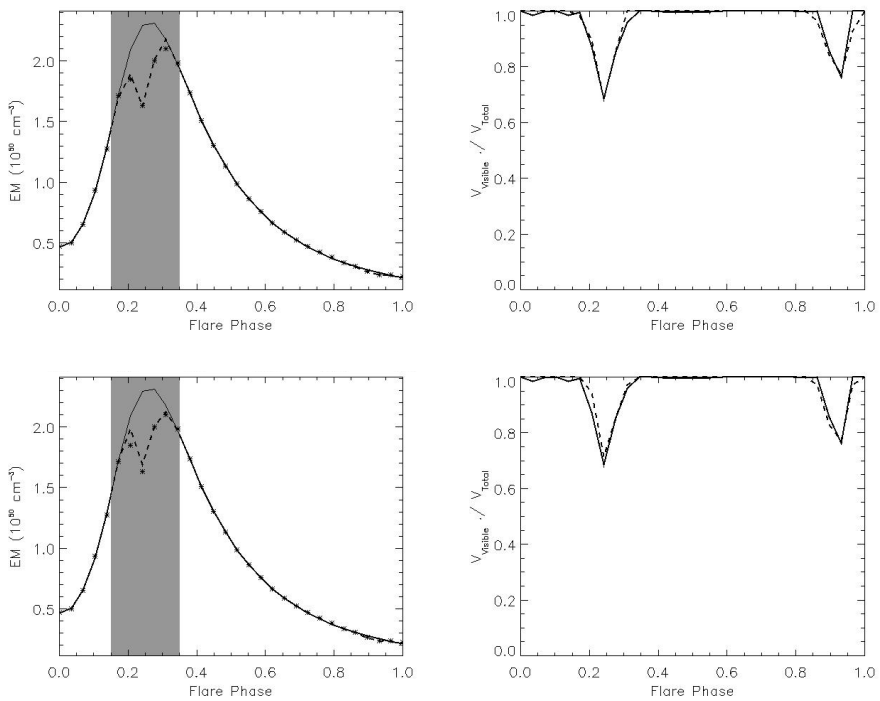

Figure 6.7: Same as Fig. 6.6 but for Test Flare B.

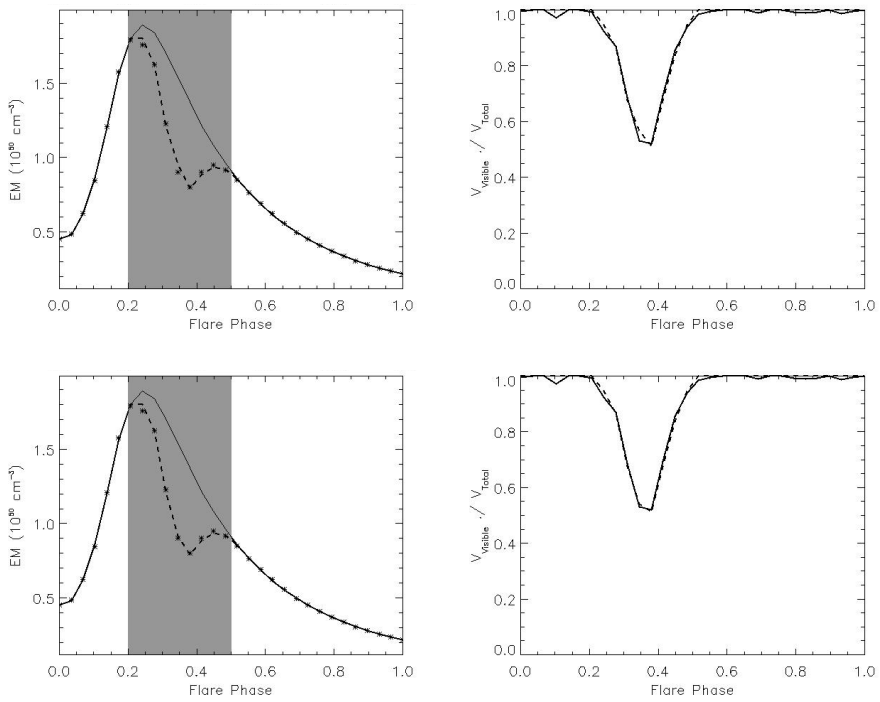

Figure 6.8: Same as Fig. 6.6 but for Test Flare C.

6.3.3 COUP flares

I have fitted model eclipse flares to three examples of eclipse candidate COUP flares. Although the fitting procedure is not able to tell us anything useful about the geometries of these flares, it is still useful to show that *real eclipse candidate flares can be produced by the eclipsing of typical flares*.

The three example flares are the flares on COUP sources 66, 649, and 942 (Getman et al. 2008a). In each case, the flares' emission measure curves have significant dips which might be a result of eclipsing. The flares are shown in Fig. 6.2. The best fit emission measure vs time curves for all three flares are shown in Fig. 6.9. In all cases, good fits to the observed emission measures are found, however, given the results of the last section, I do not present or discuss the best fit parameters.

An important difference between the test flares given above and the COUP flares selected here is that in the case of the test flares it is known that the atypical morphologies are a result of eclipsing. In the case of observed stellar flares, it is possible that the atypical morphologies are the result of some other physical mechanism such as the superposition of multiple flares.

6.4 The number of eclipsed flares

In this section, I analyse the entire COUP sample in order to determine how many flares have been eclipsed. I define non-eclipse candidate flares as flares that show single rises followed by single decays in their emission measure vs time curves (this includes both the 'typical' and the 'slow-rise top-flat' flares defined by Getman et al. 2008a). I define eclipse candidate flares as those that display sudden short duration decreases followed by increases in their emission measures.

An eclipse that has a duration comparable to the duration of the flare will generally only result in a less luminous flare without a noticeably atypical morphology, or a flare that is not visible at all. For this reason, I expect that such dips should be found predominantly on long duration flares and rapidly rotating stars.

In order to illustrate the effects that eclipsing can have on typical flares, I show in Fig. 6.9, three examples of eclipse candidate flares from the COUP sample. In the last section, I demonstrate that an eclipse candidate flare can be produced by the eclipsing of a non-eclipse

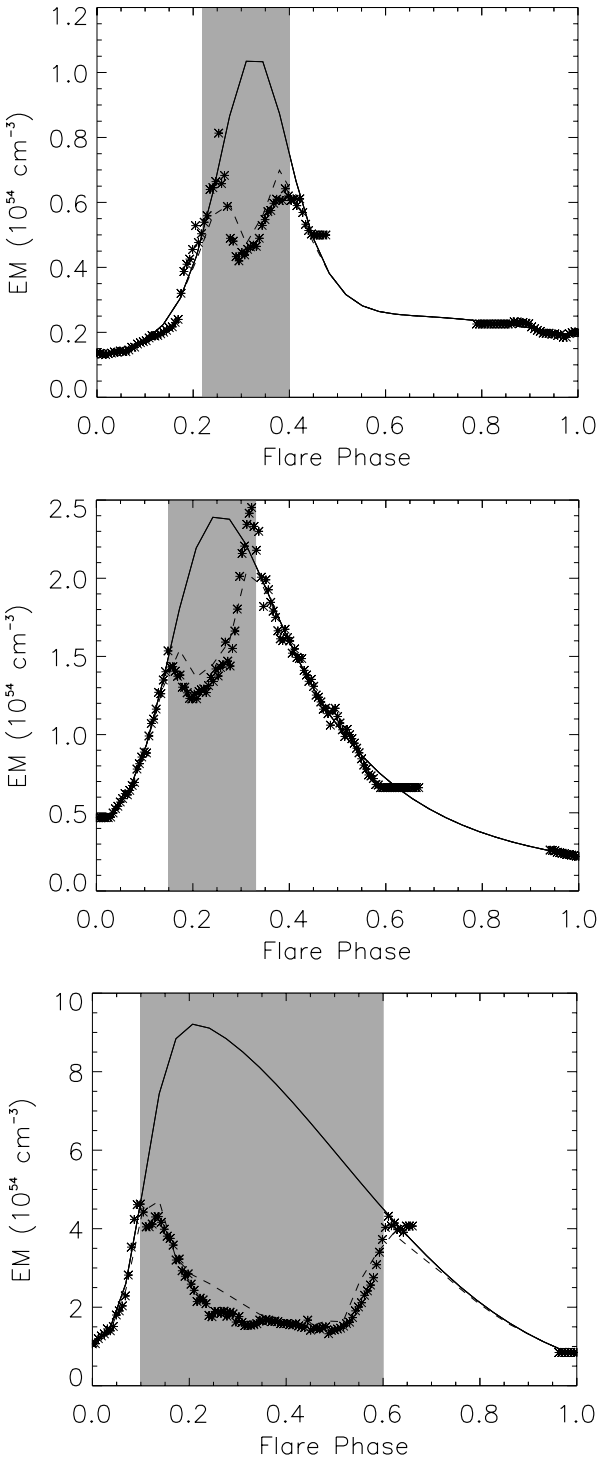

Figure 6.9: Emission measure vs time curves for the observed flares on COUP sources 66 (upper panel), 649 (middle panel), and 942 (lower panel) which represent good examples of atypical COUP flares. The asterisks' show the observed COUP emission measure data, given by Getman et al. (2008a). The shaded area represents the times when some portion of the magnetic structure containing the flare was eclipsed by the host star. The solid lines show the intrinsic emission measure curves, $EM_{tot}(t)$, which have been fitted to the observed emission measure curves in the region outside the shaded area; this represents what the flare may have looked like had the flare always remained in view. The dashed line shows an eclipsed version of the same modelled flare which gives the best fit to the observed flare's emission measure curve.

candidate flare by fitting model eclipsed flares to these observed emission measure vs time curves. I note, however, that while the forward problem of varying the model flare parameters to fit the observations is quite straightforward, the inverse problem of recovering the true flare parameters solely from the observations is in general not possible.

Of the 216 COUP flares catalogued by Getman et al. (2008a), I identify 62 (29%) eclipse candidates. This number, given different levels of scepticism by the examiner, may be between 31 (14%) and 71 (33%). For the rest of this chapter, I will take the value of 62 as the number of eclipse candidate flares in the COUP sample.

Table 6.4 gives average values for several COUP flare and host star parameters, derived from parameters given by Getman et al. (2008a), for eclipse candidate and non-eclipse candidate flares separately. I have attempted to estimate by eye any decreases in the flare durations derived from the visible emission measure curves that might have been caused by eclipsing. This is only possible for flare emission measure curves which have been broken into two parts by large temporary eclipses. Contrary to expectations, the average flare durations as a fraction of host star rotation period is shorter for eclipse candidate flares when the original flare durations from Getman et al. (2008a) are used. When the durations are calculated assuming eclipsing has occurred, this is no longer a problem because the durations are always significantly longer than their original values. It can also be seen that the average peak emission measures are lower for eclipse candidate flares than for non-eclipse candidate flares which is consistent with eclipsing hypothesis.

6.4.1 Modelling the set of COUP flares

Given that 62 of the COUP flares are classified as eclipse candidates, I now use the simple flare model to calculate the number of eclipse candidates that I would expect to see in the COUP flare sample. I assume that all flares are produced by the same energy release process acting within the simplified loop geometry, and therefore have similar typical intrinsic emission measure vs time curves (i.e. $EM_{tot}(t)$ in Eqn. 6.1). I therefore choose the flare observed on COUP source 871 from the COUP sample (shown in Fig. 6.10) as the intrinsic flare profile. I then use this profile to produce many simulated flares by scaling the peak emission measure and the flare duration in the following way

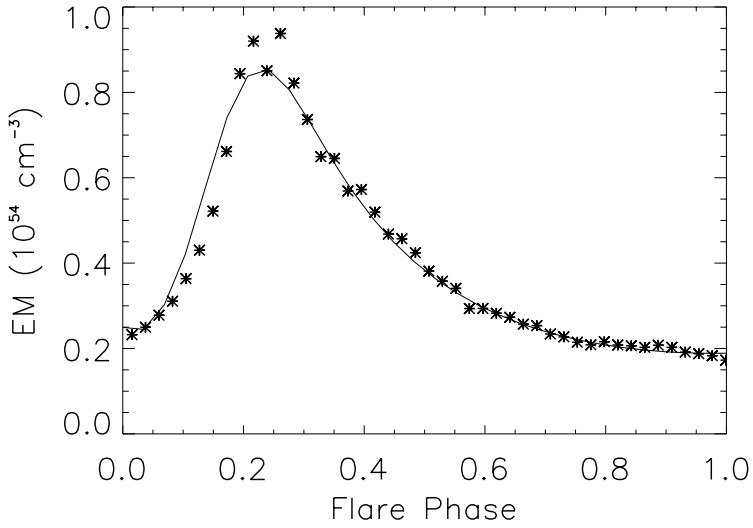

Figure 6.10: Flare on COUP source 871 which the standard 'typical' emission measure curve is based on. The full line represents the best fit to this curve which is used as the standard flare emission measure vs time curve.

$$EM_{tot,sim}(t) = EM_{tot,871}\left(t_{scaled}\right) \times \left(\frac{EM_{max,sim}}{EM_{max,871}}\right) \tag{6.15}$$

where

$$t_{scaled} = t \times \frac{t_{sim}}{t_{871}} \tag{6.16}$$

where the time t is zero at the beginning of the impulsive phase of the flare, $EM_{tot,871}$, $EM_{max,871}$, and t_{871} are respectively the intrinsic emission measure vs time curve, the maximum emission measure, and the duration for the standard flare, and $EM_{tot,sim}$, $EM_{max,sim}$, and t_{sim} are similar quantities for the simulated flare. I choose the values of $EM_{max,sim}$ and t_{sim} randomly using the model described below in Section 6.4.2. I note that although here I have focused on the emission measure vs time curve of the flare observed on COUP source 871 as the standard typical flare, repetitions of the analysis discussed below using different typical COUP flares yielded no significant difference in the results.

In order to determine the visible emission measures curves ($EM_{vis}(t)$) for the simulated flares I also need to specify the nine parameters that determine the loop geometry and position and the stellar rotation rate. Each of the randomly chosen parameters discussed above is chosen based on probability distributions that best approximate the distributions of these parameters in the COUP sample. Where it is not possible to use observed distributions of

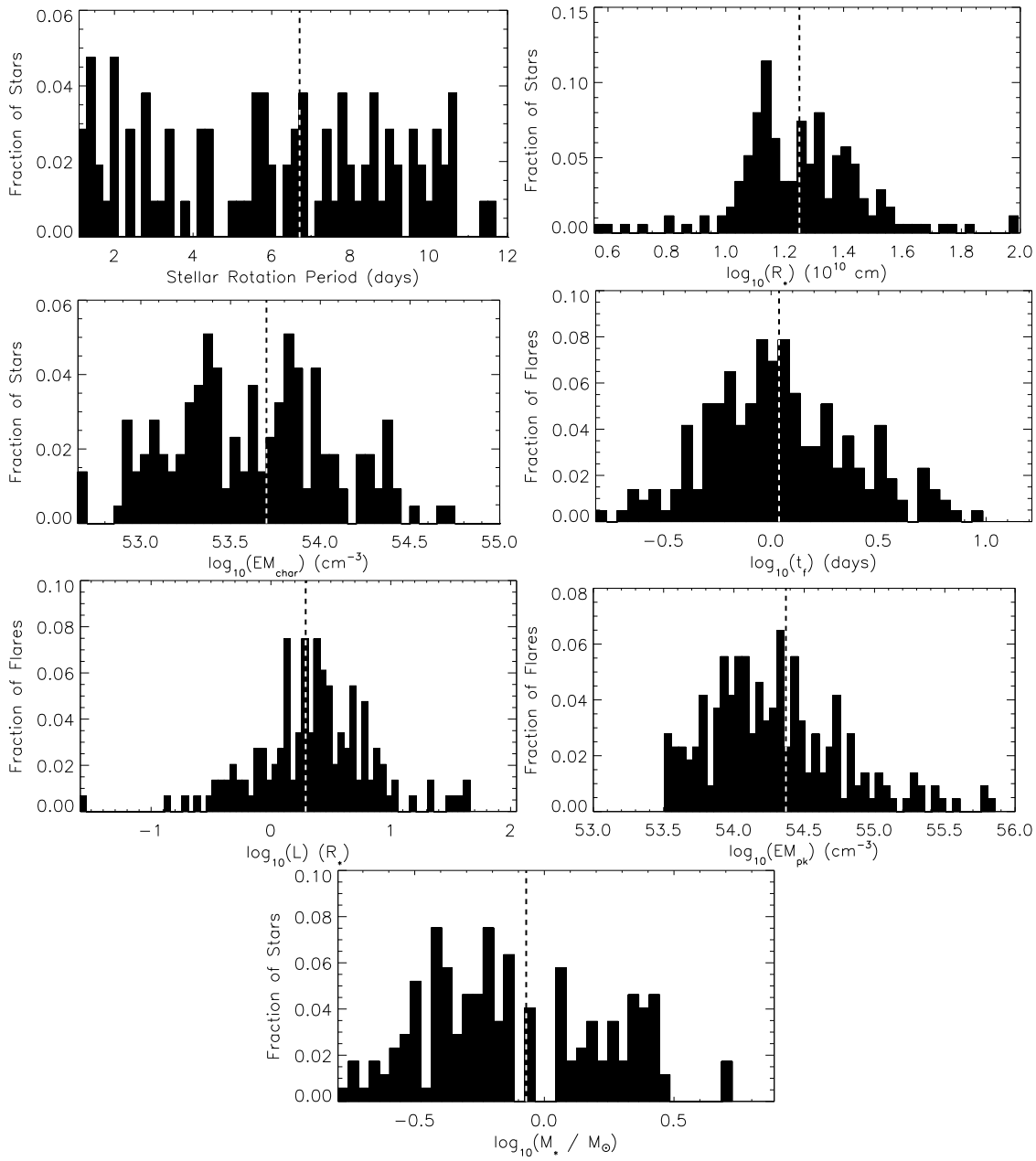

Figure 6.11: Histograms showing the distributions of relevant stellar and flare parameters derived from the data given in Tables 1-3 of Getman et al. (2008a). The histograms show, from top to bottom, stellar rotation periods, stellar radii, host star characteristic emission measures, flare durations, flare loop lengths, flare peak emission measures, and stellar masses. Dashed lines show the locations of the mean values.

parameters, reasonable assumptions, discussed below, must be made. With these parameters I calculate the fraction of the flaring loops that are visible as a function of time (i.e. the fraction V_{vis}/V_{tot} from Eqn. 6.1) and using Eqn. 6.1, I calculate the visible emission measure curves for each flare.

It is important in these calculations to define flares in the same way as Getman et al. (2008a) in order that the results can be reliably compared. For this reason, I define a flare as any energetic event with a peak emission measure exceeding four times the characteristic emission measure of the host star. In this way, flares that have been eclipsed to an extent that they would not have been classified as bright flares in the COUP sample are discarded.

6.4.2 Probability distributions for flare parameters

In Section 6.2, I listed the nine geometric and temporal parameters that can affect, through eclipsing, the soft X-ray lightcurve morphologies of stellar flares. Another factor considered in this chapter is the existence of other opaque material that can act as alternative sources of eclipsing. The two other sources of eclipsing considered here are circumstellar discs and flare associated prominences. In order to calculate the radii of the inner edges of the circumstellar discs, which I assume it is at the equatorial corotation radius, therefore, I must also model the stellar masses and radii. Thus, for the purposes of this chapter, I must model eleven probability distributions.

Fig. 6.11 shows histograms for seven of the parameters derived using the data given by Getman et al. (2008a). For these distributions, I ignore data from eclipse candidate flares. With the exception of the stellar rotation periods, all these parameters can be modelled using log-normal distributions parametrised by their mean, μ, and variance, σ^2. The means and variances for these six parameters are given in Table 6.5. I assume that the stellar rotation periods have values that are evenly distributed between 0.1 and 11 days.

The other parameters that need to be estimated in order to model the ONC flares are the starting longitudes of the flaring loops, ϕ_0, the orientation of the loops, γ, the inclination angles of the stellar rotation axes to an observer's line-of-sight, θ_{view}, and the colatitudes of the centres of the flaring loops, θ_{loop}. The former two are taken to have values that are evenly distributed over all possible values. The latter two are taken to have a higher probability for values near the equator based on the probability density function

$$pdf(\theta) = \frac{1}{2}\cos\theta_{lat} \tag{6.17}$$

where θ_{lat} is the latitude.

In these calculations, the presence of circumstellar discs around some of the stars is also considered. Getman et al. (2008a) derived near infrared colour excess ($\Delta(H-K_s)$) values for 140 of the flare host stars and used the condition $\Delta(H-K_s) > -0.06$ mag as a good indicator for the presence of circumstellar discs. Of these 140 stars, 53 indicate the presence of a circumstellar disc. Thus, in the flares sets considered in the next section, where circumstellar discs are considered, each flare has a probability of 0.38 of having occurred on a star that has a disc.

It is also necessary to calculate the heights (H) and widths (W) of flaring loops when the only available information are the loop lengths. For this reason, it is then necessary to assume a plausible relation between the heights and the widths of flaring loops. I assume the relation that would be expected for a potential arcade with a maximum width of W_{max}. This relation can be found in Browning & Priest (1986) and is given by

$$\exp\left(-\frac{H}{R_*}\right) = \cos\left(\frac{\pi W}{2W_{max}}\right) \tag{6.18}$$

where W_{max} is taken to be equal to 0.9 R_* (if the value for W_{max} is larger than R_* the largest flare loops would not touch the stellar surface). It is important to point out that even though I use the height-width relation for magnetic loops in a potential arcade, throughout this chapter, the actual loop geometries are ellipses.

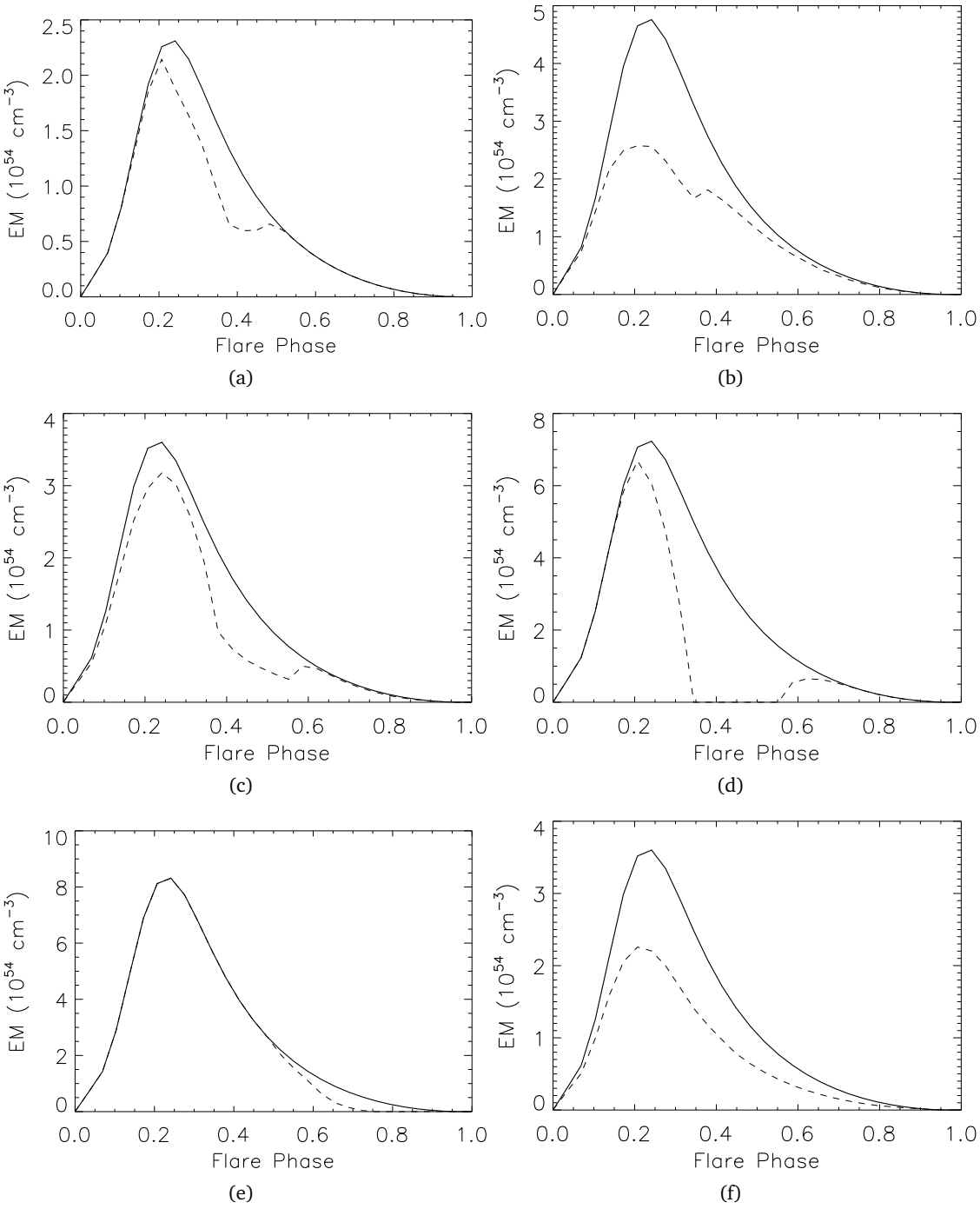

Figure 6.12: Six examples of modelled flares produced through eclipsing of the flaring plasma where the solid lines show the flare emission measure curves prior to eclipsing (i.e. the emission measure curve that would have been observed had the event always remained in view) and the dashed lines show the visible (i.e. eclipsed) emission measure curves. The latter arises by allowing the flare to enter or exit from rotational eclipse. These examples show that it is likely that atypical flare morphologies will be produced at random given a large sample of flares.

	N_{tot}	P_{rot} (days)	EM_{pk} (10^{53} cm^{-3})	L (10^{10} cm)	N_{disc}/N_{tot}	t_f (COUP) (days)	(t_f/P_{rot})	t_f (Modified) (days)	(t_f/P_{rot})
	(1)	(2)	(3)	(4)	(5)	(6)	(7)	(8)	(9)
Eclipse Candidates	62	7.08	33.92	42.71	0.33	1.28	0.27	2.36	0.47
Non-Eclipse Candidates	154	6.57	46.87	29.22	0.44	1.59	0.36	1.59	0.36
All	216	6.71	43.15	33.09	0.40	1.50	0.34	1.85	0.41

Table 6.4: *Average* values of flare and stellar parameters in the COUP set reported by Getman et al. (2008a). The data are presented for the entire set (bottom row) and separately for the flares that have been classified as eclipse candidates (top row) and non-eclipse candidates (middle row). The columns correspond to: Col. (1): the number of flares in each category. Col. (2): the host star rotation periods. Col. (3): the peak emission measures. Col. (4): the derived loop lengths. Col. (5): the fraction of flares on stars which show evidence that they possess a circumstellar disc. Cols. (6,7): the visible flare durations reported by Getman et al. (2008a) as an absolute value and as a fraction of their host star's rotation period. Cols. (8,9): the flare durations after I attempt to correct for decreases in their visible durations due to noticeable eclipses.

	$\log_{10}(t_f)$ (days) (1)	$\log_{10}(L)$ (R_*) (2)	$\log_{10}(M_*/M_\odot)$ (3)	$\log_{10}(EM_{pk})$ (cm^{-3}) (4)	$\log_{10}(EM_{char})$ (cm^{-3}) (5)	$\log_{10}(R_*)$ (10^{10} cm) (6)
μ	0.037	0.30	-0.07	54.37	53.71	1.25
σ^2	0.13	0.24	0.13	0.26	0.25	0.05

Table 6.5: Mean and variance values for the six flare and host star parameters that are to be approximated as log-normal distributions. The columns correspond to: Col. (1): flare durations. Col. (2): Flare loop lengths. Col. (3): Mass of host stars. Col. (4): Flare peak emission measures. Col. (5): Host star characteristic emission measures. Col. (6): Host star radii. The values are calculated using data given by Getman et al. (2008a), which are plotted as histograms in Fig. 6.11.

	N_{tot}	P_{rot} (days)	EM_{pk} (visible) (10^{53} cm^{-3})	EM_{pk} (original) (10^{53} cm^{-3})	t_f (visible) (days)	(t_f/P_{rot})	t_f (original) (days)	(t_f/P_{rot})
	(1)	(2)	(3)	(4)	(5)	(6)	(7)	(8)
Eclipse Candidates	698	2.07	49.0	59.7	1.51	1.91	2.26	2.63
Non-Eclipse Candidates	9302	5.77	46.5	49.6	1.31	0.47	1.33	0.48
All	10,000	5.55	46.6	50.1	1.32	0.57	1.39	0.61

Table 6.6: *Average* values of flare and stellar parameters in the set of modelled flares. The data are presented for the entire set (bottom row) and separately for eclipse candidates (top row) and non-eclipse candidates (middle row). The columns correspond to: Col. (1): the number of flares in each category. Col. (2): the stellar rotation periods. Col. (3): the visible peak emission measures. Col. (4): the *actual* peak emission measure. Cols. (5,6): the visible flare durations as an absolute value and as a fraction of the host stars' rotation periods. Cols. (7,8): the *actual* flare durations *prior to eclipsing*.

6.4.3 Results

Using the method described above, I model a set of 10,000 flares. In this section, I analyse these flares using the same method of visual inspection to select eclipse candidate flares as was used to analyse the COUP sample. In the initial results presented here, circumstellar discs and flare-associated prominences are not considered. These are included in separate results presented at the end of this section.

Due to eclipsing, not every modelled flare has a peak emission measure that is large enough to be classified as a bright flare in the COUP observations. In order to obtain 10,000 flares that make it through the observational selection criteria adopted by Getman et al. (2008a) it is necessary to model 10,878 flares in total. By inspecting the entire sample of modelled flares, I classify only 7.0% as eclipse candidates. This small value is to be contrasted with the larger number of 29% eclipse candidate flares in the COUP sample.

Six examples of flare emission measure curves that have been affected by eclipsing are shown in Fig. 6.12. I determine that eclipse candidates are likely to occur in a sample of 216 flares under the conditions present in the ONC. Thus, I conclude that it is likely that a number (some, although not necessarily all) of the eclipse candidate flares in the COUP sample have been produced by the rotational eclipsing of typical flares. However, it is unlikely that the entire sample has been produced in this way. Given that the probability of one flare being an eclipse candidate is 0.07, using the Binomial distribution, the probability of 62 flares being eclipse candidates in a sample of 216 flares is approximately 10^{-25}. In order to explain the large number of atypical COUP flares, it is thus necessary to assume other physical mechanisms, such as multiple heating events in a single flaring loop, multiple flares with lightcurves that have been superimposed, or stellar analogues of solar coronal arcades where a reconnection event triggers subsequent events and associated flares/heating of neighbouring loops.

The sample of eclipse candidates in the modelled set of flares does not represent the full sample of flares that have undergone eclipsing. The fifth and sixth flares shown in Fig. 6.12 show examples of flares that have been eclipsed but still have 'typical' emission measures. A total of 63% of the modelled flares have been partially eclipsed for at least a fraction of their durations and 49% of the flares have their peak emission measures reduced. However, in most cases, eclipsing leads to an insignificant decrease in the visible emission measure value.

This can be seen in Fig. 6.13. Of the modelled flares, 6% show significant decreases in their visible durations. Therefore, the analysis of such flares may lead to derived flare parameters that are different from the true physical properties of the magnetic structure containing the flare. I explore this point further in the next section.

One type of flare morphology seen in the COUP sample but not in the flares modelled here are the slow-rise top-flat flares, defined by Getman et al. (2008a). Such morphologies can be produced through eclipsing, as can be seen in the second peak in the fourth example shown in Fig. 6.12. However, this peak has not made it through the selection criterion for flares so it is not counted in the sample of modelled flares.

In Table 6.6, I give average values for flare and host star parameters, both before and after eclipsing has been taken into account, for eclipse candidate and non-eclipse candidate flares separately. It can be seen that eclipsing causes a reduction in the average durations and peak emission measures. It can also be seen that longer duration flares on faster rotating stars are more likely to be eclipse candidates, as expected for flares randomly distributed in latitude and longitude.

One reason why there may be more eclipse candidates seen in the observed COUP sample than in the modelled flare set could be that the COUP flares are being eclipsed by circumstellar discs or flare-associated prominences. To investigate to what extent this may be the case, I repeat the above calculations to produce two more sets of 10,000 flares. In the first set, I assume that circumstellar discs are present around 38% of the host stars; the same fraction as determined Getman et al. (2008b) based on Spitzer H-K excess emission. With this assumption, I find that 6.4% are eclipse candidates. In order to produce 10,000 visible flares, it was necessary to produce 11,689 flares in total. In the second set, I assume that prominences are present above the apex of each flaring loop. With this assumption, I find that 7.7% are eclipse candidates. In order to produce 10,000 visible flares, it was necessary to produce 11,612 flares in total. Thus, it is clear that even with circumstellar discs and flare-associated prominences I am not able to explain all of the eclipse candidates seen in the COUP sample with eclipsing of single magnetic loops only.

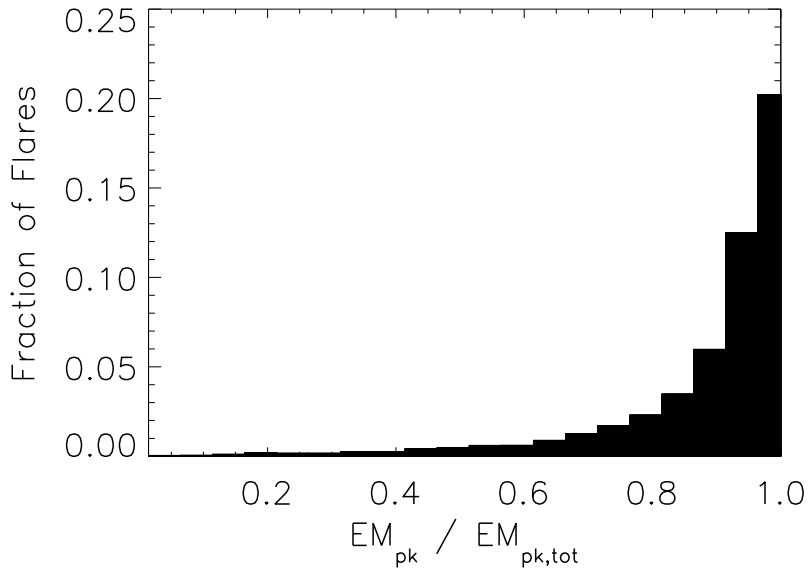

Figure 6.13: Histogram showing the visible peak emission measures, EM_{pk}, as a fraction of their uneclipsed values, $EM_{pk,tot}$, for the set of modelled flares. Only the 105 flares which had their peak emission measures decreased by eclipsing are included here.

6.5 Flare loop lengths

A common method for determining the loop length of an unresolved stellar flare involves the comparison of the flare's emission measure and temperature data with hydrodynamic flare models. This method, detailed by Reale et al. (1997), defines the loop half-length as

$$L(cm) = \frac{\tau_d(ks)\sqrt{T_{pk}(MK)}}{3.7 \times 10^{-4} F(\zeta)} \tag{6.19}$$

where

$$F(\zeta) = \frac{0.63}{\zeta - 0.32} + 1.41 \tag{6.20}$$

$$T_{pk} = 0.068 T_{obs}^{1.2} \tag{6.21}$$

where τ_d(ks) is the time that it takes for the flare's emission measure to decay by a factor of e (the e-folding timescale), T_{pk}(MK) is the temperature at the apex of the flaring loop when the flare's emission measure is at its peak, T_{obs}(MK) is the observed average loop temperature at this time and ζ is the gradient of the decay phase of the $\log EM^{\frac{1}{2}}$ - $\log T$ plot. See Reale et al. (1997) for full details (for a discussion on the validity of the single loop model, see Appendix

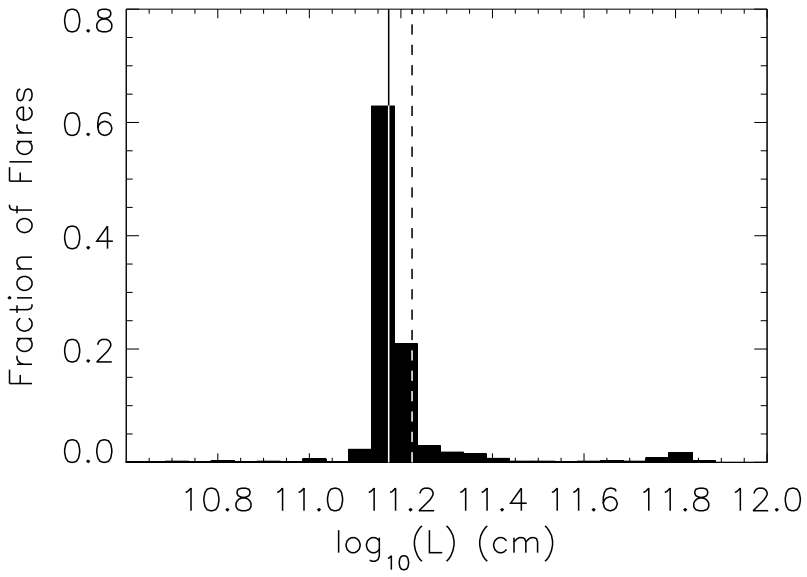

Figure 6.14: Histogram showing the derived lengths of flaring loops after eclipsing has been taken into account (flares which have not undergone any eclipsing are included). The solid vertical line shows the length that would have been derived for all of the flares if no eclipsing had occurred. The dashed vertical line shows the log of the average derived loop lengths (not the average of the log).

A of Getman et al. 2011).

In order to explore the effect that eclipsing can have on the loop lengths derived from this method, which has been commonly employed in the analysis of flares on young stars (e.g. Favata et al. 2005), I take the emission measure and temperature data for the 'typical' flare seen on COUP source 871 and produce a large set of 10,000 flares using the method described in Section 6.4.2. In these calculations, however, I only pick at random the stellar parameters (e.g. radius, rotation period) and the locations and orientations of the flaring loops. The parameters specific to the flare (e.g. peak emission measures, loop length, flare duration) are kept at the values derived by Getman et al. (2008a) for this flare. I then apply the loop length analysis to the uneclipsed and eclipsed flare emission measure curves, assuming that eclipsing has no effect on the determined temperatures.

The effect of eclipsing is shown in Fig. 6.14. The loop length based on the uneclipsed emission measure curve is 14.9×10^{10} cm. After eclipsing has been taken into account for a large set of flares, the average calculated loop length for that set is increased to 16.8×10^{10} cm. This simple estimate suggests that in most cases eclipsing has little effect on derived loop lengths.

6.6 Summary and conclusions

Although most stellar flares have typical soft X-ray lightcurve morphologies (i.e. a single rapid rise followed by a slow exponential decay), many flares have atypical morphologies. Many of these show multiple peaks or small dips in their lightcurves (Getman et al. 2008a). Based on solar analogies, such flares are often interpreted as being the result of multiple heating events in the same flaring loop or the superposition of separate overlapping flares (for example, see Reale et al. 2004; Pillitteri et al. 2005; Pandey & Singh 2008; López-Santiago et al. 2010). In this chapter, I have considered an alternative geometric interpretation in which these atypical flare morphologies are produced by the eclipsing of flaring plasma due to the rotation of the host star. This interpretation has been considered for individual flares in previous studies (Skinner et al. 1997, Stelzer et al. 1999, Schmitt & Favata 1999, Schmitt et al. 2003, Sanz-Forcada et al. 2006, Sanz-Forcada et al. 2007).

Using data from the *Chandra* Orion Ultradeep Project, Getman et al. (2008a) identified 216 stellar flares on 161 pre-main sequence stars. As the COUP sample contains a range of flare morphologies, I have used it to explore the eclipsing interpretation. I analysed the entire COUP sample by eye to determine which of them are eclipse candidate flares. In Fig. 6.9, I took three examples of these and showed that their emission measure vs time curves can easily be produced by the eclipsing of typical flares. In Section 6.4, I showed that the entire COUP sample contained 62 (29%) eclipse candidates. However, by producing a large modelled set of flares similar to the COUP sample, I showed that although 63% of the modelled flares underwent eclipsing, this was detectable in only 7.0% of them. In Section 6.5, I showed that eclipsing can effect the derived loop lengths for flares, but in most cases such an effect is negligible.

The main results from this chapter are as follows

- It may be possible to constrain the longitudinal position of a flare on its host star if the flare shows clear evidence of eclipsing in its lightcurve. However, other flare parameters cannot be constrained.

- The time variable eclipsing of stellar flares contained within single magnetic loop structures can produce the atypical morphologies observed in the COUP sample. Thus, given a flare with an atypical lightcurve, it is not necessary to invoke unusual physical mecha-

nisms to account for the flare's morphology. However, it should be noted that eclipsing is much more likely to cause an atypical morphology on longer duration flares and on more rapidly rotating stars.

- However, the observed frequency of eclipse candidate flares in the COUP sample is far higher than I would expect if eclipsing was the only mechanism by which atypical flares were being produced. Thus, alternative physical mechanisms, such as the stellar analogies of solar coronal arcades, must be responsible for most of the atypical COUP flares.

- Even in cases where an observed flare has a typical morphology, it is not possible to know from the flare lightcurve alone whether or not eclipsing has taken place.

- Eclipsing is unlikely to have a significant effect on the derived loop lengths. However, in some cases, the derived loop lengths are significantly affected by eclipsing.

7

Summary and Discussion

In this thesis, I investigate the magnetic fields of classical T Tauri stars and model several processes related to stellar magnetism, such as the X-ray emitting coronae, magnetic star-disc interactions, and stellar flares. I specifically concentrate on the sample of CTTSs with ZDI magnetograms that have been published for CTTSs and the set of large stellar flares seen in the Orion Nebula Cluster by the *Chandra* Orion Ultradeep project (COUP). In this chapter, I review the most important results of the preceding chapters.

7.1 Stellar surface magnetic fields

Although measurements of stellar surface magnetic field strengths averaged over the visible surface are useful when trying to understand the magnetic fields, and magnetically related phenomena, such studies give very limited information about the geometries of these fields. For the purposes of investigating several magnetic phenomenon, it is necessary to be able to resolve magnetic field structures. For example, in order to investigate magnetic interaction between a star and its disc, it is necessary to know the strength and structure of the magnetic

field throughout the volume surrounding the star, which is not possible if the only quantity known is a disc averaged field strength. The Zeeman-Doppler Imaging technique allows information to be learned about the large-scale structures of magnetic fields over the surfaces of unresolved stars.

Although the ZDI technique can give information about the structures and strengths of stellar surface magnetic fields, a large amount of magnetic flux that is expected to be present on these stars is not reproduced. Since ZDI magnetograms are used to model stellar coronae, it is necessary to understand how such models are affected by this missing information. There are several reasons for this missing magnetic flux.

- Stellar surfaces are often covered in dark patches that are similar to sunspots, but which cover a much larger fraction of the surface. It is possible that the Zeeman signature from these regions is suppressed, causing the magnetic field strengths to be underestimated in these regions. Based on the solar analogy, they probably correspond to the regions of strongest field, and this could cause the total magnetic fluxes, and surface averaged field strengths, to be underestimated. If flux is only missing in small scale sunspot-like active regions, then this will not affect predictions of the large scale coronal field structures. However, since a large number of stars appear to possess spots that cover a significant fraction of the stellar surface, the large scale field might be affected by missing flux.

- For the ZDI technique to work, the rotation axis of the observed star must be tilted with respect to our line-of-sight. This means that large regions of the stellar surface will not be visible, and the field in those regions cannot be reproduced. This is a fundamental problem that cannot be solved observationally. In order to use surface magnetograms to model the 3D coronal fields of stars, it is necessary to make plausible assumptions about the field in the invisible hemisphere.

- The ZDI technique has a limited ability to resolve field structures on small scales. This probably leads to a large amount of magnetic flux in small scale active regions to be missing from ZDI magnetograms. The resolution of a ZDI magnetogram can be measured by the maximum order spherical harmonic component that can be reliably fit to the observations, and this typically has values of between 2 and 10, with the fastest rotators having the best resolution. However, in order to detect small scale field structures, such as the smaller active regions seen on the Sun, it is necessary to be able to

reproduce spherical harmonic components up to $l \sim 30 - 60$.

Despite this missing magnetic flux, it is still useful to analyse the large scale structures of stellar magnetic fields. For the sample of CTTSs, the strengths and large scale field structures vary from star to star and appear to be related to the evolution of the internal structure of pre-main sequence stars. CTTSs that are too young to have developed a radiative core, and are thus still fully convective, tend to posses very simple dipole fields with kG field strengths. The best example of this is the fully convective CTTS AA Tau. More evolved CTTSs, which posses radiative cores, tend to show much weaker and more complex field structures. This can be seen on stars such as CR Cha and CV Cha. This leads to a strong anti-correlation between field strength and field complexity.

The complexity of the observed ZDI magnetograms in the sample of CTTSs is strongly correlated with rotation rate, with the most complex fields being seen on the fastest rotators, and the simplest fields being seen on the slower rotators. This could be a result of the finite resolution of the ZDI technique, which depends on the star's rotation rate, such that the fastest rotators have the best spatial resolution. However, if this was the case, one would expect that the strongest magnetic field strengths would be seen on the fastest rotators, which is the opposite to what is seen. I propose three plausible scenarios that account for these results.

- Due to star-disc interactions, the stars with the strongest fields tend to spin slower than the stars with the weakest fields. This leads to the anti-correlation between field strength and rotation rate. As the slowest rotators have the poorest resolution, such that the correlation between field complexity and rotation rate is a resolution effect, this leads to the anti-correlation between field complexity and field strength

- Alternatively, the anti-correlation between field complexity and field strength is real and not a resolution effect. In this case, star-disc interactions lead to the simplest fields being on the slowest rotators as a secondary correlation.

- The results may have nothing to do with star-disc interactions, nor the resolution of the ZDI technique. Instead, it may be a result of the spin-up of stars as they contract, and the evolution of the internal structure of pre-main sequence stars. As pre-main sequence stars age, they contract, and in order to conserve angular momentum, they spin-up. At the same time, as they age, they develop radiative cores (if they are massive

enough, which all of the stars in the sample are, except for V2247 Oph) which causes their fields to change from being strong and simple to weak and complex. This leads to the secondary correlations between field strength and rotation rate, and between field complexity and rotation rate.

7.2 3D coronal field structures

Stellar surface magnetograms can be used to predict the 3D structures of the coronal magnetic fields of stars. In order to do this, a number of assumptions must be made. The simplest extrapolation model assumes that the field is potential and decreases in strength to zero at large distances from the star. This may be realistic close to the star (though on the scales of solar active regions the potential assumption can be very poor), but it is not realistic far from the star where the magnetic field is dominated by coronal plasma and stellar winds. It is also a poor approximation for field structures that connect the star with the disc, and may not be good for coronal structures around rapidly rotating stars. Where the coronal plasma pressure dominates over the magnetic pressure, the field is blown open. This can be corrected for in the potential field model by introducing a source surface at which the magnetic field becomes entirely radial.

As this extrapolation model is used to model stellar coronae from ZDI magnetograms (e.g. Jardine et al. 2006; Gregory et al. 2006a; Jardine et al. 2008), it is important to understand how missing magnetic flux in ZDI magnetograms affects the field extrapolations. In general, missing flux in small scale active regions has little effect on the large scale field structure. This can be seen by considering the field as a series of spherical harmonic multipoles. The rate at which the field strength falls off with distance from the stellar surface is different for each multipole. The dipole component decreases as r^{-3}, where r is the distance from the centre of the star. The quadrupole and octupole components decrease as r^{-4} and r^{-5} respectively. The small scale field structures will in general contribute significantly to the higher order multipoles only, and far from the stellar surface have little effect on the field structure. Even if the field is highly complex at the stellar surface, it will still be dipolar at a few stellar radii from the surface. For this reason, I find that the structure of the open magnetic field is little affected by the loss of small scale field structures.

Missing magnetic flux in an entire hemisphere of the star has a significant effect on the extrapolated magnetic structure. If a magnetogram is missing field over almost half of the

stellar surface, large field lines that would have connected the magnetic pole of the visible hemisphere to the magnetic pole of the invisible hemisphere no longer exist. Instead, the extrapolated fields in the visible hemisphere are dominated by medium sized magnetic loops that connect the pole to mid latitude field regions.

I have used field extrapolations for the sample of CTTSs and found some interesting trends in the results[1]. The locations of open and closed magnetic field on the stellar surfaces is strongly dependent on the field complexity. In all cases, regions of open flux are found at the poles, though the sizes of the polar regions of open flux is a function of the field complexity. For simple dipole fields, such as those seen on AA Tau, regions of open field are entirely confined to the magnetic poles. Fields that are dominated by large scale octupoles, such as those seen on TW Hya, have smaller patches of open field at the poles and belts of open field at the equator. More complex fields, such as those seen on MT Ori and V2247 Oph, have very small regions of open flux at the poles, and many regions of open flux distributed over all latitudes in complex patterns.

The total open flux for each of the stars in the sample is determined by the strength of the dipole component and the stellar surface area. This may be important for our understanding of stellar winds and angular momentum loss on evolving pre-main sequence stars. As the stars age, contraction causes their surface areas to decrease. At the same time, if their mass is large enough ($M_* \gtrsim 0.35$ $M_\odot$) they develop radiative cores, which probably causes a decrease in the strength of the dipole component. Thus, it can be expected that the open flux and angular momentum loss due to stellar winds decreases with age on the pre-main sequence.

7.3 Magnetically confined coronae

TTSs show significant levels of X-ray emission with luminosities that are orders of magnitude above the solar value. The majority of this emission most likely originates from closed coronal structures similar to what is seen on the Sun. Thus, in order to properly model coronal X-ray emitting plasma, it is necessary to be able to resolve the field structures that contain the plasma.

On the Sun, other than at activity minimum between cycles, most of the X-ray emission originates from small scale active regions. These are the kind of regions that are not resolved

[1] I should remind the reader that in Chapter 4, the existence and locations of open field is a result of both the source surface assumption and the coronal plasma model.

in ZDI magnetograms, and so it is necessary to understand the effects of this missing magnetic flux. As X-ray emission primarily originates in regions of strong magnetic fields, any realistic coronal model will suffer from the loss of strong fields on small scales by not being able to predict the high plasma densities that would be present in such regions. One observational consequence of this might be the enhancement of observed coronal densities over what would be found in models based on ZDI magnetograms.

I have modelled the X-ray emitting corona for all of the stars in the sample of CTTSs. Although it is clear that large amounts of magnetic flux on small scales are missing from these magnetograms, in all cases it is still possible to explain the large observed X-ray emission measures with magnetically confined coronae based on the flux that is present. This is interesting as there is only a finite amount of emitting plasma that can be held within a corona due to the blowing open of field lines when the plasma pressure dominates over the magnetic field. It would be interesting if a case were to be found where the star's observed X-ray emission measure was above what could be held within its magnetic field. In such a case, the most probable explanation would be that a large amount of the X-ray emitting plasma is contained within magnetic structures that are not resolved on the observed magnetograms, and it may be possible to estimate a lower limit for the amount of magnetic flux that is missing.

It is interesting to try to constrain the size of the closed corona. This can be done by calculating the furthest distance from the stellar surface where the magnetic pressure dominates over the thermal and centrifugal pressures. For the sample of CTTSs, this is typically a few stellar radii. More complex fields fall off with distance from the star much faster than the less complex fields. For instance, for pure dipole fields, the magnetic pressure decreases with radius as r^{-6}. For pure octupole fields, the magnetic pressure decreases with radius as r^{-10}. This is significantly steeper than the decrease in plasma pressure (due to centrifugal forces, plasma pressure increases with radius outside of the corotation radius) and thus the coronal extent is almost entirely dependent on the complexity of the magnetic field. The stellar parameters, such as mass, are less important for determining the coronal extent. This may have implications for the evolution of the coronae in pre-main sequence stars. As pre-main sequence stars develop radiative cores, and their magnetic field structures change from being strong and simple, to weak and complex the sizes of the closed coronae might decrease. This might be observable as an increase in the electron densities derived from coronal X-ray emission spectra in stars with radiative cores.

7.4 Disc truncation and accretion

Another aspect of CTTS magnetism that can be investigated using field extrapolations from ZDI magnetograms is the truncation of the circumstellar disc and magnetospheric accretion. Most early magnetospheric accretion models assumed that the magnetic field is a simple axisymmetric dipole. Given that most of the magnetic fields of CTTSs have more complex geometries than this, it is important to understand how realistic magnetic fields affect disc truncation and accretion. In general, small scale field structures have little effect on accretion models and can be ignored. However, tilted dipole fields and strong large scale octupole components can change the location of the disc truncation radius, and the trajectories of accreting material.

The location of the disc truncation radius is determined by the strength of the magnetic field in the equatorial plane. Stronger fields lead to the disc being truncated further from the stellar surface. For an axisymmetric dipole, the field strength is at a minimum in the equatorial plane. If the dipole is tilted, the field there becomes stronger, thus pushing the disc truncation radius further from the star. For stars with significantly tilted dipole fields, such as TW Hya and MT Ori, the disc can be pushed out by up to a stellar radius. The presence of a strong octupole component can either push the truncation radius away from the star if the octupole and dipole components are anti-parallel, or pull the truncation radius closer to the star if the two components are parallel. In most cases, however, it is not necessary to take into account the tilt in the dipole component, or the higher order multipole components of the magnetic field, and the disc truncation can be approximated by assuming that the field is an axisymmetric dipole.

The trajectories of accreting material and the locations of accretion footpoints are a strong function of the complexity of the magnetic field. Simple axisymmetric dipole fields lead to high latitude accretion impacting the stellar surface in bands extended in longitude around the star. If the dipole is tilted, these bands will not extend all the way around the star, but extend to lower latitudes. Fields that are dominated by large scale octupole components lead to accretion impacting the stellar surface in mid-latitude bands extended in longitude at low latitudes. Highly complex fields lead to complex patterns of accretion footpoints distributed over the stellar surface at a range of latitudes. There are two related reasons for this. As the field complexity in the sample of CTTSs is correlated with field strength, and the strength of

the dipole component, complex fields tend to truncate the discs closer to the stellar surfaces than simple fields. This allows them to be threaded by highly non-dipolar field lines that connect to the stellar surfaces at a range of latitudes and in complex patterns. With simple dipole fields, as they tend to have strong dipole components, the discs are truncated far from the star, and they will be threaded by large dipolar field lines that connect to the stellar surfaces at high latitudes.

It is interesting to compare the disc truncation radii and accretion footpoint locations with the extent of the closed coronae and the locations of open and closed magnetic field. In most cases, the disc is truncated inside or approximately at the maximum radius at which the magnetic field can hold onto the closed corona. However, in a few cases, the magnetic field is blown open by coronal plasma well inside the disc truncation radius. For instance, I predict that the corona of AA Tau only extends out to $\sim$5 R_*, whereas the disc is truncated at $\sim$7 R_*. Although these are only approximations, it is interesting to consider what happens in cases where the field does not have a closed geometry at the inner edge of the disc. This is a possibility that is rarely considered in the literature and requires more sophisticated models than those used in this thesis to investigate further.

7.5 Eclipsing of stellar flares

Stellar flares are the stellar analogue of solar flares; they are large energetic events that involve the impulsive heating of plasma probably confined within coronal magnetic loops. Most observed flares have simple lightcurves, with a single impulsive rise phase and a slow decay phase. However, a large number of flares have significantly more complex lightcurves, with multiple rise phases, or significant dips in their lightcurves. There are several interpretations for these atypical morphologies. They could be the result of multiple heating events in the same magnetic loops, or of the superposition of multiple flare lightcurves. Alternatively, they could be produced from typical flares by the time-variable eclipsing of the flaring plasma due to the rotation of the host star. In order to investigate this possibility, I have used the 216 largest X-ray flares observed as part of the *Chandra* Orion Ultradeep Project (COUP; Getman et al. 2005b). The flares in this sample show a variety of lightcurve morphologies. Getman et al. (2008a) gave a classification scheme for these flares based on their observed lightcurves where flares where classified as *typical flares*, *step flares*, *double flares*, *slow rise top flat flares*, *incomplete flares*, or *other flares*. For the purposes of this investigation, I have used a much sim-

pler classification scheme, where flares are classified as *eclipse candidate flares* or *non-eclipse candidate flares*. I classify 29% of the COUP flares as eclipse-candidate flares.

By fitting modelled eclipsed flares to actual observed X-ray lightcurves, I have shown that the time-variable eclipsing of typical flares can produce the atypical lightcurves seen in the COUP sample. This is especially the case for the step flares and the double flares seen in the COUP sample. I also find that for a sample of flares on stars with stellar parameters similar to those seen in the Orion Nebula, we would only expect to classify 7% as eclipse candidates. This number is significant for two reason. It shows that the probability of a flare being eclipsed by its host star in such a way that its lightcurve looks like that of an eclipse candidate flare is high enough that eclipsing can be expected to produce a significant number of eclipse candidate flares in any large sample of flares. The probability is also high enough that for any flare with an atypical lightcurve, the eclipsing interpretation needs to be considered. However, the fact that the number is so much smaller than the fraction of eclipse candidate flares seen in the COUP sample shows that the time-variable eclipsing of flaring plasma is not the only mechanism responsible for all of the observed eclipse candidate flare lightcurves.

Even though the fraction of eclipse candidate flares that we can expect to see in any sample of flares is relatively low, the fraction of flares that are eclipsed to some extent is very high. In my model, I find that approximately 63% of visible flares (not including those that are eclipsed so much that they will not be counted as flares) have been eclipsed in some way, and 49% of them have reduced peak emission measures. In a large number of these cases, the size or duration of the flare is reduced significantly, while the flare's lightcurve still shows a typical impulsive rise phase, followed by a slow exponential decay. This is significant for any interpretations of flares based solely on their lightcurves as it might not be possible to know that the observed lightcurve is an accurate representation of the actual flaring event. This is significant for any estimations of the lengths of the flaring loops for flares that have been significantly affected by eclipsing.

THE END

Bibliography

Alencar, S. H. P. et al. 2012, ArXiv e-prints, 1203.6331

——. 2010, A&A, 519, A88+, 1005.4384

Altschuler, M. D., & Newkirk, G. 1969, Solar Phys., 9, 131

Angel, J. R. P. 1977, ApJ, 216, 1

Antiochos, S. K., & Sturrock, P. A. 1978, ApJ, 220, 1137

Appenzeller, I., & Wagner, S. 1989, A&A., 225, 432

Argiroffi, C. et al. 2011, A&A., 530, A1, 1102.5751

Arzoumanian, D., Jardine, M., Donati, J.-F., Morin, J., & Johnstone, C. 2011, MNRAS, 410, 2472, 1008.3613

Aschwanden, M. J. 2001, ApJ, 560, 1035

Aschwanden, M. J., & Nitta, N. 2000, ApJ Lett., 535, L59, arXiv:astro-ph/0004093

Aschwanden, M. J., Stern, R. A., & Güdel, M. 2008, ApJ, 672, 659, 0710.2563

Babcock, H. D. 1959, ApJ, 130, 364

Babcock, H. W. 1947, ApJ, 105, 105

——. 1953, ApJ, 118, 387

——. 1958a, ApJS, 3, 141

——. 1958b, ApJ, 128, 228

——. 1961, ApJ, 133, 572

Babcock, H. W., & Babcock, H. D. 1955, ApJ, 121, 349

Barrado Y Navascués, D. 2006, A&A., 459, 511, arXiv:astro-ph/0608478

Basri, G. 2007, in IAU Symposium, Vol. 243, IAU Symposium, ed. J. Bouvier & I. Appenzeller, 13–22

Basri, G., & Bertout, C. 1989, ApJ, 341, 340

Basri, G., Marcy, G. W., & Valenti, J. A. 1992, ApJ, 390, 622

Baumann, I., Schmitt, D., & Schüssler, M. 2006, A&A., 446, 307

Benz, A. O., & Güdel, M. 2010, Annual Review of Astronomy and Astrophysics, 48, 241, http://www.annualreviews.org/doi/pdf/10.1146/annurev-astro-082708-101757

Berdyugina, S. V. 2002, Astronomische Nachrichten, 323, 192

——. 2005, Living Reviews in Solar Physics, 2, 8

Berdyugina, S. V., Fluri, D. M., Afram, N., & Suwald, F. 2008, in Astronomical Society of the Pacific Conference Series, Vol. 384, 14th Cambridge Workshop on Cool Stars, Stellar Systems, and the Sun, ed. G. van Belle, 175

Bertout, C. 1989, Ann. Rev. Astron. Astrophys., 27, 351

Bessolaz, N., Zanni, C., Ferreira, J., Keppens, R., & Bouvier, J. 2008, A&A., 478, 155, 0712.2921

Blake, R. L., Chubb, T. A., Friedman, H., & Unzicker, A. E. 1963, ApJ, 137, 3

Bouvier, J. et al. 2007, A&A., 463, 1017, arXiv:astro-ph/0611787

Bouvier, J., & Appenzeller, I. 1992, A&AS, 92, 481

Bouvier, J., Bertout, C., Benz, W., & Mayor, M. 1986, A&A., 165, 110

Bouvier, J. et al. 1999, A&A., 349, 619

Bouvier, J., Covino, E., Kovo, O., Martin, E. L., Matthews, J. M., Terranegra, L., & Beck, S. C. 1995, A&A., 299, 89

Bouvier, J. et al. 2003, A&A., 409, 169, arXiv:astro-ph/0306551

Brickhouse, N. S., Cranmer, S. R., Dupree, A. K., Luna, G. J. M., & Wolk, S. 2010, ApJ, 710, 1835, 1001.0750

Brown, D. N., & Landstreet, J. D. 1981, ApJ, 246, 899

Brown, J. C. 1971, Solar Phys., 18, 489

Brown, S. F., Donati, J.-F., Rees, D. E., & Semel, M. 1991, A&A., 250, 463

Browning, P. K., & Priest, E. R. 1986, Solar Phys., 106, 335

Camenzind, M. 1990, in Reviews in Modern Astronomy, Vol. 3, Reviews in Modern Astronomy, ed. G. Klare, 234–265

Casanova, S., Montmerle, T., Feigelson, E. D., & Andre, P. 1995, ApJ, 439, 752

Catura, R. C., Acton, L. W., & Johnson, H. M. 1975, ApJ Lett., 196, L47

Charbonneau, P. 2010, Living Reviews in Solar Physics, 7, 3

Chiang, E. I., Joung, M. K., Creech-Eakman, M. J., Qi, C., Kessler, J. E., Blake, G. A., & van Dishoeck, E. F. 2001, ApJ, 547, 1077, arXiv:astro-ph/0009428

Clarke, C. J., Armitage, P. J., Smith, K. W., & Pringle, J. E. 1995, MNRAS, 273, 639, arXiv:astro-ph/9502061

Cohen, M., & Kuhi, L. V. 1979, ApJS, 41, 743

Collier Cameron, A., & Campbell, C. G. 1993, A&A., 274, 309

Collier Cameron, A., Duncan, D. K., Ehrenfreund, P., Foing, B. H., Kuntz, K. D., Penston, M. V., Robinson, R. D., & Soderblom, D. R. 1990, MNRAS, 247, 415

Curran, R. L., Argiroffi, C., Sacco, G. G., Orlando, S., Peres, G., Reale, F., & Maggio, A. 2011, A&A., 526, A104, 1011.5915

Deutsch, A. J. 1958, in IAU Symposium, Vol. 6, Electromagnetic Phenomena in Cosmical Physics, ed. B. Lehnert, 209

Devore, C. R., Boris, J. P., & Sheeley, Jr., N. R. 1984, Solar Phys., 92, 1

Donati, J.-F. et al. 2011a, MNRAS, 412, 2454, 1011.4789

Donati, J.-F., Brown, S. F., Semel, M., Rees, D. E., Dempsey, R. C., Matthews, J. M., Henry, G. W., & Hall, D. S. 1992, A&A., 265, 682

Donati, J.-F. et al. 2003, MNRAS, 345, 1145

Donati, J.-F., & Collier Cameron, A. 1997, MNRAS, 291, 1

Donati, J.-F., Collier Cameron, A., Hussain, G. A. J., & Semel, M. 1999, MNRAS, 302, 437

Donati, J.-F., Forveille, T., Cameron, A. C., Barnes, J. R., Delfosse, X., Jardine, M. M., & Valenti, J. A. 2006a, Science, 311, 633, arXiv:astro-ph/0602069

Donati, J.-F. et al. 2011b, MNRAS, 417, 472, 1106.4162

Donati, J. F. et al. 2012, ArXiv e-prints, 1206.1770

Donati, J.-F. et al. 2011c, MNRAS, 417, 1747, 1109.2447

——. 2006b, MNRAS, 370, 629, arXiv:astro-ph/0606156

——. 2007, MNRAS, 380, 1297, 0709.1414

——. 2008a, MNRAS, 386, 1234, 0802.2052

Donati, J.-F., & Landstreet, J. D. 2009, Ann. Rev. Astron. Astrophys., 47, 333, 0904.1938

Donati, J.-F. et al. 2008b, MNRAS, 390, 545, 0809.0269

——. 2008c, MNRAS, 385, 1179, 0802.1584

Donati, J.-F., Semel, M., Carter, B. D., Rees, D. E., & Collier Cameron, A. 1997, MNRAS, 291, 658

Donati, J.-F., Semel, M., & Praderie, F. 1989, A&A., 225, 467

Donati, J.-F. et al. 2010a, MNRAS, 409, 1347, 1007.4407

——. 2010b, MNRAS, 402, 1426, 0911.1080

Donati, J.-F., Wade, G. A., Babel, J., Henrichs, H. f., de Jong, J. A., & Harries, T. J. 2001, MNRAS, 326, 1265

Dunstone, N. J., Collier Cameron, A., Barnes, J. R., & Jardine, M. 2006, MNRAS, 373, 1308, arXiv:astro-ph/0610106

Duvall, Jr., T. L. 1979, Solar Phys., 63, 3

Eisner, J. A., Hillenbrand, L. A., White, R. J., Akeson, R. L., & Sargent, A. I. 2005, ApJ, 623, 952, arXiv:astro-ph/0501308

Elsner, R. F., & Lamb, F. K. 1977, ApJ, 215, 897

Fares, R. et al. 2009, MNRAS, 398, 1383, 0906.4515

Favata, F., Flaccomio, E., Reale, F., Micela, G., Sciortino, S., Shang, H., Stassun, K. G., & Feigelson, E. D. 2005, ApJS, 160, 469, arXiv:astro-ph/0506134

Feigelson, E. D., Armitage, P. J., & Getman, K. V. 2010, Highlights of Astronomy, 15, 744

Feigelson, E. D., Broos, P., Gaffney, III, J. A., Garmire, G., Hillenbrand, L. A., Pravdo, S. H., Townsley, L., & Tsuboi, Y. 2002, ApJ, 574, 258, arXiv:astro-ph/0203316

Feigelson, E. D., Casanova, S., Montmerle, T., & Guibert, J. 1993, ApJ, 416, 623

Feigelson, E. D., & Decampli, W. M. 1981, ApJ Lett., 243, L89

Feigelson, E. D., & Kriss, G. A. 1989, ApJ, 338, 262

Fisher, G. H., Longcope, D. W., Metcalf, T. R., & Pevtsov, A. A. 1998, ApJ, 508, 885

Flaccomio, E., Damiani, F., Micela, G., Sciortino, S., Harnden, Jr., F. R., Murray, S. S., & Wolk, S. J. 2003, ApJ, 582, 398, arXiv:astro-ph/0208475

Flaccomio, E., Micela, G., Sciortino, S., Feigelson, E. D., Herbst, W., Favata, F., Harnden, Jr., F. R., & Vrtilek, S. D. 2005, ApJS, 160, 450, arXiv:astro-ph/0506164

Geoffray, H., & Monin, J.-L. 2001, A&A., 369, 239

Getman, K. V., Broos, P. S., Salter, D. M., Garmire, G. P., & Hogerheijde, M. R. 2011, ApJ, 730, 6, 1101.4044

Getman, K. V., Feigelson, E. D., Broos, P. S., Micela, G., & Garmire, G. P. 2008a, ApJ, 688, 418, 0807.3005

Getman, K. V., Feigelson, E. D., Grosso, N., McCaughrean, M. J., Micela, G., Broos, P., Garmire, G., & Townsley, L. 2005a, ApJS, 160, 353, arXiv:astro-ph/0504370

Getman, K. V., Feigelson, E. D., Micela, G., Jardine, M. M., Gregory, S. G., & Garmire, G. P. 2008b, ApJ, 688, 437, 0807.3007

Getman, K. V. et al. 2005b, ApJS, 160, 319, arXiv:astro-ph/0410136

Ghosh, P., & Lamb, F. K. 1979a, ApJ, 232, 259

——. 1979b, ApJ, 234, 296

Ghosh, P., Pethick, C. J., & Lamb, F. K. 1977, ApJ, 217, 578

Grankin, K. N., Bouvier, J., Herbst, W., & Melnikov, S. Y. 2008, A&A., 479, 827, 0801.3543

Gras-Velázquez, À., & Ray, T. P. 2005, A&A., 443, 541

Gregory, S. G., Donati, J.-F., Morin, J., Hussain, G. A. J., Mayne, N. J., Hillenbrand, L. A., & Jardine, M. 2012, ArXiv e-prints, 1206.5238

Gregory, S. G., Jardine, M., Collier Cameron, A., & Donati, J.-F. 2006a, MNRAS, 373, 827, arXiv:astro-ph/0609667

Gregory, S. G., Jardine, M., Simpson, I., & Donati, J.-F. 2006b, MNRAS, 371, 999, arXiv:astro-ph/0606682

Gregory, S. G., Matt, S. P., Donati, J.-F., & Jardine, M. 2008, MNRAS, 389, 1839, 0807.0758

Grosso, N., Bouvier, J., Montmerle, T., Fernández, M., Grankin, K., & Zapatero Osorio, M. R. 2007, A&A., 475, 607, 0709.0404

Güdel, M. 2004, A&A Rev., 12, 71, arXiv:astro-ph/0406661

Güdel, M. et al. 2007, A&A., 468, 353, arXiv:astro-ph/0609160

Guenther, E. W., Lehmann, H., Emerson, J. P., & Staude, J. 1999, A&A., 341, 768

Gullbring, E. 1994, A&A., 287, 131

Gullbring, E., Barwig, H., Chen, P. S., Gahm, G. F., & Bao, M. X. 1996, A&A., 307, 791

Gullbring, E., Barwig, H., & Schmitt, J. H. M. M. 1997, A&A., 324, 155

Gullbring, E., Hartmann, L., Briceno, C., & Calvet, N. 1998, ApJ, 492, 323

Hale, G. E. 1908a, ApJ, 28, 315

——. 1908b, ApJ, 28, 100

——. 1913, ApJ, 38, 27

Hale, G. E., Ellerman, F., Nicholson, S. B., & Joy, A. H. 1919, ApJ, 49, 153

Hale, G. E., Seares, F. H., van Maanen, A., & Ellerman, F. 1918, ApJ, 47, 206

Hartmann, L., & Stauffer, J. R. 1989, AJ, 97, 873

Hillenbrand, L. A. 1997, AJ, 113, 1733

Huélamo, N. et al. 2008, A&A., 489, L9, 0808.2386

Hussain, G. A. J. et al. 2009, MNRAS, 398, 189, 0905.0914

——. 2007, MNRAS, 377, 1488, arXiv:astro-ph/0703619

Ilgner, M., & Nelson, R. P. 2006, A&A, 445, 205, arXiv:astro-ph/0509550

Imanishi, K., Nakajima, H., Tsujimoto, M., Koyama, K., & Tsuboi, Y. 2003, PASJ, 55, 653, arXiv:astro-ph/0305170

Ingleby, L., Calvet, N., Hernández, J., Briceño, C., Espaillat, C., Miller, J., Bergin, E., & Hartmann, L. 2011, AJ, 141, 127, 1102.0956

Jardine, M., Collier Cameron, A., Donati, J.-F., Gregory, S. G., & Wood, K. 2006, MNRAS, 367, 917, arXiv:astro-ph/0601213

Jardine, M., & Unruh, Y. C. 1999, A&A., 346, 883

Jardine, M., Wood, K., Collier Cameron, A., Donati, J.-F., & Mackay, D. H. 2002, MNRAS, 336, 1364, arXiv:astro-ph/0207522

Jardine, M. M., Gregory, S. G., & Donati, J.-F. 2008, MNRAS, 386, 688, 0802.2213

Johns-Krull, C. M. 2007, ApJ, 664, 975, 0704.2923

Johns-Krull, C. M., & Valenti, J. A. 2000, in Astronomical Society of the Pacific Conference Series, Vol. 198, Stellar Clusters and Associations: Convection, Rotation, and Dynamos, ed. R. Pallavicini, G. Micela, & S. Sciortino, 371

Johns-Krull, C. M., Valenti, J. A., Hatzes, A. P., & Kanaan, A. 1999a, ApJ Lett., 510, L41

Johns-Krull, C. M., Valenti, J. A., & Koresko, C. 1999b, ApJ, 516, 900

Johnstone, C., Jardine, M., & Mackay, D. H. 2010, MNRAS, 404, 101, 1001.2526

Johnstone, C. P., Gregory, S. G., Jardine, M. M., & Getman, K. V. 2012, MNRAS, 419, 29, 1108.3999

Joy, A. H. 1945, ApJ, 102, 168

Joy, A. H., & Wilson, R. E. 1949, ApJ, 109, 231

Kastner, J. H., Huenemoerder, D. P., Schulz, N. S., Canizares, C. R., & Weintraub, D. A. 2002, ApJ, 567, 434, arXiv:astro-ph/0111049

Kastner, J. H., Huenemoerder, D. P., Schulz, N. S., & Weintraub, D. A. 1999, ApJ, 525, 837, arXiv:astro-ph/9905126

Kemp, J. C. 1970, ApJ Lett., 162, L69

Kenyon, S. J., & Hartmann, L. 1995, ApJS, 101, 117

Koenigl, A. 1991, ApJ Lett., 370, L39

Ku, W. H.-M., & Chanan, G. A. 1979, ApJ Lett., 234, L59

Leighton, R. B. 1964, ApJ, 140, 1547

Lin, R. P., & Hudson, H. S. 1976, Solar Phys., 50, 153

Littlefair, S. P., Naylor, T., Harries, T. J., Retter, A., & O'Toole, S. 2004, MNRAS, 347, 937, arXiv:astro-ph/0310173

Llama, J., Jardine, M., Mackay, D. H., & Fares, R. 2012, MNRAS, L421, 1202.3785

Loinard, L., Torres, R. M., Mioduszewski, A. J., & Rodríguez, L. F. 2008, ApJ Lett., 675, L29, 0801.2192

Long, M., Romanova, M. M., Kulkarni, A. K., & Donati, J.-F. 2011, MNRAS, 413, 1061, 1009.3300

Long, M., Romanova, M. M., & Lovelace, R. V. E. 2005, ApJ, 634, 1214, arXiv:astro-ph/0510659

López-Santiago, J., Crespo-Chacón, I., Micela, G., & Reale, F. 2010, ApJ, 712, 78, 1002.1013

Lynden-Bell, D., & Pringle, J. E. 1974, MNRAS, 168, 603

Mackay, D. H., Jardine, M., Cameron, A. C., Donati, J.-F., & Hussain, G. A. J. 2004, MNRAS, 354, 737

Maggio, A., Sciortino, S., Vaiana, G. S., Majer, P., Bookbinder, J., Golub, L., Harnden, Jr., F. R., & Rosner, R. 1987, ApJ, 315, 687

McCaughrean, M. J., & O'dell, C. R. 1996, AJ, 111, 1977

Ménard, F., Bouvier, J., Dougados, C., Mel'nikov, S. Y., & Grankin, K. N. 2003, A&A., 409, 163, arXiv:astro-ph/0306552

Mendoza V., E. E. 1966, ApJ, 143, 1010

Mewe, R., Heise, J., Gronenschild, E. H. B. M., Brinkman, A. C., Schrijver, J., & den Boggende, A. J. F. 1975, ApJ Lett., 202, L67

Micela, G., Sciortino, S., Serio, S., Vaiana, G. S., Bookbinder, J., Golub, L., Harnden, Jr., F. R., & Rosner, R. 1985, ApJ, 292, 172

Morgenthaler, A. et al. 2011, ArXiv e-prints, 1109.5066

Morin, J. et al. 2008a, MNRAS, 384, 77, 0711.1418

——. 2008b, MNRAS, 390, 567, 0808.1423

Morin, J., Donati, J.-F., Petit, P., Delfosse, X., Forveille, T., & Jardine, M. M. 2010, MNRAS, 407, 2269, 1005.5552

Mullan, D. J., Mathioudakis, M., Bloomfield, D. S., & Christian, D. J. 2006, ApJS, 164, 173

Munro, R. H., & Jackson, B. V. 1977, ApJ, 213, 874

Muzerolle, J., Calvet, N., Briceño, C., Hartmann, L., & Hillenbrand, L. 2000, ApJ Lett., 535, L47

Najita, J. R., Strom, S. E., & Muzerolle, J. 2007, MNRAS, 378, 369, 0704.1681

Neuhaeuser, R., Sterzik, M. F., Schmitt, J. H. M. M., Wichmann, R., & Krautter, J. 1995, A&A., 297, 391

Neupert, W. M. 1968, ApJ, 153, L59+

Nguyen, D. C., Jayawardhana, R., van Kerkwijk, M. H., Brandeker, A., Scholz, A., & Damjanov, I. 2009, ApJ, 695, 1648, 0902.0001

O'dell, C. R., & Wen, Z. 1994, ApJ, 436, 194

O'dell, M. A., Panagi, P., Hendry, M. A., & Collier Cameron, A. 1995, A&A., 294, 715, arXiv:astro-ph/9409023

O'Sullivan, M., Truss, M., Walker, C., Wood, K., Matthews, O., Whitney, B., & Bjorkman, J. E. 2005, MNRAS, 358, 632, arXiv:astro-ph/0501506

Ozawa, H., Grosso, N., & Montmerle, T. 2005, A&A., 429, 963, arXiv:astro-ph/0407241

Padgett, D. L. 1996, ApJ, 471, 847

Pallavicini, R., Golub, L., Rosner, R., Vaiana, G. S., Ayres, T., & Linsky, J. L. 1981, ApJ, 248, 279

Pandey, J. C., & Singh, K. P. 2008, MNRAS, 387, 1627, 0805.3882

Pevtsov, A. A., Fisher, G. H., Acton, L. W., Longcope, D. W., Johns-Krull, C. M., Kankelborg, C. C., & Metcalf, T. R. 2003, ApJ, 598, 1387

Pillitteri, I., Micela, G., Reale, F., & Sciortino, S. 2005, A&A, 430, 155

Pillitteri, I. et al. 2010, A&A., 519, A34, 1004.4617

Pizzolato, N., Maggio, A., Micela, G., Sciortino, S., & Ventura, P. 2003, A&A., 397, 147

Poppenhaeger, K., Günther, H. M., & Schmitt, J. H. M. M. 2012, Astronomische Nachrichten, 333, 26

Preibisch, T. et al. 2005, ApJS, 160, 401, arXiv:astro-ph/0506526

Preston, G. W. 1967, in Magnetic and Related Stars, ed. R. C. Cameron, 3

Prosser, C. F., Randich, S., Stauffer, J. R., Schmitt, J. H. M. M., & Simon, T. 1996, AJ, 112, 1570

Reale, F., Betta, R., Peres, G., Serio, S., & McTiernan, J. 1997, A&A, 325, 782

Reale, F., Güdel, M., Peres, G., & Audard, M. 2004, A&A, 416, 733, arXiv:astro-ph/0312267

Reiners, A. 2012, Living Reviews in Solar Physics, 9, 1, 1203.0241

Reiners, A., & Basri, G. 2010, ApJ, 710, 924, 0912.4259

Reiners, A., Basri, G., & Browning, M. 2009, ApJ, 692, 538, 0810.5139

Reipurth, B., & Zinnecker, H. 1993, A&A., 278, 81

Rhode, K. L., Herbst, W., & Mathieu, R. D. 2001, AJ, 122, 3258, arXiv:astro-ph/0109418

Rieutord, M., & Rincon, F. 2010, Living Reviews in Solar Physics, 7, 2, 1005.5376

Robinson, R. D., Worden, S. P., & Harvey, J. W. 1980, ApJ Lett., 236, L155

Robinson, Jr., R. D. 1980, ApJ, 239, 961

Robitaille, T. P., Whitney, B. A., Indebetouw, R., & Wood, K. 2007, ApJS, 169, 328, arXiv:astro-ph/0612690

Robrade, J., & Schmitt, J. H. M. M. 2006, A&A., 449, 737, arXiv:astro-ph/0601234

Romanova, M. M., Long, M., Lamb, F. K., Kulkarni, A. K., & Donati, J.-F. 2011, MNRAS, 411, 915

Romanova, M. M., Ustyugova, G. V., Koldoba, A. V., & Lovelace, R. V. E. 2004, ApJ, 610, 920, arXiv:astro-ph/0404496

Romanova, M. M., Ustyugova, G. V., Koldoba, A. V., Wick, J. V., & Lovelace, R. V. E. 2003, ApJ, 595, 1009, arXiv:astro-ph/0401375

Saar, S. H. 1990, in IAU Symposium, Vol. 138, Solar Photosphere: Structure, Convection, and Magnetic Fields, ed. J. O. Stenflo, 427–441

Saar, S. H. 1996a, in IAU Symposium, Vol. 176, Stellar Surface Structure, ed. K. G. Strassmeier & J. L. Linsky, 237

Saar, S. H. 1996b, in IAU Colloq. 153: Magnetodynamic Phenomena in the Solar Atmosphere - Prototypes of Stellar Magnetic Activity, ed. Y. Uchida, T. Kosugi, & H. S. Hudson, 367–374

Saar, S. H. 2001, in Astronomical Society of the Pacific Conference Series, Vol. 223, 11th Cambridge Workshop on Cool Stars, Stellar Systems and the Sun, ed. R. J. Garcia Lopez, R. Rebolo, & M. R. Zapaterio Osorio, 292

Saar, S. H., Piskunov, N. E., & Tuominen, I. 1992, in Astronomical Society of the Pacific Conference Series, Vol. 26, Cool Stars, Stellar Systems, and the Sun, ed. M. S. Giampapa & J. A. Bookbinder, 255–258

Sabine, E. 1852, Philosophical Transactions of the Royal Society of London, 142, pp. 103

Safier, P. N. 1998, ApJ, 494, 336, arXiv:astro-ph/9709158

Sanz-Forcada, J., Favata, F., & Micela, G. 2006, A&A, 445, 673, arXiv:astro-ph/0510567

——. 2007, A&A, 466, 309, arXiv:astro-ph/0701814

Schegerer, A., Wolf, S., Voshchinnikov, N. V., Przygodda, F., & Kessler-Silacci, J. E. 2006, A&A., 456, 535, arXiv:astro-ph/0604059

Schmitt, J. H. M. M., & Favata, F. 1999, Nat, 401, 44, arXiv:astro-ph/9909040

Schmitt, J. H. M. M., Ness, J., & Franco, G. 2003, A&A, 412, 849, arXiv:astro-ph/0308394

Schmitt, J. H. M. M., & Robrade, J. 2007, A&A., 462, L41

Schmitt, J. H. M. M., Robrade, J., Ness, J.-U., Favata, F., & Stelzer, B. 2005, A&A., 432, L35, arXiv:astro-ph/0503144

Schrijver, C. J., Cote, J., Zwaan, C., & Saar, S. H. 1989, ApJ, 337, 964

Schrijver, C. J., & Title, A. M. 2001, ApJ, 551, 1099

Schwabe, M. 1844, Astronomische Nachrichten, 21, 233

Semel, M. 1989, A&A., 225, 456

Sheeley, Jr., N. R. 2005, Living Reviews in Solar Physics, 2, 5

Shu, F., Najita, J., Ostriker, E., Wilkin, F., Ruden, S., & Lizano, S. 1994, ApJ, 429, 781

Siess, L., Dufour, E., & Forestini, M. 2000, A&A., 358, 593, arXiv:astro-ph/0003477

Skinner, S. L., Guedel, M., Koyama, K., & Yamauchi, S. 1997, ApJ, 486, 886

Skumanich, A. 1972, ApJ, 171, 565

Smith, K. W., Lewis, G. F., Bonnell, I. A., Bunclark, P. S., & Emerson, J. P. 1999, MNRAS, 304, 367

Snodgrass, H. B. 1983, ApJ, 270, 288

Stelzer, B., Neuhäuser, R., Casanova, S., & Montmerle, T. 1999, A&A, 344, 154, arXiv:astro-ph/9901317

Stelzer, B., & Schmitt, J. H. M. M. 2004, A&A., 418, 687, arXiv:astro-ph/0402108

Stempels, H. C., & Piskunov, N. 2003, A&A., 408, 693

Strassmeier, K. G. 2009, A&A Rev., 17, 251

Strom, K. M., Strom, S. E., Edwards, S., Cabrit, S., & Skrutskie, M. F. 1989, AJ, 97, 1451

Telleschi, A., Güdel, M., Briggs, K. R., Audard, M., & Scelsi, L. 2007, A&A., 468, 443, arXiv:astro-ph/0611024

Terquem, C., & Papaloizou, J. C. B. 2000, A&A., 360, 1031, arXiv:astro-ph/0006113

Testa, P., Drake, J. J., & Peres, G. 2004, ApJ, 617, 508, arXiv:astro-ph/0405019

Tognelli, E., Prada Moroni, P. G., & Degl'Innocenti, S. 2011, A&A., 533, A109, 1107.2318

Torres, G., Guenther, E. W., Marschall, L. A., Neuhäuser, R., Latham, D. W., & Stefanik, R. P. 2003, AJ, 125, 825, arXiv:astro-ph/0211157

Vaiana, G. S. et al. 1981, ApJ, 245, 163

Valenti, J. A., Basri, G., & Johns, C. M. 1993, AJ, 106, 2024

van Ballegooijen, A. A., Cartledge, N. P., & Priest, E. R. 1998, ApJ, 501, 866

Vilhu, O. 1984, A&A., 133, 117

Voges, W. et al. 1999, A&A., 349, 389, arXiv:astro-ph/9909315

Vrba, F. J., Rydgren, A. E., Chugainov, P. F., Shakovskaia, N. I., & Weaver, W. B. 1989, AJ, 97, 483

Vrba, F. J., Rydgren, A. E., Chugainov, P. F., Shakovskaia, N. I., & Zak, D. S. 1986, ApJ, 306, 199

Walter, F. M., & Kuhi, L. V. 1981, ApJ, 250, 254

——. 1984, ApJ, 284, 194

Wang, Y.-M., Nash, A. G., & Sheeley, Jr., N. R. 1989, ApJ, 347, 529

Wang, Y.-M. et al. 1997, ApJ, 485, 419

Weise, P., Launhardt, R., Setiawan, J., & Henning, T. 2010, A&A., 517, A88

Williams, J. P., & Cieza, L. A. 2011, Ann. Rev. Astron. Astrophys., 49, 67, 1103.0556

Wood, B. E., Brown, A., Linsky, J. L., Kellett, B. J., Bromage, G. E., Hodgkin, S. T., & Pye, J. P. 1994, ApJS, 93, 287

Wright, N. J., Drake, J. J., Mamajek, E. E., & Henry, G. W. 2011, ApJ, 743, 48, 1109.4634

Yang, H., & Johns-Krull, C. M. 2011, ApJ, 729, 83, 1102.3662

Yang, H., Johns-Krull, C. M., & Valenti, J. A. 2005, ApJ, 635, 466, arXiv:astro-ph/0509549

——. 2007, AJ, 133, 73, arXiv:astro-ph/0609289

——. 2008, AJ, 136, 2286, 0809.3290